UNIVERSITY OF SOUTHAMPTON

FACULTY OF ENGINEERING, SCIENCE AND MATHEMATICS

School of Ocean and Earth Sciences

DEVELOPMENT AND APPLICATION OF A HIGH RESOLUTION 3D CHIRP SUB-BOTTOM PROFILING SYSTEM

Martin Gutowski

Thesis for the degree of Doctor of Philosophy

November 2004

Graduate School of the Southampton Oceanography Centre

This PhD dissertation by

Martin Gutowski

has been produced under the supervision of

Supervisors
Dr Jon Bull
Dr Justin Dix

Chair of Advisory Panel
Dr John Marshall

Member of Advisory Panel
Dr Tim Henstock

UNIVERSITY OF SOUTHAMPTON

ABSTRACT

FACULTY OF ENGINEERING, SCIENCE AND MATHEMATICS
SCHOOL OF OCEAN AND EARTH SCIENCES
~~Doctor of Philosophy~~

DEVELOPMENT AND APPLICATION OF A HIGH RESOLUTION 3D CHIRP SUB-BOTTOM PROFILING SYSTEM

by Martin Gutowski

Chirp sub-bottom profilers are widely used to collect high resolution 2D marine seismic data with high signal-to-noise ratio using repeatable source signatures. This thesis describes the development of the first 3D Chirp system.

During the design of a high resolution 3D seismic system critical factors need to be considered including correct spatial sampling of the recorded data and the sufficiently accurate positioning of source and receiver elements. Correct spatial sampling of the recorded data was assured by determining optimal source array and receiver group geometries by numerical modelling of reflection amplitudes using a model which includes frequency dependent directivities of the acquisition system components. The system design incorporates 60 receiver groups with 25 cm spacing in both horizontal directions and four source transducers arranged into a Maltese cross geometry or as a double pair. The source array and receiver groups are fixed on a 2.2 m x 2.5 m rigid structure that is surface towed from small survey vessels. Real Time Kinematic GPS and a GPS-based attitude system are used to position the source arrays and receiver groups with centimetre accuracy. Additionally the development and testing of source signatures, operating on a bandwidth of 1.5 to 13 kHz and to be used with the system, are discussed.

The first 3D Chirp dataset was acquired in the West Solent (UK), covering an area of 75 m x 750 m. It is processed, using newly developed geometry processing routines, to produce a fully sampled 3D data volume. Visualisation and analysis of the seismic data volume reveal dipping structures, which are interpreted as sedimentary rocks of the Headon Hill formation of Eocene age.

Contents

List of Figures

List of Tables

Acknowledgements

I would like to thank the following people who have made this work possible:

Primarily my supervisors Dr Jon Bull and Dr Justin Dix for their guidance and support; Dr Tim Henstock for valuable discussion and support; Prof. Timothy Leighton and Prof. Paul White from the Institute of Sound and Vibration Research (ISVR) at Southampton University for their advice and in particular for their comments on the work presented in Chapter 2.

Peter Hogarth (GeoAcoustics Ltd) for his input into the design solution and for valuable general advice. Paul King (GeoAcoustics Ltd) is thanked for help with tank tests at the company.

Dave Whatley and Michael Street from the Engineering Design and Manufacturing Centre (EDMC) of Southampton University for their contribution to the design and discussion and the latter for supplying the 3D Chirp design drawings for Chapter 5. Adrian Lester is acknowledged for his help in furthering the final design.

Ray Collins for solving storage and deployment of the 3D chirp system from R/V Bill Conway, while I am grateful to Graham Etheridge for steering the Bill Conway with such dedication and skill during data collection.

Simon Dean for the technical support with the seismic processing and interpretation systems used.

John Davis, Dr Phil Cole, Dr Angus Best, Dr Gary Robb, Dr Alex Bastos, Ed Morris for their help with field work.

Dr John Marshall who acted as chair of my advisory panel.

I dedicate this thesis to my parents and thank them for their unconditional support. I also thank my wife Eva for moral and professional support.

Finally I acknowledge financial support from the Engineering and Physical Sciences Research Council (EPSRC) and the Ministry of Defence under The Joint Grant Scheme with additional financial and logistical support from GeoAcoustics Ltd., Great Yarmouth.

List of Acronyms

A/D	Analog to Digital
AGC	Automatic Gain Control
ASCII	American Standard Code for Information Interchange
CAM	Computer Aided Manufacturing
CDP	Common Depth Point
CHAN	Channel
COG	Centre of Gravity
DDS	Digital Data Storage
DGPS	Differential Global Positioning System
EDMC	Engineering Design and Manufacturing Centre
FFID	Field File Identification number
FFT	Fast Fourier Transform
FM	Frequency Modulated
GMT	Generic Mapping Tool
GPR	Glass Reinforced Plastic
GPS	Global Positioning System
IFF	Instantaneous Frequency Function
ILN	Inline
iline	inline
Inc	Incorporation
Ltd	Limited
OFF	Ordered Parameter File
PC	Personal Computer
pps	pulse per second
PVC	Polyvinyl Chloride
QC	Quality Control
RAID	Redundant Array of Independent Disks
RTK	Real Time Kinematic
R/V	Research Vessel
SCSI	Small Computer Systems Interface
SIN	Shot Index Number

SEG	Society of Exploration Geophysicists
SNR	Signal to Noise Ratio
SOC	Southampton Oceanography Centre
TRC	**Trace**
TWT	Two Way Time
UHF	Ultrahigh Frequency
UK	United Kingdom
UTM	Universal Transverse Mercator
VHR	Very High Resolution
WGS84	World Geodetic System 1984
XLN	Crossline
xline	crossline

1 Introduction

1.1 Rationale

1.1.1 2D and 3D reflection seismology

The method of controlled source seismic exploration was first applied on a large scale in the 1920's when refraction seismic methods were used for detection of hydrocarbon resources associated with salt dome structures, although extensive theoretical and experimental work on wave propagation in the Earth had been carried out throughout the 19th century (Sheriff and Geldart, 1995). Reflection seismic surveys, also pioneered in the 1920's, took over from the refraction seismic method in hydrocarbon exploration among other applications in the following decades. The first large scale reflection seismic marine surveys were carried out in the 1940's. Advances in technology, such as digital recording of seismic data and use of computers for data processing in the 1960's lead to major advances in seismic data acquisition, handling and processing.

Initially both terrestrial and marine seismic reflection data were solely recorded along single lines, producing cross sections of the sub-surface. The representation of reflections associated with seismic waves propagating in a three dimensional half-space in 2D cross sections can produce misleading results. Features that are located out of the plane of the seismic line may be represented on the section. By recording seismic data along lines that form a closely spaced grid, a method sometimes referred to as 2.5D surveying, the three dimensional structure is deduced by interpolating between lines. Also in this case the data associated with 3D wavefield is handled independently for every 2D section. The errors introduced by this practice lead to ambiguities in the interpolation and features might be missed or misinterpreted. To fully represent the three dimensional wavefield data need to be collected over an area, instead of merely along lines, and processed with consideration to the three dimensional nature of the seismic wave propagation. The result is a volume of seismic data rather than a grid of seismic cross-sections.

The terrestrial 3D reflection seismic method was introduced in the late 1970's and the first large scale 3D marine surveys were carried out in the 1980's for hydrocarbon exploration. Advances in positioning technology, such as the commercial use of the global positioning system (GPS) and ever evolving computing power in the 1990's and recent years made 3D seismic reflection surveying the standard tool for hydrocarbon exploration. Reducing costs of data acquisition and the ability to handle the data on low cost computer systems made the method also available to the academic research community in recent years for the study of sub-surface structures (e.g.; Hobbs et al., 2003, Huvenne et al., 2003; Huuse and Mickelson, 2004).

1.1.2 High resolution 2D seismics - sub-bottom profilers

The marine seismic reflection systems used for hydrocarbon exploration typically have a penetration into the sub-surface of some kilometres and resolution of tens of meters. High resolution seismic in this context refers to sources with some hundred Hertz mean frequencies. As Earth acts as a low pass filter for seismic waves there is a trade-off between penetration and resolution. A number of high resolution marine reflection systems with frequency contends of some hundred to some kilohertz, often referred to as sub-bottom profiling systems, have been developed to delineate the upper tens to hundreds of meters of the sub-surface. These are mostly used as single channel normal incidence systems. Their application lies in **geological/geophysical,** geo-technical, archaeological and offshore engineering studies of the shallow sub-surface. The most commonly used systems comprise the pinger, boomer, sparker or the Chirp system, whose specifications are compared in Table 1.1, together with those of watergun and airgun sources used for high resolution 3D seismic application described in section 1.1.4.

System	Frequency content **[kHz]**	Vertical resolution [m]	Penetration [m]
Chirp	**0.4-20**	**<0.1-0.2"**	**10-40**
Pinger[f]	**3-12**	**0.2**	**10-40**
Boomer^	1-5	**0.5-1**	**50 -100**
Sparker[1]	0.1 - 1	2	**100 - 1000**
Modified Watergun*	**0.1-0.6**	2	**100**
Mini Airgun **(SOLERA)"**	**0.05-0.65**	**1.25**	**200**

Table 1.1 Typical frequency content, vertical resolution and penetration of conventional sub-bottom profiling systems. Note that the penetration strongly depends on the sampled sub-surface. *Vertical resolution depends on the source signature used as discussed in Chapter 2. f After Kearey and Brooks (1991). # Used in high resolution 3D seismic application described in section 1.1.4, the resolution and penetration listed are estimates of the authors.

1.1.3 Chirp technology

Chirp systems are wide-band, frequency-modulated (FM), sub-bottom profilers. They produce high-quality, high-resolution, normal incidence seismic reflection data. They were first developed at the University of Rhode Island under a program that started in 1981

(Schock and LeBlanc, 1990). The researchers found the existing systems (boomer, sparker, pinger) insufficient for quantitative measurements. These systems showed poor pulse repeatability (the variations of amplitude and phase of the transmitted pulse), low signal to noise ratio, poor vertical resolution caused by source ringing and inadequate system bandwidth, variation of the projector response with submergence pressure and uncalibrated and non-linear electronics. The Chirp system was designed to overcome these deficiencies. Chirp systems comprise calibrated, linear electronics that are capable of producing a highly repeatable source signature (Schock and LeBlanc, 1990). They transmit a frequency modulated signal that is corrected for the source and receiver phase and amplitude responses. Due to the wide bandwidth of the signal optimum penetration as well as resolution can be achieved. The signal to noise ratio is improved through matched filter processing by correlating the reflection data with the transmitted pulse.

Chirp sub-bottom profilers have been widely used for geological/geophysical (e.g. Quinn et al, 1997a, Jakobsson, 1999), geo-technical (e.g. Selby and Foley, 1995, Kim et al., 1999) and archaeological (e.g. Quinn et al., 1997b, Bull et al., 1998) applications. Using the characteristics of the Chirp data various methods for sediment classification based on seismic properties estimations have been developed (Schock et al., 1989; LeBlanc et al., 1992; Panda et al., 1994; Stevenson et al., 2003).

1.1.4 High resolution 3D seismics - previous research

There have been various attempts over recent years to downscale the 3D reflection seismic method to produce high resolution 3D seismic data volumes by using sub-bottom profiler sources. This downscaling must include reducing the data sampling grid spacing to a metre or sub-metre scale to increase horizontal and vertical resolution.

To produce a high resolution 3D seismic data volume the wavefield generated by the sub-bottom profiler source needs to be sampled adequately. The acquisition geometry needs to be designed to avoid spatial aliasing, which is dependent on the source signal used. Furthermore the absolute positions of source and receiver need to be known with accuracy on the same scale as the wavelengths present in the dataset.

Henriet et al. (1992) and Versteeg et al. (1992) describe a system using boomer and watergun sources positioned on a catamaran towing 12 dual-channel streamers. The catamaran is positioned using an on-shore based laser ranging theodolite system with a corresponding prism crown situated on the catamaran. The receiver elements positioned in the streamers are assumed to maintain a constant relative position to the catamaran. The

system is designed to sample a 1 x 1 m bin grid. Marsset et al. (1998) discuss processing techniques applicable to data collected with the system including corrections for tidal heights and different migration algorithms and show that the data quality can be improved. In the framework of the European Commission MAST3 project 'VHR3D - Very high resolution marine 3D seismic method for detailed site investigation' (Marsset et al., 2001), a so called compact flexible system (Missiaen et al., 2002), was developed consisting of a rigid hull inflatable boat, **flanked** by two **inflated** parts with an overall width of 14 m from which eight dual channel streamers are deployed. The boomer source with a mean frequency of 2 kHz is towed from the boat. During the project the positioning technology was changed from the previously used laser tracking theodolite to a global positioning system (GPS) based real-time-kinematic (RTK) system, offering centimetre accuracy. The data was collected aiming at a bin size of 1 m with the acquisition geometry designed to avoid spatial aliasing.

In this system, as in the system described by Henriet et al. (1992), only the absolute position of the source is known and the relative positions of the receiver groups are assumed to be fixed. However, the relative positions of the receiver elements, positioned in towed streamers, are in reality variable and depend on wave motions and currents. Therefore a methodology based on seafloor reflection time information was developed to correct for small scale variations in the relative positions of source as part of the data processing (Wardell et al., 2001). However, as this presents an under-determined inverse problem, this method has resulted in sub-optimal data quality. It is pointed out by the authors that a more accurate positioning of source and receivers is desirable for optimal performance of the system.

Mtiller et al. (2002) propose a 3D high resolution system using a boomer source and multi-channel streamers, emphasizing the importance of accurate positioning, the stability of the source signature and the importance of adequate acquisition geometry for the source signal used in particular the spacing of receiver elements within the group to avoid destructive interference of signals stacked within the group.

Scheidhauer et al. (2003) and Dupuy et al. (2004) describe a system using a mini airgun source and three 24 channel streamers towed from a small (13 m) research vessel to collect a 3D high resolution dataset with a bin size of 1.25 m in inline and 3.75 m in crossline direction over an area of approximately 1 km^2. Differential GPS (DGPS) antennas are mounted on the towing vessel as well as on floats attached to the ends of the streamers, allowing the computation of absolute positions of the source and receiver groups with adequate accuracy. A dataset was collected at Lake Geneva, Switzerland, converted into a high quality 3D data volume imaging lacustrine sediments with approximately 200 m penetration, a vertical resolution of approximately 1.25 m and a horizontal resolution of up to 4.5 m after application of 3D post-stack migration.

Schock et al. (2001) describe a deep towed buried object scanning sonar using Chirp technology. It operates with a line source array that uses beam-steering and a planar receiver array with 32 hydrophones distributed in an area of 83 x 83 cm^2. It operates near the seabed and collects a 3D data volume along its track which is then processed to image shallow buried objects in real time. The authors claim a spatial resolution of 10-20 cm and a vertical resolution of 3 - 4 cm and a penetration of some meters. It is designed to detect small scale buried objects along a single profile rather than producing a high resolution 3D data volume.

Table 1.2 summarises the specifications of the above mentioned high resolution 3D seismic systems.

System	Source	Channels	CDP bin size [m]	Positioning system
Henriet at al. (1992), Versteeg et al. (1992), Marsset et al. (1998)	Boomer, modified watergun	24	1	Laser ranging theodolite
Marsset et al (2001), Missiaen et al. (2001)	Boomer	16	1	RTK-GPS
Müller et al. (2002)	Boomer	48 + 12	†	DGPS
Scheidhauer et al. (2003), Dupuy et al. (2004)	Airgun	24	1.25x3.75	DGPS
Schock et al. (2001)*	Chirp	32	#	#

Table 1.2 Comparison of existing 3D high resolution systems. † no 3D data processing performed to date, system development in progress. # Deep towed buried object scanning sonar that produces a 3D data volume along single profile using specialised data processing techniques. RTK-GPS: Real-Time-Kinematic GPS. DGPS: Differential GPS.

1.2 Objectives

The objectives of this thesis are:

- The development and testing of source signatures for the Chirp sub-bottom profiler system to investigate different compromises between resolution and penetration.
- The development of a 3D Chirp sub-bottom profiler system capable of producing a 3D data volume imaging sub-surface structures on a decimetre horizontal and vertical scale with some tens of meter penetration over a typical survey area of some hundred metres on a side.
- Acquisition and processing of a high resolution 3D data volume.
- Visualisation, analysis and interpretation of the data volume.

1.3 Context of thesis

This thesis was completed as part of a larger project on the design and testing of a 3D Chirp system which was funded by the Engineering and Physical Sciences Research Council and the Ministry of Defence as part of the Joint Grant Scheme. Additional funding was provided by GeoAcoustics Ltd. which are a partner company in the development of the system. The project overlaps the period of the PhD and is due to finish in late 2004. The principal investigators on this Southampton University based project were Jon Bull, Justin Dix and Tim Henstock from the Southampton Oceanography Centre and Tim Leighton and Paul White from the Institute of Sound and Vibration Research. The author worked as a research assistant in the project and was named on the project proposal.

The aims of the larger project overlap with the thesis objectives, and it is important to emphasize the relative contributions of the Principal Investigators and the author of the thesis. The design solution described in Chapter 5 was not led by the author and represents the input from all principal investigators, Peter Hogarth from GeoAcoustics Limited, and Dave Whatley and Mike Street from the Engineering and Manufacturing Design Centre (University of Southampton), as well as the author. Responsibility for final design decisions rests with the lead investigator Jon Bull. Work presented in other Chapters is by the author, carried out under supervision of Jon Bull, Justin Dix and Tim Henstock.

1.4 Synopsis

The contents of the thesis are briefly outlined below.

Chapter 2 describes the development and testing of Chirp source signatures. Methodologies are developed and applied to seven contrasting source signatures to assess their resolution and attenuation characteristics.

Chapter 3 presents acquisition geometry considerations for the 3D Chirp acquisition array design. A model of seismic reflection amplitudes, based on the frequency-dependent directivity of source elements and arrays and receiver groups, is used to determine an optimal configuration of the source arrays and receiver groups and the receiver group spacing to avoid spatial aliasing of the recorded data and ensure optimum horizontal resolution. The acquisition geometry is constrained by the maximum dimension of the array of 2.5 m in either horizontal direction to make it deployable from small survey vessels and a total of four source elements and a maximum of 60 receiver groups.

Chapter 4 introduces the acquisition element positioning solution. It is explained why a centimetre positioning accuracy for the source array and receiver groups is required. The use of a GPS based attitude system and a Real-Time-Kinematic (RTK) GPS system are proposed to determine the absolute positions of the elements mounted on a rigid array by utilising a newly determined algorithm. The accuracies of the positioning system are tested against the manufacturer's specification and the required accuracies. Additionally its reliability and suitability for the marine application are tested.

Chapter 5 incorporates initial constraints, additional considerations, including towing behaviour and ground coverage, and findings from Chapters 3 and 4 into the 3D Chirp sub-bottom profiler design. The final design is presented together with the specifications for a recording system. Finally, the assembly and successful towing tests of the 3D Chirp system are described.

Chapter 6 presents the acquisition and processing of a 3D high resolution seismic dataset that images dipping sedimentary rocks from a location in the West Solent (UK).

Chapter 7 presents the 3D Chirp data volume. Representative inline, crossline, traverse and time-slice sections are shown, and the data are analysed by comparing the 3D data volume to 2D sections and furthermore by comparing the data quality to the data coverage expressed by the CDP fold of the data grid. An integrated study of the imaged geological structures is presented putting the imaged strata into a geological context.

Chapter 8 contains the conclusions of this work.

2 Chirp source signature design and field testing*

2.1 Introduction

Chirp systems comprise calibrated, linear electronics that are capable of producing a highly repeatable source signature (Schock and LeBlanc, 1990). They transmit a frequency modulated (FM) signal that is corrected for the source and receiver phase and amplitude responses. Owing to the wide bandwidth of the signal, optimum penetration as well as resolution can be achieved. The signal-to-noise-ratio (SNR) is improved through matched filter processing by correlating the reflection data with the transmitted pulse. Chirp systems typically operate within a range of 400 Hz - 24 kHz and offer a vertical resolution on a decimetre scale in the top c. 20-30 m of unconsolidated sediments. The land analogue of the Chirp systems, albeit much lower frequency, typically below 1 kHz, is the Vibroseis mechanical vibrator technique. One of the main concerns with land swept frequency systems is validation of the form of the pulse actually transmitted into the sub-surface. Validation of Chirp source signatures is much more straightforward, and is commonly completed in water-filled test tanks. There has been some work completed on Vibroseis and Chirp source signatures, which is summarised below.

Goupillaud (1976) investigated sweeps for the Vibroseis system and discussed sweeps with a constant amplitude function but varying instantaneous frequency function (IFF). He studied the difference between sweeps with linear and non-linear IFFs, here referred to as linear and non-linear sweeps. He concluded that a non-linear sweep could be viewed as a filter which controlled the spectrum shapes, and that the use of such a sweep is equivalent to the use of a linear sweep with successive filtering provided that the earth resembles a linear filter. Although Goupillaud found that this is approximately true for the frequency range of 12-75 Hz of the investigated sweeps, this might not be true for high frequency, wider bandwidth sweeps. Additionally he presented one experimental example, which showed some differences between the non-linear and the filtered linear sweep.

---

* The work presented in this Chapter has been published as: Gutowski, M., Bull, J., Henstock, T., Hogarth, P., Leighton, T., White, P., 2002, Chirp sub-bottom profiler source signature design. *Marine Geophysical Researches* 23, 481-492.

The influence of the envelope function for linear sweeps on the auto-correlation function was investigated by Cunningham (1979). He points out that by using an envelope function the correlation side-lobes of the correlated signal will be significantly reduced. However, the use of envelope functions led to a reduction of energy output and reduced the bandwidth of the signal, resulting in a wider main-lobe of the correlation function and a reduced spatial resolution.

Schock et al. (1994) suggested a linear sweep for a Chirp system with a Blackman-Harris envelope shape (Harris, 1978) for the use in Chirp systems. These authors indicate that such a sweep would have a very low side-lobe level. Moreover they showed that the sweep maintains its bandwidth and shape when attenuated with a linear frequency dependency, experiencing only a decrease in amplitude. Additionally, if a non-linear attenuation for seafloor sediments occurs (such as that demonstrated by Jacobson, 1987 and Hamilton, 1980), then the loss in bandwidth and the resulting widening of the autocorrelation function of the sweep, known as the Klauder wavelet, are relatively small compared to sweeps with other envelope functions.

The advantage of being able to control precisely the source signature is that the source sweep used can be optimised according to survey task and the vertical resolution and penetration characteristics required. In order to discriminate quantitatively between different source signatures, a new methodology is described that provides useful data on *relative* vertical resolution and rate of attenuation. A number of newly developed source sweeps are presented, that differ in their envelope and instantaneous frequency functions. The sweeps were used in sea trials off the north coast of the Isle of Wight (UK) in which a 650 m long seismic profile was repeatedly measured with different source sweeps. The sections are analysed for their resolution and attenuation, and compared with theoretical predictions. To analyse the resolution a new vertical resolution criteria is presented, as traditional criteria can not be applied for a quantitative comparison.

2.2 Sweep design

Seven different source sweeps listed in Table 2.1 are examined.

sweep	frequency range [kHz]	envelope function	IFF	-3dB amplitude bandwidth [kHz]	f_{mean} [kHz]
SI	2-8	Blackmann-Harris	linear	1.72	4.50
S2	1.5-11.5	Blackmann-Harris	linear	3.38	6.50
S3	1.5-13	Gauss	quadratic	2.54	4.48
S4	1.5-13	Chi reversed	logarithmic	1.94	3.25
S5	1.5-13	Chi	linear	2.66	4.30
S6	1.5-13	sine-squared 4th	linear	7.82	7.25
S7	1.5-13	sine-squared 8th	linear	9.65	7.25

Table 2.1 A summary of the characteristics of the source sweeps examined. IFF: instantaneous frequency function.

Figures 2.1 - 2.7 summarise the characteristics of each sweep detailing, in each case, (a) the time domain representation; (b) the amplitude spectrum; (c) the spectogram which shows the variation in spectral content with time on a dB scale, revealing the sweeps instantaneous amplitude function; and (d) the Klauder wavelet.

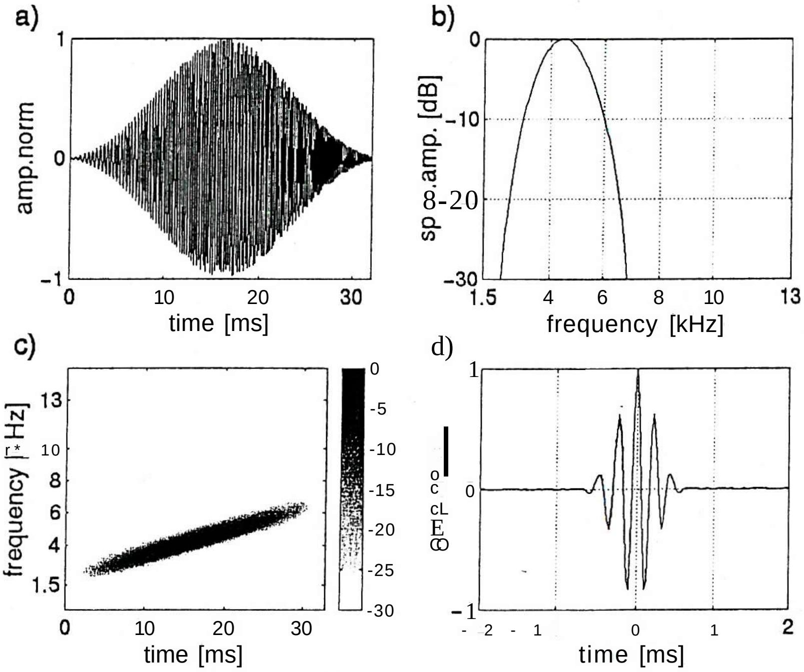

Figure 2.1 Source sweep SI. Standard linear low frequency sweep with Blackmann-Harris envelope function, a) Time domain representation, b) Power spectrum with a mean frequency of 4.5 kHz. c) Spectrogram showing the linear IFF. The greyscale represents the same dB scale as in the spectrum, d) Klauder wavelet, the normalised auto-correlation function of the sweep.

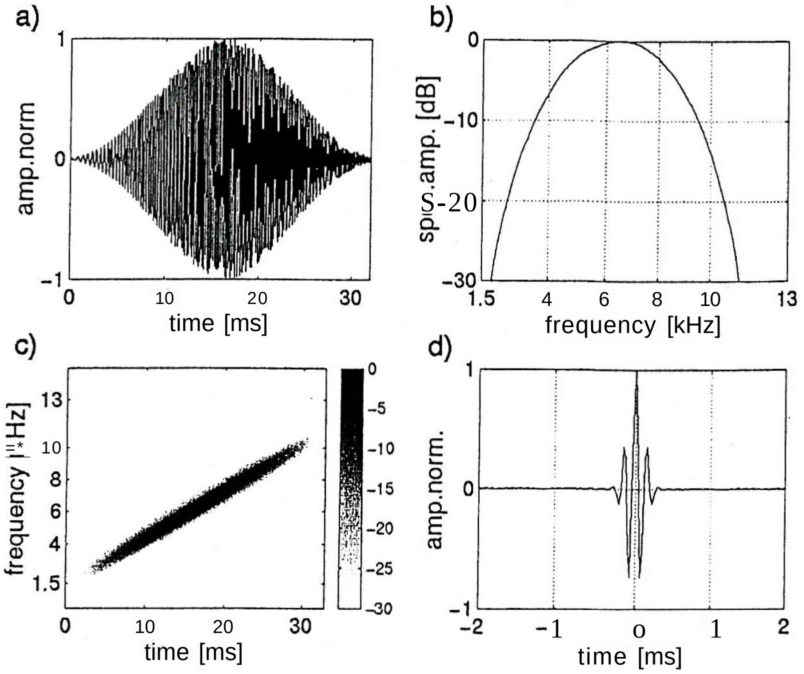

Figure 2.2 Source sweep S2. Standard linear high frequency sweep with Blackmann-Harris envelope function, a) Time domain representation, b) Power spectrum with a mean frequency of 6.5 kHz. c) Spectrogram showing the linear IFF. d) Klauder wavelet.

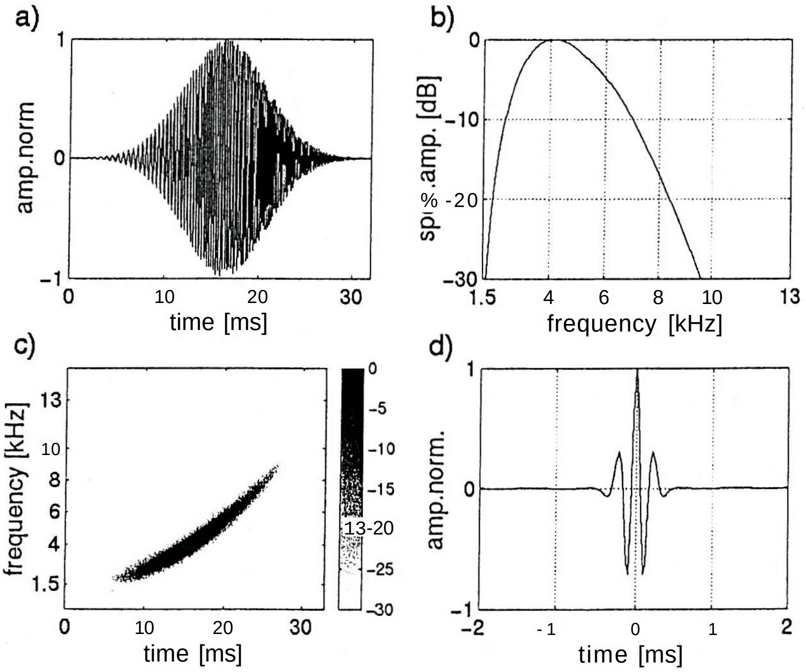

Figure 2.3 Source sweep S3. Quadratic sweep with Gaussian envelope function, a) Time domain representation, b) Power spectrum with a mean frequency of 4.48 kHz. c) Spectrogram showing the quadratic IFF. d) Klauder wavelet.

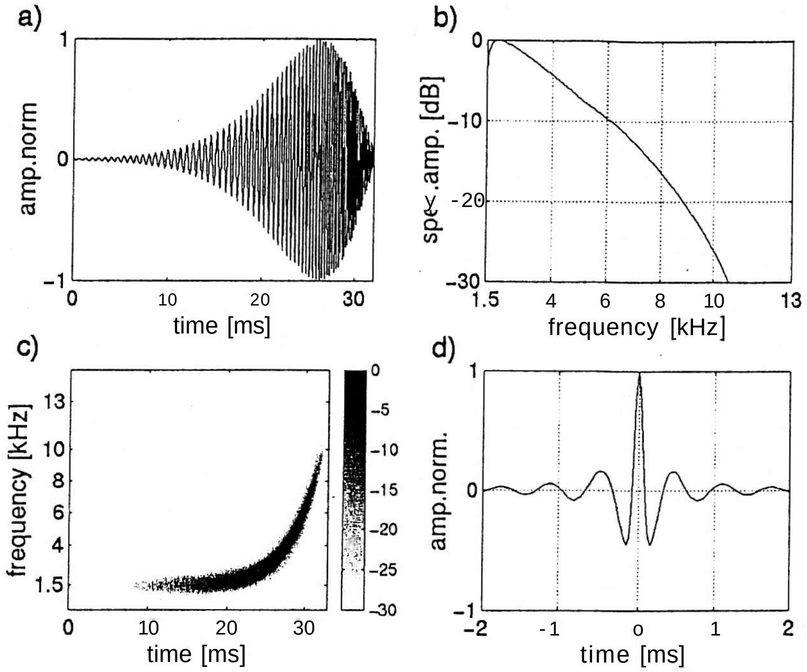

Figure 2.4 Source sweep S4: Logarithmic sweep with Chi reversed envelope function, a) Time domain representation, b) Power spectrum with a mean frequency of 3.25 kHz. c) Spectrogram showing the logarithmic IFF. d) Klauder wavelet.

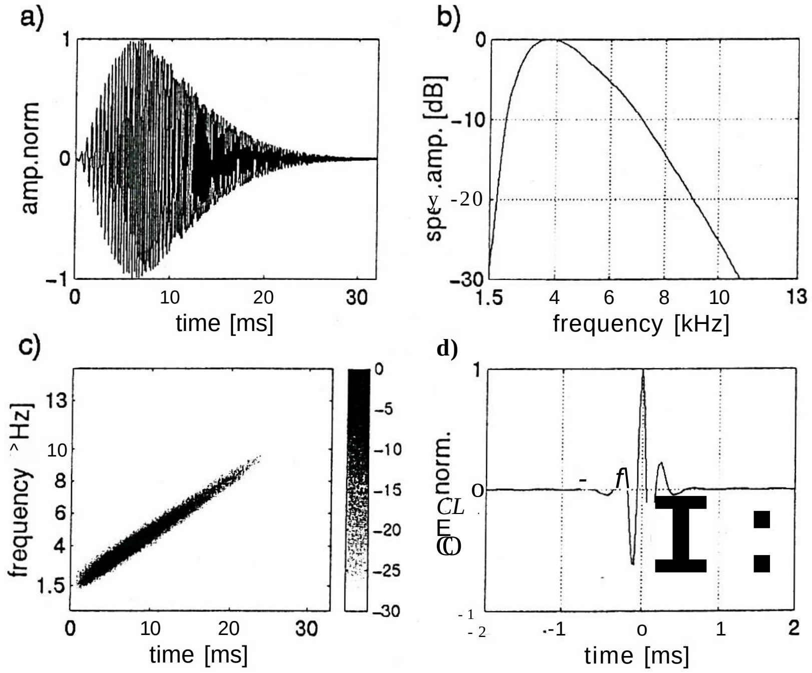

Figure 2.5 Source sweep S5 Linear sweep with Chi envelope function, a) Time domain representation, b) Power spectrum with a mean frequency of 4.3 kHz. c) Spectrogram showing the linear IFF. d) Klauder wavelet.

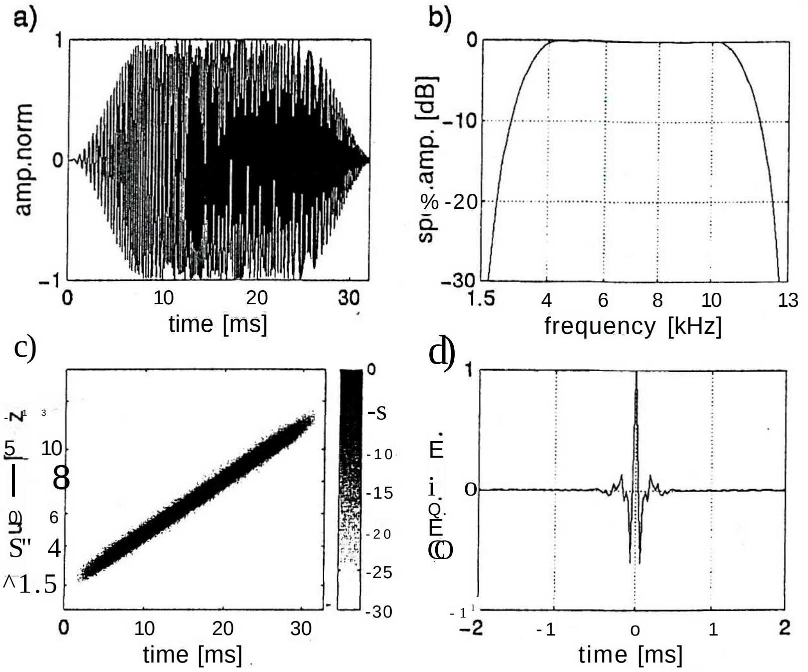

Figure 2.6 Source sweep S6. Linear sweep with sine-squared taper function, covering 174th of the time duration, a) Time domain representation, b) Power spectrum with a mean frequency of 7.25 kHz. c) Spectrogram showing the linear IFF. d) Klauder wavelet.

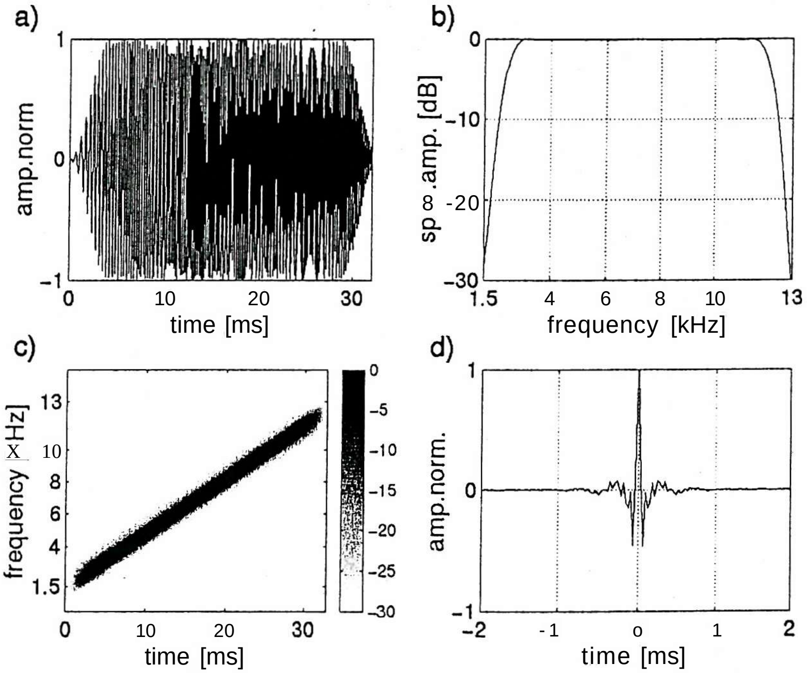

Figure 2.7 Source sweep S7. Linear sweep with sine squared taper function, covering 1/8th of the time duration, a) Time domain representation, b) Power spectrum with a mean frequency of 7.25 kHz. c) Spectrogram showing the linear IFF. d) Klauder wavelet.

The different source sweeps were generated by changing three attributes: the frequency content, the IFF and the envelope function. The transducer frequency response (transducer model T135 Neptune Sonar Ltd.) allows the frequency content of the sweep to be in the range 1.5-13 kHz. The IFF details how the frequency content changes over the length of the sweep; here linear, quadratic and logarithmic functions are used. The envelope function defines the variation with amplitude with time, and in this study Blackmann-Harris, Gaussian, Chi, reversed Chi, and Sine-Squared functions are tested. The newly developed sweeps were compensated for the transducer's frequency response, which had been determined in test-tank experiments, before integrating them into the system.

Sweeps SI and S2 (Figures 2.1 and 2.2) are widely used in commercial Chirp systems, and use a Blackmann-Harris envelope function and linear IFFs, with S2 having wider bandwidth and higher mean frequency (c.f. Table 2.1). These two traditional sweeps will be used as a reference for comparison with the newly generated sweeps. Unlike these conventional signals, all of the new sweeps utilise the full bandwidth of the transducers.

Three different sweeps, all with relatively low mean frequency and asymmetric spectra are detailed in Figures 2.3 - 2.5. For Sweep S3 (Figure 2.3) the relatively low mean frequency and asymmetric spectrum is produced using a quadratic IFF, which causes more time to be spent at lower frequencies, and a Gaussian envelope function. Sweep S4 (Figure 2.4) was produced using a reversed Chi function giving high amplitudes at high frequencies, but with a logarithmic IFF with long duration at low frequencies. A Chi envelope function, with relatively high amplitudes at low frequencies, and a linear IFF was used to produce sweep S5 (Figure 2.5). For the linear sweeps S6 and S7 (Figures 2.6 and 2.7) a sine-squared taper function was used to optimise the power output over the frequency range while suppressing correlation side-lobes. For sweep S6 the sine-square taper covers half the duration of the waveform, for sweep S7 it covers a quarter of the duration.

2.3 Seismic data acquisition, processing and visualisation

Sea trials were undertaken in the West Solent off the north coast of the Isle of Wight (UK) in which the same seismic line was repeatedly recorded using different source sweeps. The survey area is shown in Figure 2.8a. A standard 2D Chirp system was used for the trials, consisting of a source catamaran housing a quadratic array of four source transducers together with a seismic streamer with a hydrophone group consisting of eight elements towed behind the source catamaran (Figure 2.8b).

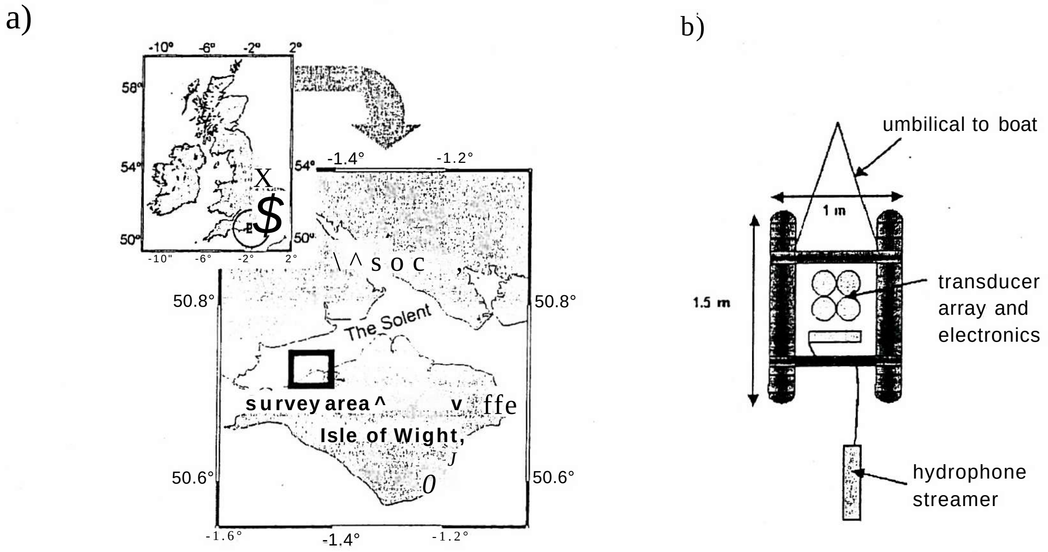

Figure 2.8 a) Survey area in the West Solent (UK) off the north coast of the Isle of Wight. The box shows the area in which a 650 m long seismic profile was repeatedly recorded using different Chirp source sweeps, b) Plan view of Chirp sub-bottom profiler system used in the experiment. The source comprises a quadratic array of four transducer elements (Neptune Sonar Ltd.) located in a catamaran together with the controlling electronics. The receiver array consists of a group of 8 hydrophone elements within a 1 m streamer, which is towed 2 m behind the catamaran. The catamaran itself is towed at a distance of approximately 10 m behind the survey vessel to reduce the impact of engine noise and to ensure a stable towing behaviour.

Sweeps could be selected and changed on-board the survey vessel without the need to retrieve the source catamaran. The single channel seismic data were recorded with a shot interval of 250 ms together with DGPS navigational data.

Figure 2.9 shows seismic sections of part of the repeatedly surveyed seismic line recorded with the different source sweeps. All the profiles are 650 m long, with the exception of Figure 2.9f where the profile is truncated at the south-west end. Figure 2.10 shows the navigation data for the seismic sections together with a close-up of raw correlated data for the area highlighted in Figure 2.9a.

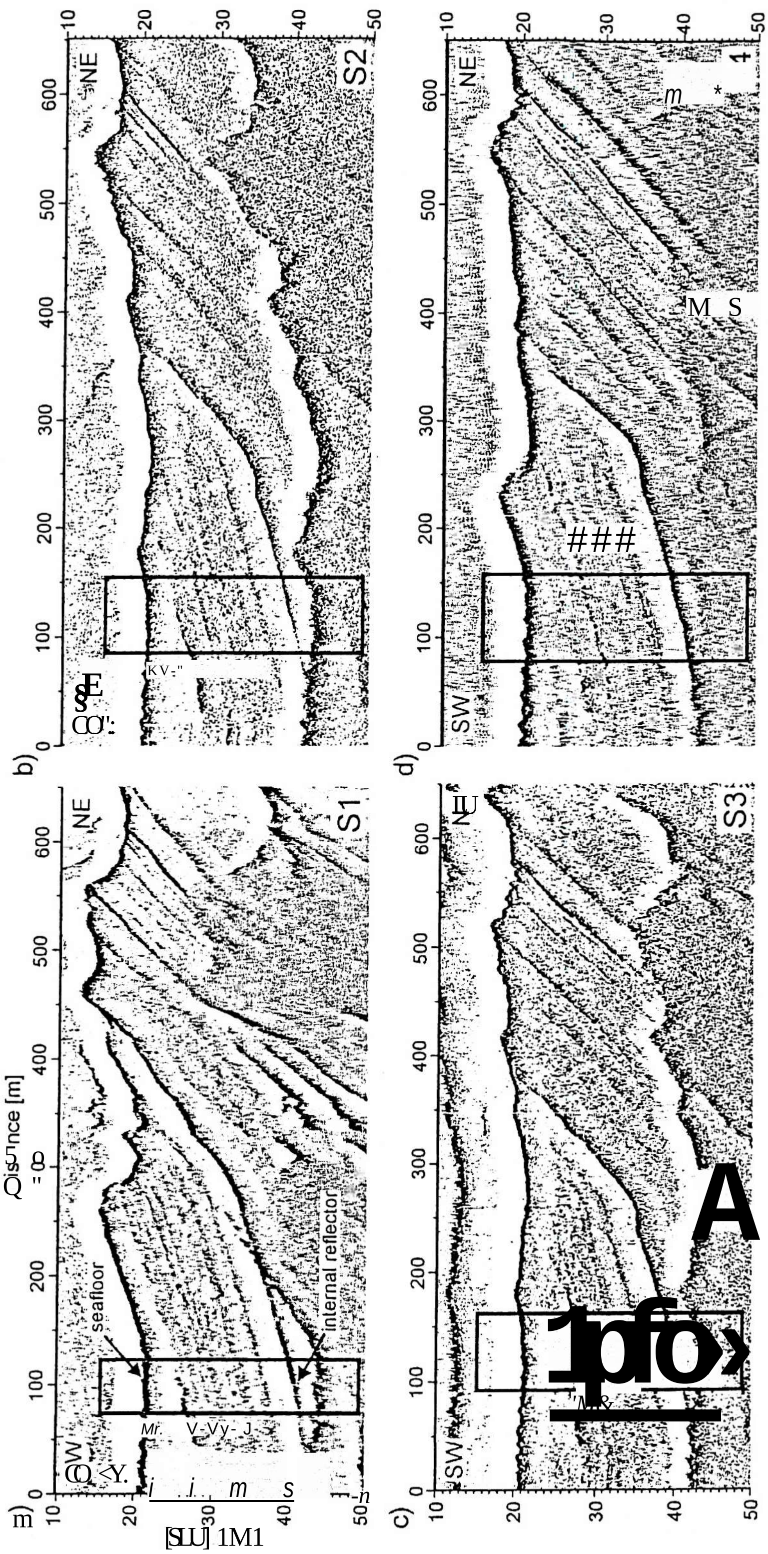

Figure 2.9 Seismic sections recorded in the area in the West Solent (UK) (Figure 2.8). Note the seafloor and internal reflection events used in the analysis, a) Sweep SI. Standard linear low frequency sweep with Blackmann-Harris envelope function. Note the seafloor and internal reflection events used in analysis, b) Sweep S2. Standard linear high frequency sweep with Blackmann-Harris envelope function, c) Sweep S3. Quadratic sweep with Gaussian envelope function, d) Sweep S4. Logarithmic sweep with Chi reversed envelope function.

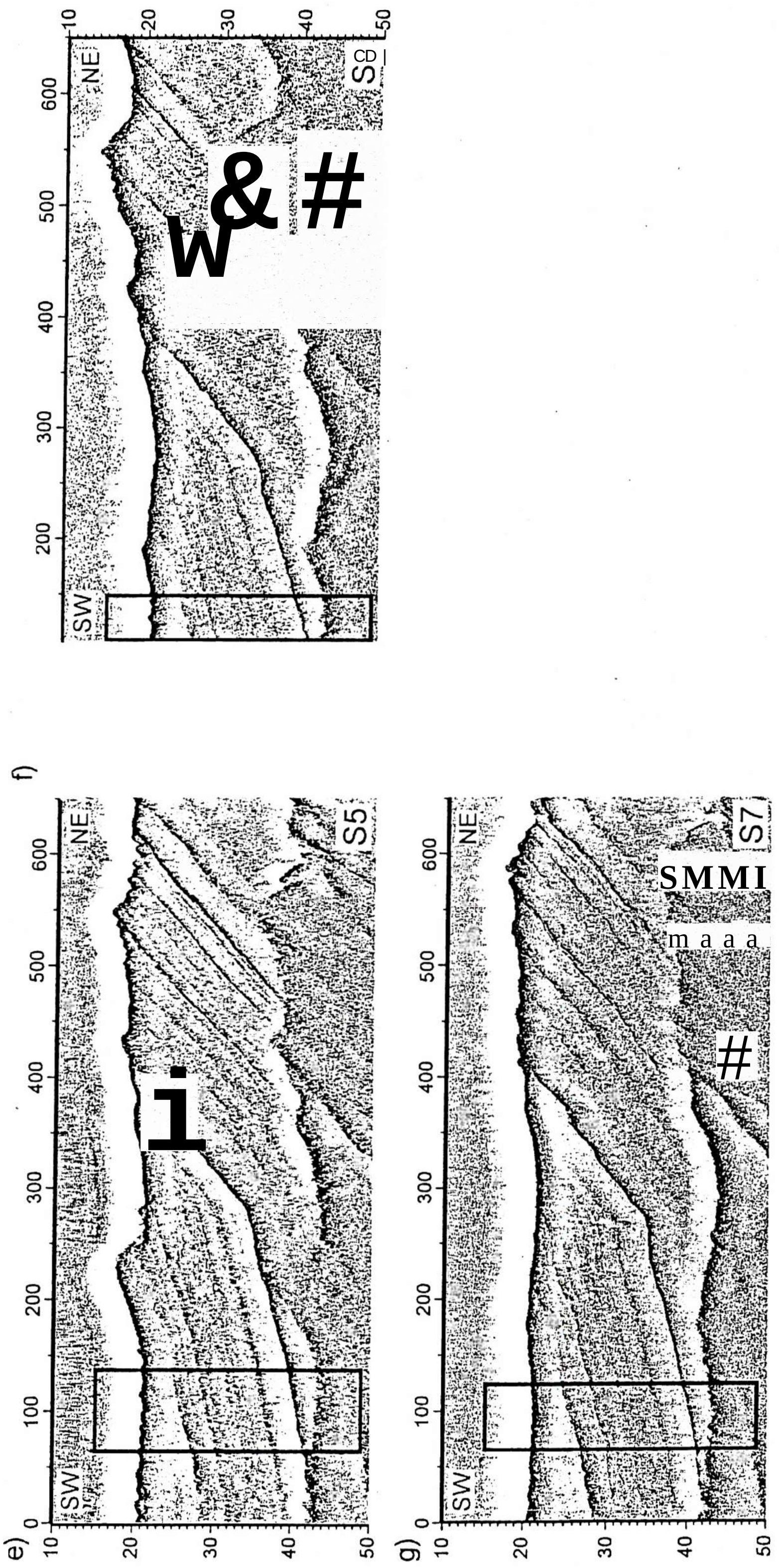

Figure 2.9 continued e) Sweep S5. Linear sweep with Chi envelope function, f) Sweep S6. Linear sweep with sine-squared taper function, covering 1/4* of the time duration, g) Sweep S7. Linear sweep with sine-squared taper function, covering 1/8th of the time duration. The sections image limestones, marls, clays and shales of Eocene and Oligocene age.

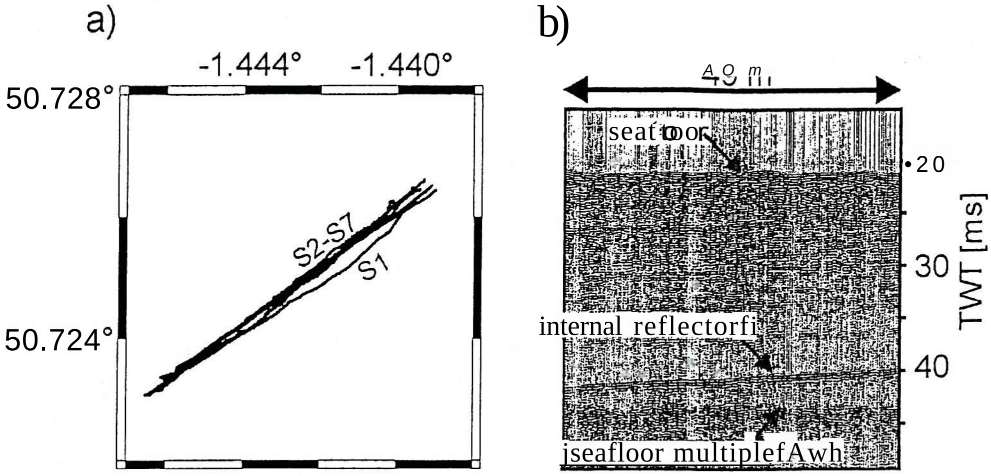

Figure 2.10 a) Plot of the navigational data for the seismic lines for sweeps SI to S7. b) Raw correlated data from sweep SI from area highlighted in Figure 2.9a.

The sections image clays, marls, shales and limestones of the Bouldnor formation of Eocene and Oligocene age, situated at the eastern flank of the Bouldnor syncline. See Chapter 7 for an integrated study of the geology in this area. The variations in the structures imaged on the seismic profiles are due to variations in navigation between the profiles shown in Figure 2.10a. Note that line SI, showing the strongest variation in the imaged structures, has an offset of up to 30 m to the other lines. The seismic data were processed using a flow described by Quinn et al. (1997(c)) including bandpass filtering, instantaneous amplitude calculation, f-x deconvolution, dynamic signal to noise filtering and automatic gain control. The same parameters were used for each data-set with a different bandpass filter applied within the limits of the frequency range of the sweeps (Table 2.1).

The areas used later for the quantitative comparison of attenuation and vertical resolution are highlighted, although for the qualitative comparisons, the entire sections are taken into account. The raw data (Figure 2.10b) are included to indicate clearly the reflection events used for quantitative analysis, and to demonstrate the improvement in the interpretability of the processed sections. The seafloor multiple reflection present at about 40 ms two-way-travel time (TWT) prevents the imaging of deeper structures, although for some data-sets primary events can be traced below the multiple reflection.

The general data quality varies within and between the sections owing to source and receiver movements, which were dependent on the changing tidal currents. Generally the lines recorded running against the tidal current are less noisy (sweeps SI, S4, S5, S7), but this did not affect our analysis.

Major differences are apparent when comparing the sections for the relatively low mean frequency sweeps (SI and S3-S5). Sweeps S3 and S5 show tighter reflection horizons compared to sweeps SI and S4. This is especially clear when comparing the pronounced reflector in the south-western part of the section (reflector at c. 40 ms TWT within each boxed area on Figure 2.9). Some reflection horizons north-east of 500 m along each profile can be interpreted which are not visible for SI. In the section for sweep S4 (Fig 2.9d at 450 m) some reflectors can be traced beyond the seafloor multiple reflection suggesting lower loss of amplitude for this sweep.

Comparing the sections with the relatively higher mean frequency sweeps (S2, S6 and S7) it is apparent that they strongly differ in their noise content, with S2 and S6 being much noisier then S7. However, the sections for the sweeps S6 and S7 show slightly tighter reflections compared to S2, and this is especially clear north-east of 500 m along each section where there is a lower noise level. Section S7 shows the greatest resolution of all the sections. In some places (e.g. 525 m along section at c. 25 ms TWT) two separate reflection horizons can be interpreted, where in other sections only one horizon is visible.

2.4 Data analysis

2.4.1 Vertical resolution

The vertical resolution states how close two reflectors in the sub-surface can be spaced in the vertical direction and still be distinguished. Conventionally, vertical seismic resolution is expressed in relation with the dominant frequency of the source signature used. Yilmaz (1987) defines the vertical resolution as one quarter of the mean wavelength X_{mean}, or as time resolution t_{res_cj} , taking the two way travel path into account

$$t_{res,c\,1} = \frac{1}{2 f_{m\ ean}}, \tag{2 1}$$

where f_{mean} is the mean frequency of the signal.

Claerbout (1976) states a criterion for wide-band source signatures, based on the uncertainty principle

$$A/A/ \geq 1, \tag{2 2}$$

where *Af* is the bandwidth and *At* the time duration of the signal. He claims the time duration of the signal as the resolution limit. Schock and LeBlanc (1990) state the same criterion for the standard Chirp source signature, which can be written as

$$t_{res,c2} = \frac{1}{\Delta f}. \tag{2 3}$$

See Table 2.2 for a summary of the criteria for the proposed source sweeps.

sweep	frequency range [kHz]	-3dB amplitude bandwidth [kHz]	f mean [kHz]	tres,cl [ms]	tres,c2, range [ms]	tres,c2, -3dB [ms]
S I	2.-8	1.72	4.5	0.111	0167	0.581
S2	1.5-11.5	3.38	6.5	0.077	0100	0.296
S3	1.5-13	2.54	4.48	0.112	0.087	0.394
S 4	1.5-13	1.94	125	0154	0.087	0.515
S5	1.5-13	2.66	4.3	0116	0.087	0.376
S6	1.5-13	7.82	7.25	0.069	0.087	0.128
S7	1.5-13	9.65	7.25	0.069	0.087	0104

Table 2.2 A summary of resolution of the source signatures for different criteria together with their frequency characteristics. $t_{res,\ ci}$ after (2.1), $t_{res,\ c2,\ range}$ after (2.3) using the frequency range as bandwidth and $t_{res,\ c2,\ \cdot 3dB}$ after (2.3) using the -3dB width of the spectrum as bandwidth.

Note that criterion $t_{resx}i$ (2.1) gives identical values for source sweeps S6 and S7 and criterion $t_{resX}2$ (2.3) for source sweeps S3 - S7, taking the entire bandwidth into account. The values for the bandwidth at -3dB points differ for all source signatures, owing to the difference in their envelope functions. Additional vertical resolution criteria have been proposed for different source signature types, also based on their bulk characteristics like mean wavelength or bandwidth (Widess, 1973; Kallweit and Wood, 1982). Though the proposed sweeps have partly the same frequency range, they vary significantly in their -3dB bandwidth and their instantaneous frequency function and therefore in the shape of their Klauder wavelet. Due to the fact that both criteria are based in bulk characteristics all the source signatures have partly the same resolution threshold. However, by observation of their Klauder wavelets different vertical resolution limits are expected. Therefore the previously described criteria can not be applied for a comparison of the vertical resolution, instead a criteria should be used that takes into account the characteristics of the Klauder wavelet. The characteristics of the Klauder wavelets can be compared in more detail by calculating the integral amplitude build-up of the Klauder wavelet $A(t_{inl})$, which is given as

$$A(t_{\text{int}}) = \underset{h}{\overset{\text{im}}{\mathrm{j}}}|\mathrm{a(f)}|'\ {}^{\text{-J+}}, \tag{2 4}$$

where t_{im} is the integration time, *to* is the start time of the integration and *s(t)* is the Klauder wavelet. This time domain analysis quantifies the amplitude distribution within the Klauder wavelet.

To facilitate a comparison of theoretical and experimental data, the same start time to was chosen for the amplitude build-up calculation. Although the calculation of the amplitude build-up of the theoretical Klauder wavelet, to can be chosen to be -co, due to the noisiness of the experimental data, to was set to be -1 ms before the correlation maximum at a correlation lag-time $t\{_{ag}=0$. The upper limit for the integration is the time at which the Klauder wavelet maximum occurs, which for the theoretical signal occurs when $t[_{ag}=0$. The best theoretical resolution would be expected from a signal whose amplitude build-up function is concentrated at $ti_{„s}=0$. The tighter the amplitude build-up curve towards $ti_{ag}=0$, the better the resolution capabilities of the source sweep. The analysis of the experimental data was carried out before the data were processed as described above.

Figure 2.11 shows the normalised theoretical amplitude build-up functions for the source sweeps examined. The shape of the respective Klauder wavelet controls the form of each curve: the undulations in the amplitude functions correspond to the side-lobes of the wavelet; the time at which the amplitude function starts increasing corresponds to the time duration of the wavelet.

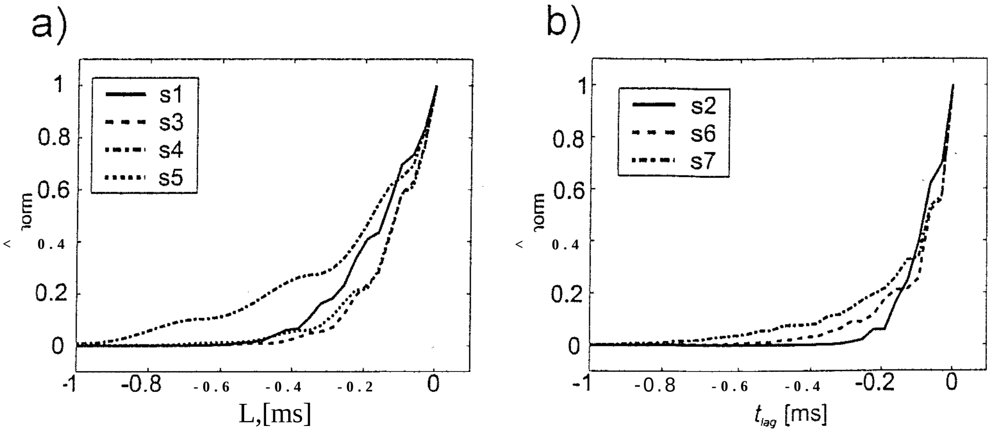

Figure 2.11 Normalised amplitude build-up curves of the examined source sweeps, a) Low mean frequency sweeps SI, S3, S4 and S5. b) High mean frequency sweeps S2, S6 and S7. The curves comprise the evaluation of (2.4) with integration limits of $t_0\sim$-1 ms to $t_{in},=0$ ms.

The steeper the ascent towards $t\{_{ag}=0$ the tighter the main-lobe of the Klauder wavelet. Comparing the sweeps with relatively low mean frequency shows that S4 has the widest amplitude build-up curve and a low ascent rate owing to the wide main-lobe and wide primary side-lobes together with a slow decay of the side-lobe amplitudes of the Klauder wavelet. Sweeps S3 and S5 show similar, relatively tight curves due to fast decay of side-lobe amplitudes and tight primary side-lobes. The curve for SI is wider compared to S3 and S5 owing to high amplitude primary side-lobes. Comparing the sweeps with a higher mean frequency shows that the amplitude build-up curves for sweeps S6 and S7 have a very steep ascent compared to S2 due to a very tight main-lobe of the Klauder wavelet. Owing to the slower decay of the side-lobe amplitudes, the curves for S6 and S7 are broad, compared to S2, with S7 showing the fastest amplitude accumulation, because its envelope function is most similar to a box function.

To facilitate a quantitative comparison, the time duration from the half amplitude build-up to the full build-up ($ti_{ag}=0$) can be used to compare the resolution capabilities of the sweeps. Time durations were calculated for the theoretical, as well as for the experimental data. The experimental values were computed from the amplitude build-up curves for seafloor reflections in the highlighted area of the seismic sections shown in Figure 2.9. The values are listed in Table 2.3.

	f_{mean}	amplitude build-up half-width fmsj			^{a}app fdB/ml		
sweep	[kHz]	theory	data	standard deviation	theory	data	standard deviation
SI	4.50	0.143	0143	0.007	0.29	0.38	013
S2	6.50	0.081	0.097	0.020	0.59	0.63	0.15
S3	4.48	0.113	0.127	0.023	0.29	0.38	012
S4	125	0180	0.224	0.012	016	0.25	0.17
S5	4.30	0.114	0119	0.016	0.27	0.38	018
S6	7.25	0.066	0.070	0.015	0.71	0.64	018
S7	7.25	0.070	0.088	0.030	0.70	0.56	019

Table 2.3 Analysis of time duration from the half amplitude build-up to the full build-up for the Klauder wavelet and attenuation (a_{app}), as discussed in section 2.4.2, expected from theory and from experiment, for each sweep. The stated errors are standard deviation errors calculated for the experimental results.

Compare the half amplitude build-up values in Table 2.3 with the values for the traditional vertical resolution **criteria** in Table 2.2. They are of the same scale. The half amplitude build-up values differ for every source signature, thus representing a comparable criterion for the comparison of the resolution characteristics of the source signatures.

Figure 2.12 plots the time duration from the half amplitude build-up to the full build-up for both theoretical and experimental data for each sweep examined (a), and against the mean frequency of each sweep (b).

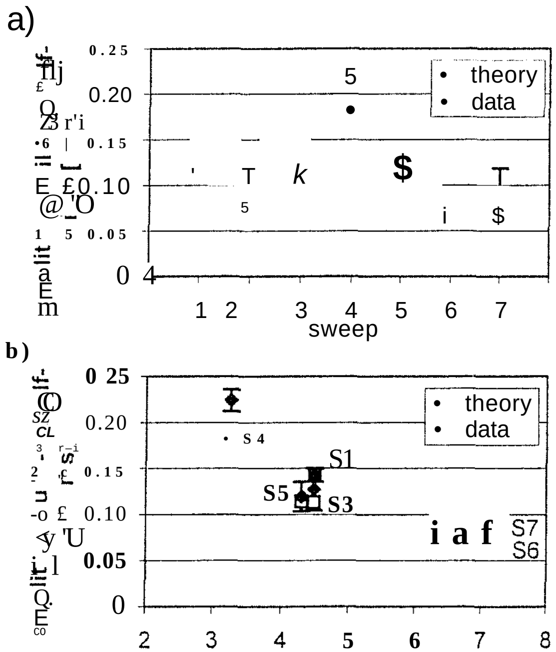

Figure 2.12 Half amplitude build-up widths for examined theoretical sweeps and extracted from the seafloor reflections in the highlighted area of the seismic sections shown in Figure 2.9. a) Plotted against sweep label, b) Plotted against the sweeps' mean frequency.

The theoretical and experimentally-derived measurements agree within error, except for sweep S4. The experimental half-width values are systematically higher than the theoretical. This is a result of the presence of ambient noise, which causes temporal widening of the build-up curves. The experimental data for sweep S4 has a relatively noisy seafloor reflection signal, which explains the discrepancy.

Comparing the newly developed low mean frequency sweeps (Table 2.2) S3, S4 and S5 with the traditional sweep SI, shows that S3 and S5 both have a theoretical half-width value with temporal duration approximately 25% lower than SI, while S4 has an increased temporal duration c. 25% more than SI. From this analysis sweeps S3 and S5 would be expected to offer improved resolution, while having similar mean frequency. S4 has substantially lower mean frequency (38% lower than SI), while its resolution capabilities are reduced by 25%, based on the theoretical amplitude half-width.

The newly developed high mean frequency sweeps S6 and S7 all have smaller half-widths values than their traditional counterpart S2 (23% and 17% respectively, from the theoretical amplitude build-up curves) and should enable enhanced resolution. Some of this improvement can be attributed to an increase in the mean frequency of the new sweeps **(12% higher).**

Figure 2.13 shows a cross plot between two vertical resolution criteria: the amplitude build-up half-width and criteria from equation (2.3) using the -3 dB bandwidth.

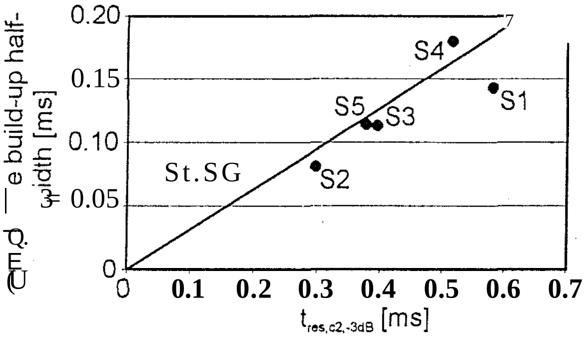

Figure 2.13 Cross-plot between amplitude build-up half-width (Table 2.3) versus the vertical resolution criterium $t_{res,c2,-3dB}$ (Table 2.2) for the different source sweeps discussed.

The linear relationship between the criteria suggests that the can be used interchangeably for the relative bulk comparison of vertical resolution capabilities of source sweeps. However, the study of the amplitude build-up curves reveals additional details about the Klauder wavelets which are not covered by the bulk criteria.

2.4.2 Attenuation

To study the attenuation of the different source sweeps, seafloor reflection amplitudes are now compared with the amplitudes of a pronounced internal reflection horizon (see Figure 2.9). The reflection amplitude is dependent on the attenuation of the sweep between the respective horizons as a result of various mechanisms, as well as their reflection coefficients. Since the reflection coefficients are not known an apparent attenuation is expressed, which includes the reflection coefficients and assumes that the attenuation is constant with depth. The apparent attenuation coefficient a_{app}, which depends on the frequency content of the used source sweep can be described as

$$a_{app}(\omega) = \frac{20}{z}\log\frac{R_1(\omega)}{R_0(\omega)}, \qquad (2.5)$$

where *RQ* is the seafloor reflection amplitude, *Rj* the internal reflection amplitude, co angular frequency and z the depth between the two reflectors, assuming an average sediment velocity of 1800 m/s. Equation (2.5) expresses the attenuation in units of dB/m. Before carrying out the calculation, an amplitude correction is applied, assuming spherical spreading. To compare the results of the different data sets, the same internal reflection horizons at the same depth interval are analysed, as shown in Figure 2.9. The area has been chosen to be homogenous with dipping reflectors to avoid amplitude alteration effects due to internal multiple reflections.

Additionally the attenuation of the sweeps was modelled using a model based on relaxation time as described by LeBlanc et al. (1992). The attenuated frequency domain signal *Y(co)* can be obtained by multiplying the signal in the frequency domain, *S(co)* by the frequency transfer function *H(co)*

$$Y(\omega) = \qquad \mathbf{(2.6)}$$

where

$$H(\omega) = \qquad \mathbf{(2.7)}$$

The real part of the exponent represents the attenuation of the sweep magnitude and for small frequencies (<100 kHz) the coefficient *a* is given as

$$\text{or} = \frac{\omega^2\tau}{2}, \qquad (2.8)$$

where **GO** is the angular frequency of the signal and r the average relaxation time of the sediment, the measure of the finite time needed to change the density by application of a sudden pressure due to different mechanisms. The imaginary part of the exponent describes the time delay and phase dispersion of the signal and for small frequencies (<100 kHz) the coefficient *k* can be approximated by

$$k \approx \frac{co}{(1+i\,a/r')} . \qquad \textbf{(2.9)}$$

The attenuated time domain signal is calculated by computing a Fast Fourier Transform (FFT), multiplying the signal by the frequency transfer function *H(co)* as described in equation (2.6) and lastly computing the inverse FFT. The apparent attenuation value is then calculated by comparing the amplitudes of the attenuated and original signal as described by equation (2.5). Since the relaxation time r is not known, this parameter is changed in the model to obtain the best least-square fit between model results and data for the entire data-set. This gives a relaxation time of r=0.135ps. This is a typical value for coarse-grained marine sediments (LeBlanc et al., 1992).

Table 2.3 shows results of the calculations with standard deviation errors and the best least-squares fit model results. Figure 2.13 displays the experimental data and model results plotted against sweep (a), and against the mean frequency of the respective sweep (b).

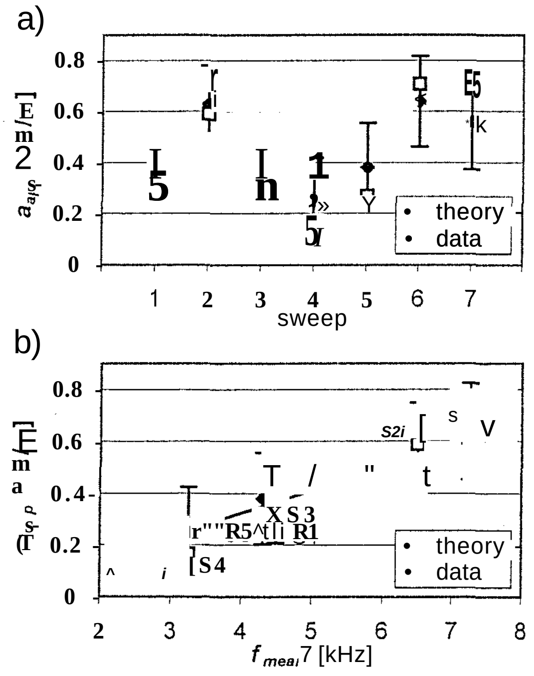

Figure 2.14 Experimental and modelled apparent attenuation values for the examined source sweeps. The experimental results were computed for the highlighted reflectors in the seismic sections shown in Figure 2.9. a) Plotted against sweep label, b) Plotted against the sweeps mean frequency. The best fit straight line corresponds to a quality factor Q=169± 56.

Assuming that the intermediate reflection coefficients are negligible, and the velocity does not significantly increase with depth, an estimate for a constant quality factor Q can be obtained. The best-fit straight line for the experimental data in Figure 2.14b corresponds to a constant quality factor of Q=169±56. This minimum bound estimate reflects the consolidated nature of the imaged strata, which facilitates sound propagation with relative low attenuation (Solomon, McCann and Sothcott, 1999).

We have measured the attenuation within the sediment based on the different source sweeps. The measured results can be fitted by both a relaxation time model and a constant Q model-. In each case the results are similar to other estimates for marine sediments, however to unequivocally distinguish which method provides a better fit to the data would require a broader range of frequencies. Sweeps S2, S6, S7 are consistently more attenuated than the other sweeps, and sweep S4 is the least attenuated. Although not our primary aim, the methodology described, that is using data acquired with different source sweeps with a wide range of mean frequencies, can be used to estimate the relaxation time and the Q values.

2.5 Discussion

The two main considerations for choosing a particular sweep for a specific survey task are vertical resolution and penetration. As discussed earlier, the length of the Klauder wavelet controls the vertical resolution, while the depth of penetration is controlled by the attenuation of the sweep as it propagates through the sub-surface. Here the vertical resolution and attenuation of each of the sweeps examined are discussed.

In this work it was demonstrated that seismic reflection sections over the same ground (Figure 2.9) can be used to provide qualitative comparison of the vertical resolution for each sweep used. For quantitative analysis of vertical resolution, measurements of the time duration from the half amplitude build-up to the full build-up of the Klauder wavelet can be used (Figure 2.11 and Table 2.3). There is excellent agreement, on a sweep-by-sweep comparison, between the vertical resolution observed on the seismic sections (as qualitatively judged by the interpretability of the sections, and the imaging of additional horizons), and the quantitative approach. Comparing the low frequency sweeps (SI and S3 - S5), sweeps S3 and S5 offer the shortest Klauder wavelet (the temporally fastest amplitude build-up, Table 2.3), and also provided the seismic sections with greatest spatial resolvability. For the high frequency sweeps (S2, S6 and S7), sweeps S6 and S7 offer better vertical resolution as judged by both the seismic sections (Figure 2.9) and Klauder wavelet considerations. Sweeps S6 and S7 which have a sine-squared envelope function have broader bandwidth (for example at -3dB, see Table 2.1) than sweep SI with the Blackman-Harris envelope function, and this explains their better resolution capabilities.

The limited water-depths in the chosen survey area meant that the multiple reflection hampered analysis of attenuation from the seismic data. Despite this, the modelled and observed attenuation values agree within error (Figure 2.14). Sweep S4, which has the lowest apparent attenuation value (Table 2.3), shows little change in the noise level with depth indicating low attenuation, and provided the imaging of the deepest reflectors observed on any of the seismic profiles (Figure 2.9).

The selection of the optimal sweep for a particular task is a compromise between resolution and penetration. Normally there is a reduction in the depth of penetration achieved when using higher resolution sweeps. Thus, the improvement in resolution offered by the high frequency 'Sine-Squared' sweeps (S6 and S7) compared to the traditional high frequency sweep S2 is remarkable, given the absence of a major increase in attenuation. For the low frequency sweeps (S3 and S5) an improvement in resolution can also be observed in comparison with the traditional sweep SI. The modelled and observed attenuation values are very similar for these sweeps, thus achieving an overall improvement for the newly developed low frequency sweeps over the traditional sweep.

2.6 Conclusions

This work reports on the development of a number of Chirp source sweeps, which exploit the entire bandwidth of the transducer, but which differ in their envelope and instantaneous frequency functions. The sweeps were tested in a seismic reflection sea trial by recording the same profile with the different source sweeps. To compare the resolution capabilities of the sweeps, analysis was made of the amplitude build-up of the Klauder wavelet, calculated for the theoretical waveform and extracted from the data-sets. To compare the attenuation of the sweeps an apparent attenuation value was calculated from the data-sets, and numerically modelled using a relaxation time based model. A comparison of the low and high mean frequency sweeps characteristics showed that the newly developed sweeps offer advantages over the traditional sweeps as they improve the resolution capabilities, while having similar or better resistance to attenuation.

3 Acquisition geometry considerations

3.1 Introduction

In this chapter the geometries of the source array and receiver groups for the 3D Chirp system are considered. Both the source array and receiver groups are characterised by frequency dependent directivity, which is controlled by the directivity of their individual elements as well as by the directivity resulting from their spatial distribution. Knowledge of the system's directivity is important for optimising the spacing of receiver groups to avoid spatial aliasing and to secure optimal horizontal resolution. Frequency dependent energy reflected from the seafloor is modelled for different acquisition geometries in order to investigate spatial sampling and horizontal resolution. On the basis of the model results an optimal geometry for the source array and receiver groups for the 3D Chirp system is chosen together with appropriate receiver group spacing.

3.2 Spatial sampling

For a signal to be correctly sampled in the time domain, the sampling frequency needs to be larger or equal to the Nyquist frequency, which is twice the frequency of the highest frequency in the signal's spectrum. Equally, in order to correctly spatially sample a wavefield, the receiver group spacing needs to be equal or smaller than half the apparent wavelength of the field (Yilmaz, 1987)

$$\Delta x_{\min} = \frac{1}{2}\lambda_{app} \qquad <^{3}\text{-1)}$$

with

$$\lambda_{app} = \frac{\lambda}{\sin\alpha}, \qquad (3.2)$$

where *X* is the wavelength of the field and *a* the angle of incidence, shown in Figure 3.1.

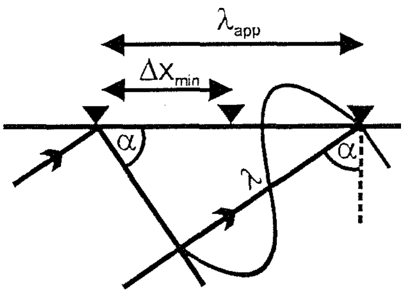

Figure 3.1 Definition of apparent wavelength l_{app} as the horizontal wavelength depending on the angle of incidence a of the wavefront. Ax^in is the minimum receiver group spacing to avoid spatial aliasing for the given apparent wavelength calculated using equation (3.1).

For a given receiver group spacing, if the maximum angle of incident is exceeded the recorded data will be spatially aliased.

Spatial aliasing has serious consequences on the performance of seismic data processing algorithms, and particular on migration (Yilmaz, 1987), for which the aliased energy is moved to the wrong position resulting in smearing of reflector horizons, depending on their dip *a* and frequency contents. In order to avoid spatial aliasing the acquisition geometry needs to be designed according to the frequency content of the source signatures used.

3.3 Horizontal Resolution

The horizontal resolution determines how close two reflectors in the sub-surface can be situated laterally and still be distinguished in the seismic record. The Fresnel zone concept, generally used to establish the resolution capabilities of seismic reflection systems (Yilmaz, 1987), states the radius of the zone on a reflection surface, from which the reflected wave energy interferes constructively, as the threshold value. It is given as

$$r_{Fresnel} = \frac{v}{2}\sqrt{\frac{TWT}{f_{eff}}}, \qquad (3.3)$$

where v is the seismic velocity of the medium above the reflection surface, f_{eff} the effective frequency of the source signal and *TWT* the two way travel time to the reflection surface. Table 3.1 states values of the Fresnel zone for effective frequencies that encompass the source signatures used (Chapter 2) and typical target depths. A water sound velocity of v=1500 m/s is assumed for the case that the reflection horizon is the seafloor.

f_{eff} [kHz]	λ_{eff} [m]	Depth [m]	$r_{Fresnel}$ [m]
3.25	0.46	10	1.52
4.5	0.33	10	1.29
6.25	0.24	10	1.10
7.25	0.21	10	1.02
3.25	0.46	20	2.15
4.5	0.33	20	1.83
6.25	0.24	20	1.55
7.25	0.21	20	1.44

Table 3.1 Fresnel zone radii after equation (3.3) and effective wavelength (v_{water}=1500 m/s) for different depths of the seafloor reflector and typical effective frequency f_{eff} of the source signatures used with the 3D Chirp system.

The Fresnel zone radii range from 1.02 m to 2.15 m for this example. However, migration of the seismic data tends to collapse the Fresnel zone to up to the effective wavelength of the source signature (Stolt and Benson, 1986), which ranges from 21 cm to 46 cm in this case, thus significantly improving the horizontal resolution. It should be noted that the effectiveness of migration algorithms will be limited by the range of horizontal wavenumbers present in the data. In addition the directivity of a seismic system, determining the relative amplitudes for different angles of incidence of the reflected seismic wave energy, can affect the horizontal resolution. Single lobe directivity for the system is desirable, resulting in a footprint concentric around the vertical acoustic axis.

Directivities with high amplitude side-lobes should be avoided as these result in contribution of **reflected** seismic wave energy away from the vertical acoustic axis, impeding effective migration. Schock et al. (1994) studied the effect of the directivity of a seismic system on the horizontal resolution when transmitting a frequency modulated (FM) signal. The directivity of a seismic system, consisting of a source array and receiver groups is frequency dependent. For the broadband transmission and consecutive correlation of the FM source signature of the Chirp system the directivity is spatially averaged. The reflections arriving off-axis are modified due to the frequency-dependent directivity and these reflections do not resemble the transmitted pulse on-axis, used for the correlation. They state that the effective directivity of the FM signal is approximately equal to a single frequency directivity corresponding to the effective frequency of the source signature.

In order to optimise the resolution capabilities of the system it should be designed so that its directivity results in a single concentric footprint.

To study the effective directivity of an FM signal it can be represented by the directivity corresponding to the centre frequency of the signal.

3.4 Reflection amplitude modelling

In order to assess the horizontal resolution and amount of potential spatial aliasing for a **reflection** seismic system its spatial distribution of the reflection amplitudes is modelled. By comparing the models for different configurations of source arrays and receiver groups the configuration providing the best horizontal resolution and least spatial aliasing under the given constraints is chosen for the 3D Chirp system.

The recorded amplitude of the frequency dependent energy returned from any given point on the seabed is the product of the following factors:

1. directivity of individual source and receiver elements
2. directivity of source arrays and receiver groups
3. geometrical spreading
4. seismic properties of the reflector
5. properties of the seismic medium

To simplify the model some assumptions are made. The model calculates the amplitude of the energy that would be returned on the seafloor for specular reflection back towards the receiver group at a given point with a reflection coefficient of 1, assuming no transmission losses in the water column, thus overestimating the amplitude of any possible return. It also assumes that the source array and receiver group are centred at the same location; this assumption is valid as the actual offsets are likely to be less than 1.5 m, which is small compared with typical survey water depths of 10 to 30 m.

The model results for a number of different configurations are presented. These were chosen under the constraints of the project and general system design (for details see Chapter 5). For the source array up to four transducers (T135 model, Neptune Ltd.) are considered, which can be arranged in two dimensions. Due to their arrangement in the 3D Chirp system only one-dimensional receiver groups (line-arrays) are considered. Their length is limited by the overall size of the 3D Chirp array and the minimum separation of its constituent elements is limited by their size. The optimal configuration for the given design constraints is to be used in the 3D Chirp system. The model results for a frequency of 7.5 kHz are shown, which is slightly higher than the highest mean frequency of the source signatures used with the system (Chapter 2).

3.4.1 Source and receiver directivity

The isotropic radiated pressure p of several point sources can be expressed as (Medwin and **Clay, 1998)**

$$p \wedge \wedge \frac{\%\quad \exp[;(wf - \&\#)]}{R} \wedge \cdot \mathbf{a.}, \tag{3.4}$$

where R_0 is the reference distance, *PQ* the reference pressure at *Rg.* *R* is the distance from the acoustic centre, *co* is the circular frequency of the radiated wave; *k* is the wave number of the radiated wave and a is the attenuation coefficient. *D* is the directional response function and its magnitude expresses the directivity of the array.

It can be shown that for a three dimensional point source array (Burdic, 1984)

$$D\ (\psi,\theta,\lambda) = \sum_n g(x_n, y_n, z_n)\exp[i2\pi(x_n \frac{\textbf{sinty}}{\mathrm{A}} + \mathrm{x}, — \frac{\cos ur \sin 9}{X} + z_n \frac{\cos w \cos\theta}{X})], \quad (3\ 5)$$

with *g(*x_n, y_n, z„) the relative amplitudes of the point sources, X the wavelength and x_n, y_n, z_n the positions components of the *n* point sources. The directional angles *y/, 9* are shown in Figure 3.2.

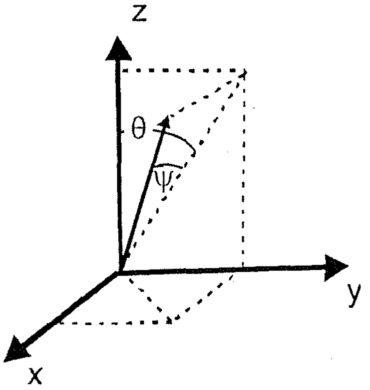

Figure 3.2 Definition of the directional angles *y/* and *9* in the system of coordinates *(x,y, z).*

The source arrays discussed are planar, thus z_n=0 and the receiver groups discussed are one dimensional along the y-axis of the system, thus x_n-z_n=0. Since the arrays comprise identical elements the relative amplitudes, *g,* are equal.

3.4.1.1 Source array directivity

Within the project we are constrained, due to weight and practicable size, to a maximum of four transducers for the source array. The T135 model considered is manufactured by Neptune Sonar Ltd.

Four configurations are presented:

1. Maltese cross
2. Square
3. Four in a row
4. Pair (two pairs used alternately)

Figures 3.3a, 3.4a, 3.5a and 3.6a show the geometry of the configurations. Sections b, c and d of Figures 3.3 to 3.6 show the source array directivity in three perpendicular planes, corresponding to the three coordinates planes, derived from equation (3.5) for a frequency of 7.5 kHz. Note that this part of the directivity only takes the array's geometry into account, not the individual transducer's properties, which are considered in section 3.4.2.

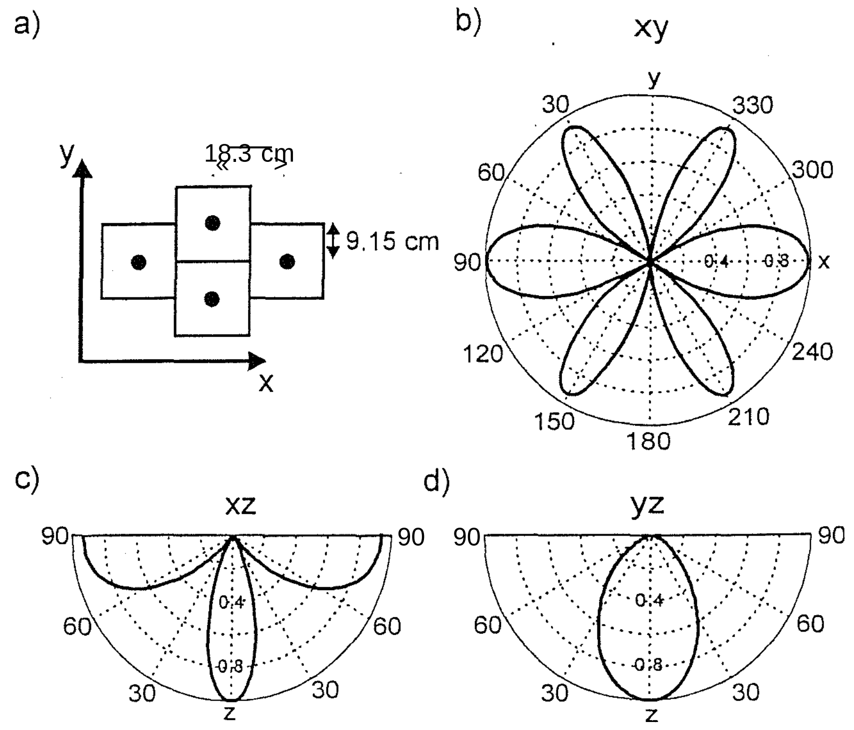

Figure 3.3 Directivity of the source array for 7.5 kHz arranged as a **Maltese cross** after equation (3.5). a) Source array configuration as Maltese cross with longitudinal direction parallel to x-axis. b) Horizontal plane directivity, c) xz-plane directivity, corresponding to the longitudinal direction of Maltese cross, d) yz-plane directivity corresponding to the transversal direction of the Maltese cross.

The separation between the transducers' centres of the **Maltese cross array** in the x-direction is 18.3 cm, twice as large as in the y-direction (9.15 cm). This results in different directivities in the xz and xy-planes. The directivity in the xz-plane, shown in Figure 3.3c), corresponds to the wider source separation. It shows a tight main lobe, centred in the z-direction, with a half-width opening of 28°, together with high amplitude side-lobes, centred in horizontal directions, with a half-width value reaching to **55°.** Due to the tighter source spacing in the y-direction the directivity observed in the yz-plane shows a wider main-lobe with an opening angle of 60° at half-amplitudes, with no side-lobes present. The directivity pattern in the xy-plane is symmetric about the x and y axis with a wide lobe in the x-direction and tighter, slightly lower amplitude lobes at 32° each side of the y-axis.

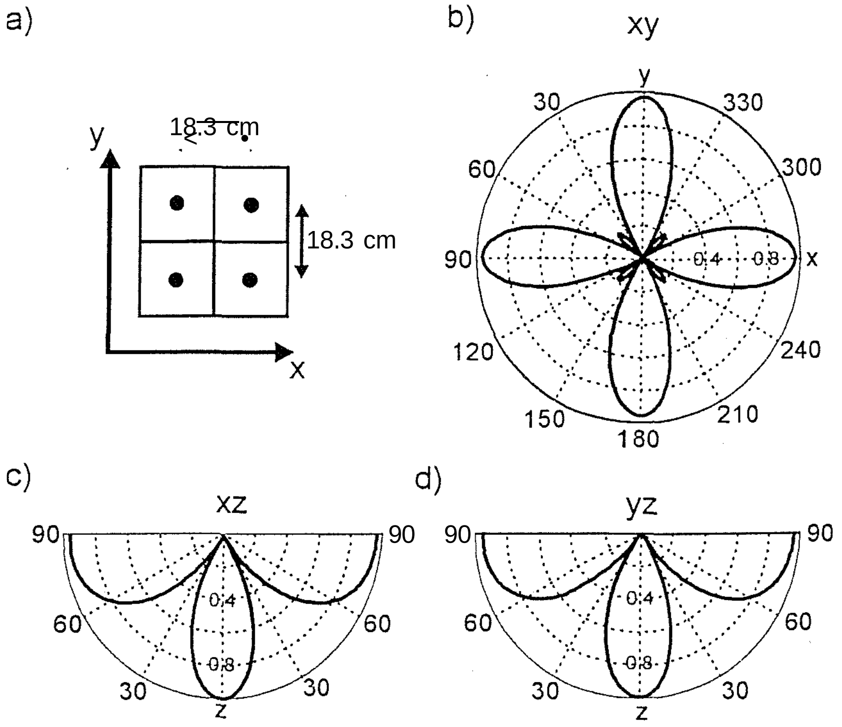

Figure 3.4 Directivity of the source array for 7.5 kHz arranged as a **square** after equation (3.5). a) Source array configuration as square, b) Horizontal plane directivity, c) xz-plane directivity, d) yz-plane directivity.

The symmetry of the **square array** results in symmetry of the directivity in the xy plane with respect to the x- and y-axis (Figure 3.4a) and identical directivities in the xz- and yz-planes (Figure 3.4b and c respectively). The main-lobe, centred in the z-direction, has an opening angle **of 38°** at half-width in either vertical plane. There are large amplitude side-lobes present in the vertical planes, which extend to 42° on either side of the z-axis. The directivity in the xy-plane shows four lobes aligned with the x- and y-axis with opening angles **of 36°** at half-width. Lobes with 10% of the maximum amplitudes are centred at **45°** to the main axes.

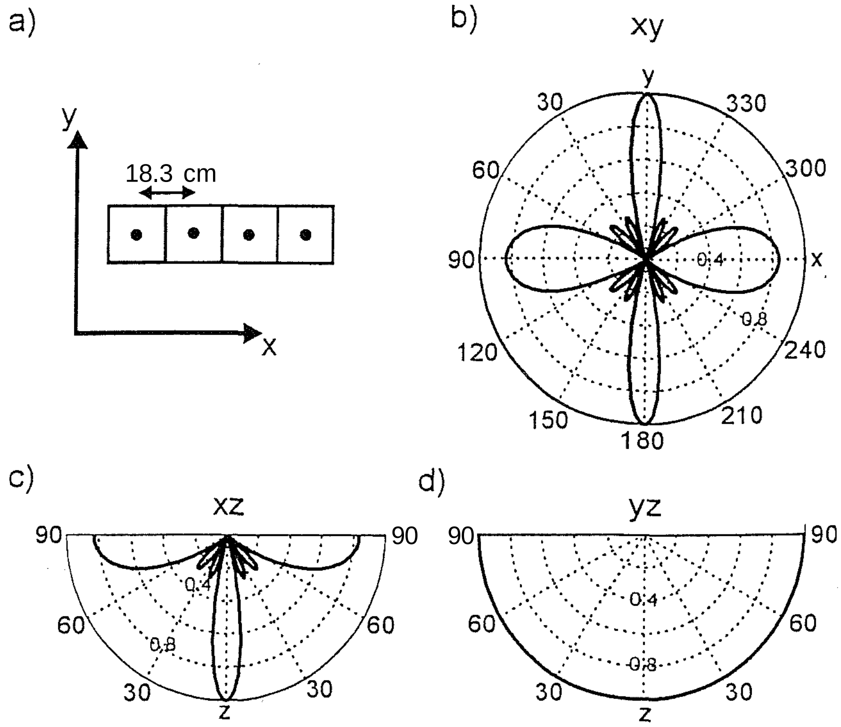

Figure 3.5 Directivity of the source array for 7.5 kHz arranged as **four in a row** configuration after equation (3.5). a) Source array configuration as four in a row with longitudinal direction parallel to x-axis. b) Horizontal plane directivity, c) xz-plane directivity, corresponding to the longitudinal direction of the array, d) yz-plane directivity corresponding to the transversal direction of the array.

The one-dimensionality of the **four in a row** array results in an omni-directional directivity in the yz-plane (Figure 3.5d), as effectively only one element contributes to the directivity in this plane. The directivity in the xz-plane (Figure 3.5c) shows a very tight main-lobe, centred at the z-axis, with an opening angle of only 16° together with larger amplitude side-lobes in the **x-direction,** extending to **70°. A** further four side-lobes with amplitudes of 15% are present at **20°** and **45°.** The xy-plane (Figure 3.5b) directivity shows tight lobes **(16°** at half-width) in the y-direction and wider **(40°** at half-width), lower amplitude lobes in the x direction with a number of tight very low amplitude (13%) lobes in diagonal directions.

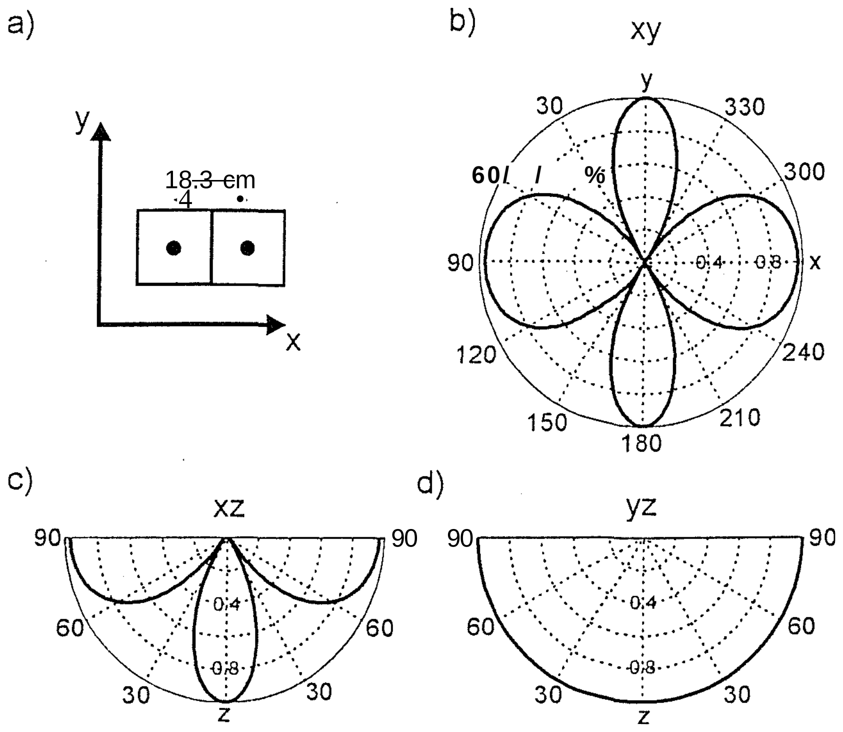

Figure 3.6 Directivity of the source array for 7.5 kHz arranged as a **pair** after equation (3.5). Note that it consists of only two elements as opposed to four elements in the other discussed configurations, a) Source array configuration as a pair with longitudinal direction parallel to the x-axis. b) Horizontal plane directivity, c) xz-plane directivity, corresponding to the longitudinal direction of the array, d) yz-plane directivity corresponding to the transversal direction of the array.

The directivity of the **pair** configuration is similar to the four in a row configuration. Due to the smaller numbers of elements the lobes are wider. The one-dimensionality of the array results in an **omni-directional** directivity in the yz-plane (Figure 3.6d), as effectively only one element contributes to the directivity in this plane. The directivity in the xz-plane (Figure 3.6c) shows main lobe, centred in the z-direction, with an opening angle **of 40°** at half-width together with larger amplitude side-lobes in the x-direction, extending to 40° at half-width. The xy-plane (Figure 3.6b) directivity shows tighter lobes **(40°** at half-width) in the y-direction and wider (80° at half-width), lower amplitude lobes in the x-direction.

In summary all configurations, except the square, have tighter main-lobe in the xz-plane, since their longitudinal direction is parallel to the x-axis. The four in a row and pair configurations are omni-directional in the yz-plane; the Maltese cross configuration has a significantly wider lobe in this plane than in the xz-plane.

The one-dimensional receiver groups are aligned with the y-axis due to the overall design of the 3D Chirp system. They are omni-directional in the yz-plane and have a tight lobe in the xz-plane, contrary to the source arrays. By combining the source array and receiver group directivities, tight lobes in all vertical planes can be achieved, as will be demonstrated in the model.

3.4.1.2 Receiver group directivity

The directivity of the receiver group is calculated using the same equation as for the source array (equation 3.5). The group is constrained to one dimension coinciding with the y-direction for design reasons explained in Chapter 5. The minimum separation of the elements is limited by the size of the individual elements of 5 cm; the maximum separation is limited by the overall length of the array, which is dictated by design considerations and the optimal receiver group spacing needed to avoid spatial aliasing. Five different configurations are discussed, varying in their number of elements and in the element separation.

1. four elements with 6.25 cm separation
2. four elements with 5 cm separation
3. four elements with 12.5 cm separation
4. two elements with 6.25 cm separation
5. two elements with 13.75 cm separation

Each individual receiver element is much smaller than the wavelengths used. Therefore they can be considered omni-directional and the point array approach can be used to describe fully the group's directivity. Figure 3.7 shows the directivity of a four element group with 6.25 cm element separation for the frequency of 7.5 kHz.

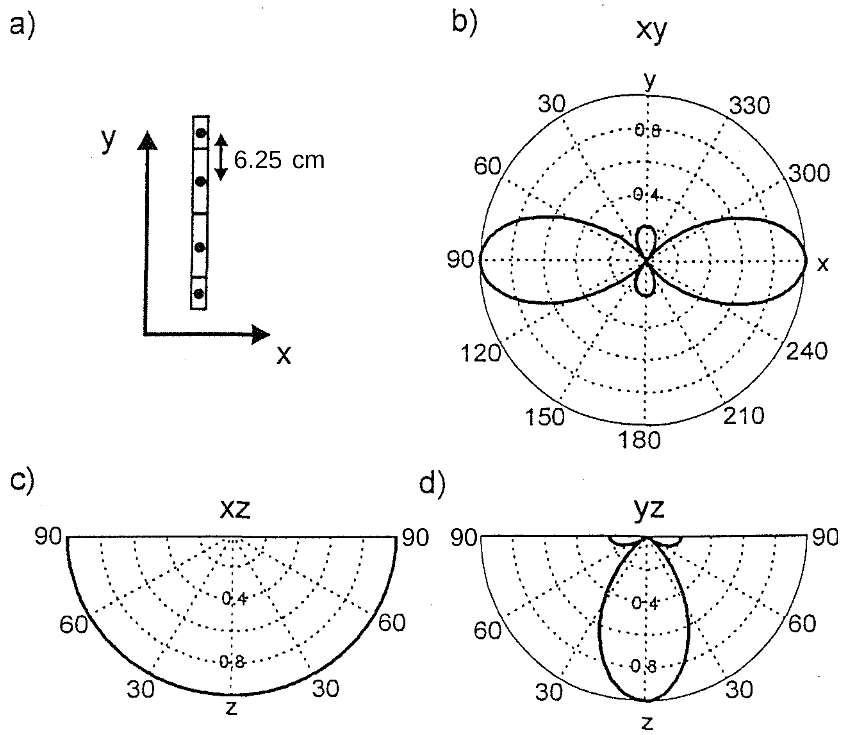

Figure 3.7 Directivity of a one dimensional receiver group for 7.5 kHz consisting of four elements after equation (3.5). a) Receiver group consisting of four elements with 6.25 cm separation aligned along the y-axis. b) Horizontal plane directivity, c) xz-plane directivity, corresponding to transversal direction of array in which only a single, **omni-directional** element contributes to the directivity, d) yz-plane directivity corresponding to the array's longitudinal direction.

In the xz-plane (Figure 3.7c), for which effectively only a single element contributes, the group is omni-directional. In the yz-plane (Figure 3.7d) a main lobe, centred at the z-axis, with an opening angle of 56° at half-amplitude values can be observed with small amplitude side-lobes in horizontal directions. The xy-plane (Figure 3.7b) shows two lobes in the x-direction, which are identical to the main-lobe in the yz-plane, and the low-amplitude side-lobes are present. Due to the omni-directionality in the xz-plane and the mirroring of the yz-plane directivity in the xy-plane, only the yz-plane directivity is shown for the other four configurations in Figure 3.8.

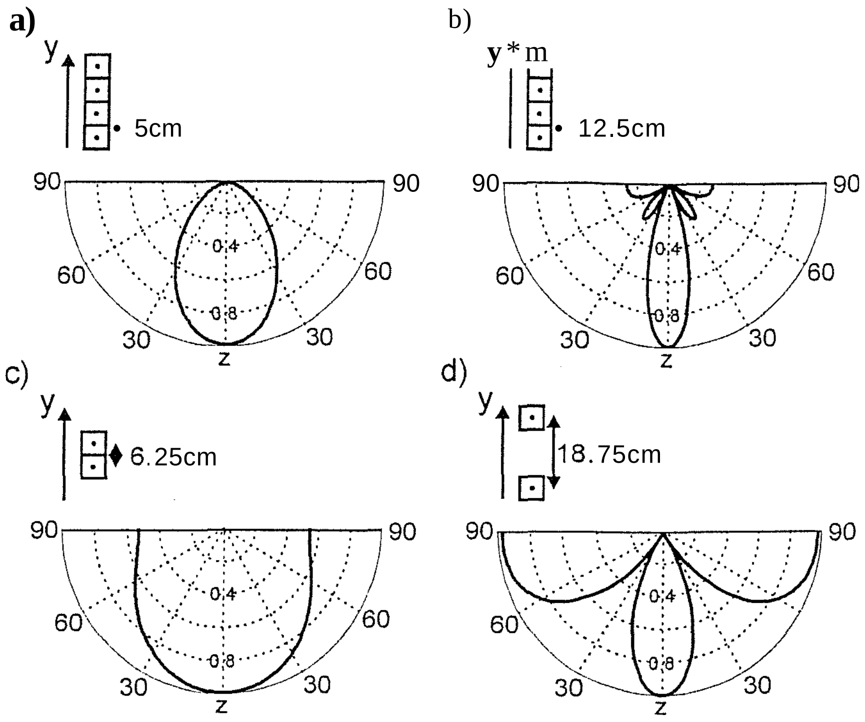

Figure 3.8 Receiver group directivities in the yz-plane. The xz-plane directivities of the shown configurations are omni-directional and the xy-plane directivities mirror the yz-plane directivities. See Figure 3.7 for details, a) Four element array with 5 cm separation, b) Four element array with 12.5 cm separation, c) Two element array with 6.25 cm separation, d) Two element array with 18.75 cm separation.

Comparing the four-element groups with different separations (Figures 3.7d, 3.8a and 3.8b) shows that by increasing the element separation the main-lobe, centred in the z-direction, half-width decreases from 64° (for 5 cm) to 56° (for 6.25 cm) to 28° (for 12.5 cm). At the same time the number and amplitude of the side-lobes increases with four side-lobes for the 12.5 cm separation with amplitudes of up to 28%. The two-element configurations (Figures 3.8c and d) are obtained by omitting the outer and inner elements respectively of the array shown in Figure 3.7a. The array with 6.25 cm spacing shows a main-lobe with 130° half-width at half amplitude, significantly wider than the four element group with the same element spacing (Figure 3.7). The group with 18.75 cm spacing shows a main-lobe with 38° opening angle at half-width but two large amplitude side-lobes **reaching down to 47°.**

In summary,' it is advisable to use as many elements as possible as this significantly decreases the main-lobe width together with side-lobe numbers and amplitudes. For this example it shows that a wide separation is desirable, as it narrows the main-lobe while increasing the side-lobes to a tolerable extent. However, the separation is limited by the 3D

Chirp design considerations and the desired receiver group spacing to avoid spatial aliasing that is discussed later in this chapter.

Taking all these considerations into account, the four element receiver group with 6.25 cm element spacing and an overall length of 25 cm, shown in Figure 3.7a, is the optimal choice for the 3D Chirp system. It will be used for the modelling presented in this chapter. It will be shown later that a receiver group spacing of 25 cm results in an acceptable level of spatial aliasing. From the modelling in this section it is clear that four elements within each receiver group with 6.25 cm element spacing give the best directivity with a tight main-lobe and low-amplitude side-lobes.

3.4.2 Transducer directivity

Figure 3.9 shows the measured directivity of the model T135 transducer (Neptune Sonar Ltd.) for four different frequencies. Due to the circular symmetry of the transducer the directivity shows symmetry with respect to the z-direction.

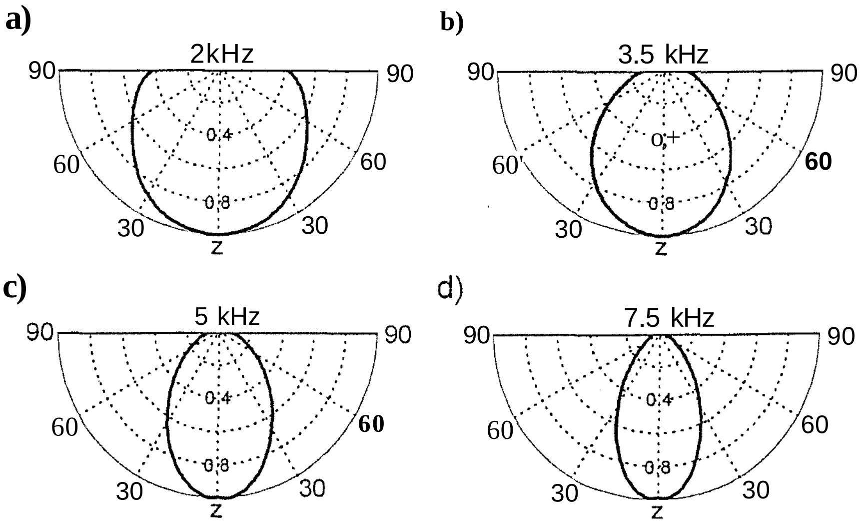

Figure 3.9 Single transducer directivity (T135 Neptune Sonar Ltd.) measured for different frequencies. Due to symmetry of the piston type transducer the directivity is symmetrical with respect to the z-direction. a) 2 kHz. b) 3.5 kHz. c) 5 kHz. d) 7.5 kHz.

There are no side-lobes present for these frequencies, as the transducer plate dimensions of approximately 18 cm are similar to the wavelength corresponding to the given frequencies of 20-75 cm. The half-amplitude opening angles range from **120°** for a frequency of 2 kHz to 56° for a frequency of 7.5 kHz.

3.4.3 Reflection amplitude model

With the assumption that the source array and receiver group are centred at the same location, the reflected amplitude, *A,* as a function of seabed location can be calculated as

$$A(\theta,\psi,f) = \frac{\text{A . -D. -f)}_r}{r^2} \tag{3.6}$$

where D_T is the directivity of the transducer, D_S the directivity of the source array and D_R the directivity of the receiver group, depending on the frequency *f.* The distance from the source array and receiver group to the reflection point is given by *r*. The angles *6* and *i/z* are directional angles of the vector originating at the source array and receiver group and pointing towards the reflection point on the seafloor (Figure 3.2). Figure 3.10 shows a sketch of the model.

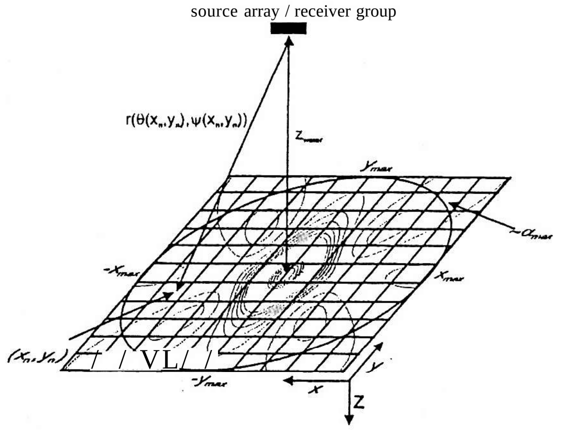

Figure 3.10 Reflection amplitude model. Amplitudes are calculated depending on the source array and receiver group directivities as specular reflections returning to the receiver group on the evenly spaced grid for a given water depth z_{wat}er and directional angles 9 and i// using equation (3.6).

In the model the reflection amplitude is calculated using equation (3.6) for each point *(x_n,y„),* distributed on an evenly spaced grid, whose directional angles can be expressed as

$$9 = \tan^{-1}\frac{y_n}{z_{water}} \tag{3.7}$$

and

$$\backslash j/ = \cos^{-1}\frac{\wedge\sqrt{y_n^2 + z_{wafer}^2}}{K\sqrt{\ +y_n^2 + z_{water}^2}}, \tag{3.8}$$

where z_{waler} is the water depth.

The geometrical spreading is accounted for in the factor $\frac{1}{r^2}$, where

$$r = \frac{z_{water}}{\cos 0 \cos y/}. \tag{3.9}$$

The maximum reflection angle corresponding to the circle on the seafloor in Figure 3.10 can be written as

$$\alpha_{\max} = \cos^{-1}\frac{TWT_{water}}{TWT_{wafer} + TWT_s}, \qquad (3.10)$$

where $$\cos a = \cos 9 \cos y/ \qquad (3.11)$$

and TWT_{water} is the two way travel time of the seismic signal in the water column. It is calculated from z_{water} and v_{water}, the seismic velocity in water, assumed to be $v_{wa}zer^{=}$ 1500 m/s. TWT_S is the expected penetration of the signal. $TWT_{wa}ter^{+}TWT_s$ is hence the recording duration of the seismic signal during data acquisition.

Appendix A contains the model in Matlab code with detailed explanations. The required model parameters are $z_{watS}r$, TWT_S, frequency / and the positions of the source and receiver elements for the calculation of the directivity functions given in equation (3.5).

For the model results shown in this chapter a water depth of 20 m (c. 26 ms TWT) and an expected penetration of 35 ms TWT and a frequency of 7.5 kHz were assumed, typical for survey targets of the 3D Chirp system. Figure 3.11 shows the single transducer directivity, the receiver group directivity and the geometrical spreading for the given model parameters. The receiver group consists of four elements aligned in the y-direction with 6.25 cm spacing and a resulting overall length of 25 cm of the group.

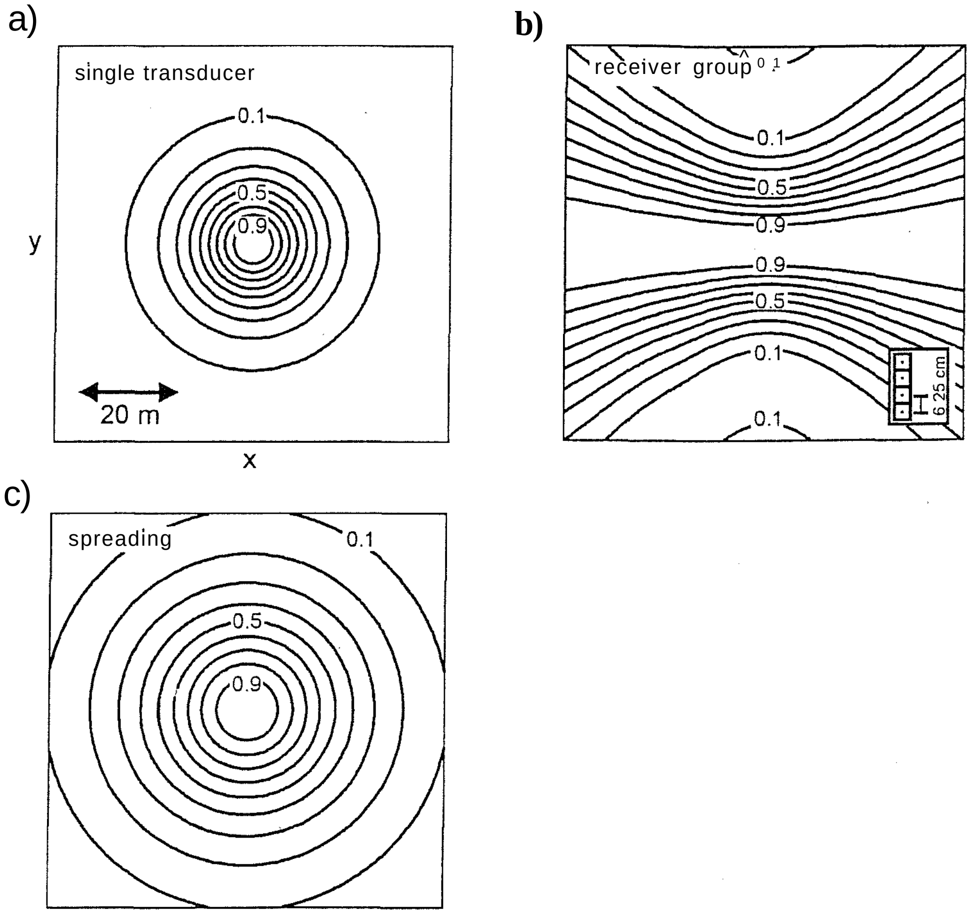

Figure 3.11 Model results of the normalised reflected ampkitudes for 20 m water depth and a frequency of 7.5 kHz. a) Single transducer directivity. See Figure 3.9d for polar plot, b) Receiver group directivity for four-element group aligned in y direction with 6.25 cm element spacing. See Figure 3.7 for directivity, c) Geometrical spreading.

The single transducer reflection amplitude pattern (Figure 3.11a) is concentric, corresponding to its directivity D_H which is symmetric with respect to the z-axis (Figure 3.9d). The receiver group reflection amplitudes reflect the **omni-directionality** of the directivity D_R in the xz-plane and the single lobe in the yz-plane (Figure 3.7). The geometrical spreading (Figure 3.11c) also shows concentricity.

Figure 3.12 shows the source array directivity components of the reflection amplitude model for the four discussed arrays.

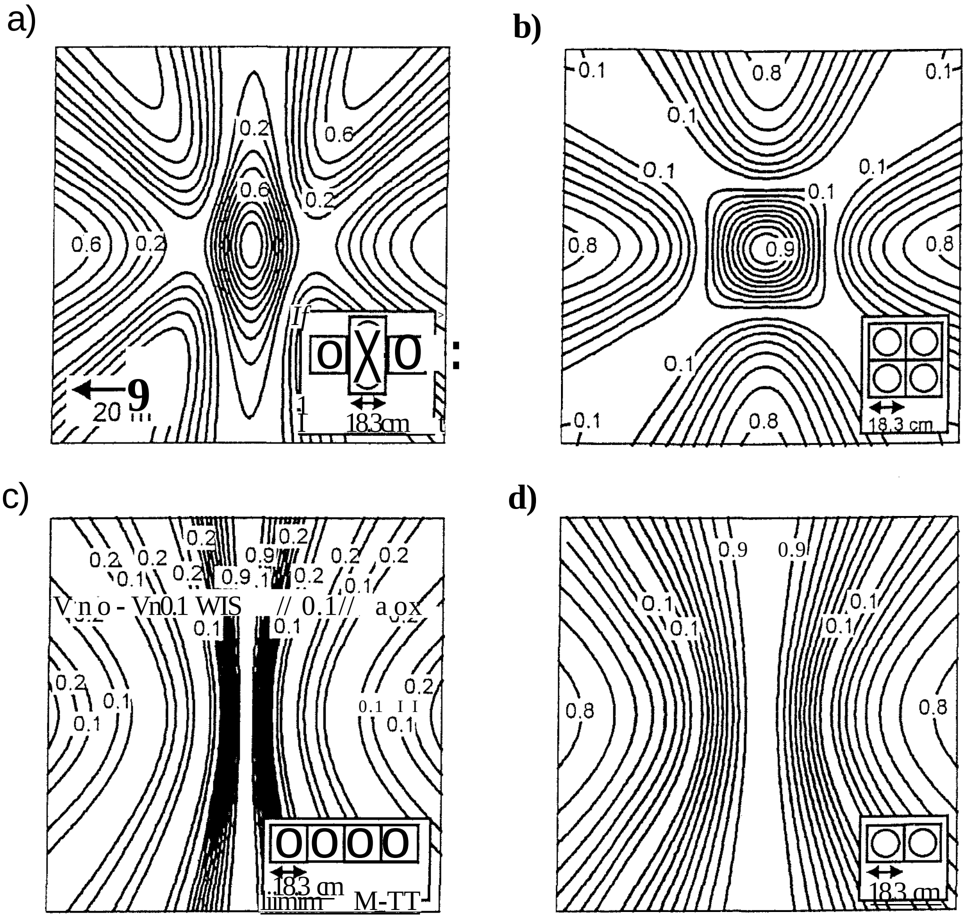

Figure 3.12 Source array reflection amplitude model results of the normalised reflected amplitudes for 20 m water depth and a frequency of 7.5 kHz. a) **Maltese cross** configuration, b) **Square** configuration, c) **Four in a row** configuration, d) **Pair** configuration.

The reflection amplitude pattern of the source arrays correspond to their respective directivities D_S shown in Figures 3.3 to 3.6. The **Maltese cross** reflection amplitude model results (Figure 3.12a) show a high amplitude feature in the centre, elongated in the y-direction, corresponding to the main-lobe of the array's directivity in the yz-plane (Figure 3.3c). The tighter main-lobe of the array's directivity in the xz-plane is responsible for the smaller extension of the reflection pattern in the x-direction. A number of high amplitude side-lobes are present as reflection patterns left and right and in the diagonal directions from the centre. The **square** reflection amplitude pattern (Figure 3.12b) represents the main-lobe of the arrays directivity (Figure 3.4), which is identical in the xz- and yz-plane, as a point symmetric feature. The high amplitude side-lobes of the directivity are present as high amplitude reflections offset from the centre, symmetric with respect to the x- and y-axis. The **four in a row** reflection amplitude model results (Figure 3.12c) reflect the omni-directionality of the array's directivity in the yz-plane (Figure 3.5) and the tight main-lobe with small amplitude side-lobes in the xz-plane. The main-lobe is represented as tightly spaced contours elongated along the y-direction with increasing curvature away from the centre. The **pair** reflection amplitude model results are similar to the results for the four in a row configuration. It also reflects the omni-directionality of its directivity in the yz-plane (Figure 3.6) and its main-lobe with, in this case, higher amplitude but wider side-lobes in the xz-plane.

In summary, corresponding to the arrays directivities, all configurations have tighter reflection patterns in the x-direction, since it corresponds to their longitudinal direction. The symmetrical square configuration is an exception. The reflection amplitude results for the receiver group show a tighter reflection pattern in the perpendicular y-direction. By combining the source array and receiver group reflection amplitudes a circular reflection amplitude pattern is expected.

Figures 3.13 to 3.16 show the total reflection amplitude A modelled from equation (3.6) for the four different source arrays, in each case using the single transducer directivity, geometrical spreading and the directivity of the four-element receiver group with 6.25 cm spacing shown in Figure 3.11. The model results are shown as a contour plot (section a of Figures 3.13 to 3.16) and as cross sections along the x- and y-axis (section b of Figures 3.13 to 3.16). In the cross section in addition to the reflection amplitude the apparent wavelength is plotted, calculated using equation (3.2). The plots can be used to determine which part of the reflected seismic energy will be spatially aliased for a given receiver group spacing, using equation (3.1). For example, for a receiver group spacing of 25 cm from equation (3.1) all reflection amplitudes corresponding to apparent wavelength smaller or equal to 50 cm are spatially aliased. These correspond to the reflections amplitudes outside the marked areas in section b of Figures 3.13 to 3.16.

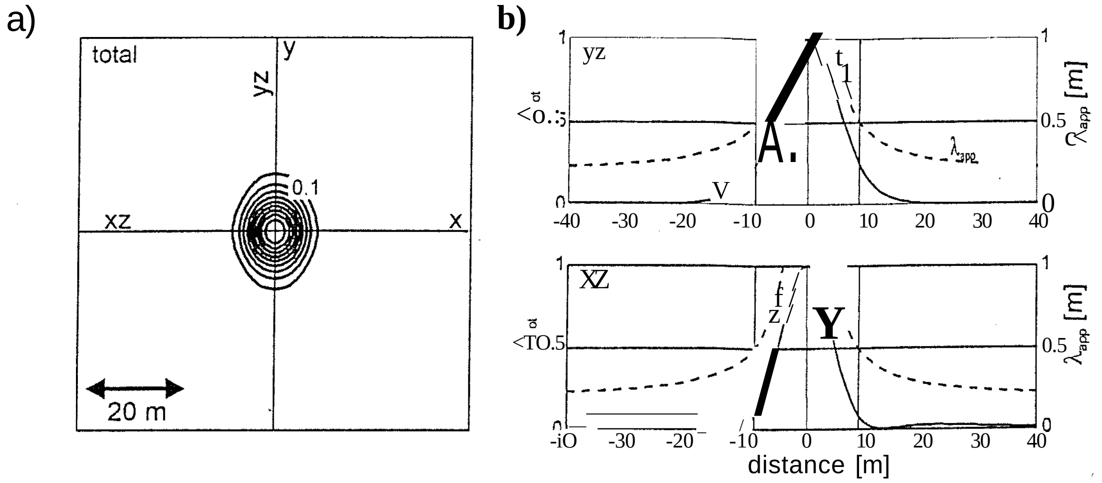

Figure 3.13 Total reflection amplitude for 20 m water depth and a frequency of 7.5 kHz for a **Maltese cross** source array. The model is based on equation (3.6). The individual reflection amplitudes for the transducer and the four-element receiver group with 6.25 cm element spacing and the geometrical spreading is shown in Figure 3.11. The source array reflection amplitude is shown in Figure 3.12a. a) Total reflection amplitude as a contour plot, b) Total reflection amplitude cross-sections together with apparent wavelength λ_{app} calculated from equation (3.2).

The total modelled reflection amplitude for the **Maltese cross** source configuration shows an elongated shape in the y-direction with a 23% wider lobe at half the maximal amplitude in the y-direction than in the x-direction. The source array directivity with the longitudinal direction along the y-axis over-compensates the receiver directivity, which is elongated in the perpendicular x-direction, resulting in the elongation in the y-direction of the total reflection amplitude pattern. The cross section in the yz-direction shows that with 50 cm apparent wavelength 23% of the maximum amplitude is reached. Smaller apparent wavelengths, outside the area are spatially aliased. In the xz-direction only 9% of the maximum amplitude is present at 50 cm apparent wavelength. Table 3.2 shows the receiver group spacing with the corresponding not spatially aliased minimum wavelength from equation (3.1) together with the percentage of the total amplitude aliased in the yz- and xz-directions from Figure 3.13b.

Receiver group spacing [cm]	**Minimum apparent wavelength $X_{,app}$ not aliased fcm|**	**% of amplitude aliased in yz-direction**	**% of amplitude aliased in xz- direction**
15	30	1.5	2.3
20	40	**9.8**	**0.4**
25	50	**212**	9.3
30	**60**	**38.4**	**211**
35	70	**54.2**	**319**
40	**80**	**60.3**	**415**
45	90	**67.1**	**54.8**

Table 3.2 Receiver element spacing and corresponding minimum apparent wavelength l_{app} that is not spatially aliased after equation (3.1) together with the corresponding percentage of the total reflection amplitude in yz- and xz-direction from Figure 3.13.

The percentage of aliased amplitude increases in a non-linear manner with increasing receiver group spacing, with a fast increase of slope between 20 cm and 25 cm receiver group spacing. For 25 cm the average percentage of aliased amplitude in yz- and xz-direction is 16.3%. Keeping in mind that the reflection amplitudes are over-estimated, due to the model assumptions this value is acceptable. A 25 cm receiver group spacing is also suitable according to general design considerations discussed in Chapter 5 and is therefore used in the 3D Chirp system. For the remaining model results only the percentage of aliased amplitude corresponding to 25 cm receiver group spacing is discussed.

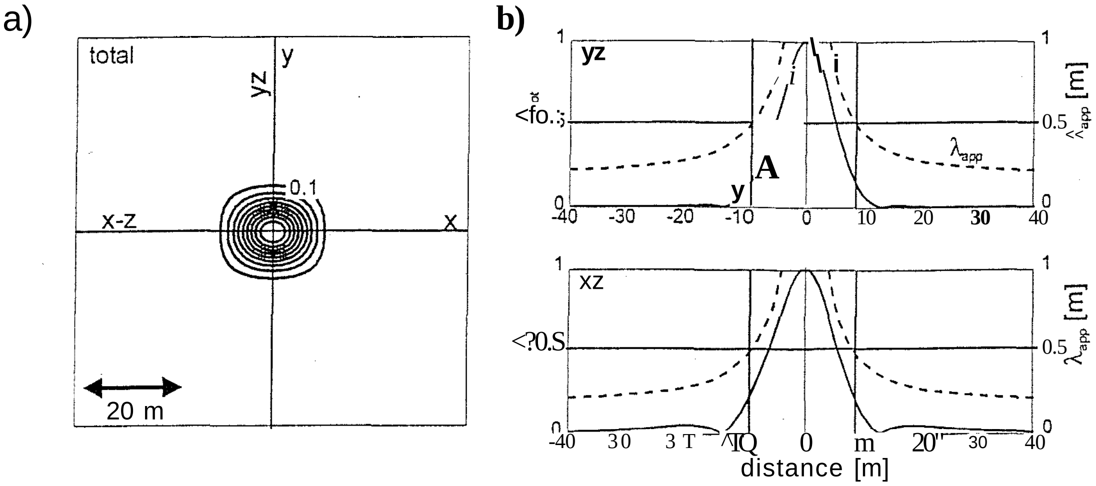

Figure 3.14 Total reflection amplitude for 20 m water depth and a frequency of 7.5 kHz for a **square** source array. The model is based on equation (3.6). The individual reflection amplitudes for the transducer and the four-element receiver group with 6.25 cm element spacing and the geometrical spreading is shown in Figure 3.11. The source array reflection amplitude is shown in Figure 3.12b. a) Total reflection amplitude as a contour plot, b) Total reflection amplitude cross-sections together with apparent wavelength X_{app} calculated from equation (3.2).

The total modelled reflection amplitude for the **square** source configuration shows a slightly elongated shape in the x-direction with a 9% wider lobe at half maximum amplitude in the x-direction than in the y-direction. This is due to the effect of the receiver directivity, which is elongated in the x-direction. The symmetrical directivity of the square source array does not compensate for this. The cross section in the yz-direction shows that for 50 cm apparent wavelength only 16% of the maximum amplitude is reached. Smaller apparent wavelengths, outside the area are spatially aliased. In the xz-direction 23% of the maximum amplitude is present at 50 cm apparent wavelength.

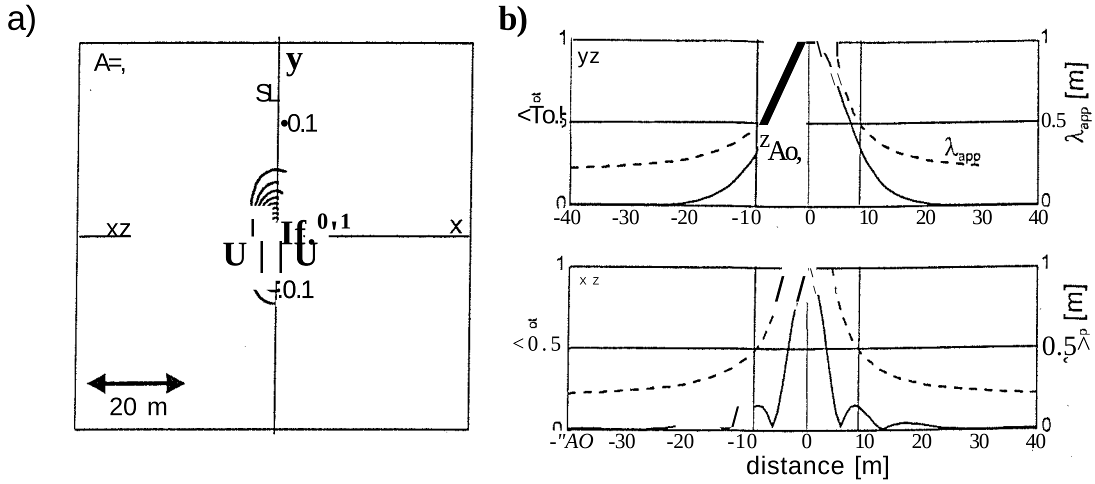

Figure 3.15 Total reflection amplitude for 20 m water depth and a frequency of 7.5 kHz for a four in a row source array. The model is based on equation (3.6). The individual reflection amplitudes for the transducer and the four-element receiver group with 6.25 cm element spacing and the geometrical spreading is shown in Figure 3.11. The source array reflection amplitude is shown in Figure 3.12c. a) Total reflection amplitude as a contour plot, b) Total reflection amplitude cross-sections together with apparent wavelength X_{app} calculated from equation (3.2).

The total modelled reflection amplitude for the **four in a row** source configuration shows an elongated shape in the y-direction with a 21% wider lobe at half maximum amplitude in the y-direction than in the x-direction. Additionally side-lobe reflections with 16% of the total energy are present right and left from the centre along the x-axis. The source array directivity with the longitudinal direction along the y-axis over-compensates the receiver directivity, which is elongated in the perpendicular x-direction, resulting in the elongation in the y-direction of the total reflection amplitude pattern. The cross section in the yz-direction shows that for 50 cm apparent wavelength 35% of the maximum amplitude is reached. Smaller apparent wavelengths, outside the area are spatially aliased. In the xz-direction only 15% of the maximum amplitude is present at 50 cm apparent wavelength. Beside the main-lobe reflection side-lobe reflections are present in the non-aliased area with a nodal point from which no reflection energy is returned.

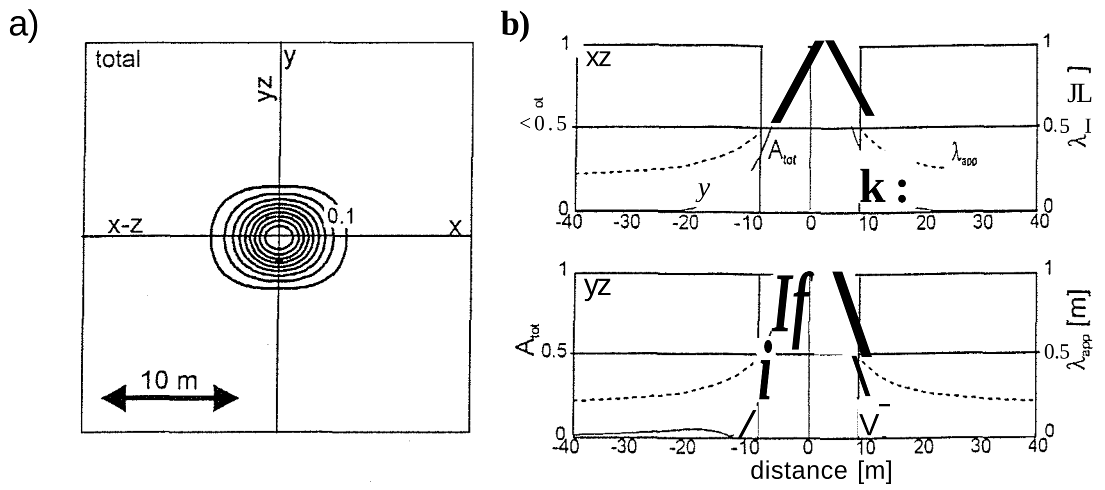

Figure 3.16 Total reflection amplitude for 20 m water depth and a frequency of 7.5 kHz for a pair source array. The model is based on equation (3.6). The individual reflection amplitudes for the transducer and the four-element receiver group with 6.25 cm element spacing and the geometrical spreading is shown in Figure 3.11. The source array reflection amplitude is shown in Figure 3.12c. a) Total reflection amplitude as a contour plot, b) Total reflection amplitude cross-sections together with apparent wavelength k_{app} calculated from equation (3.2).

The total modelled reflection amplitude for the **pair** source configuration shows an elongated shape in the x-direction with a 14% wider lobe at half maximum amplitude in the x-direction than in the y-direction. The source array directivity with the longitudinal direction along the y-axis does not compensate the receiver directivity, which is elongated in the perpendicular x-direction, resulting in the overall elongation in the x-direction. The cross section in the yz-direction shows that for 50 cm apparent wavelength 35% of the maximum amplitude is reached, similar to the four in a row result in this direction. Smaller apparent wavelengths, outside the area are spatially aliased. In the xz-direction only 23% of the maximum amplitude is present at 50 cm apparent wavelength, similar to the results of the pair configuration.

In summary, with the model assumptions of specular reflection and no attenuation, the amplitudes are overestimated and in reality lower energy levels would be aliased for a given receiver group spacing than in the model. A receiver group spacing of 25 cm, used in the above example, has been chosen for the 3D Chirp system considering not only the spatial aliasing but also the overall size and ground coverage of the system as explained in Chapter 5. The model shows that the receiver group spacing of 25 cm is sufficient, with the right choice of source array and receiver group configurations, to spatially sample the reflection energy and avoid high energy returns being spatially aliased. A relative comparison of the different configurations shows that the Maltese cross configuration achieves the best results in compensating for elongated receiver directivity and achieving an overall tight and slightly elongated foot-print. Due to its symmetry the square configuration does not compensate for the elongated receiver directivity and achieves slightly worse results than the Maltese cross configuration in avoiding spatial aliasing. The four in a row configuration shows a non-symmetrical foot-print with large amplitude side-lobe reflections, which is undesirable for horizontal resolution considerations of the system. The pair configuration, consisting only of two source elements, results in a larger footprint than for the four-element source configurations. The Maltese cross and a double pair source configuration are used in the 3D Chirp system. In the double pair source configuration each pair could be fired independently, as discussed in Chapter 5.

3.5 Conclusions

A model was presented that provides the spatial distribution of reflection amplitudes for a seismic system. It assumes that the reflections are specular and the signal is not attenuated on its travel path. The distribution depends on the source array and receiver group directivities as well as on the directivity of the individual source elements and geometrical spreading. The model is used to find the acquisition geometry for a seismic system, under given constraints that optimises spatial sampling and horizontal resolution. Different source arrays and receiver groups are discussed and model results for different configurations are compared. By comparing the reflection angle dependent apparent wavelength of the returned signal with the reflection amplitudes, the expected amount of spatial aliasing can be determined. The receiver group spacing has to be chosen in accordance with the findings as only apparent wavelength at least twice the length of the receiver group spacing are correctly spatially sampled. A comparison of the percentage of spatially aliased energy for different receiver group spacing was presented. A receiver group spacing of 25 cm largely avoids spatial aliasing and is chosen for the application on the basis of the comparison and general design constraints discussed in Chapter 5. The optimal choices of the source array and receiver group under the given constraints are a one-dimensional four-element receiver group with 6.25 cm element spacing and an overall length of 25 cm and a four-element source array in Maltese cross configuration. Additionally a double-pair configuration is utilized in the 3D Chirp system, where each pair is fired individually. The longitudinal axis of the source arrays are chosen to be perpendicular to the receiver group's longitudinal axis to compensate for its elongated directivity and achieve an overall circular footprint.

4 Positioning of source arrays and receiver groups

4.1 Introduction

In order to successfully produce a high resolution 3D seismic volume it is crucial that the absolute source and receiver positions are known with sufficient accuracy. In this chapter an analysis of the position accuracy needed for the 3D Chirp system will be presented and it will be shown that the source and receiver elements need to be known to a centimetre scale. The 3D Chirp design incorporates sources and receivers fixed relative to each other on a rigid frame. This is in contrast to conventional marine seismic systems, as well as to previously described 3D high resolution systems (Chapter 1), where sources and receivers are towed and positioned independently. The position of a rigid array with respect to a system of Cartesian coordinates can be described by the position of one point fixed with respect to the array and three angles expressing its attitude: heading, pitch and roll. A number of positioning systems were considered for the 3D Chirp application, including inertia, magnetic, GPS-based and acoustic systems. The only system which promised to meet the requirements and lay within the budget of the project was a GPS-based position and attitude system.

The system is described and an algorithm is presented to calculate the positions of elements on a rigid array from the output of the system, a single absolute position together with heading, pitch and roll values.

The system was tested against the manufacturer's specifications and the accuracy requirements for the proposed 3D Chirp system. Additionally the reliability and suitability of the system were confirmed by simulating a marine survey situation.

4.2 Position accuracy requirements

The accuracy to which the positions of the source and receiver elements of the seismic system need to be known depends on the source signature used (see Chapter 2). The requirement for the vertical accuracy is that seismic traces associated with the same reflection point on the seafloor show static shifts due to vertical positioning inaccuracies less than the peak to trough distance of the reflection signature. This prevents destructive interference between the traces during data processing (Gutowski et al., 2002). The source signature with the tightest Klauder wavelet (S7, Figure 4.1) to be used with the system can be used to derive a threshold value. Two wavelets will interfere destructively when they are shifted, so that the peak and the trough of the main-lobe coincide, which for this wavelet is 60 ps (Figure 4.1). Assuming a seismic wave velocity of 1500 m/s for the recorded wave-front this converts into a vertical distance of 4.5 cm. This is an estimated threshold value for the required vertical accuracy.

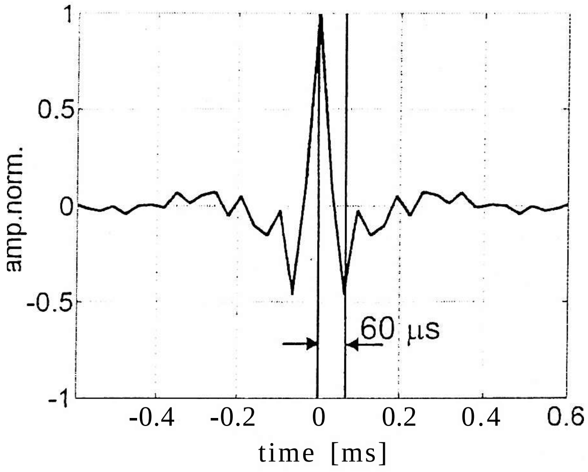

Figure 4.1 Klauder wavelet of the sine squared 8th enveloped 1.5-13 kHz sweep S7 discussed in Chapter 2 (Figure 2.7). The distance between main-lobe peak and trough is 60 (.is.

In order to reconstruct the wavefield adequately, the horizontal position needs to be known within a quarter of the dominant wavelength of the used source signature, $X_{mea}n/4$. For the source signature S7 discussed, where A.$_{mean}$=21 cm, this is approximately 5 cm. Furthermore the position needs to be measured reliably with an update rate similar to the seismic shot rate, expected to be as high as 4 Hz (Chapter 5).

In summary navigational control is needed which will provide less than 4.5 cm vertical and less than 5 cm horizontal resolution with a minimum update rate of 4 Hz.

4.3 The RTK-GPS positioning and attitude systems

4.3.1 The RTK-GPS system

The RTK-GPS technology is based on carrier phase measurements of GPS satellite signals and resolving the integer ambiguities by using a reference station connected to the roving station via a UHF radio link. Figure 4.2 shows the system's set-up. An Ashtech Sagitta system was used consisting of two dual frequency receivers as reference and roving stations connected via a UHF radio link (Ashtech Sagitta Series User Manual, 2002). The reference station's GPS antenna is positioned on a known location. The system uses the Long Range Kinematic processing method LRK®, which offers a maximum operating range of 40 km but is, in practice, limited by the range of the radio link. The radio range depends on the environmental conditions and is generally smaller than 40 km. The accuracy depends on the chosen output mode. Two different types of LRK© solutions are available. LRK-A is the most accurate solution, delivering a position every time a correction signal is received by the roving station. The typical output rate is lower than 1 Hz. The LRK-R solution delivers positions based on extrapolated correction data in constant update rates of up to 20 Hz. Table 4.1 shows the claimed position accuracies achieved in the different modes. If an RTK solution can not be found due to lack of correction data (no radio connection) or lack of tracked satellites, the system switches into a non-RTK mode with significantly lower accuracy on a decimetre or even meter scale. The system is controlled via serial port using a laptop computer running specialist software. The data output is via a second serial port in ASCII format stored on the laptop computer.

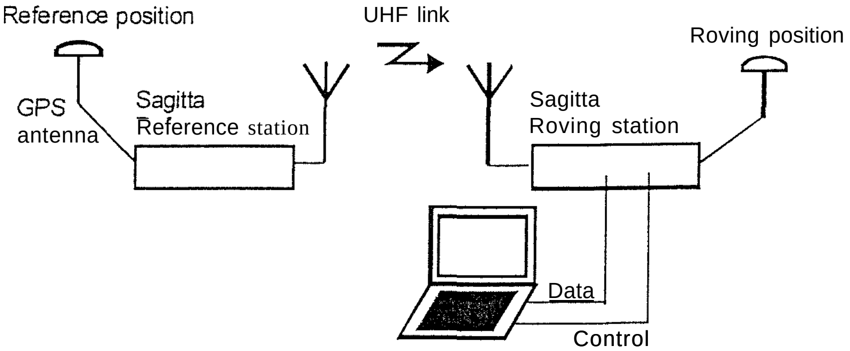

Figure 4.2 The Ashtech Sagitta dual frequency RTK-GPS system. The system comprises a reference and roving station, which are connected via an UHF radio link. The antenna of the reference station is located at a precisely known reference position. The stations are controlled by a laptop computer via a serial connection.

	LRK-A	**LRK-R**
x-, y-position	5 mm + 0.5 ppm	10 mm + 0.5 ppm
z-position	10 mm + 1 ppm	20 mm + 1 ppm

Table 4.1 The Ashtech Sagitta RTK-GPS positioning accuracy as quoted in the Ashtech Sagitta Series User Manual (2002). LRK-A is the accurate mode, output every time the roving station receives a correction signal from the reference station, typically smaller than 1 Hz. LRK-R: is the interpolation mode, output rate up to 20 Hz. ppm: part per million.

4.3.2 The GPS based attitude determination system

The attitude determination of the Ashtech ADU5 system is based on differential carrier phase measurement of the GPS signal between four **GPS-antennas,** arranged into a plane array and connected to a single frequency receiver (Ashtech ADU5 operation and reference manual, 2002). The system delivers heading, pitch and roll information in real time, with a maximum update rate of 5 Hz. The accuracy of the solution depends on the antenna separation and is summarised in Table 4.2.

Antenna separation [m]	**heading [° rms]**	**pitch, roll rms]**
1	0.4	0.8
3	0.06	0.12
10	0.02	0.04

Table 4.2 Ashtech ADU5 attitude accuracies depending on the antenna separation of the system's four antenna array. Quoted by Ashtech ADU operation and reference manual (2002).

The system is controlled with a laptop computer that runs specialised software. The data is logged on the same computer. One of the system's GPS antennas is shared with the RTK-GPS system.

4.4 Source and receiver position determination from position and attitude information

The source and receiver elements of the seismic system are positioned on a plane and rigid array. The positions of the elements can be determined using a single position, fixed with respect to the array, and its heading, pitch and roll values.

The aim is to express the positions of the *n* source and receiver positions (X_n,Y_n,Z_n) given in the intrinsic coordinate system of the array, defined by the unit vectors $(\vec{c},\vec{b},\vec{k})$, in Universal Transverse Mercator (UTM) coordinates. The UTM coordinates are derived from the UTM position of the RTK-GPS antenna A, fixed to the rigid plain array and the heading, pitch and roll values of the array provided by the attitude system installed on it. It is assumed the pitch and roll movement are with respect to axis running though the centre of gravity of the system. Note that the centre of the antenna array that determines the attitude values (section 4.3.2) needs to be vertically above the centre of gravity.

Figure 4.3 shows the UTM coordinate system (x,y,z) together with a local system (x',y',z') with the origin A, given by the antenna, which can be obtained by the following translation of coordinates:

(x,y,z) = (y,/,z') + (a,,a2,«3) , (4.1)

where [illegible] is the position of A in the [illegible] UTM system of coordinates.

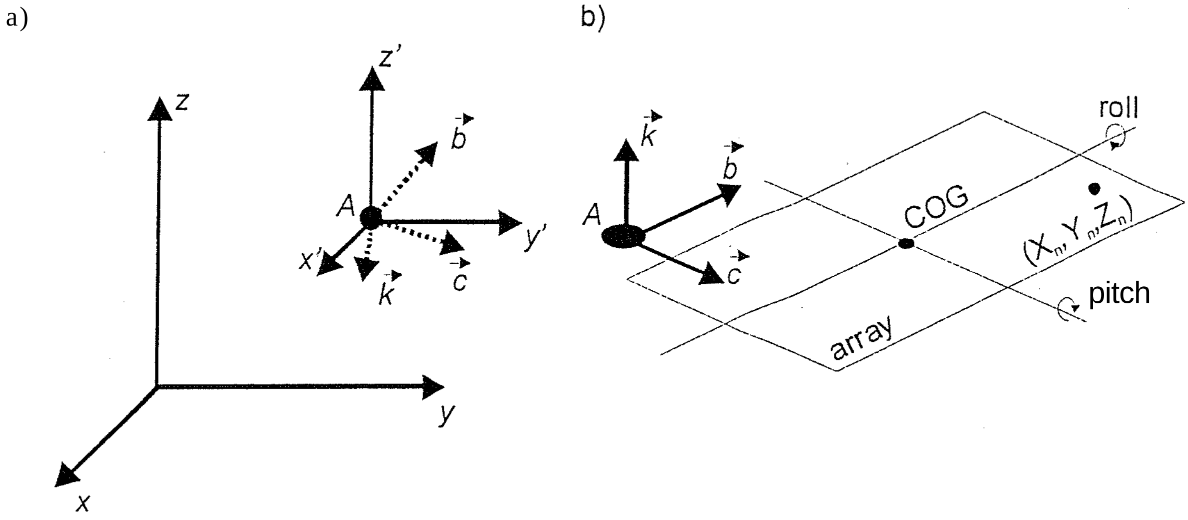

Figure 4.3 a) UTM system of coordinates *(x,y,z)* with a local system *{x'.y'.z')* with origin A, obtained by a single translation. A is the position of the antenna, with known UTM coordinates, fixed to the plane rigid array. A third coordinate system, intrinsic to the array, represented by the unit vectors $(\vec{c},\vec{b},\vec{k})$ with origin A, obtained by rotation of the *(x'.y'.z')* system, b) The plane rigid array with its intrinsic system of coordinates given by the unit vectors $(\vec{c},\vec{b},\vec{k})$and the origin A. The roll and pitch rotation axis run through the centre of gravity (COG).

Unit vectors $\vec{b}$ and$\vec{c}$ (Figure 4.3), originating from the RTK-GPS antenna's position A, are parallel to the array's axis and define together with the perpendicular unit vector $\vec{k}$ the array's intrinsic system of coordinates. Heading ⟨E⟩ and pitch 0 are defined as shown in Figure 4.4.

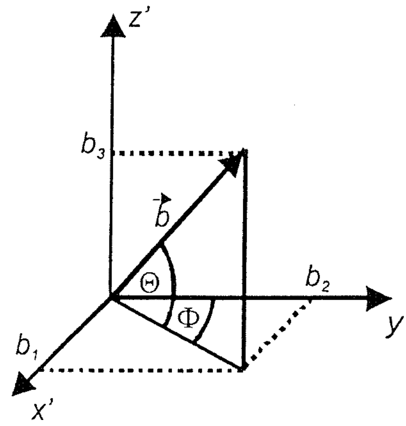

Figure 4.4 Definition of heading 0 and pitch 0 in the system of coordinates *(x'.y'.z')*- Heading 0 is defined as the angle between the projection of vector $\vec{b}$ in the horizontal %'y'-plane and the *y'* direction, which is parallel to geographic north, whereas vector $\vec{b}$ points in the longitudinal direction of the array. Pitch © is defined as the angle between vector $\vec{b}$ and the horizontal *x'y'*-plane.

Writing $\vec{6}$ as with respect to the y', z' axis of coordinates

$$6, = 6\% \tan \lhd D \tag{4.2}$$

$$b_1^2 + b_2^2 + b_3^2 = 1, \tag{4.3}$$

$$b_3 - \sin © \tag{4.4}$$

Substituting (4.2) and (4.3) into (4.4) yields

$$b_2 = \cos© \cos O \tag{4.5}$$

and substituting (4.4) into (4.3) yields

$$b_x = \sin 0 \ \cos © . \tag{4.6}$$

Hence

$$\vec{b} = (\sin 0 \ \cos ©, \cos 0 \ \cos 0, \sin ©). \tag{4.7}$$

The definition of the roll angle ¥ is shown in Figure 4.5.

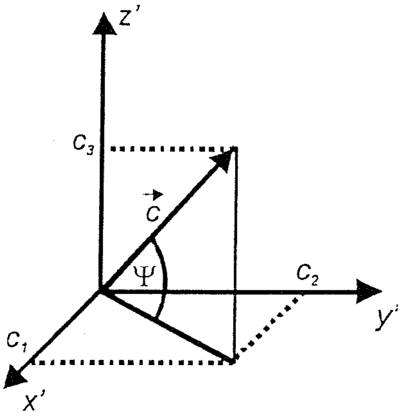

Figure 4.5 Definition of roll Y as the angle between the horizontal *x'y'*-plane and the vector $\vec{c}$, that is parallel to the transversal direction of the array.

Since $\vec{c}$ is a unit vector

$$\sin Y = c_{\cdot} \tag{4.8}$$

and

$$C \wedge + C^2 2 + C^2, = l . \tag{4.9}$$

Substituting (4.8) into (4.9) yields

$$c \wedge + f \overset{3}{2} = \cos \wedge Y \tag{4.10}$$

and since $\vec{b}$ and $\vec{c}$ are perpendicular

$$\vec{b} \cdot \mathbf{\vec{c}} = \mathbf{0}, \tag{4.11}$$

thus

$$b_1 c_1 + 62C2 + \&3C3 \leftarrow 0- \tag{4.12}$$

From (4.7) and (4.8)

$$c_l \sin 0 \ \cos© + c_2 \cos \$ \ \cos O + \sin ©\sin ¥ = 0. \qquad (4.13)$$

Dividing (4.13) by sin 0 cos 0 and simplifying yields

$$c, = \frac{1}{\sin 0}(c_7 \cos 0 + \tan ©\sin W). \qquad (4.14)$$

Substituting (4.14) into (4.10) and simplifying yields the quadratic equation

$$c\backslash + 2C_2 \cos \ \tan ©\sin ¥ + \tan^2 ©\sin^2 ¥ - \cos^2 ¥\sin^2 0 = 0, \qquad (4.15)$$

with solution

$$c_2 = -\cos 0 \ \tan ©\sin Y - \sin \$\sqrt{\cos^2 - \tan^2 ©\sin^2 Y} \ . \qquad (4.16)$$

Hence the vector components of the unit vectors **$\bar{6}$ and $\bar{c}$ in** the *(x\ y', z')* system of coordinates are given as

$$\begin{aligned} b_x &= \sin 0 \ \cos©, \\ b_2 &= \cos 0 \ \cos©, \\ b_3 &= \sin 0, \\ c_1 &= -\frac{1}{\sin 0}(c_2 \cos 0 + \tan 8 \ \sin Y), \\ c_2 &= -\cos 0 \ \tan ©\sin Y - \sin 0\sqrt{\cos^2 W - \tan^2 ©\sin^2 ¥}, \\ c_3 &= \sin Y. \end{aligned} \qquad (4.17)$$

For **0=0,** 7t ,2tc *cj* is not defined. It can be shown that for **0=0** and 0=2tu the vector components are

$$\begin{aligned} 6, &= 0, \\ b_2 &= \cos©, \\ b_3 &= \sin 0, \\ c, &= \sqrt{1 - (\tan^2 0 + 1)\sin^2 Y}, \\ c_2 &= \tan 0 \ \sin Y, \\ c_3 &= \sin T. \end{aligned} \qquad (4.18)$$

and for 0=tt

$$\begin{aligned} 6] &= 0, \\ b_2 &= -\cos©, \\ b_3 &= \sin©, \\ c, &= -\sqrt{1 - (\tan^2 0 + 1)\sin^2} \\ c_2 &= \tan ©\sin T, \\ c_3 &= \sin ¥. \end{aligned} \qquad (4.19)$$

Any point (X,Y,Z) in the intrinsic array system of coordinates $(\vec{c},\vec{6},\vec{\&})$, rotated by the given heading, pitch and roll around the centre of gravity of the rigid array, can be **converted into the system of coordinates by performing the transformation**

$$\vec{x}' = A(\vec{X} - \vec{X}_{COG}) - A(-\vec{X}_{COG}) \qquad \textbf{(4.20)}$$

where

$$\vec{x}' = \begin{pmatrix} x' \\ / \\ z' \end{pmatrix}, \ \vec{\%} = \begin{pmatrix} X \\ Y \\ Z \end{pmatrix}, \ {}^\wedge\vec{\text{COG}} \ \bar{-} \begin{pmatrix} X_{COG} \\ {}^\wedge\text{COG} \\ 7 \end{pmatrix} {}^\wedge\text{COG V} \qquad \textbf{(4.21)}$$

and

$$A = \begin{pmatrix} c_1 & b_1 & k_1 \\ \% & 6, & *2 \\ c_3 & {}^\wedge 3 & K \end{pmatrix} \qquad \textbf{(4.22)}$$

with

$$\vec{k} = \vec{c} x \vec{b} \qquad \textbf{(4.23)}$$

and (XcoG,ycoG,Zcoo) the coordinates of the centre of gravity in the intrinsic system. By performing the translation given by equation (4.1) the global UTM **coordinates** are obtained.

4.5 System test

Four experiments were completed in order to verify the claimed accuracy of the Ashtech Sagitta RTK-GPS and the Ashtech ADU5 attitude systems and to evaluate its suitability for the use with the 3D Chirp system.

In a static experiment, aimed to verify the systems' accuracies, the GPS antenna array remained motionless while the position and attitude data were logged over a period of time.

In a dynamic experiment the antenna array was installed on a catamaran, which was towed behind a survey vessel. This experiment simulates a survey situation with the 3D Chirp system and was carried out to evaluate the reliability of the system and the suitability for the use with the 3D Chirp system.

In both the static and dynamic experiment two different antenna configurations for the ADU5 attitude system were used to study the effect on the accuracy and acquisition reliability. The antenna separations correspond to the dimensions of the proposed 3D Chirp array (Chapter 5). Figure 4.6 shows the cross and rectangular antenna configurations used mounted on the catamaran.

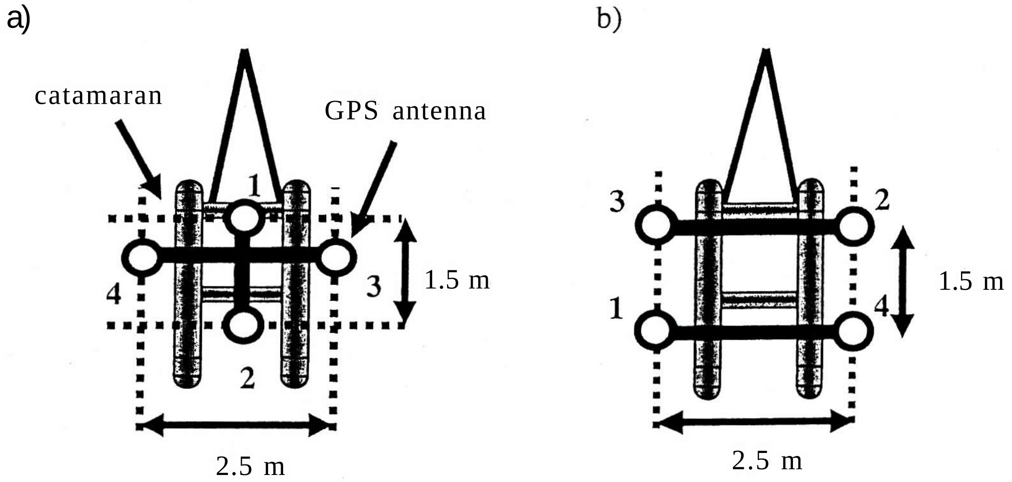

Figure 4.6 The Ashtech ADU5 and Sagitta attitude and position systems' GPS antennas mounted on a catamaran. Antenna 1 is shared by both systems, antennas 2-4 are used solely by the ADU5 attitude system, a) Cross antenna configuration, b) Rectangular antenna configuration.

To determine whether the accuracies, both of the position and attitude data, meet the threshold values derived in section 4.2, the movement of an imaginary receiver element on a rigid plane was simulated from the position and attitude values. The element's position is assumed to be (2.57 m, 1.38 m, -0.99 m) with respect to the RTK-GPS antenna in the arrays intrinsic system of coordinates $(\vec{c},\vec{b},\vec{k})$ for the rectangular antenna configuration (Figure 4.7). This corresponds to the position of the receiver element furthest away from the RTK-GPS antenna and the centre of gravity (COG) in the proposed geometry of the 3D **Chirp array (Chapter 4), as such simulating the largest positioning error. For the cross** antenna configuration the coordinates for the element furthest away from the antenna are (1.29 m, -1.38 m, -0.99 m). Its absolute position is calculated using the algorithm described in section 4.4, using the measured RTK-GPS antenna position and attitude values. The implementation of the algorithm in a FORTRAN code is presented in Chapter 6.

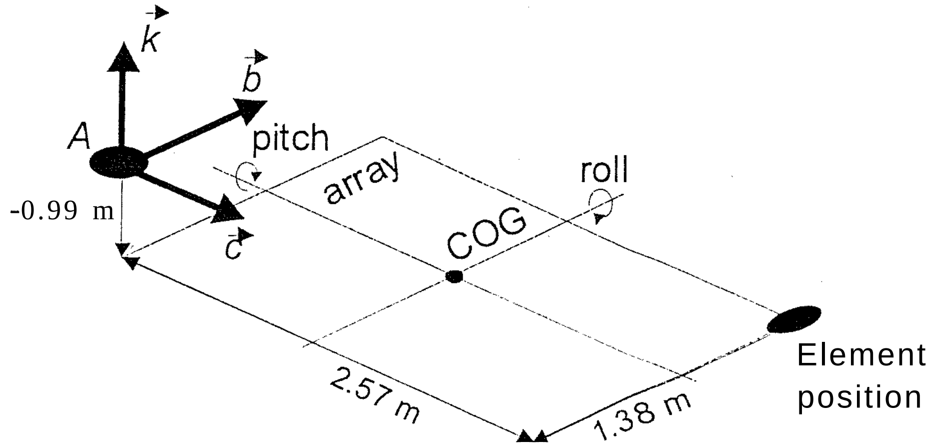

Figure 4.7 Position of element with coordinates (2.57 m, 1.38 m, -0.99 m) in the intrinsic system of coordinates $(\vec{c},\vec{b},\vec{k})$ for rectangular antenna configuration. In both the static and dynamic positioning experiments the absolute position of the element are derived from the absolute position of the antenna A and the heading pitch and roll values with respect to the centre of gravity (COG) of the system. The position corresponds to the receiver element furthest away from the RTK-GPS antenna and COG in the proposed 3D Chirp system (Chapter 5) and is thus expected to have the largest positioning error.

The experiments were carried out in January 2003 for the cross antenna configuration and June 2003 for the rectangular antenna configuration. The radio antenna of the RTK reference station was installed on the roof of the Southampton Oceanography Centre (SOC), in order to achieve a good radio connection with the roving station. A surveyed reference position was used for the reference station's GPS antenna (50°53'32.48966"N 01°23'41.80296"W , 74.947 m height in the WGS84 system). However, for the tests using the cross antenna configuration this reference location could not be used, as it was occupied by another antenna, and the reference GPS antenna needed to be positioned with an offset of about 1 m. Although the new position was estimated and accounted for in the set-up of the reference station, this could have an effect on the system's accuracy.

4.5.1 Static experiments

4.5.1.1 Static cross antenna configuration experiment

The cross antenna array mounted on the catamaran (Figure 4.6a) was positioned at the SOC and position and attitude data were recorded over a period of approximately 20 minutes. Figure 4.8 shows the three RTK antenna position components and the array's attitude values. Additionally the simulated position of the element furthest away from the RTK-GPS position antenna on the 3D Chirp array is shown as single component time series and as a 3D plot. All values are shown as deviations from their respective mean,

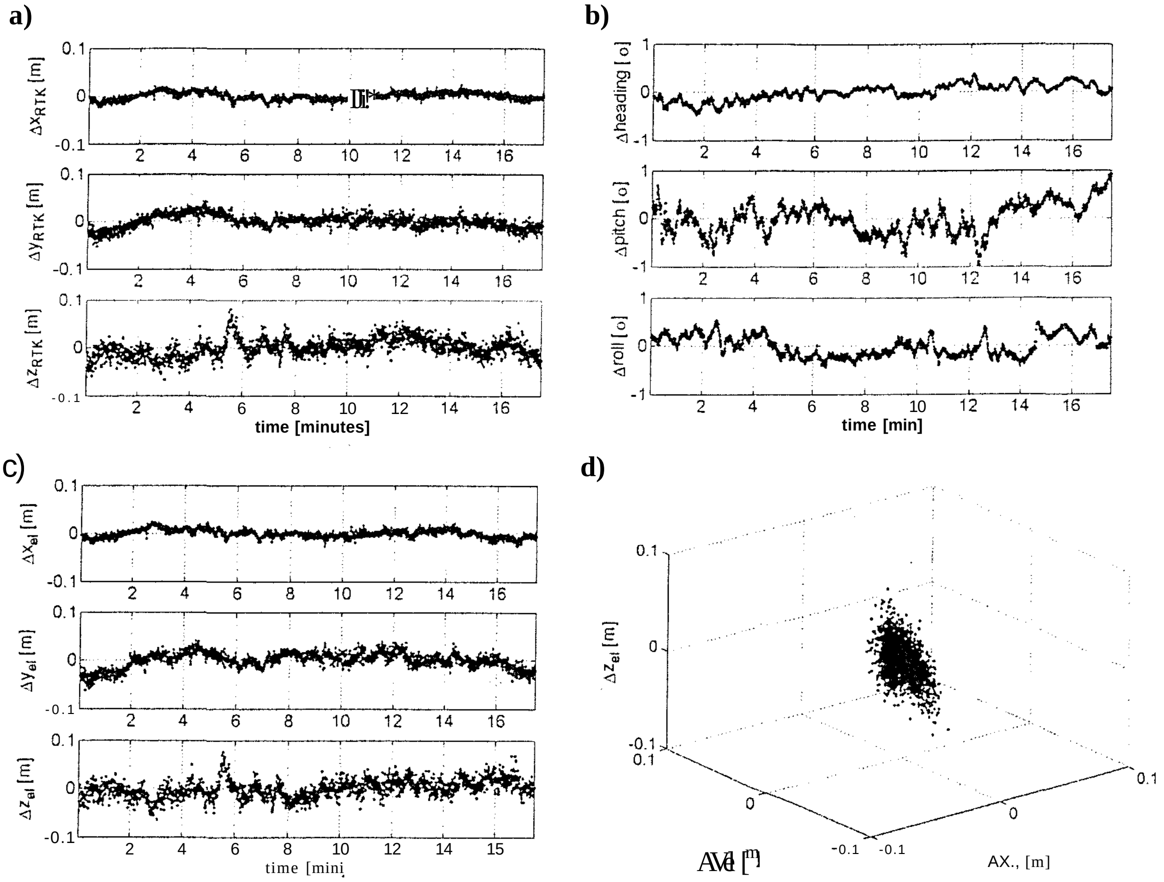

Figure 4.8 Position and attitude values for the static experiment using the cross antenna configuration. All values are shown as deviations from their respective means a) RTK-GPS antenna position components determined by the Ashtech Sagitta system, b) Attitude values heading, pitch and roll, in degrees, determined by the Ashtech ADU5 system, c) Simulated position components calculated from RTK-GPS position and attitude data, assuming a constant offset from the RTK-GPS position of an element (el). See text for details, d) Simulated position in 3D representation.

Table 4.3 summarises the standard deviation of the attitude values, heading, pitch and roll.

	Heading	Pitch	Roll
rms dev [°]	**0.16**	**0.32**	**0.22**

Table 4.3 Root mean square (rms) deviation for the cross antenna configuration static experiment.

The attitude determination is carried out by using phase difference measurements of all four antennas. The geometry of the antenna array has an impact on the accuracy of the different attitude values. The heading and pitch values are to a greater part determined using the antennas in the longitudinal direction of the array (antenna 1 and 2 in Figure 4.6a), which have a smaller separation of 1.5 m than antenna 3 and 4 in the transversa] direction, which have a separation of 2.5 m and are used to a greater part for the roll determination. The non-linear relationship between antenna separation and accuracy is reflected by the values in Table 4.2. From these values the heading accuracy is expected to be a factor 2 better than the pitch accuracy and lie closer to the specified value for 1 m antenna separation than to the value for 3 m. From Table 4.3 it is found that the pitch rms deviation is a factor 2 larger than the heading rms deviation. The absolute values are smaller than the specified values for the 1 m separation. For the reasons mentioned above it is expected that the roll rms deviation is smaller than the pitch rms deviation and lie within the specifications for 1 m and 3 m antenna separations, closer to the 3 m value. The roll value is in fact a factor 1.47 smaller and lies in the expected limits.

Overall the experimental results confirm the manufactures accuracy specifications.

Table 4.4 summarised the standard deviation of the position components for the RTK-GPS antenna position, antenna 1 in Figure 4.6a, and the simulated element position (Figure 4.7).

	XRTK	YRTK	ZRTK	XEL	y,,i	ZE]
rms dev [mm]	**7.9**	**118**	**20.3**	**7.9**	**14.2**	**214**

Table 4.4 Standard deviation for the RTK-GPS components (RTK) together with the accuracies of the simulated position components (el) (Figure 4.7) for the cross antenna static experiment.

Table 4.5 summarises the correlation coefficients between the position components.

	xRTK- YRTK	XRTK - zRTK	JR-FK - zRTK	Xei _ .Vd	Xei - Zd	y=i- zd
corr. coeff.	**0.63**	**-0.29**	**-0.13**	**0.58**	**-0.38**	**-0.05**

Table 4.5 Correlation coefficient for the RTK-GPS position (RTK) and the simulated position components (el) for the cross antenna configuration experiment.

The values in Table 4.4 show that the x-component deviation is a factor 1.74 smaller than that of the y-component and a factor 2.57 smaller than the z-component's. The deviation of the y-component is a factor 1.47 smaller than that of the z-component. On average the

horizontal component deviations are a factor 2.02 smaller than those of the z-component. This corresponds with the systems specification listed in Table 4.1, which claims a factor of 2. The large correlation coefficients between the x- and y-component from Table 4.5 suggest that the horizontal position needs to be analysed in conjunction, justifying the comparison of the mean value with the specification. Comparing the measured to the specification values shows that the average horizontal component rms deviation of 10.85 mm is close to the specified value of 10 mm. The z rms component deviation of 20.3 mm as well is very close to the specified value of 20 mm. Although the measured values lie 5 % above the manufacturer's specification, given the issues with the position the RTK-GPS reference station, whose position was not accurately known, these results are satisfactory. The deviation of the simulated position of the element furthest away from the antenna and COG (Figure 4.7) from Table 4.4 shows that the horizontal components have an average deviation of 1.1 cm. The large correlation coefficient from Table 4.5 between the horizontal directions suggests that these components should be considered together. This value complies well with the demanded horizontal accuracy of 5 cm. The deviation of the vertical components of 2.3 cm also lies well within the demanded vertical accuracy threshold of 4.5 cm.

4.5.1.2 Static rectangular antenna configuration experiment

The rectangular antenna array mounted on the catamaran (Figure 4.6) was again positioned at the Southampton Oceanography Centre. The position and attitude data were recorded over a period of approximately 30 minutes. Figure 4.9 shows the three RTK antenna position components, the attitude values and the simulated position of the element furthest away from the antenna on the 3D Chirp array, as single component time series and as a 3D plot. All values are shown as deviations from their respective mean. The data gap of approximately 2 minutes at approximately 17 minutes corresponds to the accidental obstruction of the RTK-GPS antenna and the resulting signal loss while the system **automatically re-initialised.**

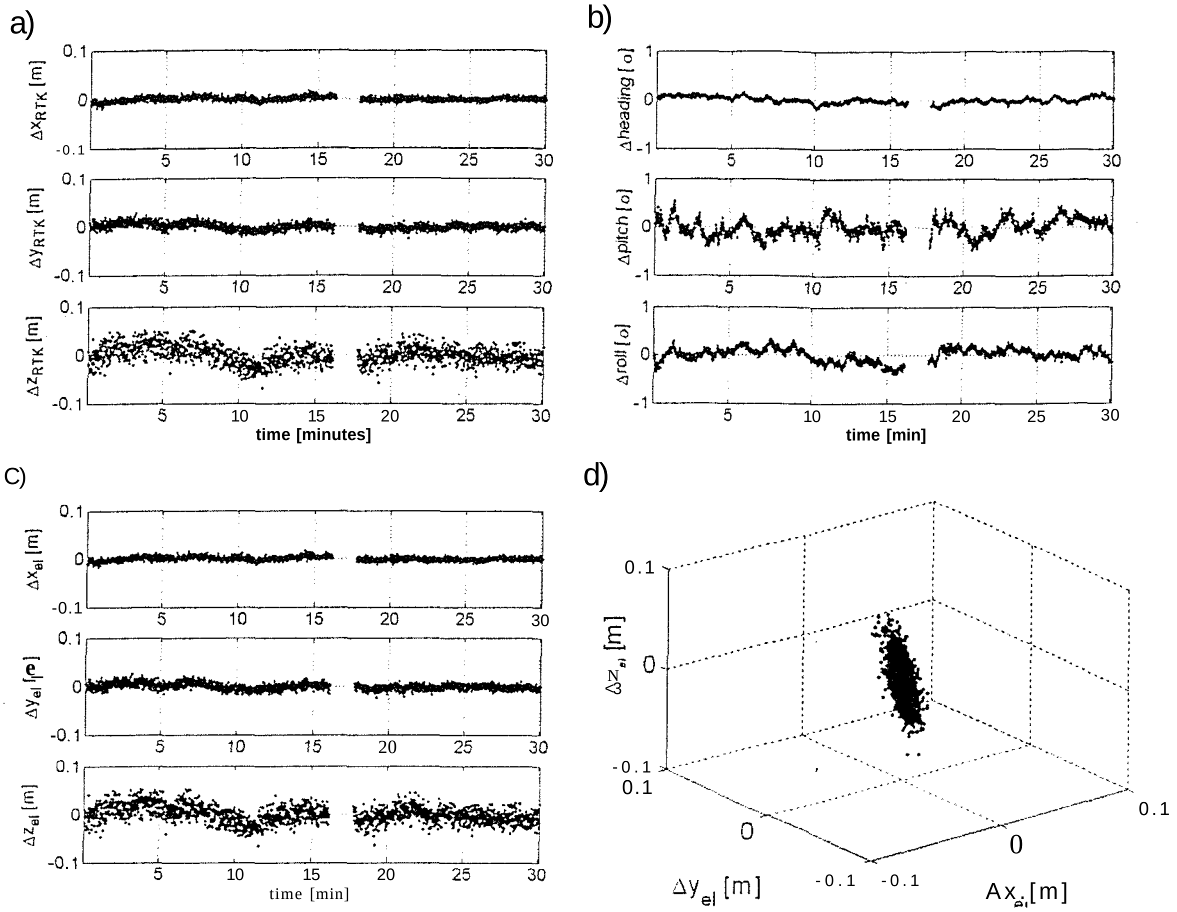

Figure 4.9 Position and attitude values for the static experiment using the rectangular antenna configuration. All values are shown as deviations from their respective means a) RTK-GPS antenna position components as determined by the Ashtech Sagitta system, b) Attitude values heading, pitch and roll as determined by the Ashtech ADU5 system, c) Simulated position components calculated from RTK-GPS position and attitude data, assuming a constant offset from the RTK-GPS position of an element (el), d) Simulated position as 3D representation.

Table 4.6 summarises the standard deviation of the attitude values.

	Heading	**Pitch**	**Roll**
rms dev [°]	**0.06**	**0.18**	**0.14**

Table 4.6 Attitude accuracies derived for the rectangular antenna configuration static experiment.

For this array geometry the heading value is mainly determined using the antennas in the oblique direction of the array (antenna 1 and 2 in Figure 4.6). The value is then corrected for the constant offset to the real heading direction, corresponding to longitudinal direction defined by antenna 1 and 3. Antennas 1 and 2 have a separation of 2.91 m. The pitch and roll values are determined using information of all four antennas with a separation between 2.91 m and 1.5 m. By comparing these values with the manufacturer's specification listed in Table 4.2 a factor of 2 between the heading and pitch and roll accuracy is expected. The pitch and roll values are 2.7 times larger on average than the heading value. The heading value is equal to the specification for a 3 m antenna separation. The roll and pitch value lie between the specification for the 1 m and 3 m antenna separation, closer to the 3 m specification. Overall the values comply with the manufacturer's specifications.

Table 4.7 shows the standard deviation of the position components, both for the RTK-GPS position of the antenna and the simulated position of the element furthest away from the antenna and COG in the proposed 3D Chirp system (Figure 4.7).

	x_{RTK}	y_{RTK}	z_{RTK}	x_{el}	y_{el}	z_{el}
rms dev [mm]	**4.6**	**7.4**	**18.1**	**4.6**	**7.0**	**18.2**

Table 4.7 Standard deviation for the RTK-GPS components, together with the accuracies of the simulated position components for the cross antenna static experiment.

Table 4.8 summarises the correlation coefficients between the position components.

	$x_{RTK}-y_{RTK}$	$x_{RTK}-z_{RTK}$	$y_{RTK}-z_{RTK}$	$x_{el}-y_{el}$	$x_{el}-z_{el}$	$y_{el}-z_{el}$
corr. coeff.	**0.16**	**-0.05**	**0.71**	**0.24**	**0.02**	**0.72**

Table 4.8 Correlation coefficient for the RTK-GPS position and simulated position components for the cross antenna configuration experiment.

The values in Table 4.7 show that the **x-component** deviation is a factor 1.61 smaller than that of the y-component and a factor 3.93 smaller than that of the z-component. The y-component deviation is a factor 2.45 smaller than that of the z-component. On average the horizontal components' deviation are a factor 3.02 smaller than that of the z-component. This does not correspond with the systems specification listed in Table 4.1, which claims a factor 2. However the absolute values show that the x-component deviation is 2.18 smaller than the specified value, the y-component deviation 1.35 and that of the z-component 1.1. In this case there is a large correlation coefficient between the y and the z-component.

The deviation of the simulated position of the element furthest away from the antenna and COG given in Table 4.7 shows that the x-component has deviation of 0.46 cm and the y-component 0.7 cm, which lies well within the threshold value of 5 cm derived in section 4.2. The vertical deviation is 1.82 cm which also complies with the required accuracy of 4.5 cm.

4.5.2 Dynamic experiments

4.5.2.1 Dynamic cross antenna configuration experiment

The experiment was completed using the same cross antenna configuration (Figure 4.6a) and reference station set-up as used in the static experiment. The catamaran was towed approximately 10 m behind the survey vessel along the track shown in Figure 4.10. The sea state throughout the experiment was very calm. In order to achieve rolling and pitching movements the antenna platform was navigated close to passing ships to cross their wash. These wash events were noted to be later identified in the data. Attitude and position data were collected over a period of approximately 55 minutes.

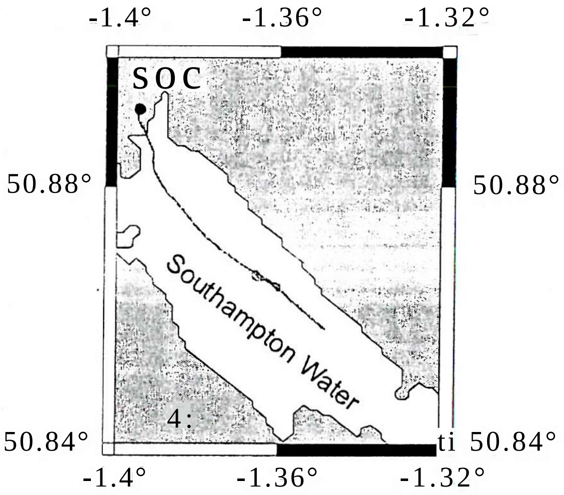

Figure 4.10 The RTK-GPS horizontal positions for the dynamic experiment using the cross antenna configuration (Figure 4.6a).

Figure 4.11 shows the attitude data together with the vertical component of the position data.

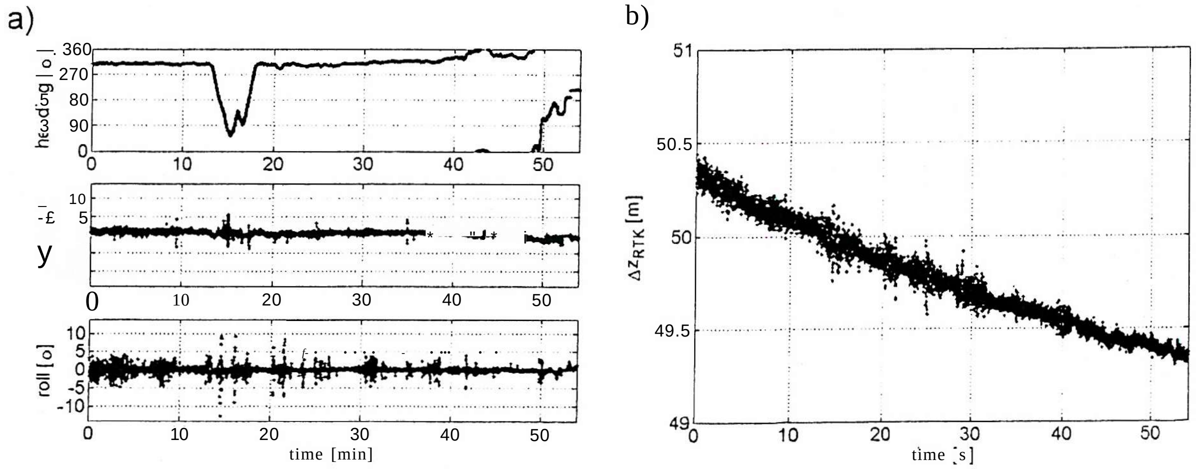

Figure 4.11 Cross antenna configuration dynamic experiment, a) Attitude: heading, pitch and roll data, b) RTK-GPS height. The decay of about 1 m is due to the outgoing tide.

The high frequency amplitude changes both in pitch, roll and height data are associated with the platform's movements due to waves. The low frequency decay of height of approximately 1 m throughout the experiment is due to the outgoing tide. The vertical movement amplitude is normally smaller than 15 cm reflecting the calm sea state, with pitch and roll values smaller than 5°. The events with vertical movements of up to 50 cm, pitch movement up to 6° and roll movements up to 13° are associated with the passing of the platform through a wash, generated by larger vessels. To investigate the wash events in more detail the data reflecting an event at about 15 min from the start of the experiment is shown as a close-up in Figure 4.12.

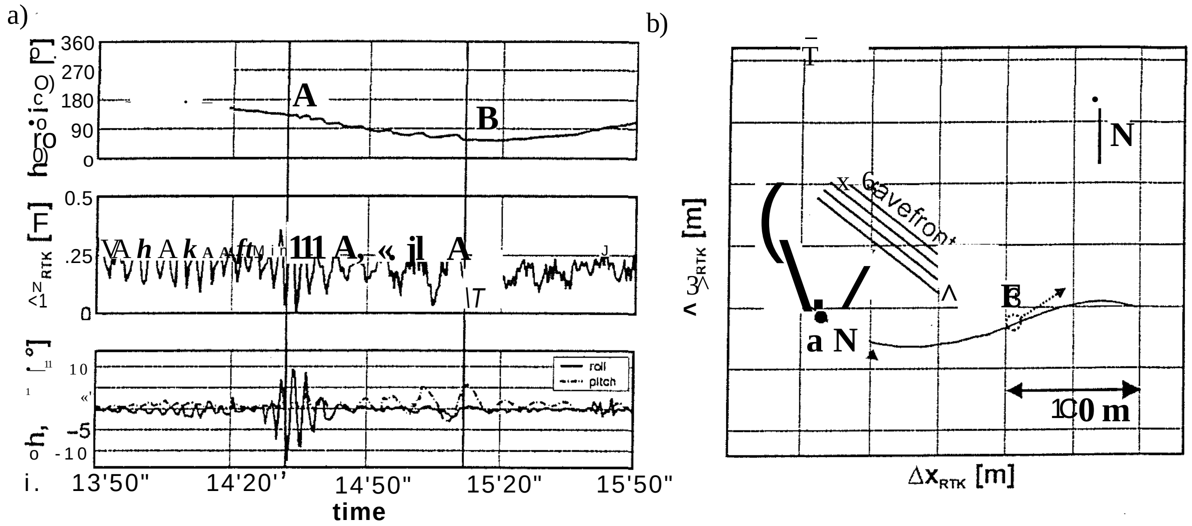

Figure 4.12 Dynamic experiment using the cross antenna configuration. The catamaran is passing through a ship's wake, a) Associated movements reflected in the height, heading, pitch and roll (close up of Figure 4.11). b) Trajectory of the catamaran during the passing of the wave front. See text for discussion.

The wave front of the wash in this example travelled in direction approximately 220°, shown in Figure 4.12b, which also shows the trajectory of the catamaran describing a bend. Figure 4.12a shows that the heading changes from 200° to 130° at point A, where the catamaran is parallel to the incoming wave front. It experiences a roll motion with amplitude of up 12° and change of vertical position of up to approximately 40 cm. It turns further while the roll motion decreases and the pitch movement increases. At point B the heading value is approximately 55° it is nearly perpendicular to the wave front, and it experiences a maximum pitch motion of approximately 5°, reflected in a change of vertical position of up to 32 cm. The towing behaviour of the catamaran is such that it is reluctant to point directly into the wash, and it is towed with a yaw angle as apparent from the difference between the measured heading and the heading values derived from the trajectory.

Overall throughout the experiment the position and attitude data were reliably recorded without data gaps with a rate of 4 Hz.

4.5.2.2 Dynamic rectangular antenna configuration experiment

The measurement was done using the same rectangular antenna configuration as that used in the static experiment and shown in Figure 4.6b. The aim of the experiment was twofold:

1. Determine the maximum operating range of the RTK-GPS system in a typical survey setup given as the radio range between reference and roving station.
2. Test the reliability of the attitude and RTK-GPS systems.

The catamaran was deployed in Southampton Water and towed to the East Solent. Figure 4.13 shows a map of the region with part of the catamaran's trajectory where GPS position data were recorded. The attitude data logging was established before the position data recording. A total of 2 hours of attitude data and 1 hour 20 minutes of position data were recorded, with an overlap of 18 minutes. The data is shown in Figure 4.14. The sea state throughout the experiment was rough with winds of approximately 4 to 5 on the Beaufort scale and wave heights of up to 1 m in particular towards the eastern part of the Solent.

4.5.2.2.1 Radio range test

The part of the catamaran's trajectory where RTK- GPS quality data were recorded is highlighted in red in Figure 4.13.

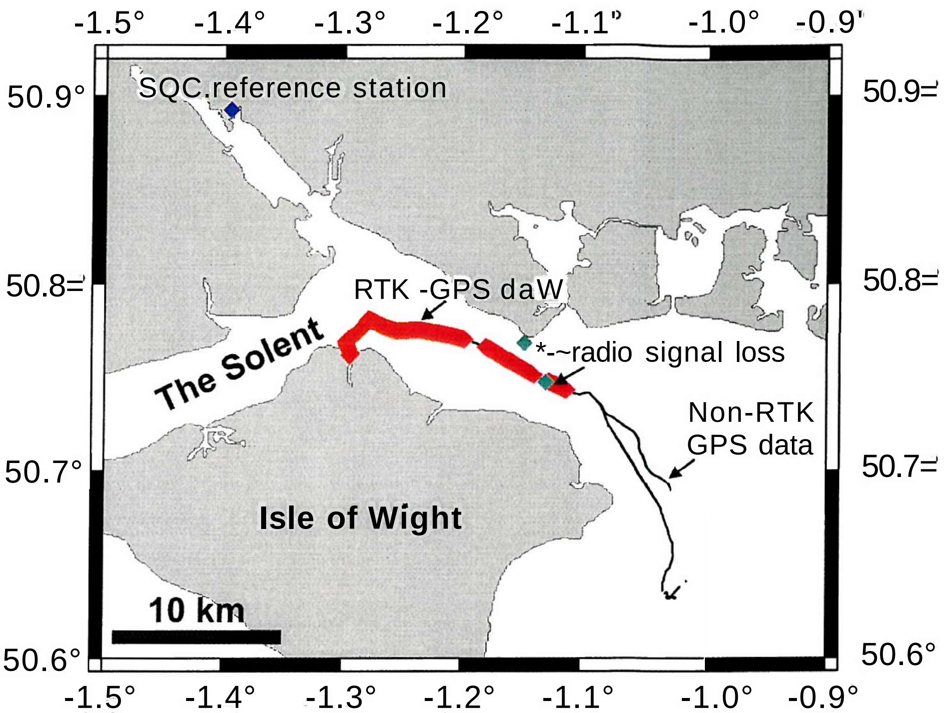

Figure 4.13 Navigation data collected in the East Solent during the dynamic experiment using the rectangular antenna configuration. The RTK -GPS quality data are highlighted. Two positions are indicated, where the radio connection to the reference station, situated at the SOC, was lost.

The part of the trajectory plotted in black indicates that the GPS data were of lower quality due to the lack of the radio connection between the reference station at the SOC and the roving station. The data gap in the trajectory is due to a break in the data recording. Additionally two positions are highlighted where the radio signal was lost, while not recording position data. The maximum range that was achieved was approximately 26 km, which is a typical value for the system using an UHF radio link (oral communication Ashtech Ltd., UK).

4.5.2.3 System reliability

Figure 4.14 shows the heading, pitch and roll, together with the RTK-GPS height data recorded in the experiment with an update rate of 4 Hz. Note that there is an overlap of just 18 minutes with the attitude data recording starting earlier than the RTK -GPS data.

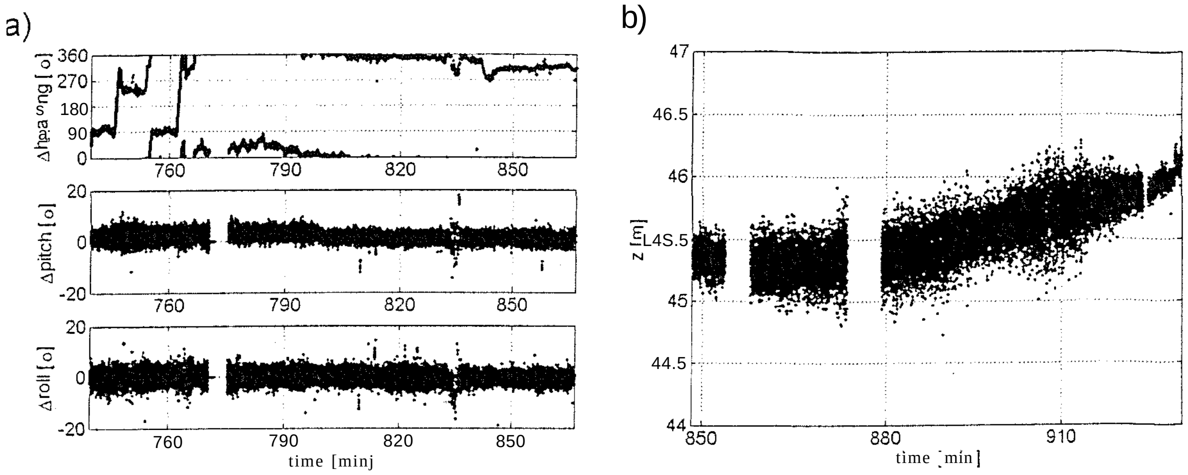

Figure 4.14 Square antenna configuration dynamic experiment, a) Attitude: heading, pitch and roll data, b) RTK-GPS height. The rise of about 1 m is due to the incoming tide. The data gaps are due to loss of satellite coverage and subsequent automatic re-initialisation of the positioning systems.

The data reflect the rough sea state throughout the experiment. The buoyant catamaran reacts readily to the wave action with constantly high amplitude roll, pitch and heave movements. Both the roll and pitch values throughout the experiment have amplitudes of 10° with maximum amplitudes up to 18°. From the approximately 37000 recorded data points, 9% of the heading, 13% of the pitch and 13% of the roll value determinations were unsuccessful.

The wave motion also results in high-frequency changes in the height data with amplitudes (measured from trough to peak) up to approximately 1 m. The long time trend in the height, associated with the incoming tide results in a change of approximately 0.7 m over the duration of measurement. The two data gaps correspond to the gaps in the RTK-GPS navigation data shown in Figure 4.13 and are probably associated with a loss of sufficient satellite coverage and the subsequent automatic **re-initialisation** of the system, rather than a loss of radio contact to the reference station. In support of this is that the data gaps have a similar length of 2 - 3 minutes, a typical period for the automatic start-up of the system, also seen in the static experiment using the rectangular antenna configuration (Figure 4.9). The lower amplitudes towards the end of the time series are recorded at the western part of the trajectory shown in Figure 4.13 in the sheltered waters of Cowes Bay on the north coast of the Isle of Wight.

Overall the sea state seems to affect the reliability of the measurements. Both attitude and RTK-GPS data show data gaps and bad readings throughout the experiment.

4.6 Conclusions

The centimetre accuracies needed for the source arrays and receiver groups positions make it essential to co-locate them on a rigid array, whose location can be described by a single position and its attitude angles: heading, pitch and roll. The positions of the elements located on the array are calculated using a newly developed algorithm. The required positioning accuracy depends on the source signal used. For the proposed 3D Chirp system a vertical positioning accuracy of 4.5 cm and a horizontal positioning accuracy of 5 cm are required. The values need to be determined with an update rate of 4 Hz. The only system that promised to meet the accuracy threshold that lay within the project budget was an RTK-GPS based position and attitude system. The manufacturer claims a position accuracy of 1 cm in horizontal and 2 cm in vertical direction with an update rate of up to 20 Hz and a sub-degree attitude accuracy with an update rate of up to 5 Hz. Static experiments with different GPS antenna array configuration were completed verifying the claimed accuracy. Additionally the position of a receiver element furthest away from the centre of gravity of the proposed 3D Chirp system was simulated from the position and attitude values using the presented algorithm. This element is expected to experience the largest positioning **errors.** Standard deviations of its horizontal position are maximum 1.1 cm and maximum 2.3 cm for its vertical position for the tested antenna array configuration. These values lie within the threshold for the positioning accuracy. Dynamic experiments were completed in which a marine survey was simulated and the performance of the positioning systems tested. The RTK-GPS positioning system operates within a range of approximately 26 km from the reference station due to limited radio range. Both the positioning and attitude system operate reliably in survey conditions although their performance deteriorates in rougher sea-states. However, the proposed 3D Chirp system is expected to be a significantly more stable towing platform than the platform used for the dynamic experiments. Therefore it is expected that the systems will perform reliably with the 3D Chirp system in all survey situations. Overall the experiments suggest that the systems meet the positioning requirements for the 3D Chirp system.

5 3D Chirp sub-bottom profiler design

5.1 Introduction

In this chapter conclusions from Chapter 3 and Chapter 4 are combined with considerations on the towing behaviour of the system and its deployment from small survey vessels to produce a complete design of the 3D Chirp sub-bottom profiler. Moreover, along track and across track ground coverage are taken into consideration, which, together with the towing speed and shot-rate, govern the survey time. The final design comprises a 2.5 m x 2.2 m structure holding 60 receiver groups with 25 cm spacing in either direction and a source array arranged as a Maltese cross or alternatively as a double pair. The construction materials include lightweight but strong glass reinforced plastic (GRP), polyurethane foam, stainless steel and aluminium. The specifications of a suitable recording system for the seismic data are documented and future development of a custom system described and compared to the specification of the system used in the data acquisition. Finally, the assembly and successful towing tests of the 3D Chirp system are described.

5.2 Design constraints

5.2.1 Handling, deployment, transport

The system should be deployable from small survey vessels (approximately 12 m length), such as the R/V Bill Conway, run by the Southampton Oceanography Centre. For rapid deployment to the survey area the system should be stored on-board or secured outside the vessel during transit. Additionally it should be transportable in standard sized vans or trailers to and from operational areas. Thus the maximum size of the array is limited to approximately 2.5 m in either direction. The weight outside water should enable easy handling during deployment and recovery of the system using modest winches with a small crew. The system needs to be rugged in order to be handled during deployment and recovery. Additionally it needs to withstand forces due to towing through water and wave action.

5.2.2 Towing behaviour

The array needs to be towed close to the sea-surface in order for the GPS antennas of the positioning and attitude system to function. If the antennas are submerged, even for a short duration, the GPS signal is lost and both the RTK-GPS and attitude system will be automatically re-initialised, resulting in a loss of some minutes of navigation data (Chapter 4). However, the antennas are designed for marine application and short-term submersion will not cause permanent damage. The array should have a stable towing behaviour, which should minimise pitch, roll and vertical movements even in rougher sea states, thus ensuring the reliable functioning of the positioning system. In order to minimise drag during tow and to reduce noise, the array needs to be designed for a laminar flow at normal survey speeds of three to five knots (1.54 - 2.57 m/s). Additionally the array needs to be designed to have neutral buoyancy as this ensures small interaction with wave action and movements introduced by towing as the buoyancy forces do not change with the array's position in water.

5.2.3 Source array and receiver group geometry

The spacing of the receiver groups needs to be chosen to minimise spatial aliasing (Chapter 3) together with consideration of ground coverage per shot. The across track and along track coverage should be as large as possible in order to minimise the survey time and assure a high data coverage.

5.2.3.1 *Across track ground coverage*

The across track ground coverage is the width of the area, perpendicular to the survey direction, incorporating the reflection midpoints for a single shot. It depends on the geometry of the source array and receiver group in cross-track direction. Figure 5.1 shows two different geometries resulting in minimum and maximum ground coverage for a given overall width of the array.

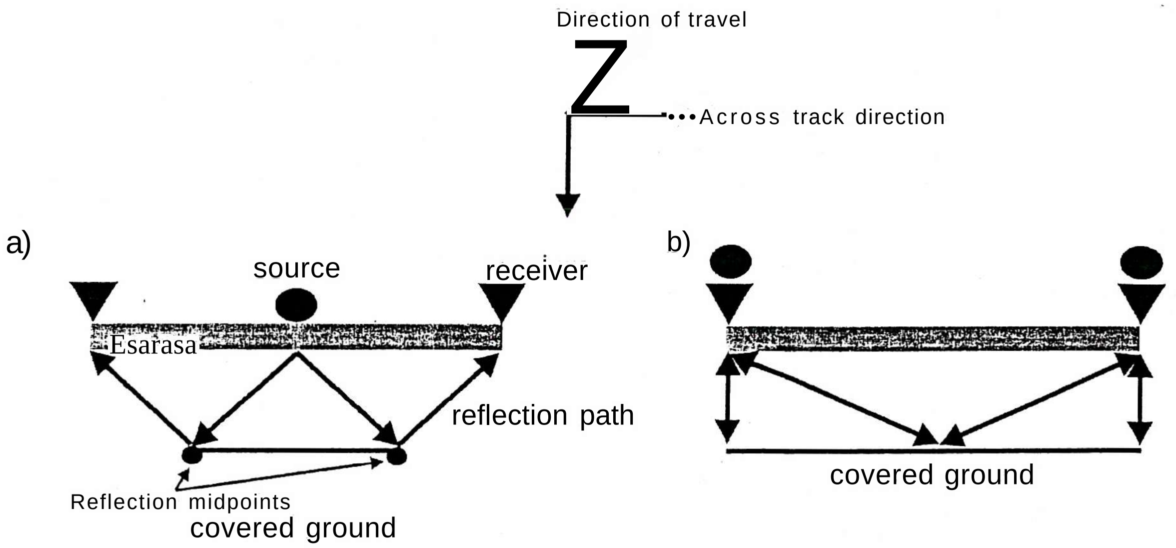

Figure 5.1 Across track ground coverage. The source and receiver positions on the acquisition array in a cross-section perpendicular to the survey direction are shown together with corresponding reflection paths, a) A single central source array, b) Peripherical source array pair.

Figure 5.1a shows the source array positioned in the centre and the receivers on the peripheries of the array. The reflection midpoints for the shown elements are marked. All possible reflection midpoints for additional receiver elements fall in the area marked as covered ground. The across track ground coverage for this case equals half the width of the array. Figure 5.1b shows both sources and receivers positioned on the peripheries of the array. Two source arrays are used, which need to be fired alternatively to assure unique reflection passes for the recorded signals. Alternatively they can be fired simultaneously using different source sweeps. In a later processing stage the data for different reflection paths can then be separated by correlating with the different source signals. The across track ground coverage in this case equals the entire width of the array.

When the survey is conducted by sailing parallel lines to cover the area, the separation of the lines needs to be half the across track ground coverage plus an overlap to allow for navigation inaccuracies. An estimate of the survey duration is given by

$$T_{survey} = \frac{A_{survey}}{v_{survey}\left(C_{trans} - overlap\right)}, \qquad (5.1)$$

where T_{survey} is the survey time estimate, A_{survey} the survey area, v_{survey} the average vessel speed over ground and C_{trans} the across track ground coverage. This estimate is the minimum threshold, as it does not allow for line turns and additional coverage in order to fill eventual data gaps due to navigation inaccuracies.

5.2.3.2 Along track ground coverage

The along track ground coverage is the length of the area, in the survey direction, incorporating the reflection midpoints for a single shot. It depends on the geometry of the source and receiver array in along track direction. Figure 5.2 shows the along track ground coverage for two consecutive shots for an array with a centrally positioned source.

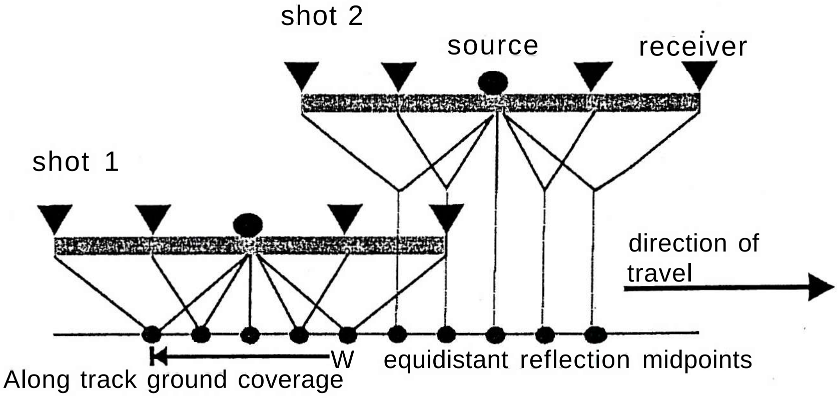

Figure 5.2 Along track ground coverage. The source array and receiver group of the seismic system are shown as cross-section in the direction of travel for two consecutive shots. Note the reflection paths and the corresponding reflection midpoints. Refer to text for discussion.

It needs to be assured that the ground is fully covered by reflection midpoints in the along track direction. For a symmetric array with a central source the distance travelled between two shots should therefore not exceed the maximum offset in the direction of travel plus half the receiver element spacing as can be seen in Figure 5.2. For example for an array with 62.5 cm maximum offset and 25 cm receiver group spacing in the direction of travel the maximum distance travelled between two shots is 75 cm. The travelled distance between shots depends on the survey speed and shot-rate it can be determined using

Figure 5.3, which shows the relationship between shot-rate, survey speed and travelled distance.

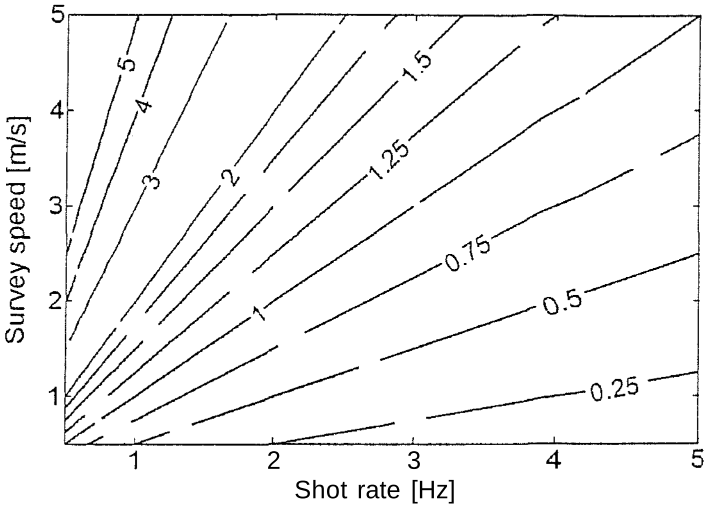

Figure 5.3 Distance between consecutive shots in meters depending on shot-rate and survey speed. For a given acquisition geometry and survey speed the minimum shot-rate for single fold coverage can be determined.

The contour lines correspond to travelled distances according to shot-rate and survey speed. For a given shot-rate and survey speed the distance travelled between two shots can be taken from the figure. For the above example at a typical survey speed of 4 knots = 2.06 m/s the shot-rate needs to be approximately 2.8 Hz.

5.3 Design solution

5.3.1 Geometry

The overall dimensions of the system are limited by the handling, deployment and transport considerations to a maximum length of 2.5 m. The across track ground coverage should be maximised, by extending the width of the system as far as possible, to minimise the survey time. Additionally the limited number of channels governs the receiver group spacing, which is crucial to avoid spatial aliasing of the collected seismic data as outlined in Chapter 3, which also limits the overall size of the array. The length of the array has to comply with the along track ground coverage considerations depending on the anticipated survey speed and shot-rate of the recording system (section 5.2.3). Figure 5.4 shows the geometry that optimises these factors.

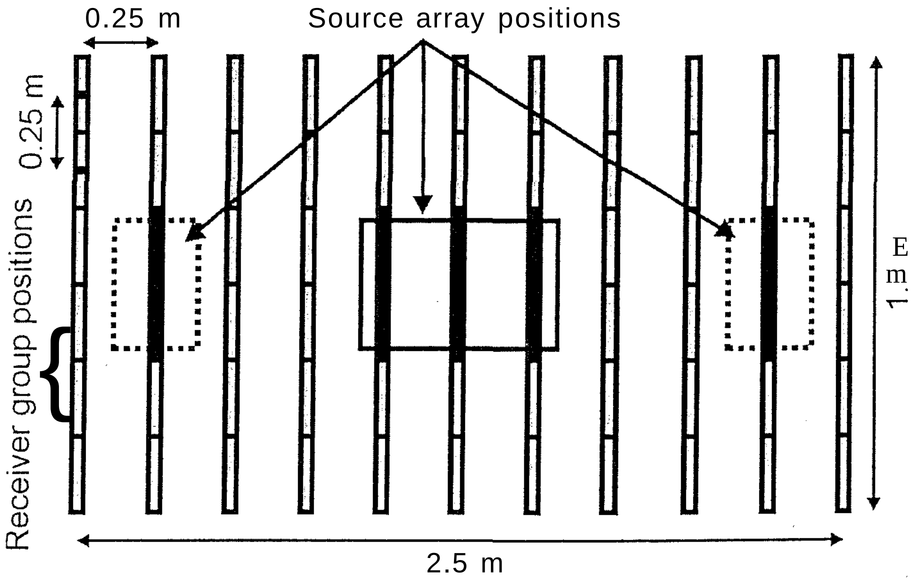

Figure 5.4 Acquisition geometry of the 3D Chirp system. Eleven longitudinal sections hold up to 66 receiver group positions with 25 cm separation in either direction. Two possible source array positions are marked: a central Maltese cross array and a peripherical double pair.

The overall width of the geometry is 2.5 m with a length of 1.5 m. It is divided in eleven longitudinal sections with 25 cm separation, giving the receiver group spacing in the transverse direction. The spacing in the longitudinal direction is equally 25 cm, thus offering a total of 66 possible receiver group positions, with only 60 being populated at any one time. The positions not used are taken up by the source array. Two possible source array configurations are proposed, firstly a Maltese cross configuration of the four available transducers in the centre of the array and secondly a pair to each side of the array

(Chapter 3). The across track ground coverage is 1.25 m, half the overall width of the system, for the central position of the source array and 2.25 m for the double pair configuration, spanning nearly the entire width of the array. From Figure 5.3 the along track ground coverage with a maximum offset of 62.5 cm and the given receiver group spacing allows a maximum survey speed of 6 kn (3.08 m/s) for the proposed maximum shot-rate of the recording system of 4 Hz. A survey speed of 4 kn is envisaged, but this can be accidentally exceeded, especially when surveying in an area with strong surface currents, for example due to tides, making the safety margin of 30 % necessary. In Chapter 3 the source array and receiver groups are designed to minimise spatial aliasing and with the receiver group separation of 25 cm, apparent wavelengths larger than 50 cm are sampled correctly, thus spatial aliasing is largely avoided for typical surveys. The receiver groups are arranged in longitudinal sections. This allows changing of their separations for future development to improve spatial sampling, for example when higher source frequencies are used. Furthermore additional sections can be added to increase the number of channels and the overall width of the array.

5.3.2 Structural design

The design concept was the collective effort of Dave Whatley of the engineering design and manufacturing centre (EDMC) of Southampton University, Jon Bull, Justin Dix, Tim Henstock and the author. The detailed design was completed in collaboration with Michael Street and James Chitty of EDMC, who also provided the technical design drawings and manufactured system parts. The hydrodynamic behaviour of the system was investigated in collaboration with the department of ship science of Southampton University (Lester, 2002). Responsibility for final design decisions lies with Jon Bull.

5.3.2.1 Acoustic properties

For good acoustic coupling both the source array and receiver groups need to be partly exposed to the water. For the source array it is essential that the transmitting plates of the transducers are submerged at all times, and for cooling purposes, it is advisable that the entire transducer is frequently in contact with water. A towing depth of some decimetres had shown to be successful for the existing 2D Chirp system. The receiver group's lower surface should similarly be exposed to the water at all time.

5.3.2.2 *Towing behaviour*

In order to minimise drag and reduce hydrodynamic noise while towing, the system should be designed for laminar flow. To achieve this, longitudinal sections with cone-shaped ends are used, which are connected by hydrofoils. Hydrodynamic modelling, carried out by Adrian Lester, suggests that two single foils with relatively small surface area at the extreme ends assure a laminar flow and additionally provide a more stable towing behaviour than, for example, a single hydrofoil spanning the entire length. A test section, consisting of three longitudinal sections of the given dimension connected by hydrofoils at the extreme ends, was built and towing tests carried out. The test verified the findings of the modelling. The test sections towed stably without excessive roll or pitch movements and by comparing the tow speed with the drag of the array it showed that at least up to 4.5 kn (2.3 m/s), the flow was laminar. Additionally, hydrofoil shaped housings for the source array and additional components were suggested to ensure laminar flow behaviour for the final array. Moreover, to ensure stable towing behaviour the array is designed to be neutrally buoyant with the centre of mass in the centre of the array for both the Maltese cross and double pair source configurations. To minimise the effect of wave action, in addition to the positive effect on the towing behaviour, large surface areas were avoided in the design.

5.3.2.3 *Materials and their properties*

As the system needs to be neutrally buoyant low density materials need be used to balance the weight of the relatively heavy source transducers and additional electronics components. Furthermore the materials need to withstand the forces exerted on the structure during towing, deployment and transport. The array's main structure, the longitudinal sections and their linking hydrofoils are manufactured with glass reinforced plastic (GRP) pultrusions, manufactured in a special process to obtain the continuous length sections, lined with high density Polyurethane foam (Cibatool), a strong and easily machinable material. The source arrays are embedded in low density closed cell polyvinyl chloride (PVC) foam (Herex C70.90) panels, which deliver extra buoyancy. Additionally stainless steel and alloy components are used, all of which are suitable for use in seawater. The material properties are summarised in Table 5.1 together with a list of the components they were used for.

Material	**Density (kg/m^3)**	**Components**
Glass reinforced plastic (GRP) pultrusion (Grating Company Ltd.)	**180**	Longitudinal and hydrofoil sections
Closed cell PVC foam (Herex C70.90)	**100**	Source array supporting panels
Polyurethane foam (Cibatool)	**725**	End cones and fillings of longitudinal sections
Aluminium	**2720**	Antenna poles, transverse sections
Stainless steel	**8000**	Rods connecting the hydrofoil sections
Nylon (Delrium)	**1360**	Connections and spacer blocks

Table 5.1 Use of materials on the 3D Chirp system and their density. See Figures 5.5 to 5.11 for named system components.

5.3.2.3.1 Towing, deployment and recovery

The system's towing points are located in the front transverse hydrofoil section (Figure 5.5). Two stiff, transverse stainless steel rods, located in the hydrofoil sections and linked to the towing points, distribute the stress equally between the longitudinal sections. Although four towing points are available, on experimentation it was found that towing from the central pair resulted in the most stable towing behaviour. For deployment and recovery straps connected to three points on the central panel are used, which remain on the system during the survey.

5.4 Final design

Figure 5.5 shows the final design of the 3D Chirp in top view. The system comprises eleven longitudinal sections manufactured from glass reinforced plastic (GRP) and Polyurethane foam, which contain the 60 receiver groups. Their connecting cables are joined in two splices (30 channels each) on the front end, from which two cables lead to the recording system on board the towing survey vessel. At the front and back, the longitudinal sections are joined by hydrofoil sections to improve the hydrodynamic behaviour and ensure stable towing characteristics. The front sections also contains two stainless steel rods, which are connected to the towing points, distribute the towing stress equally over the longitudinal sections. The central panels, housing the Maltese cross transducer array, are made from low density closed cell PVC foam to compensate for the weight of the transducers and electronics bottle, located on the panels. Table 5.2 summarises the weight of major components in the final design.

	Weight in air [kg]	**Elements**	**Total weight [kg]**
Transducer	**9.36**	4	**37.4**
Electronic bottle	**9.80**	2	**19.6**
Antenna	**0.35**	4	**1.4**
Receiver group	**0.10**	**60**	**6.0**
Array structure			**111.6**
Total			**176.0**

Table 5.2 Partial weight in air of source, receiver and positioning components and structure, together with the total weight of the 3D Chirp system.

The overall volume of the array of 0.1843 m^3 displaces 190.2 kg of seawater (density=1026 kg/m^3). The mass difference is hence 14.2 kg. This slight excess buoyancy of 7.5% is compensated by the weight of the umbilical cables in water during towing, which can be altered by changing the towing distance, thus regulating the towing behaviour. The centre of buoyancy coincides with the centre of gravity due to the symmetrical design and homogenous materials.

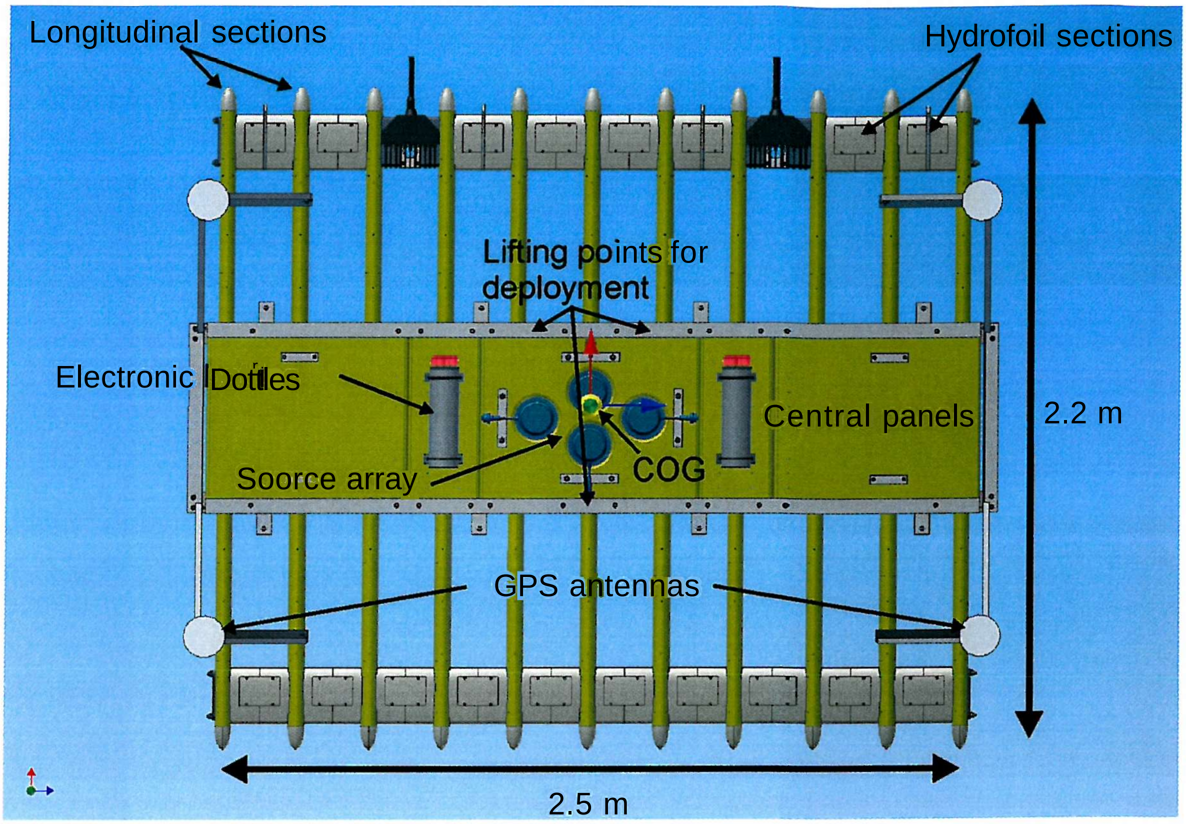

Figure 5.5 Top view of the 3D Chirp system. Its overall dimensions are 2.5 x 2.2 m. It consists of eleven longitudinal sections, holding the 60 receiver groups. The central panels hold the source array together with its electronic bottles. The central Maltese cross configuration is shown. A second set-up, in which the source array consists of two pairs positioned in the outer panels can be realised (Figure 5.4). The front and back members consists of hydrofoil sections to improve the hydrodynamic towing behaviour. GPS antennas are mounted on poles as a square array. The positions of the lifting points are indicated, used for deployment and recovery. The Centre of gravity (COG) is close to the centre of the array, due to the symmetry of the assembly and homogeneity of the used materials.

To use the system in the double pair source configuration the outer panels can be replaced by panels housing a pair of transducers and the inner panel is replaced with a solid foam panel. The location of the receiver groups change accordingly. The GPS antennas, used to determine the system's position and attitude are arranged in a square separated by 1.5 m in longitudinal and 2.63 m in transverse direction. These measurements are similar to the values for the antenna array used to test the necessary positioning accuracy in Chapter 4. Straps are used to lift the system, during deployment and recovery. They are connected to three lifting points and joined above the centre of gravity. Figure 5.6 shows the 3D Chirp system in a side view.

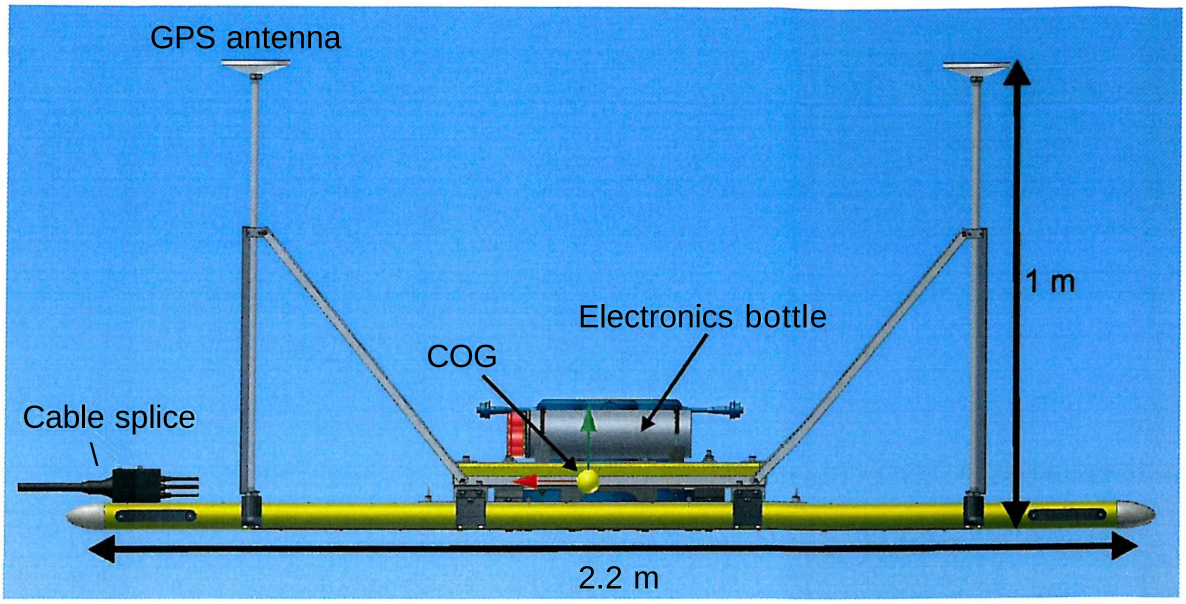

Figure 5.6 Side view of the 3D Chirp system. The overall length is 2.2 m. Note the position of the source array in the central foam panel. The transducer and receiver group faces are level with the bottom of the array. The GPS antennas are positioned on 1 m long poles. The Centre of Gravity (COG) is about 10 cm above the bottom of the array. Two splices are positioned at the front end, combining 30 receiver group channels each and connect to the ship-board recording system.

The centre of gravity is located approximately 10 cm above the base of the system. The GPS antennas are located on 1 m long alloy poles, which are reinforced by additional alloy sections, avoiding movement of the antenna relative to the array during survey. Each antenna is connected via a 30 m coaxial cable to the ship-board navigation system (Chapter 4). The transducers are joined by a splice, not shown in the figure, and are connected to an electronic bottle. For the Maltese cross configuration only one electronic bottle is used, the second bottle is included for symmetry reasons. In the double pair configuration both bottles are used, to enable alternate firing of the transducer pairs or simultaneous firing using different source signals. Figure 5.7 shows the front view of the 3D Chirp system.

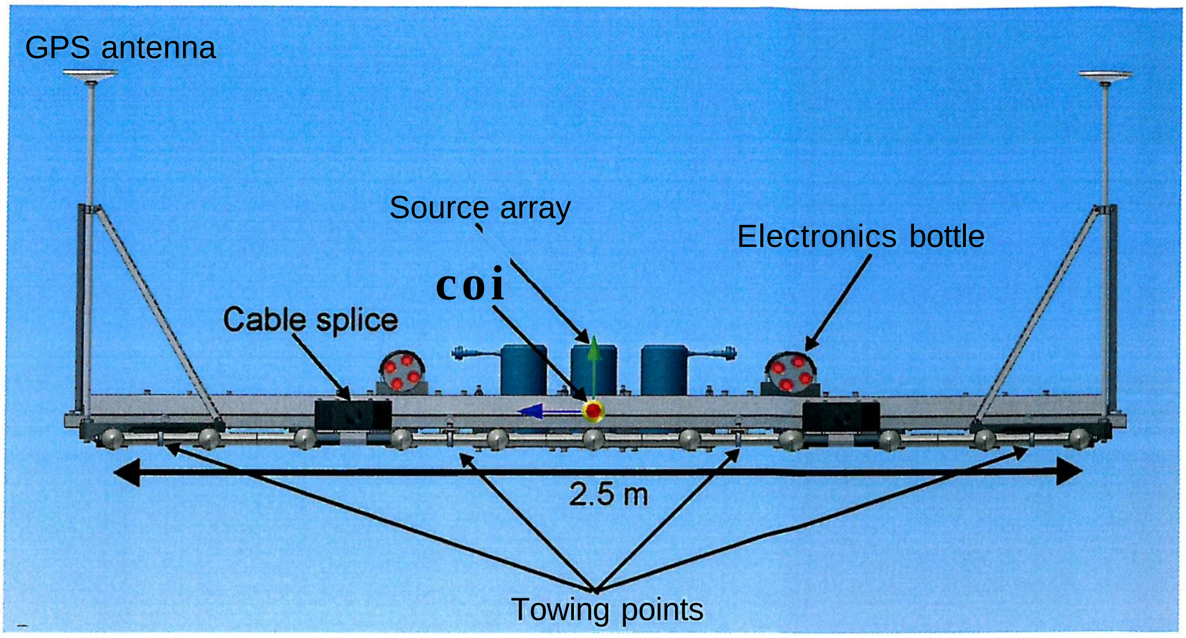

Figure 5.7 Front view of the 3D Chirp system. The overall width is 2.5 m with eleven equidistantly spaced, longitudinal sections containing the receiver groups. The GPS antennas of the positioning system are placed on the peripheries to maximise their separation. Four towing points are present at the front end. They are connected to a stainless steel rod within the transverse sections, distributing the towing stress equally over the entire width of the array. The middle pair was used for towing during survey work.

Four towing points are located on the front transverse sections, linked to the stainless steel rods within the hydrofoil sections (Figure 5.8).

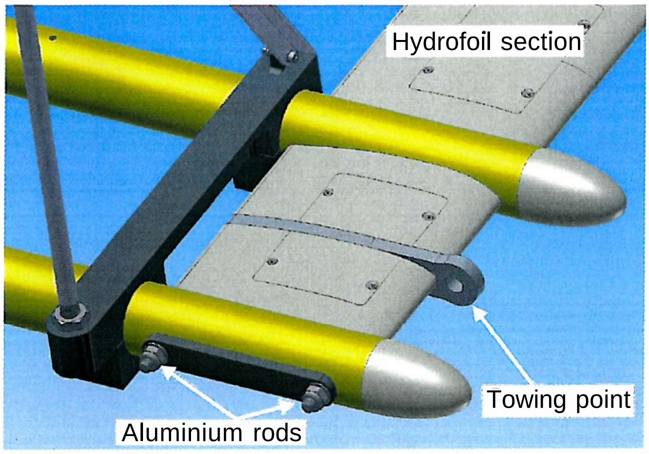

Figure 5.8 Close-up of the towing point connected to two stainless steel rods within the hydrodynamically shaped transverse section, connecting the longitudinal section. The cone shaped front ends of the longitudinal sections help to achieve laminar flow to reduce hydrodynamic noise.

Figure 5.9 shows a close-up of the Maltese cross source array, supported from the central foam panel in the centre of the array.

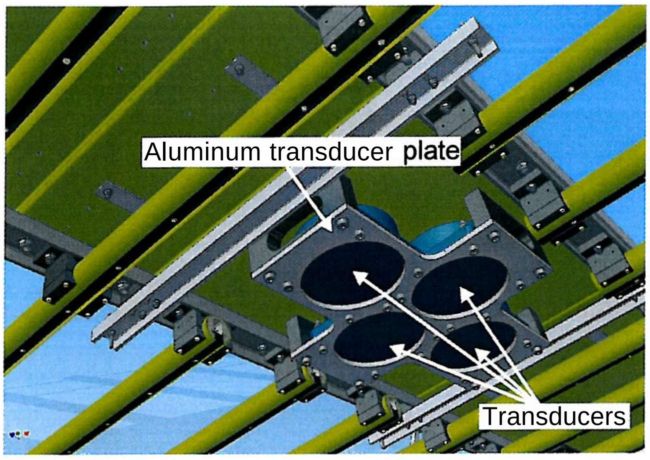

Figure 5.9 Close-up of the Source array made up of four transducers arranged as a Maltese cross and fitted on an aluminium plate that is suspended from the central foam panel of the 3D Chirp array. When the double pair configuration is used the longitudinal sections, holding receiver groups can be fitted in the space.

The four transducers arranged in Maltese cross configuration are placed on an aluminium plate which is suspended from the central foam panel using Nylon blocks as placers. The base of the transducer plate coincides with the base of the receiver group. The transducers are exposed to sea water during the survey, guarantying good acoustic coupling and cooling. Figure 5.10 shows a close-up of a longitudinal section containing the receiver groups, together with a cross-section through a longitudinal section.

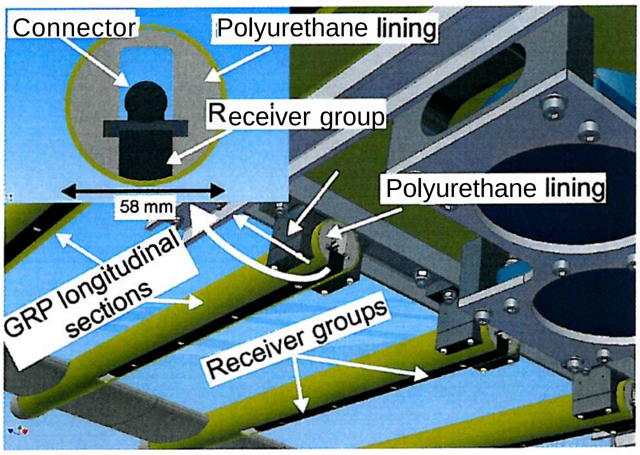

Figure 5.10 Close-up and cross sections of a longitudinal section with a receiver group. The cross sections are lined with polyurethane foam holding the receiver group whose bottom is shaped to the tube section. The free space in the longitudinal section holds the connecting cables of the group and is water filled during deployment.

The longitudinal sections accommodate the 25 cm long receiver groups, which are held in place by Nylon screws attached to movable Nylon blocks. These blocks fit into slits in the lining for easy assembly. The connection between the longitudinal sections and the central panels consists of Nylon saddle blocks connected with Nylon screws to custom shaped blocks, avoiding the obstruction of the bases of the receiver groups. The base of the receiver group is designed to have the same curvature as the longitudinal section to avoid disruption of hydrodynamics, thus avoiding noise due to turbulence. The hydrodynamically shaped housing for the source and array and electronic bottles was not implemented in the final design, because of time limitations. The presence of the vertical surfaces on the central panel will generate turbulence and in particular the receiver groups behind the source array may be affected by the associated noise. Figure 5.11 shows the 3D Chirp array in views from top and bottom as an overview of the components.

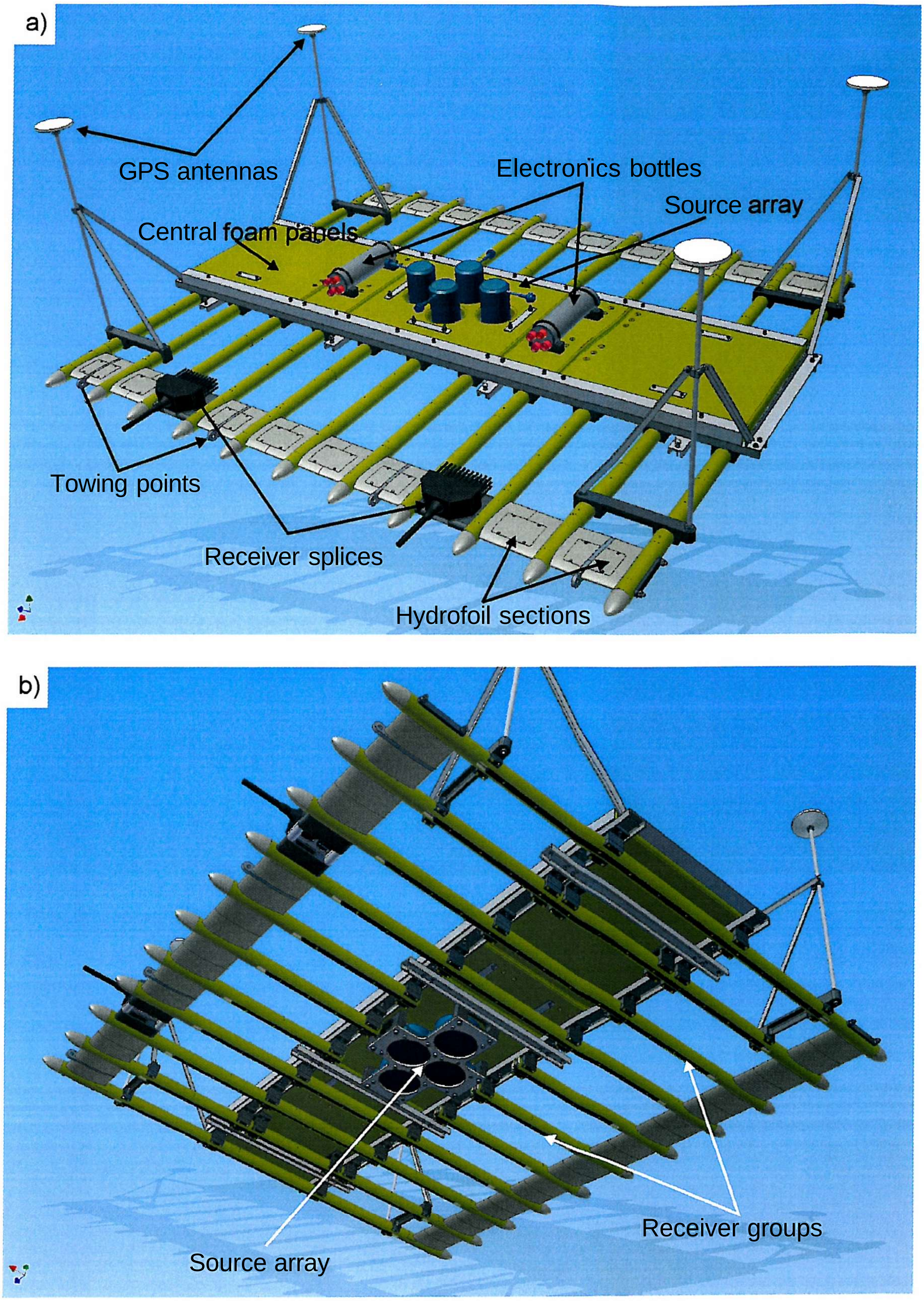

Figure 5.11 The 3D Chirp system in perspective view, a) Top view, b) Bottom view. The 2.5 m wide and 2.2 m long structure has an overall weight of 176 kg and a seawater displacement of 190.2 kg, resulting in a positive buoyancy of 14.2 kg which can be neutralised by the weight of the umbilicals. The longitudinal sections are water filled during deployment.

The design concept of connected longitudinal sections makes it easy to expand in future developments. Future 3D Chirp systems will have greater numbers of longitudinal sections and carry more receiver groups. It is envisaged that these larger systems will be collapsible for transport. Possibly additional panels, containing longitudinal sections, will be hinged to the central array and expanded during the deployment. The greater width would increase the transverse coverage and thus decrease the survey time estimated in equation (5.1).

5.5 Signal generation and data recording

5.5.1 Transmitting system

The transducer array, consisting of four T135-type transducers (Neptune Ltd.), is driven by electronics situated in electronic bottles on the 3D Chirp array. For the double pair configuration two transducer electronic bottles are used, one for each pair, while for the Maltese cross configuration only a single electronic bottle is used. The system is linked to the ship-board unit via a single umbilical. A wide range of source signals, including the ones described in Chapter 2, are stored in the bottle electronics and can be selected from the ship-board system. The overall power output is equally programmable from the ship-board system, ranging from 10 W to 4 kW (peak). It can achieve a maximum shot-rate of 4 Hz for 32 ms long source signatures.

5.5.2 Receiver groups

The 25 cm long receiver groups contain four individual elements with 6.25 cm separation (Chapter 3). The 3D Chirp system contains 60 receiver groups.

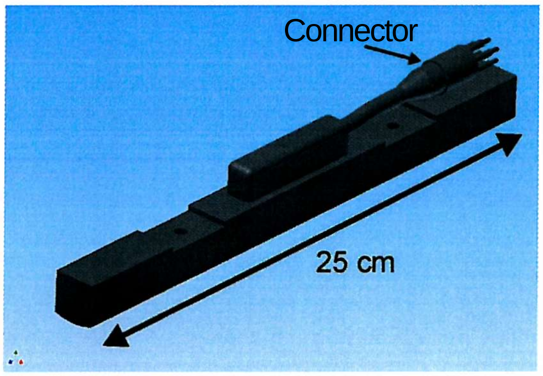

Figure 5.12 The receiver group with an overall length of 25 cm consisting of 4 serial elements with 6.25 cm separation connected to a pre-amplifier.

The individual output is added and pre-amplified with a gain of 8. The individual elements connect to two splice units on the front end of the array with 30 channels each (Figure 5.5). Two umbilicals take the analogue signals to the ship-board recording system. The Polyurethane material used in the linings of the longitudinal sections (Figure 5.10, Table 5.1) dampens acoustic reverberations and therefore shields the receiver group from reflection energy arriving from directions others than the upward direction, thus avoiding reflections from the sea-surface being detected.

5.5.3 Recording system

5.5.3.1 Desired specifications

The system needs to record the 60 channels of the 3D Chirp array. In order to correctly sample the data its sampling frequency needs to equal twice the Nyquist frequency for the source sweeps used. The maximum source sweep frequency is 13 kHz (Chapter 2), hence the minimum sampling frequency is $f_{\text{sampie, mm}}$— **26** kHz, equalling a maximum sample rate of At=38.4 |j.s. The record length needs to at least exceed the length of the source sweep used of 32.74 ms and should be chosen according to water depth and expected signal penetration. For typical water depth of 20 m and penetration of some 40 m it needs to be approximately 120 ms, including the length of the source sweep. From Figure 5.3 the minimum shot-rate for typical survey speeds is 2.8 Hz to ensure sufficient coverage, although ideally the shot-rate would be higher to increase the fold. The shot triggering should be synchronised with the navigation data recording and the datasets merged for later processing.

5.5.3.2 Acquisition system used

The presently available system, used for the data acquisition is the Geometries StrataView seismograph (Geometries Inc., San Jose, USA) operated with marine seismic controller software from the same manufacturer running on a separate PC. The analogue data, transferred from the 3D Chirp array, is pre-amplified and converted by a 24 bit AZD converter, offering a measured dynamic range of 94 dB for the used sampling rate (StrataView user manual), before being transferred to the control PC and written to a SCSI DDS-4 tape drive in modified SEG-2 format, which are subsequently converted into SEG-Y format (Pullan, 1990; StrataView user manual). The system operates with a sampling rate of At=31.25 p,s (f_{sampie}=32 kHz). The recording length is chosen, depending on water depth and expected signal penetration, as 70 ms. The maximum shot-rate for which the system can transfer the data to the control PC via a 100 MBits/s Ethernet connection is 1 Hz. The system is triggered by the GPS clock signal on every full second. It recorded the system's clock time as an integer value into the seismic header, as the SEG-2 format only allows integer entries as time values. The system has three major drawbacks when used with the 3D Chirp system:

1. Fixed pre-amplification: The system's pre-amplifler has too high settings for the full power output of the 3D Chirp system and hence the power output had to be reduced to prevent clipping of data.
2. Insufficient shot-rate: The maximum shot-rate of 1 Hz does not comply with the necessary minimum shot-rate of 2.8 Hz for the system, resulting in spatial under-sampling of the survey area.
3. Bad time synchronisation between navigation and seismic system: although the system is triggered by the GPS one pulse per second (1 pps) output, the header value in the seismic data is the truncated integer value taken from the system's clock, which results in inaccuracies. Additionally the system's clock needs to be synchronised with the GPS time at the beginning of each survey day and it undergoes a drift throughout the day, resulting in faulty positioning of the seismic data.

5.5.3.3 Future recording system development

Development specifications for a custom recording system for the 3D Chirp system include:

1. Acquisition unit placed on the 3D Chirp array assuring an electrically quiet environment and enabling direct coupling of recording system and receiver groups, thus avoiding large gain settings for signal transfer over large distances through umbilical cables, and increasing the signal to noise ratio of the seismic data.
2. Data transfer to the ship-board recording and quality control (QC) system via Ethernet link, thus making analogue umbilical cables as part of the recording system obsolete and facilitating the system's deployment and improving its towing behaviour.
3. 96 recording channels to accommodate future expansions of the system.
4. 16 bit A/D converter with sampling frequency of 40 kHz to assure correct sampling of the seismic data.
5. Adjustable pre-amplification of the raw analogue data, such that for deep water application it can be set to clip the outgoing pulse, which is recorded before the reflection signal is returned. For shallow water application it can be set that no clipping of the signal occurs, as the outgoing pulse is recorded simultaneously with the reflected signal.

6. The ship-board QC and recording system should reformat the data to modified SEG-D (Allen et al., 1994) to be written firstly to a RAID hard-disk system and later transferred to a digital tape after conversion into SEG-Y format for transfer to **a processing system. It is expected that 10-20 GB of data will need to be stored per** hour.
7. Triggering of the system with GPS 1 pps signal, synchronising it with navigation data that is merged on-line with the seismic data in QC and recording system.

Developments of the recording system were carried out involving personnel from GeoAcoustics Ltd., D-Tacq Solutions Ltd., a company specialised in data acquisition technology, and the researchers involved in the 3D Chirp research project at the Southampton Oceanography Centre in particular Tim Henstock. In July 2004 a 3D Chirp dataset was collected successfully using a ship-board based preliminary version of a new recording system. The system comprises a Linux based A/D converter unit controlled by a Linux based control, QC and data storage PC. The system is triggered using the GPS 1 pps signal from the Sagitta RTK-GPS system (Chapter 4), thus synchronising the navigation and seismic data. At present it is capable of recording 60 channels with 16 bit and 40 kHz sampling rate, although an increase of recording channels to 96 is easily implemented. The system converts the recorded data into SEG-Y format, which is transferred via an Ethernet link to a second PC, which stores it on digital DDS-4 tapes. Adjustable pre-amplification of the data before digitisation and mounting of the acquisition unit on the 3D Chirp array have not been implemented to date.

5.5.4 Conclusions

Table 5.3 summarises the properties of the 3D Chirp system.

3D Chirp sub-bottom profiler

Tow Platform	
Tow speed	1 to 6 kn (0.51 - 3.1 m/s)
Weight in air	176 kg
Weight in water	0 kg to 14.2 kg selectable
Dimensions	Length: 2.2 m, width: 2.5 m, height: 0.5 m
Construction	GPR, PVC foam, stainless steel, polyurethane
Source array	
Transducers	4 T135 Neptune Ltd.
Configuration	Maltese cross, double pair
Frequency range	1.5-**13 kHz**
Power output	10 W to 4 kW (peak), programmable
Source level	**205 dB±3 dB,** programmable
Pulse length	typically 32.74 ms, programmable
Pulse repetition rate	4 Hz envisaged
Protection	Open and short circuit protection
Efficiency	**>90%**
Receiver group	
Configuration	4 elements 6.25 cm separation
Spacing	25 cm in x and y
Frequency range	**200 Hz - 25 kHz**
Filter type	High/Low pass 4th order linear phase
Sensitivity	-205dB±3 dB re **IV/uPa**
Output	differential signal
Gain	**x 8**

Positioning	
Systems	
Position system	Ashtech Sagitta **RTK-GPS**
Position accuracy	1 cm x,y and 2 cm z
Update rate	Up to 20 Hz
Attitude system	Ashtech ADU5
Update rate	Up to 5 Hz
Heading accuracy	0.2°
Roll, pitch accuracy	**0.4°**
Digital acquisition*	
System	Geometries Strata View
Number of channels	**60**
sample rate	Up to 32 kHz
sampling	simultaneous all channels
Resolution	**24 bit/94 dB**

* to be changed in future development

Table 5.3 3D Chirp sub-bottom profiler properties.

5.6 Construction and testing

5.6.1 Manufacturing and assembly

The array components were manufactured by the Engineering Design and Manufacturing Centre (EDMC) of Southampton University, using Computer Aided Manufacturing (CAM) machinery, apart from the central foam panels, whose manufacturing was sub-contracted. The manufacturing of the individual parts was carried out in parallel with the design process over a period of approximately one year prior to the assembly. The receiver groups were manufactured by Neptune Ltd. and their basic functionality was tested at the SOC. The system, made up of approximately 600 major parts, was assembled in July 2003 with the help of members from EDMC and the SOC in a total of approximately 150 man-hours. The single most laborious task consisted of connecting the receiver groups to the receiver splices at the front end of the array. The cables are guided through the longitudinal and hydrofoil sections. Figure 5.13 shows the array during the assembly process.

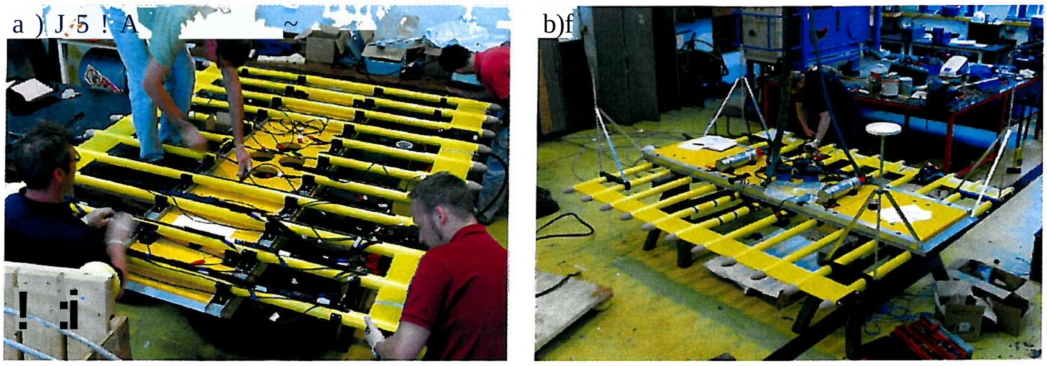

Figure 5.13 Assembly of the 3D Chirp system, a) Connection of the 60 receiver groups to the splices at the front end of the array. A total of approximately 110 m of cable was used, b) Fitting of the positioning system's GPS antennas.

5.6.2 Deployment and towing

For towing tests and survey work the SOC R/V Bill Conway was used. During transit to the survey area the 3D Chirp array is suspended from its A-frame and secured to the stem (Figure 5.14). For deployment the array is lowered into the water using the A-frame, released from lifting straps and towed from the central towing points using a single towing line (Figure 5.14b, and 5.15).

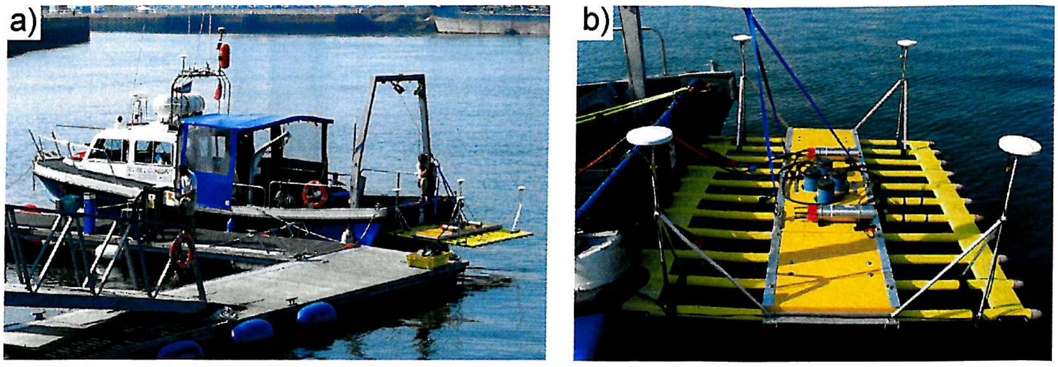

Figure 5.14 Transport of the 3D Chirp system on the survey vessel Bill Conway, a) The array is suspended from the A-frame and secured on the stern, facilitating deployment and recovery, b) The system is lifted form three points situated on the central foam panel (Figure 5.5). During deployment the connection is released and the system towed from two connections on the front end.

The umbilical cables for the transducer array and the two receiver splices (30 channels each) together with four coaxial antenna cables are connected independently from the towing line.

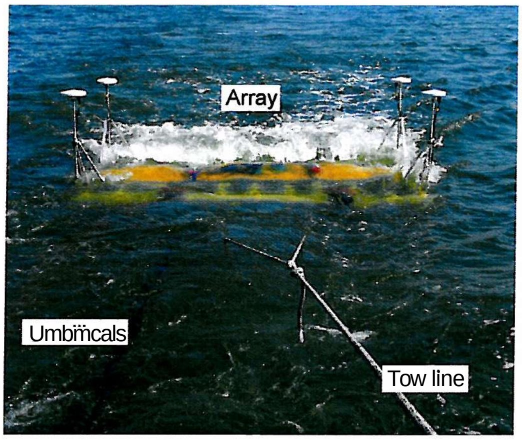

Figure 5.15 The 3D Chirp system during tow. A single line is connected to the central pair of towing points on the array's front end (Figure 5.7). A total of seven umbilical cables connect the source array and receiver groups and the GPS antenna to the systems on-board the survey vessel.

Towing tests were carried out in Empress Dock (SOC), Southampton Water and the Solent. The array was towed with speeds up to 6 kn (3.1 m/s) and line turns with different radii were performed. The system towed stably for the entire range of tested survey speed with increasing turbulence with increasing speed. The turbulence is generated mostly by the central panels and the source arrays with the associated electronic bottles, as these are not hydrodynamically shaped. The receiver groups most affected by the associated noise are the groups behind the central panel and in particular the central groups behind the source array. For slower speeds the array tends to tow deeper below the sea-surface, this can be corrected by decreasing the distance between vessel and array. For the survey speed envisaged and an approximate distance of 8 m from the stern of the towing vessel the system tows stably approximately 20 cm below the sea-surface with relatively little turbulence generation. In line turns the system tends to tilt in the inward direction. Tests showed that line turns with a radius of approximately 10 m at a speed of 3 kn (1.54 m/s) avoided over-tilting and submersion of the GPS antenna on the inward side of the array. Towing tests in rougher sea states in the East Solent showed that the system towed stably without large roll and pitch movements due to wave action. The system was tested in wind speeds up to 3 on the Beaufort scale. For rougher conditions the safe deployment and recovery from the R/V Bill Conway became increasingly difficult, thus being the limiting factor for surveys in these conditions.

5.7 Conclusions

The 3D Chirp system design presented comprises an acquisition geometry optimised for spatial sampling, horizontal resolution and ground coverage within the given constraints of 60 available receiver channels and a maximum envisaged shot-rate of 4 Hz. With an array design based on eleven longitudinal sections housing the receiver groups it is easily expandable to a greater number of recording channels. The overall size of 2.5 m x 2.2 m and the rugged and lightweight structure make it easy to transport and deploy using small survey vessels. Its hydrodynamic behaviour, resulting in low noise generation, allows surveying in typical near coast settings in good sea states.

6 Data acquisition and processing

6.1 Introduction

In this Chapter the acquisition and processing of a 3D high resolution seismic dataset is presented. The 3D Chirp system was used to collect a dataset over an area of 75 m x 750 m in the West Solent (UK), imaging dipping horizons below the seafloor at approximately 15 m water depth that shows a depression and sedimentary waves. The control and recording system configuration is described and the recorded seismic and navigation data are discussed. Both the navigation systems and the 3D Chirp array performed reliably. A total of approximately 46 GB of seismic data were collected over a period of five days together with RTK-GPS position and attitude data. A data processing flow is presented, which combines seismic and navigation data into a 3D data volume that can be imported into standard visualisation and interpretation software for further analysis. Bandpass filtering and correlation with the source sweep are performed before merging the seismic with the navigation data. It is necessary to correct for time-shifts between the seismic and navigation data, which results from non-synchronised recording of the datasets. A 3D pre-stack Kirchhoff migration algorithm is applied to produce an evenly sampled 3D data volume which is exported in SEG-Y format.

6.2 Survey target

The survey target comprises dipping limestones, marls and clays of the Headon Hill, Bouldnor and Bembridge Limestone formations. They are of Eocene and Oligocene age and part of the Bouldnor syncline situated off the north coast of the western part of the Isle of Wight. The stratigraphy of this area is well known and has been imaged previously using the 2D Chirp system for the source signature comparison study presented in Chapter 2. Figure 6.1 shows a map of the survey area with the position of the 2D Chirp lines recorded previously and the proposed area for the 3D Chirp survey. Additional 2D Chirp lines, marked in the figures, were acquired to allow an integrated geological interpretation of the area.

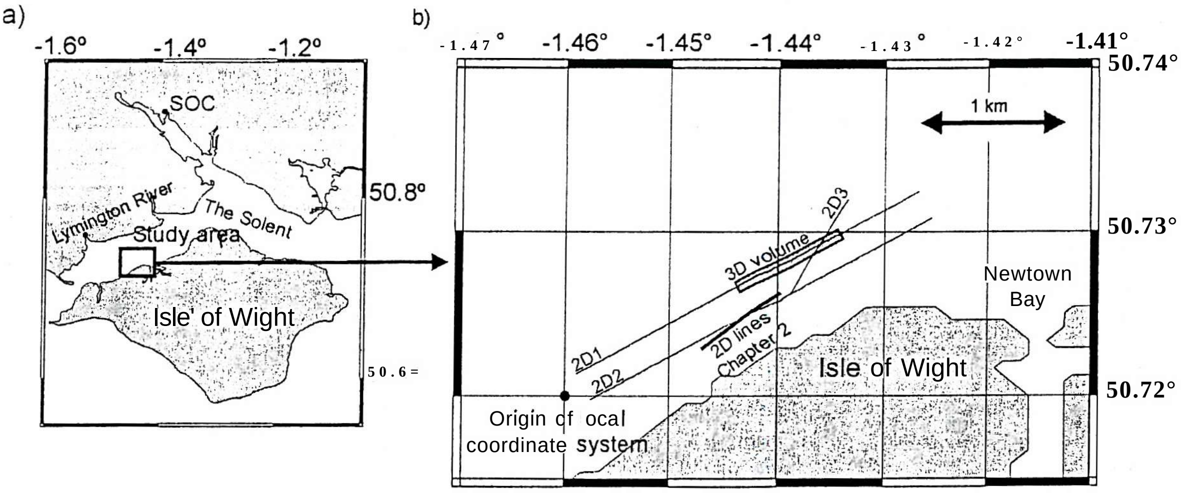

Figure 6.1 Location of the 3D Chirp survey in the West Solent off the north coast of the Isle of Wight, a) The survey area approximately 2 hours boat passage from the Southampton Oceanography Centre (SOC). A tidal gauge is located in the Lymington River north-west of the survey area highlighted, b) Location of the 3D Chirp survey, a 750 m long and 75 m wide area in approximately 15 m water depth. The position of the 2D Chirp lines collected for the source signal study, presented in Chapter 2, are marked together with 2D Chirp lines 2D1, 2D2 and 2D3 recorded to allow an integrated geological interpretation of the area which is presented in Chapter 7. Note the position of the local UTM coordinate system used for data processing.

The area chosen as the 3D Chirp survey target is located to the north-east of the previously collected seismic lines. The 2D lines are characterised by good data quality with a penetration of greater than 30 ms TWT (Figure 2.9). The data images a south-westerly dipping stratigraphy with units of different thicknesses with a range of reflection amplitudes. The area chosen for the 3D Chirp survey is expected to contain a similar stratigraphy and is located in greater water depth of approximately 15 m which makes it possible to acquire data over the entire tidal cycle, which was difficult for the 2D seismic line. Therefore it is an ideal target for testing the 3D Chirp system and analysing the dataset for horizontal and vertical resolution. The survey area was chosen to stretch 750 m in the north-easterly direction, parallel to the previously recorded seismic lines. The prevailing tidal currents are parallel to this direction, thus facilitating the navigation of straight lines. The width of the area was limited by the allocated survey time. By sailing parallel lines with 1 m spacing a width of 75 m was achieved over the five survey days.

6.3 Data acquisition

6.3.1 Narrative

The survey was conducted over five days from 9th to 13th of August 2003 from the R/V Bill Conway. The weather conditions throughout the period were very good with a calm sea-state. The 3D Chirp towing behaviour proved to be reliably stable as expected from the tests described in Chapter 5. The deployment and recovery at the start and end of each survey day was carried out efficiently using the boat's A-frame and a crew of four. A total of 24.25 hours of navigation data were recorded and during this period 22.5 hours of seismic data were collected. As the system has 1.25 m across-track coverage (Chapter 5) it was decided to use 1 m line spacing, resulting in 25 cm overlap between lines to allow for navigation inaccuracies. 75 parallel 750 m long lines were recorded in south-west north-east direction, parallel to the prevailing tidal current direction. The ground coverage was monitored by displaying the navigational data on a laptop computer at the end of each survey day.

6.3.2 Acquisition system configuration

Figure 6.2 shows the configuration of the systems used to record the seismic and navigation data.

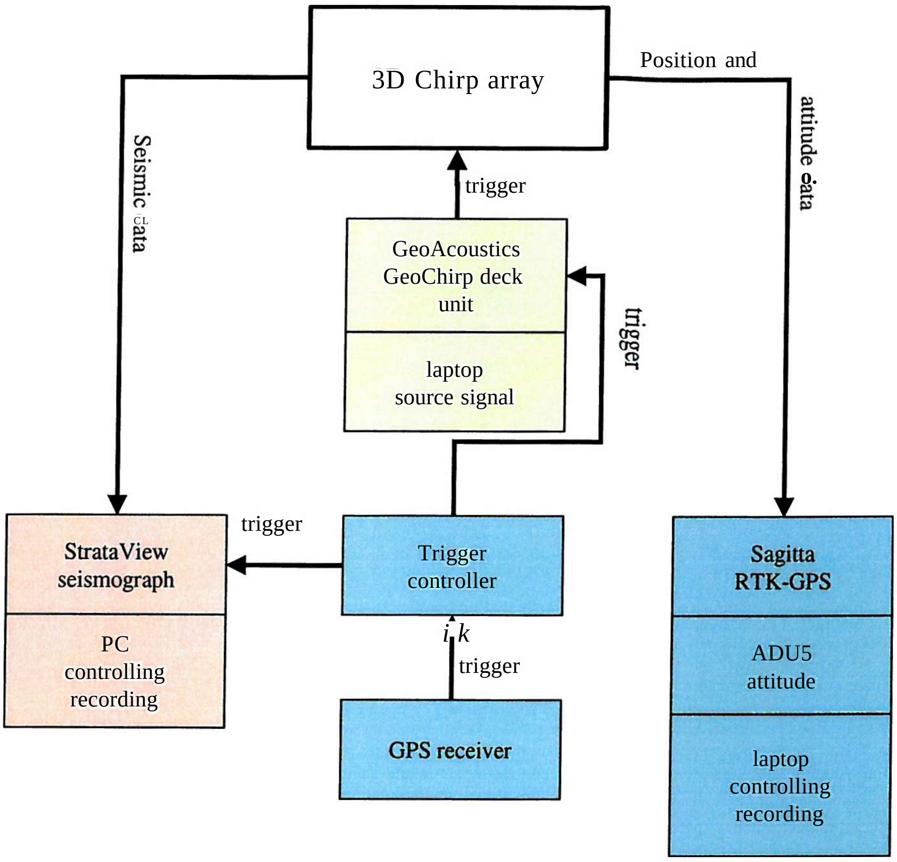

Figure 6.2 3D Chirp control and recording system configuration. A standard GPS receiver provides a one pulse per second output. A trigger control amplifies this output and triggers the seismograph as well as the 3D Chirp source array via the GeoAcoustics GeoChirp deck unit. The source array emits a source signal, which can be selected via a laptop computer connected to the GeoAcoustics GeoChirp deck unit. The 60 channel seismic data are transferred as analog signals from the 3D Chirp array to the StrataView seismograph where they are amplified, digitised and stored on DDS-4 digital tapes. The seismograph and the tape devices are controlled by a PC. The signals from the four GPS antennas located on the 3D Chirp array are converted into RTK-GPS position and attitude data by the Sagitta and ADU5 systems respectively. Both systems are controlled by a laptop computer, which also stores the navigation data.

The analog seismic data are transferred from the 3D Chirp array to the on-board seismic recording system via two 30 channel umbilical cables. The StrataView seismic recording system is described in Chapter 5. The raw GPS signals from the four antennas, placed on the 3D Chirp array, are transferred via umbilical cables to the on-board systems. The RTK-GPS position and the GPS-attitude system are described in Chapter 4. The signal from the system's dual frequency antenna 1 is duplicated, using a custom signal splitter and fed into the Sagitta RTK-GPS system and, together with the signal of the remaining three GPS antennas, into the ADU5 attitude system. The GeoAcoustics GeoChirp deck unit, used as standard with the company's 2D GeoChirp system, is used to power and control the Chirp sources. It is connected via an umbilical to the electronic bottles, placed on the 3D Chirp array, which drive the source transducers. The source signatures, stored in the electronic bottles, can be selected via the trigger unit, using a laptop computer, connected via an RS-232 connection and running standard terminal software. Additionally the power output level can be selected.

A standard GPS system provides a one pulse per second trigger signal that is fed into a trigger control unit, which allows selection of the trigger rate. It provides signals that trigger simultaneously the GeoAcoustics GeoChirp deck unit, which then triggers the source array, and the recording system. The systems are triggered with a rate of 1 Hz on every exact second from the GPS-time signal. However, the time stamp from the RTK-GPS system is not recorded by the seismic recording system, but the system's internal clock time is written in the seismic data trace header as integer values for hours, minutes and seconds, whereby the second value is converted from the system clock's floating point output. The control and recording PC's system clock is synchronised with the seismograph at every system start-up. At the beginning of every survey day the system clock of the seismic recording system was synchronised with the GPS time-signal. However, the recording system clock drifted with time over the duration of the data recording as was found during data processing, resulting in a mismatch between the time recorded in the seismic data and the true time recorded with the RTK-GPS position and attitude data. This leads to considerable errors in the positioning of the seismic data, which need to be corrected in the processing stage. **A** discussion and a correction method are presented in section 6.4.6.

6.3.3 Seismic data recording

In the trials the 1.5-13 kHz source sweep with a sine-squared 8th envelope function described in Chapter 2 was used (S7). The length of the outgoing source sweep of 32.74 ms overlaps with the arrival of the signal reflected from the seabed at 20 ms for the approximate water depth of 15 m in the survey area. Hence the outgoing signal is recorded as a direct arrival at the same time as the incoming reflections. Since the outgoing signal has significantly higher amplitude than the reflected signal a large dynamic range is needed to record the two signals simultaneously. Empirical testing showed that the power output of the source array needed to be reduced to 27 % of the maximum value (70/255) in order to avoid clipping of the recorded data since the analog to digital converter of the recorder system clipped larger amplitude signals. The seismic recording system worked reliably throughout the survey and a data volume with the following attributes was recorded:

• shots:	81028
• seismic traces:	4861680
• shot rate:	1 Hz
• sample interval:	31.25 (is
• recording length:	70 ms - 80 ms
• samples/trace:	2241-2561
• size of data in SEG-Y-format:	46.37 GB.

The data were recorded to DDS-4 tape in a modified SEG-2 format (Pullan, 1990; StrataView user manual) and transferred to SEG-Y for later processing using code provided by Tim Henstock.

6.3.4 Position and attitude data recording

The RTK-GPS reference station for the survey was set-up on the roof of Lymington Town Hall. The coordinates of the reference position are:

- **50° 45'38.26451" N**
- **01° 32'44.98242" W**
- **78.610 m(WGS84).**

The RTK-GPS position was recorded onto the hard-disk of a laptop computer connected to the Sagitta system using manufacturer provided software at an update rate of 5 Hz as a number of ASCII-files throughout the survey. The data format used is the GPGGA string (Appendix B). It contains time and the position as latitude, longitude and altitude in the

WGS84 reference system, together with data quality indicators and information about satellites used and the reference station.

The attitude data were recorded using a laptop computer connected to the ADU5 system and running manufacturer provided software at an update rate of 5 Hz. The data string used is the GPPAT string (Appendix B), which contains time, position as latitude, longitude and altitude in the WGS84 reference system together with heading, pitch, roll and a number of data quality indicators. The position given by the attitude system is in stand-alone-GPS meter-scale accuracy and was not used in later processing.

Figure 6.3 shows the horizontal position data recorded by the RTK-GPS position system.

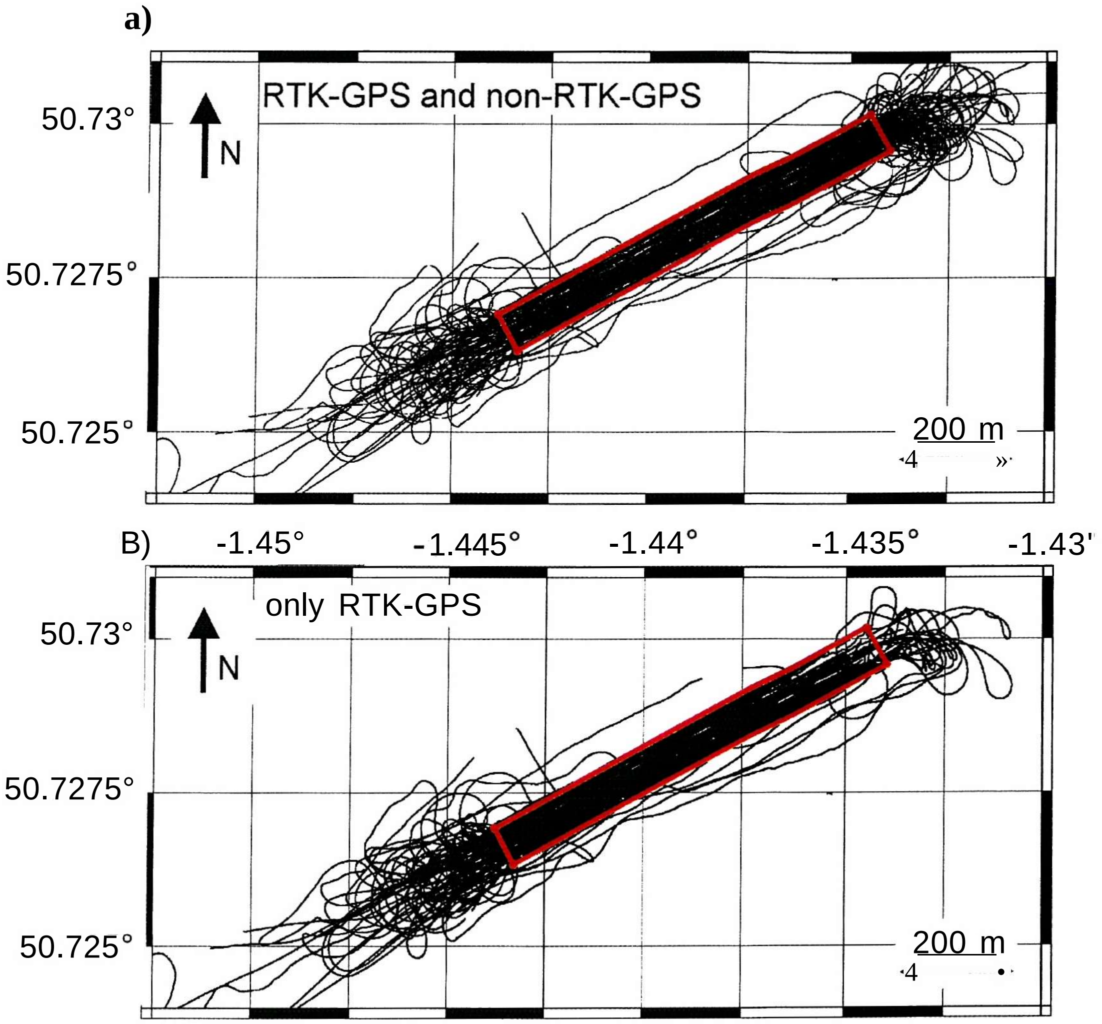

Figure 6.3 Horizontal positions recorded with the Sagitta RTK-GPS system during the survey. The 3D Chirp survey area is highlighted. See Figure 6.1 for an overview map. a) All recorded GPS positions, b) Only positions with RTK-GPS quality. Note the sparser RTK-GPS quality position data coverage at the north-eastern end compared to the south-western end.

The data in Figure 6.3a include positions with RTK-GPS and less accurate non-RTK-GPS modes, whereas the data in Figure 6.3b only show the data with RTK-GPS accuracy. The wide line-turns north-east and south-west of the survey area were necessary so that the antennas of the 3D Chirp system did not submerge during the turn and to ensure that the array pointed in the correct direction at the start of each survey line.

The average survey speed over ground calculated from the horizontal positions was approximately 1.5 m/s (2.9 kn).

Figure 6.4 shows the z-component of the navigation data recorded with the RTK-GPS system for the five survey days, together with tidal data collected at the a tidal gauge situated in the entrance of Lymington river (Figure 6.1). The tidal data have a constant offset to the WGS84 heights measured with the RTK-GPS system, as it is measured with respect to chart datum. The RTK-GPS height is the WGS84 height of the **GPS-antenna** positioned on the 3D Chirp array. For comparative purposes the constant offset was estimated by performing a best fit analysis. It should be noted that the time and spatial distribution of tidal amplitudes is complex in the Solent and that the long term height differences measured with the RTK-GPS system not only depend on the tidal height, but also on the towing depth of the 3D Chirp array, which itself depends on the general towing configuration, the towing speed and the speed and relative direction of the tidal currents. Therefore the tidal data shown should be seen only as an estimate of the expected height measured with the RTK-GPS system.

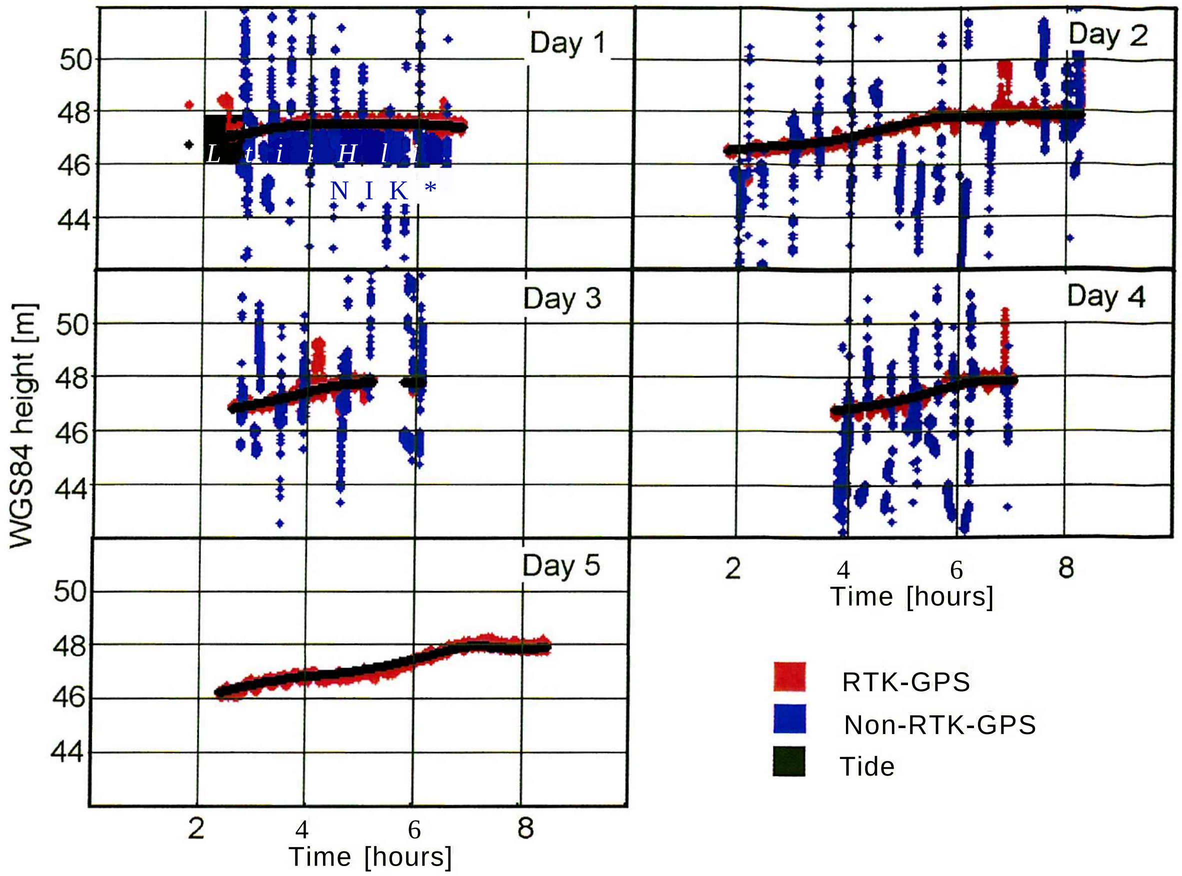

Figure 6.4 GPS height recorded during the 3D Chirp survey together with sea-level data collected with a tidal gauge located in Lymington River (Figure 6.1). The tidal gauge height was shifted a constant value to best fit the RTK-GPS height data. The RTK GPS data have different accuracies, RTK and non-RTK, depending if a radio connection with the RTK-reference station could be established. Note that throughout day 5 consistent radio connection was established, in contrast to the first four survey days at which the radio connection was frequently lost, possibly due to interference with a second radio transmitter operating close to the survey area.

The height data with RTK-GPS accuracy are shown in red, the non-RTK-GPS data are shown in blue. In general there is a good match between the tidal data and the long term variations of the RTK-GPS height. The RTK-GPS height shows a change on decimetre scale from one measurement to the next, whereas the non-RTK-GPS data show jumps on a metre scale because of its lower accuracy (Chapter 4). The non-RTK-GPS data are associated with the north-eastern end of the survey area, where on days 1 to 4 the UHF radio connection to the RTK-GPS reference station could not established reliably, with consequent loss of the RTK-GPS accuracy. This was probably due to interference of the radio signal with a second transmitter, whose signal was stronger in the north-eastern region than in the rest of the survey area. After changing the communication UHF frequency of the RTK-GPS system from 458.6 GHz to 458 GHz at the end of day 4 the interference was avoided, resulting in good radio coverage and subsequent RTK-GPS data throughout the fifth survey day. Comparison of Figures 6.3a and b shows that the non-RTK-GPS data were in the north-eastern part of the survey area. The short term variations on decimetre scale of the height (Figure 6.4) are associated with movement due to waves. This can be seen in a close-up of the height data for day 5 in Figure 6.5, which also shows the attitude data: heading, pitch and roll. Changes with amplitudes of some decimetres over time duration of some minutes are associated with different survey lines. The towed array experienced different drag, going with or against the tidal current such changing its towing behaviour, which is reflected in its towing depth and attitude.

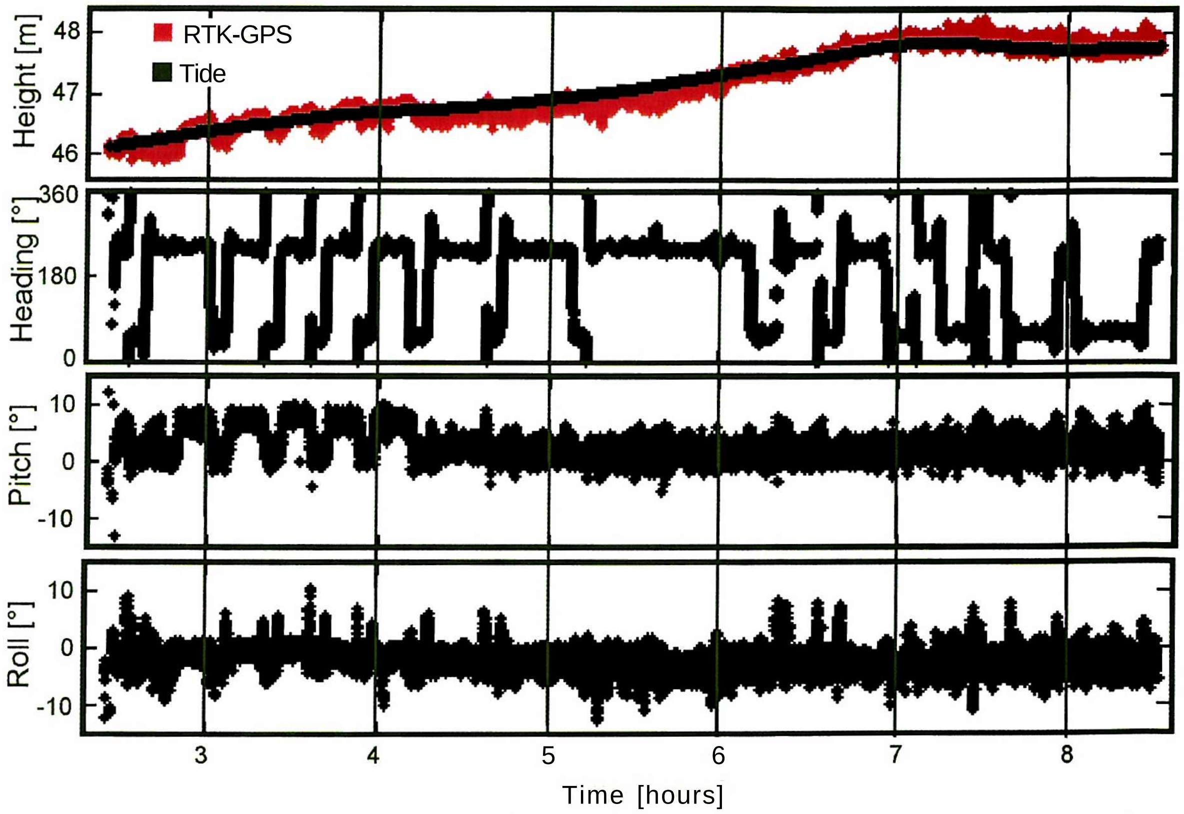

Figure 6.5 RTK-GPS height, together with sea-level data, and attitude data for the survey day 5 (Figure 6.4). See text for discussion.

The heading value in Figure 6.5 indicates the direction of travel. At the start of the survey day at around 2.2 hours it takes longer to cover a survey line in the south-western direction than in the north-eastern direction due to the north-easterly tidal current. The duration increases until between 5.3 and 6.3 hours the coverage of the survey line in south-western direction takes approximately 1 hour as opposed to 5 minutes for the survey line in north-eastern direction starting at 5.2 hours. At around 7.3 hours the duration in either direction are equal. For later times the duration for the lines in north-eastern direction are greater than for the lines in south-western direction indicating a change of tidal current direction to the south-west. Note the difference in array height depending on the direction of travel. In particular between 2.8 and 4.3 hours the height is approximately 50 cm higher for south-westerly lines than north-easterly. Towing in south-westerly direction, against the current, the 3D Chirp shows a pitch of approximately 8°, with the bow higher than the stern. Towing in north-easterly direction, going with the current the array shows a lower pitch of approximately 2°. For later times this is not apparent. The towing behaviour is complex and a change in a parameter like the speed or the length of towing rope can have a strong effect. The average standard deviation from the respective mean value during the recording of a single line is approximately 6 cm for the height, 4.5° for the heading, **1.7**° for the pitch and **1.6**° for the roll value, reflecting the stable towing behaviour of the array. Changes in average roll and pitch values from one line to the next are highly variable. They range from approximately 0° to 8° for the pitch and 0° to 6° for the roll value, resulting in height changes in the range of approximately 0 - 40 cm. The maximum absolute roll value, recorded during a line-turn is 16°, the maximum absolute pitch value 20°.

Some abrupt changes in height values are observed at day 2 at hour 6.8, at day 3 at hour 4 and day 4 at hour 7, which are not reflected in the attitude data. It is assumed that these measurements are inaccurate, although marked as RTK-GPS by the system. The seismic data recorded at during these periods is omitted in later processing stages.

6.4 Data processing

6.4.1 Introduction

An important stage in the production of a 3D seismic volume is to combine the seismic and navigation data. In this section the processing stream used is presented and the processing stages discussed. The effect of the processing algorithm is demonstrated on a single channel record for a single profile where possible. For the seismic data processing 3D ProMAX (Landmark Graphics, 2003) is used, a 3D seismic processing software package offering state of the art algorithms together with an integrated database. For merging of the navigation information with information from the seismic database FORTRAN and shell script programs are used. The result consists of a SEG-Y format file that can be imported into 3D seismic visualisation and interpretation software. The processing flow is summarised in Figure 6.6.

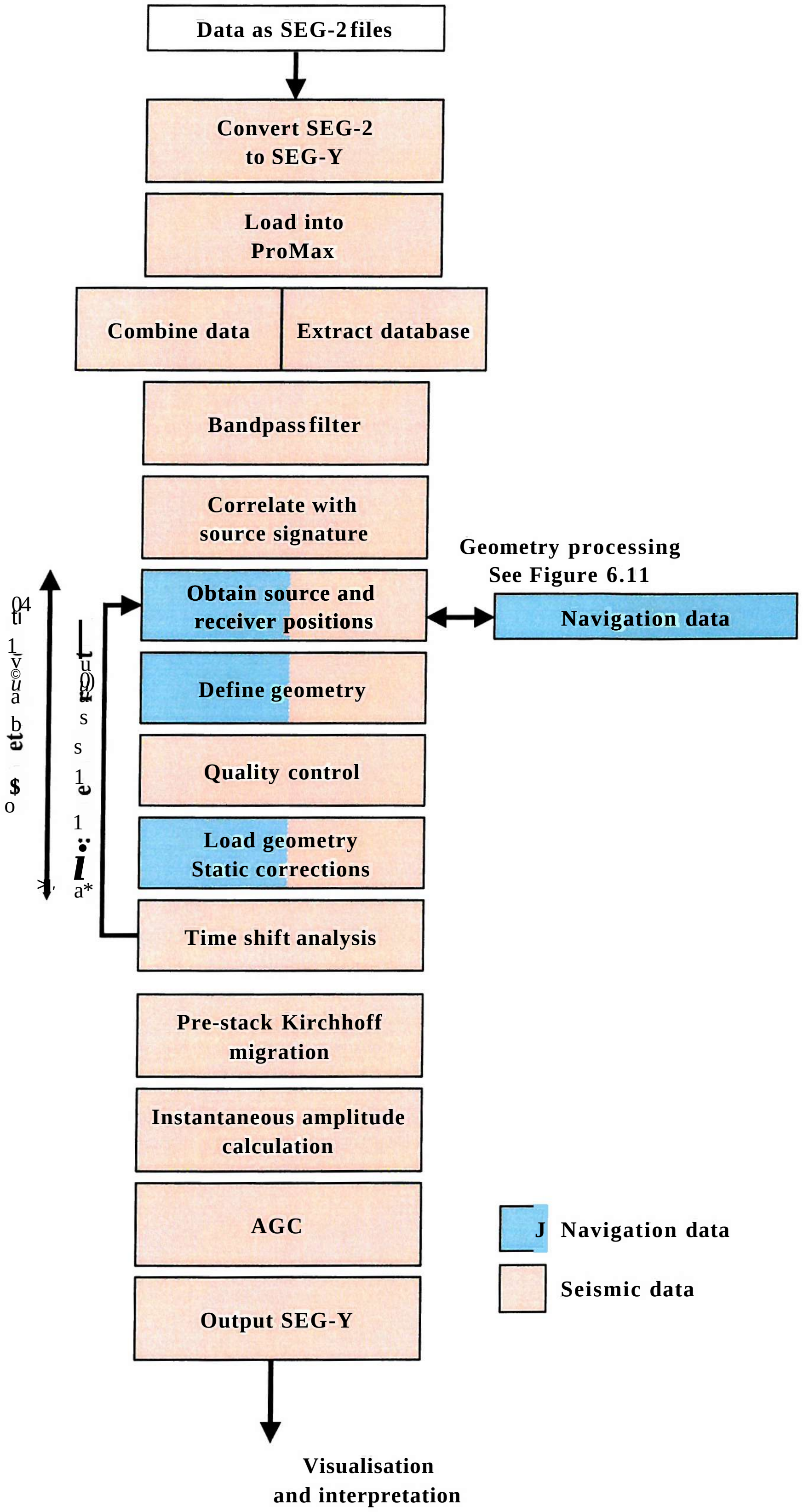

Figure 6.6 3D Chirp data processing flow. Each processing stage is described in individual sections in the main text.

6.4.2 Seismic data import and database extraction

The seismic data in SEG-Y format were imported into ProMAX as individual datasets prior to the formation of a single dataset for which a database is extracted. Beforehand the field file identification (FFID) in the trace headers is set such that it is unique for every shot of the survey, assuring that the source ensembles are ordered correctly. By extracting the ProMAX database all information from the seismic trace headers are stored in a specific order in binary files, called ordered parameter files (OPFs). Specific orders used in the database include shot order (SIN), common depth point order (CDP), trace order (TRC), inline order (ILN), crossline order (XLN) and channel order (CHAN). Information is stored in the files of the relevant order. Additionally cross domain lookup information is created to allow efficient data exchange between the orders. For example the time and date of a shot are stored in the SIN order. This information is relevant for the, in this case, 60 traces associated with the specific shot; hence the TRC order is linked via the shot identification number (SIN) to the relevant information in the SIN order. The main reasons for this approach are to avoid the redundant storage of information and to allow quick access. In particular the crucial part of the geometry processing described in section 6.4.5 consists of creating the relevant information in the database, thus describing the 3D seismic data volume.

Figure 6.7 shows an example of the imported raw uncorrelated data for a single channel seismic line, together with its associated power spectrum and its position in the survey area shown in Figure 6.1.

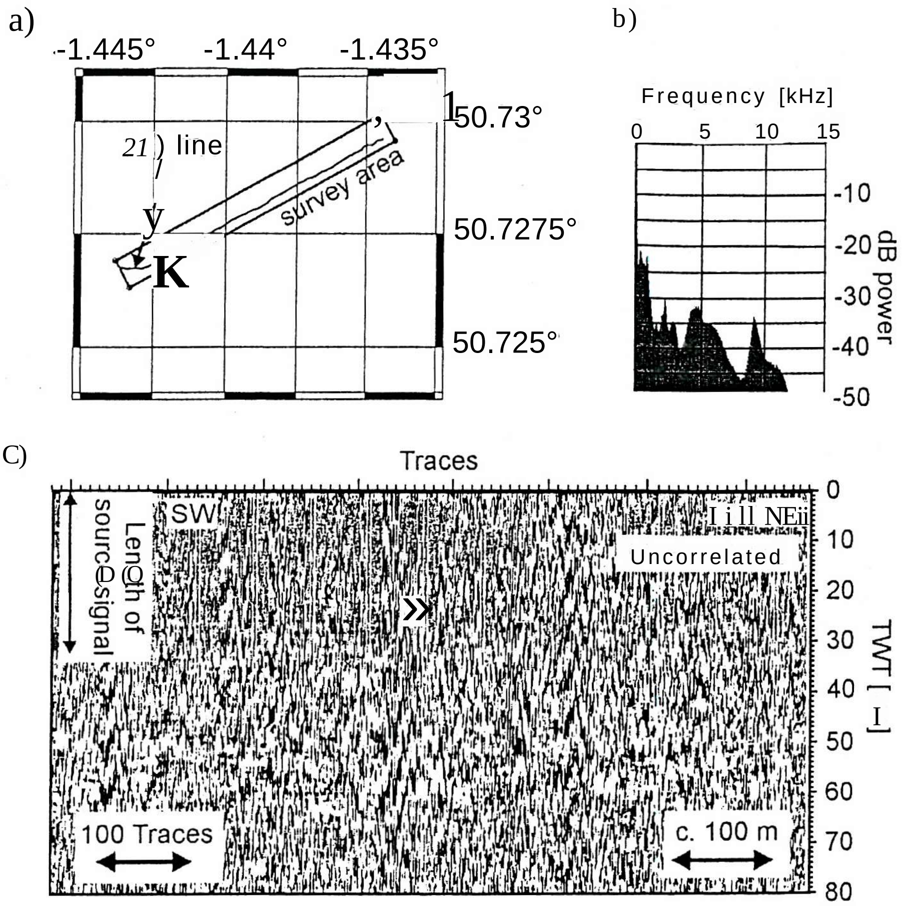

Figure 6.7 Example of a single channel section of raw uncorrelated data of a 2D line within the survey area, a) The position of the 2D seismic line within the survey area, b) Power spectrum, c) Seismic section.

The line consists of 792 traces recorded along a line in the 750 m long box shown in Figure 6.3. The data are dominated by high amplitude low frequency noise as is apparent from its power spectrum. It shows prominent peaks below 1 kHz. In the seismic section the pattern in the upper 32.74 ms TWT, the length of the source sweep, differs from the pattern at later times for the majority of the traces.

6.4.3 Bandpass filtering

The data are bandpass filtered using an Ormsby zero phase frequency domain filter with Harming taper functions. It is set such that the source signal bandwidth of 1.5 - 13 kHz is conserved (see Figure 2.7 for the source signal S7 used). The parameters are 0-1.5-13-15 kHz, where the first and the last values are respectively the start and end of a Harming windows stretching to the start and end frequencies of the source signal. Figure 6.8 shows the effect of the bandpass filter on the uncorrelated data shown in Figure 6.7.

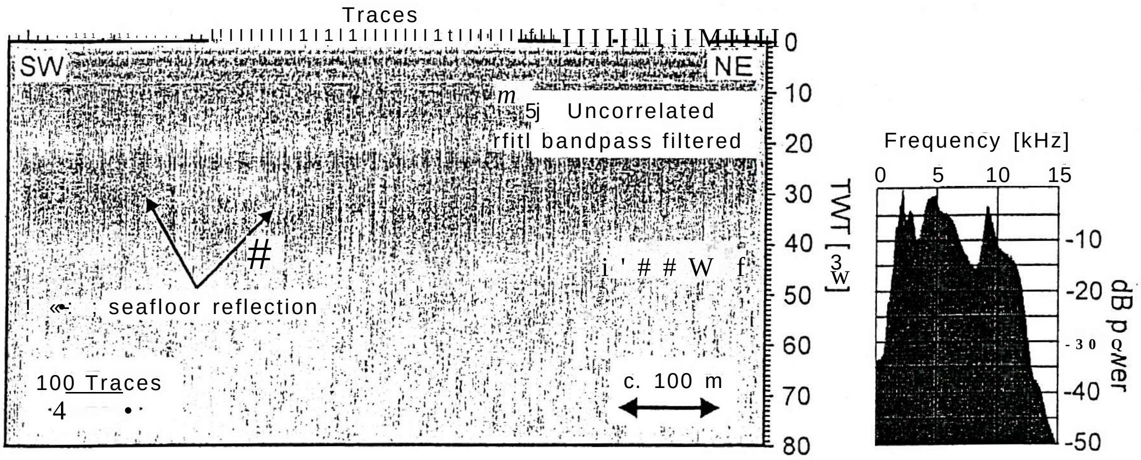

Figure 6.8 Uncorrelated seismic data of single channel 2D line (Figure 6.7a) after application of bandpass filter. The seafloor reflection is apparent.

By applying the bandpass filter the low frequency noise dominating the uncorrelated data (Figure 6.7) was omitted. The power spectrum shows peak values at 2 kHz, 4.5 kHz and 9.5 kHz and a trough reaching to -16 dB at approximately 8 kHz. The power spectrum significantly differs from the spectrum of the source sweep (Figure 2.7b), which shows a full amplitude for frequencies between approximately 2.5 kHz and 11.5 kHz. In contrast the power spectrum of data collected with the 2D seismic system for the source sweep comparison study discussed in Chapter 2, shown in Figure 2.10, shows a power spectrum very similar to the source signal spectrum, which is discussed in section 6.4.4.

The seismic section reveals the seafloor reflection at TWTs between 15 and 30 ms. The seafloor reflections are hence recorded while the source signal, with a length of 32.74 ms, is transmitted.

6.4.4 Source signal correlation

The seismic traces are correlated with the source sweep S7 (Figure 2.7) and the resulting correlated data are effectively the convolution of the Klauder wavelet of the source signature with the Earth's impulse response plus noise components. Furthermore the length of the correlated traces is reduced to 58 ms, the approximate maximum length of useful data since the seafloor multiple reflection obscures reflection returns with greater TWT. Figure 6.9 shows the correlated seismic section together with its associated power spectrum.

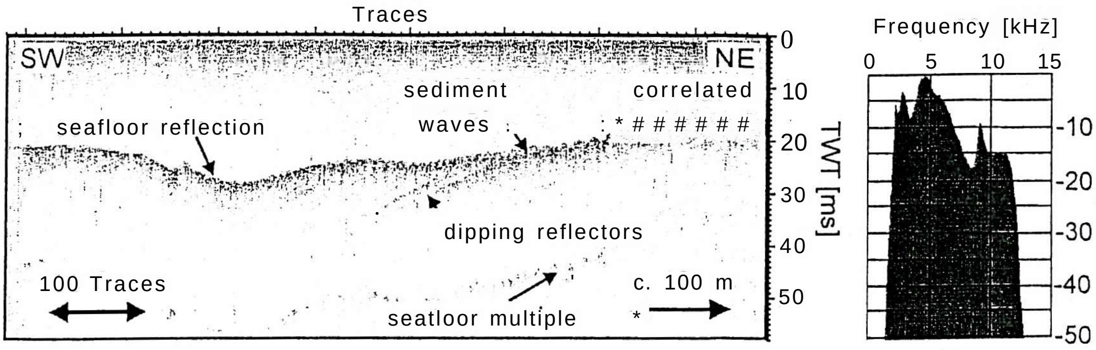

Figure 6.9 Seismic data of single channel 2D line (Figure 6.7a) together with power spectrum. The data were correlated with the source sweep S7 shown in Figure 2.7. The seafloor reflection showing sedimentary waves in the north-eastern part is located between 10 and 30 ms TWT. Some internal reflectors with an apparent dip in south-western direction are apparent. The seafloor multiple is located at twice the TWT to the seafloor reflection.

The power spectrum is similar to the power spectrum of the uncorrected data (Figure 6.8) as it shows the peak and troughs at the same frequencies. Frequencies outside the bandwidth of the source sweep of 1.5-13 kHz have powers smaller than -50 dB. Within the bandwidth the power drops to a value of approximately -18 dB at 8 kHz. The mean frequency is 4.95 Hz.

The seismic sections shows the seafloor reflections between 15 ms and 30 ms, mirrored by the seafloor multiple at double the TWT. The seafloor shows undulations, which are interpreted as sediment waves. They are accompanied by bowtie structures associated with structural depressions and diffraction hyperbolas. A number of internal reflectors are present, showing an apparent dip to the south-west.

Figure 6.10 shows the power spectrum of correlated and filtered data section collected with the 2D Chirp system used for the source signature study discussed in Chapter 2 for the same sweep.

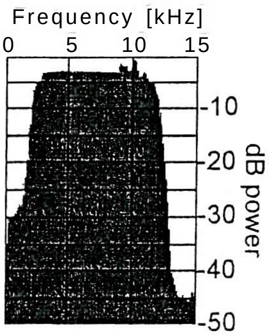

Figure 6.10 Power spectrum of bandpass filtered and correlated Chirp data recorded with the 2D Chirp system, which is presented in Chapter 2. The spectrum corresponds to the data shown in Figure 2.9g.

The power spectrum shows a peak at approximately 10 kHz and a plateau at approximately -3 dB between approximately 3-12 kHz. There is a stark contrast between this spectrum and the spectrum for the data collected with the 3D Chirp system, which was expected to be similar to the 2D system's spectrum. The same transducers are used in both systems. The receiver and recording systems are different. However, using a newly developed recording system during data collection in July 2004 showed the same frequency content of the data, thus ruling out an unwanted filter effect of the recording system. Additionally the transducers have been newly calibrated for their frequency response and a new transfer function was applied to compensate the source sweeps for the transducer frequency response. From the data it is not possible to decide which of the changed factors is responsible for the change in the power spectrum of the recorded data. It is necessary to investigate experimentally the frequency response of the receiver within the 3D Chirp array as well as the newly calibrated transducers. A correction for future data collection is desirable.

The next processing steps comprise 3D geometry processing and 3D pre-stack migration together with quality control and their effects are hence not shown on the example 2D section. The subsequent processing steps, instantaneous amplitude calculation and automatic gain control application, are performed on the migrated 3D data volume, however, for consistency their effects are demonstrated using the 2D example section (sections 6.4.8 and 6.4.9).

6.4.5 Geometry processing

The following three processing stages represent the geometry processing, in which navigation and seismic data are combined with the aim of computing a mid-point for every seismic trace and subsequently assigning it to a CDP, inline and crossline.

6.4.5.1 Specification of source and receiver positions

By extracting the ProMAX database from the seismic data the SIN and TRC orders have been created, containing information about shots (FFID, date, time, SIN) and the traces (TRC, CHAN) respectively. This information is exported from the database in ASCII format and merged with the navigation information to compute the source array and receiver group positions. The positions are then imported into the database to complete the necessary information to assign the geometry. Figure 6.11 shows the detailed flow used for **the geometry processing stage.**

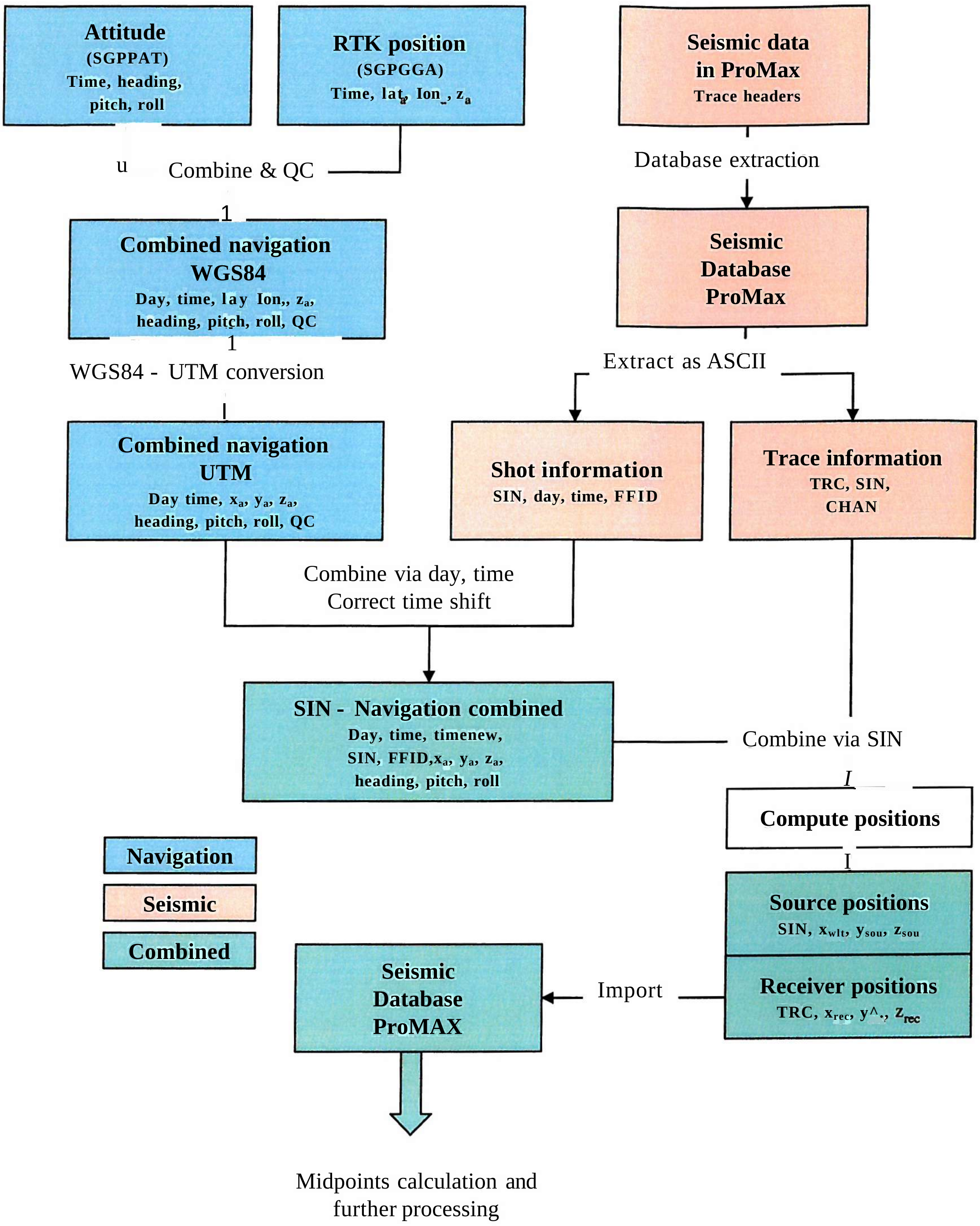

Figure 6.11 Geometry processing as part of the 3D Chirp data processing flow shown in Figure 6.6., which combines the navigation and seismic data.

1) The attitude and RTK-position data consist of a number of files in ASCII format containing $GPPAT and SGPGGA data strings respectively. The data strings formats can be found in Appendix B. A quality control of the navigation data is performed using quality indicators within the data strings. The data strings are then combined into a single file, using the timestamps. They contain the RTK-GPS position in WGS84 system together with heading, pitch and roll values with 1 s update rate. Appendix C contains the shell-script code with detailed explanations together with the output data-file format.
2) Subsequently the position data are converted from WGS84 into Universal Transverse Mercator (UTM) format, using a local origin. The use of a local origin is necessary in order to limit the size of coordinate values to assure sufficient precision. The local origin is chosen to be 50.72° N 1.46° W, which lies to the south-west of the survey area (Figure 6.1). Appendix C lists the combined Generic Mapping Tool (GMT) and shell-script code to perform the transformation together with explanation of the output data-file format.
3) Two files are extracted from the ProMAX database. The shot information file contains SIN, day, time and FFDD. The trace information file contains the trace number (TRC), SIN and the channel number (CHAN).
4) The shot information file is then joined with the combined navigation file in UTM format via the day and time information. Appendix D contains the FORTRAN code together with input and output file formats. Previous to joining the files the time shift of the seismic recording system is corrected as described in section 6.4.6.
5) The file containing the shot-file and navigation information is joined with the trace-file via the SIN. Using the navigation information the positions of source and receiver groups are computed using the position determination algorithm described in Chapter 2. Appendix E contains the FORTRAN code together with the input and output file formats. Figure 6.12 shows source and receiver positions for different attitude values computed using the algorithm for illustration.
6) The source output file contains SIN together with the source positions. The shot output file contains TRC together with the receiver group positions. They are imported into the ProMAX database to be used for the subsequent geometry processing stages.

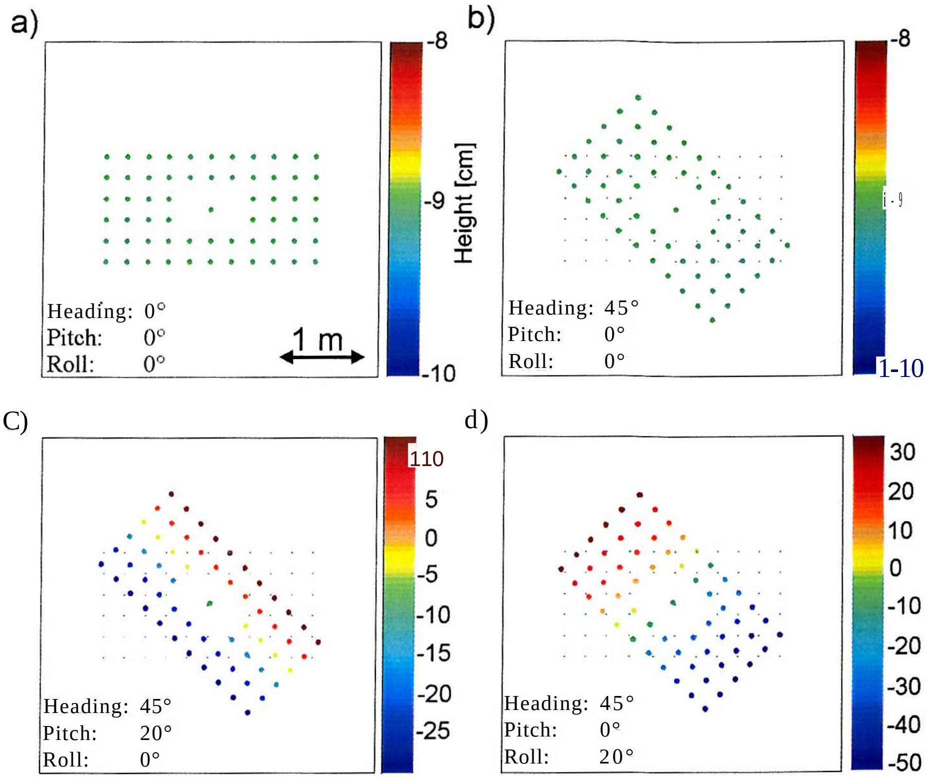

Figure 6.12 Source and receiver positions depending on attitude: heading, pitch and roll values. The positions are calculated using the algorithm presented in section 4.4.

Figure 6.12a shows source array and receiver group positions for the case that all attitude values are zero. The positions are given with respect to the centre of gravity, which is in the centre of the array and 9 cm above the source array. Figure 6.12b shows the case of a heading value of 45°. The elements remain on the same height. Figure 6.12c introduces a pitch of 20°, resulting in the elements at the bow of the array being approximately 39 cm elevated with respect to the elements along the stem. Figure 6.12d shows the array with a heading of 45° and a roll of 20°, resulting in the elements on the starboard side of the array being approximately 80 cm lower than on the portside.

The subsequent processing steps are performed within the ProMAX software package, as all relevant information for the geometry processing are now contained in the ProMAX database.

6.4.5.2 Define geometry

To define the geometry the interactive 3D Marine Geometry spreadsheet module in ProMAX is used. The reflection midpoints are assigned by mapping the source positions in the SIN order to the receiver positions in the TRC order and computing the midpoint positions centre between the source and receiver positions.

A binning grid is defined that covers the area highlighted in Figure 6.3. The square bins have a side-length of 12.5 cm. It was chosen to equal the midpoint spacing of the 60 channels for one shot, given as half the receiver spacing of 25 cm. As outlined in Chapter 5 the aim is to achieve equal spacing also between shots by choosing appropriate shot rates depending on the survey speed. However, due to the specifications of the seismic recording system used, discussed in section 5.5.3, this is not expected to be achieved for the recorded dataset. The inline separation between shots exceeds the envisaged 75 cm (section 5.2.3), owing to the small shot-rate of 1 Hz used. The cross-line separation is equally expected to exceed the envisaged 1 m (section 5.2.3), due to navigation inaccuracies and insufficient number of lines covering the area.

The grid has the origin (50.726909° N, 1.443815°W) and an azimuth of 60°. It is 75 m wide and 750 m long, hence including 600 inlines and 6000 crosslines.

Note that the grid is only used to define the imaging geometry for the pre-stack migration. The traces are not binned into CDPs to be stacked for conventional post-stack processing. Figure 6.13 shows the midpoints together with the binning grid.

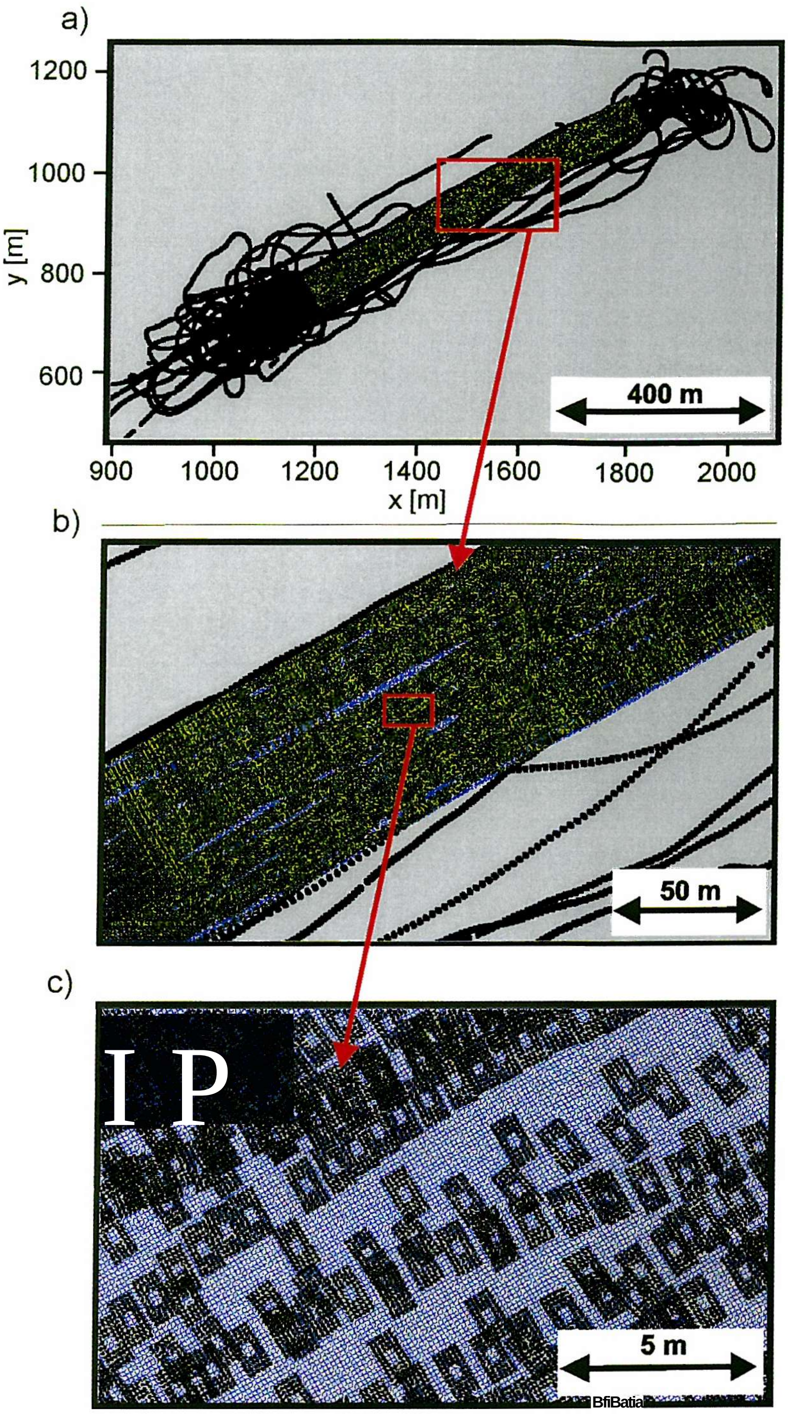

Figure 6.13 Reflection midpoints, calculated as the centre between source and receiver locations for each shot, together with binning grid. The binning grid is used to define the imaging geometry for the pre-stack Kirchhoff migration discussed in section 6.4.7. , rather than stacking traces within a CDP. a) Entire survey. A local UTM coordinate system is used, b) Zoomed image showing approximately 3% of image a. Note the alignment of midpoints along lines in the longitudinal direction of the grid, c) Zoomed image showing approximately 0.6% of image b. Note the arrangement of midpoints in rectangles corresponding to individual shots.

Figure 6.13 shows the midpoints calculated using good quality navigation data (section 6.4.3) with positions expressed in local UTM coordinates. Compare to Figure 6.3b, which shows the RTK-quality positions of the antenna used for the calculation, together with the outline of the grid in WGS84 coordinates. The close-up in Figure 6.13b reveals the arrangement of midpoints along acquisition lines aligned in south-western direction and elongated areas of insufficient coverage within the grid. Although the aim was to sail parallel lines with 1 m line spacing, this was not always possible when strong surface currents were present, resulting in patches of poor coverage. The individual lines in the south-eastern part of the area reveal differences in midpoint separation from one shot to the next. This is due to variations in the towing speed of the array, owing to differences in the tidal currents as discussed in section 6.3.4. The further close-up shown in Figure 6.13c reveals the arrangement of the 60 midpoints for each shot in a rectangle with side-length of 75 cm in the longitudinal and 1.25 m in transversal directions. This corresponds to half the side-lengths of the receiver geometry shown in Figure 5.4. Again the arrangements of these rectangles in lines are apparent. Note the difference in the spacing of the shot-rectangles between the lines owing to differences in the towing speed of the 3D Chirp array: the central line has a separation of approximately 3.4 m equating to a speed of 3.4 m/s with the shot-rate of 1 Hz. Other lines have a shot separation of just 1 m, equating to 1 m/s.

By assigning the traces midpoints to bins each trace is associated with a common depth point (CDP), inline (ILN) and crossline (XLN) number. Figure 6.14a, c and d show the position of the CDP with their fold, the number of traces associated with the particular CDP. Figure 6.14b shows the CDP fold versus inline and crossline numbers.

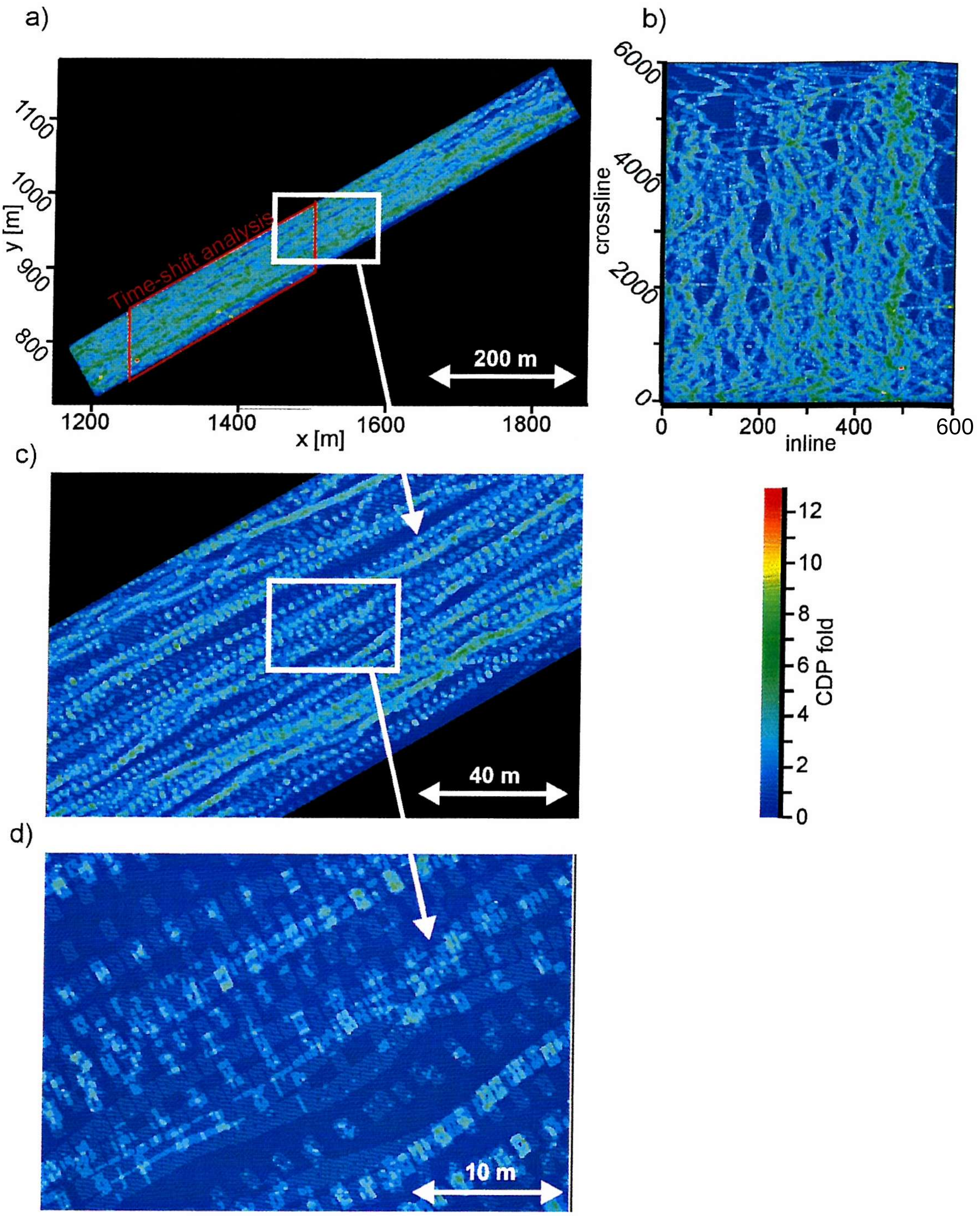

Figure 6.14 CDP fold, the numbers of traces within a CDP bin. a) Entire survey fold vs CDP position. The area used for the analysis of the time shift between the seismic and navigation recording systems (section 6.4.6) is highlighted, b) The fold for the entire survey area plotted against inline and crossline numbers, c) Zoomed image showing approximately 3% of the area in image a. Note the alignment of non-zero values along longitudinal lines, d) Zoomed image showing approximately 6% of the area in image c. Note the clustering of non-zero values in squares associated with individual shots. Values higher than 1 are generally associated with crossing of recording lines.

Figure 6.14a shows the CDP fold for the entire binning grid shown in Figure 6.13a. The CDP fold ranges from 0 to a maximum value of 13, which is achieved for a single CDP in the south-western part of the area. The close-up in Figure 6.14c reveals lines parallel to the areas longitudinal direction, associated with the acquisition lines. Generally for an isolated line only single CDP fold is achieved whereas multiple CDP fold is associated with line-crossings. The further close-up in Figure 6.14c reveals the square CDP fold patterns associated with individual shots. The extent of the area with zero CDP fold is due to the lack of coverage. Figure 6.14b shows the fold for the entire binning grid plotted against inline and crossline numbers. It is apparent that the fold for crossline numbers greater than 4500 is smaller than for lesser crossline numbers with the exception of the inline numbers around 300 and 500. The reason is the lack of good quality navigation coverage in the north-eastern part of the area on the first four survey days (section 6.3.4), which is represented by crossline numbers greater than approximately 4500. The lack of good quality navigation coverage resulted in the associated seismic data being omitted (section 6.4.5). During survey day 5 good quality navigation data were collected throughout the area. Inline numbers around 300 and 500 are associated with the fifth day and hence show equal CDP fold values throughout the crossline numbers.

A total of 2210140 traces are binned, 45.5% of the acquired data volume. With a total number of 3,6 million CDPs an average CDP fold of 0.61 is achieved for the binning grid used. It is worth stressing at this point that the traces are not stacked within a CDP for subsequent post-stack processing: the bin geometry is merely used to define the geometry for the pre-stack migration processing step described in section 6.4.7.

By creating all relevant ordered parameter files and cross-reference tables the database is finalised and includes all the geometry information necessary for subsequent 3D seismic processing.

6.4.5.3 Quality control of seismic and navigation data

A final quality control (QC) of the seismic and associated navigation data is carried out and bad quality data omitted from further processing. A previous quality control of the navigation data, described in section 6.4.5, was completed taking quality indicators within the navigation data strings into account. However, as described in section 6.3.4, some data marked as having RTK-GPS accuracy shows unrealistic altitude values (Figure 6.4). A total of 7692 traces (0.2 %), associated with these bad navigation data are omitted. The quality of the seismic data is analysed by displaying a number of single recording channels for the entire data volume and omitting traces with apparent low signal to noise (s/n) ratio; a total of 539640 traces (11.1%), mostly associated with line-turns, are excluded. Additionally two receiver groups (channels 35 and 39) were not functioning and therefore not used for processing (3.3% of data).

6.4.5.4 Load geometry — static correction

The final step in the geometry processing is the transfer of the geometry information from the database into the headers of the seismic traces. A new dataset is created which omits the traces which were not assigned to a bin due to lack of position information or because they lay outside the binning grid. All traces in the new dataset fall into the area covered by the binning grid (Figure 6.13). A static correction is applied by shifting the traces to the reference height of 48 m in the WGS84 reference system by subtracting the static t_{smic}, given as

$$t_{static} = \frac{z_{sou} + z_{rec}}{v_{water}} \cdot \tag{6.1}$$

where z_{sou} is the z-position of the source array, z_{rec} the z-position of the receiver group and Vwater the velocity of the seismic p-wave in water. The velocity was measured in the survey area previously using a velocity-depth-profiler during a multi-beam seafloor topography survey conducted by GeoAcoustics in August 2002. It showed that the water column is well mixed and has a sound velocity of 1518 m/s throughout. This was confirmed by time-series of salinity and water temperature in the West Solent measured by Simon Boxall, which were converted into sound velocities. The static shifts correct for the height differences of source array and receiver groups due to tides and towing movements of the acquisition array. See Figure 6.4 and 6.5 for the variations in the height for the RTK-position antenna. By applying the static corrections static shifts between traces should have been removed and the seafloor reflection for traces in the same bin should occur at the same time. However, after an investigation of CDP bins this was found not always to be the case because of false association between seismic and navigation data due to offsets in the recorded time of the systems. The following section 6.4.6 explains the effects and describes an algorithm to correct the offset.

6.4.6 Time shift correction

As described in section 6.3.2 the navigation data are recorded independently from the seismic data. The seismic sources and recording system are triggered using a GPS-clock signal but the time of the recording system's internal clock is stored in the seismic trace headers with seconds as integer values instead of the GPS time. However the navigation data are stored with the GPS time values. Differences between the time recorded with the seismic data and with the navigation data leads to bad positioning of seismic traces, resulting in static shifts between traces sorted in the same CDP as became clear after processing the data as described in section 6.4.5.

By picking the seafloor reflections in the traces of the area highlighted in Figure 6.14a it demonstrated that the seafloor reflection time values are displaced in a regular manner. Figure 6.15a shows the seafloor reflection picks within the picking area for the data collected during the survey day 4 only.

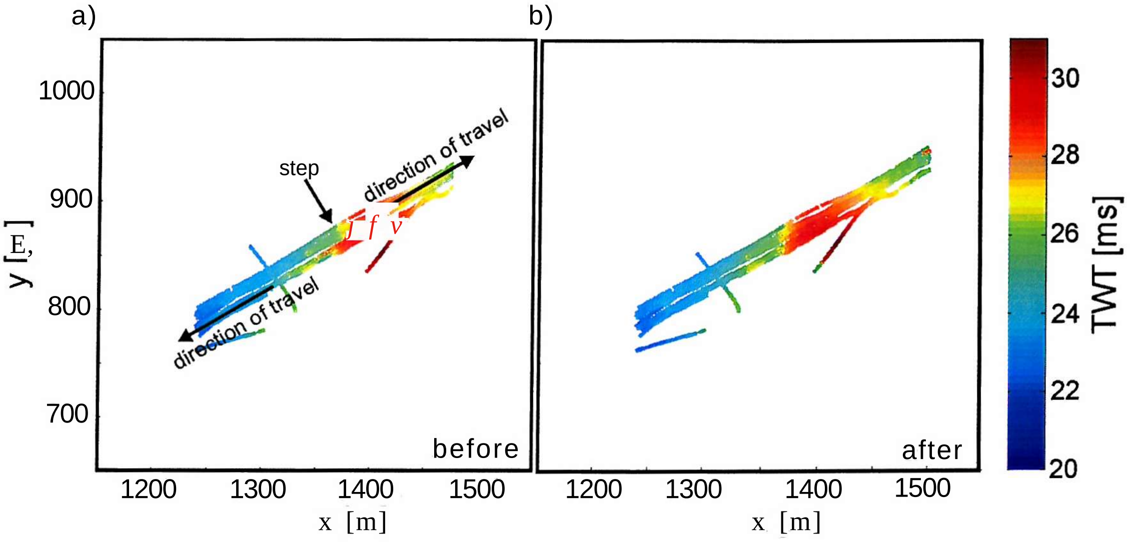

Figure 6.15 Seafloor reflection picks in the area highlighted in Figure 6.14a for data from survey day 4 only, a) The individual lines in the northern part were recorded travelling in north-easterly direction and the lines in the southern part travelling in south-westerly direction. The apparent step in the TWT values in the centre is due to a shift of the time recorded with the seismic and navigation data, b) Picks after simulated time-shift correction.

The data were collected along straight lines by sailing in north-easterly and south-westerly directions. The individual lines are apparent in the figure with the lines running in the south-westerly direction in the southern part of the area and the lines running in north-easterly direction in the northern part. Close to the middle of the lines there is a sharp change in the picked TWT of the seafloor reflection of approximately 4 ms, which represent the south-westerly flank of a depression with approximately 3 m maximum depth (assuming water sound velocity of 1518 m/s). This step offsets the north-easterly and south-westerly running lines. This is explained by an offset between the time recorded in the seismic header and the real GPS time recorded in the navigation data. With the time in the seismic header being ahead of the real time, thus $t_{seis} - t_{nav} > 0$, where t_{seis} is the time in the seismic header and t_{nav} the real time recorded with the navigation data. In this case the seafloor reflection associated with the seismic traces is shifted along the direction of travel. Since the seismic recording is triggered by the GPS-clock signal every exact second, offsets of full seconds are expected with a drift over the survey day. To correct for the offset the difference of the time in the seismic header and the real time, recorded in the navigation data needs to be established and the time from the seismic header changed accordingly before merging the seismic and navigation data as described in section 6.4.5.

To establish the time differences the effect of correcting the time recorded with the seismic data before merging with the navigation data is simulated using a Matlab code shown in Appendix F. Since the time shifts between the seismic and real time are full seconds the simulation is implemented by shifting the seafloor pick TWT values stored as a vector, while not altering the vectors containing the x- and y- components of the positions associated with the seafloor TWTs. Beforehand it is assured that there are no datagaps present, such that there is a position and TWT value for every exact second. A shift of one element forward equals an addition of 1 s to the seismic time, a shift of one vector element backwards equals a subtraction of Is of the seismic data. The algorithm allows the simulation of a linear drift throughout the survey day. For a linear increase of the difference $t_{seis} - t_{nav}$ vector elements are subtracted at evenly spaced positions, for a linear decrease of the difference $t_{seis} - t_{nm}$ vector elements are added at evenly spaced positions (Figure 6.16). The spacing of the position at which elements are added or subtracted is calculated as the ratio between total length of the days in seconds and the time difference of seismic and navigation time at the beginning and end of the period. In case of an offset at the start of the day a constant shift in the appropriate direction is performed to simulate its correction.

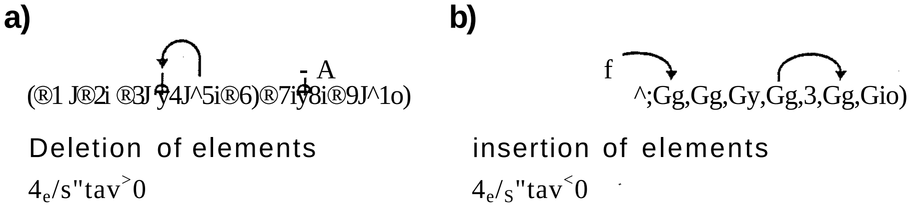

Figure 6.16 Simulation of time-shift between seismic and navigation data by shifting elements in the vector storing the seafloor picks. The vectors storing the x- and y-components of the positions associated with the picks remain unchanged, a) Deletion of elements simulates the case that the time in the seismic data is ahead with respect to the time value in the navigation data, b) Insertion of elements for the case that the navigation time is ahead of the seismic time.

The simulation was carried out for a range of parameters for each survey day and the best fit result was chosen as the displayed seafloor picks showing the smallest of TWT offsets for adjacent lines. The best fit result for survey day 4 is shown in Figure 6.15b. In this case at the start of the survey day seismic and navigation time were equal and at the end of the day the seismic time is five seconds ahead (t_{seis} - t_{nav} =5 s), therefore the correction was simulated by deleting vector elements as shown in Figure 6.16a.

The time offset values leading to the optimum results are used to correct the seismic time before merging with the navigation data. The time shift correction is implemented in the FORTRAN code shown in Appendix D, which performs the joining of the seismic shot information file with the navigation data file. In contrast to the Matlab code simulating the time shift, in the FORTRAN code the appropriate correction times are added or subtracted to or from the seismic times prior to data merging. Figure 6.17 shows the best simulation results for the entire survey (see Figure 6.14a for area).

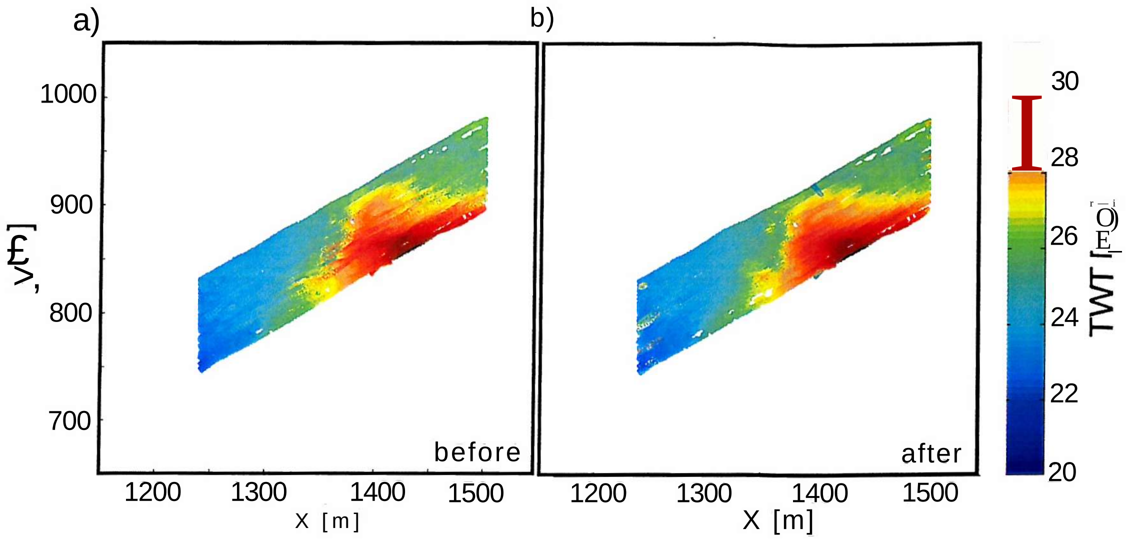

Figure 6.17 Seafloor picks for area highlighted in Figure 6.14a for entire seismic data, a) Before simulated correction for time-shift between seismic and navigation data, b) After simulated time-shift correction.

After establishing the time-shift correction values, listed in Table 6.1 and plotted in Figure 6.18, and applying those before merging of navigation and seismic data all subsequent geometry processing steps are repeated using the corrected data.

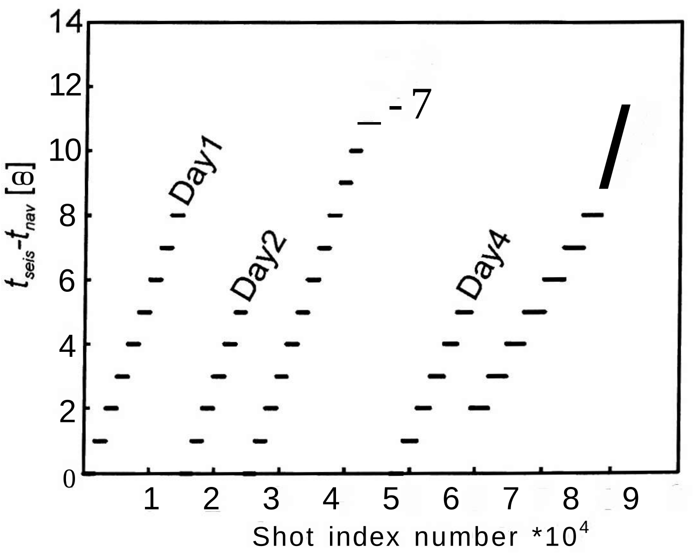

Figure 6.18 Correction values for time-shifts between seismic and navigation data against shot index number. The values are obtained by simulating the effect of the time-shifts on seafloor picks. The correction values are subtracted from the seismic times before merging with the navigation data described in section 6.4.5.

The time differences t_{seis}-t_{nav} are plotted against the shot index number. This value is subtracted from the seismic time before merging with the navigation data.

	tseis'tnav Start [s]	*tseis'tnav* end [*s]	Δt_{seis}-t_{nav} ["s/hourl
Dayl	0	8	**1.80**
Day2	0	5	**1.38**
Day3	0	13	**1.97**
Day4	0	6	**1.78**
Day5	2	9	**1.14**

Table 6.1 Offset between seismic and navigation data time at the start and end of each survey day. The time-shift correction values shown in Figure 6.18 are calculated assuming a linear drift. The linear gradient for the different days lies between 1.14 s/hour and 1.97 s/hour.

The time-shift corrections do not lead to a perfect match of adjacent lines as can be observed in Figure 6.17b. There are still minor offsets between lines indicating static shifts between traces within a CDP. A potential reasons for the residual errors is the assumption of a linear drift during the survey day as it is possible that the drift is non-linear, introducing an error in the time-offsets used for corrections. Furthermore there is an error associated with picking of the seafloor reflections estimated to be as large as 0.2 ms, resulting in errors in the best fit analysis. The algorithm could be improved by allowing non-linear drifts and by applying statistical methods to assess the best fit results rather than estimate it from the seafloor pick plot. However, the time shift between navigation and seismic data will be eliminated in the recording system to be used in future surveys by synchronising seismic and navigation data recording (Chapter 5). Hence it was decided not to develop the algorithm further and to use the values presented for the processing of the dataset.

Table 6.2 lists the errors in depth and TWT measured to the reflector resulting from residual time shifts. The values are calculated as depths differences between the actual position and the position related to the residual time-shift depending on the survey speed and dip of the reflector using equation (6.2). The depth difference *Ad* is given as

$$Ad = Af - v, \wedge tana \qquad (6.2)$$

with *At* the residual time-shift, v_{survey} the survey speed and *a* the apparent reflector dip.

The associated TWT errors were calculated assuming a sound speed of 1518 m/s. Apparent dips of **4.4°,** the average apparent dip of the internal reflector shown in the sample section (Figure 6.9), and **15°,** a typical value of the slope of the sedimentary waves at the seafloor in the section, are examined. Survey speeds of 1.5 m/s and 3 m/s are considered, reflecting the average speed and a typical speed for some lines recorded in direction of a strong tidal current respectively. Residual time-shifts of Is and 2 s are used for the calculations.

Survey speed over ground fm/s]	Apparent reflector **dip[°]**	Residual time-shift [si	Resulting error in depth [ml	Resulting error in **TWTCmsl**
1.5	**4.4**	1	**0.12**	**0.15**
3	4.4	1	**0.23**	**0.30**
1.5	15	1	**0.40**	**0.53**
3	15	1	**0.80**	**1.06**
1.5	4.4	2	**0.23**	**0.30**
3	4.4	2	**0.46**	**0.61**
1.5	15	2	**0.80**	**1.06**
3	15	2	**1.61**	**212**

Table 6.2 Errors in depths and TWT to reflector resulting from residual time-shifts for different survey speeds and apparent reflector dips.

For lines recorded sailing in opposite directions the errors are summed. Thus even for the case of only 1 s residual time shift and a survey speed of **1.5** m/s the depth to an internal reflector between two traces associated with the same position can differ by 24 cm (0.3 ms TWT), which is approximately **5** times larger than the vertical positioning accuracy threshold derived in section 4.2 and approximately 10 times larger than the RTK-GPS positioning error in z-direction determined in section 4.5.1. Thus it has a significant impact on functioning of processing algorithms like migration, in which amplitudes of adjacent traces are summed, affecting the data quality. Refer to Chapter 7 for further analysis.

6.4.7 Pre-stack Kirchhoff migration

Migration moves recorded seismic reflection energy to their true position in the time/space domain. In particular it moves dipping reflectors into their true positions, increasing their dip, and collapses diffraction hyperbolas, thereby delineating subsurface features. Thus it increases spatial resolution, up to the mean wavelength of the source signatures used (Yilmaz, 1987). Some migration techniques use the wave-equation, which describes the propagation of the seismic waves in the sub-surface, to down-ward continue the wavefield recorded at the surface to reconstruct the sub-surface reflectors. It is therefore essential that the wavefield is recorded correctly at the surface and spatial aliasing is avoided. The general effect of spatial aliasing on the data is the same for different migration algorithms. The algorithm used for the 3D Chirp data is based on the Kirchhoff migration. The post-stack zero-offset Kirchhoff algorithm is based on the summation of amplitudes along hyperbolic paths. The summation is assigned to the hyperbola apexes, which are considered as point diffractors generating the diffraction hyperbolas. Imaged reflection interfaces are produced by superposition of diffraction points. The amplitudes are previously corrected for the effects of spherical spreading, the obliquity factor (angular dependency of amplitudes) and phase shifts. The curvature of the hyperbola is governed by the seismic velocity.

See for example Schneider (1978) for formulation of the Kirchhoff algorithm for 2D and 3D data.

In case of 3D migration the summation is performed over the surface of a hyperboloid and assigned to its apex after applying the mentioned corrections. Spatial aliasing of the recorded data would result in the amplitudes not being moved to the apexes but away from the flanks of the hyperboloids thus worsening the spatial resolution (Yilmaz, 1987).

For the pre-stack migration algorithm used here the source receiver offsets are taken into account and the amplitudes are summed along travel time trajectories that depend on velocity structure and acquisition geometry, or travel time surfaces for the 3D case. Common offset sections are imaged separately and subsequently superimposed to the migrated section. Hence the pre-stack algorithm is more computational expensive than the post-stack algorithm.

The practical advantage, and the reason this migration algorithm was chosen over other available algorithms, is that it deals with erratic distribution of reflection mid-points as is the case in the 3D Chirp dataset (section 6.4.5, Figure 6.14). The existing distribution with the low CD? fold makes it difficult to produce a stacked dataset with appropriate bin sizes without large data-gaps. The presence of data-gaps impedes the functioning of the post-stack migration algorithms, which would make it necessary to interpolate data.

The choice of parameters for the migration is governed by the migration time of this computer intensive algorithm. The geometry of the imaged data volume is defined on the basis of the binning grid presented in section 6.4.5. The image grid has the same outline and origin as the binning grid but only every 4th inline and crossline defined by the binning grid is imaged, resulting in a line spacing of 50 cm in either direction. The migrated dataset thus contains 150 inlines and 1500 crossline, equating to a total of 225000 traces. The migration time increases linearly with the number of imaged traces. Tests showed that an image dataset with 50 cm line-spacing is sufficient for the given quality of the dataset, as no better data quality is achieved by decreasing the line-spacing further.

A constant migration velocity of 1518 m/s is used as it is not possible to extract a velocity model from the 3D data set since a velocity analysis is not feasible with the offsets smaller than 2 m. It is expected that the lack of velocity information leads to errors in the location of events but equally should not adversely affect the image quality.

The migration aperture, the radius of a circle centred at the imaging trace defining the area **from which traces are considered for the migration, is the most important factor affecting** performance as the performance is proportional to the number of traces considered for the migration, which is in turn proportional to the square of the aperture. The smaller the aperture the less capable the migration is of collapsing diffraction hyperboloids and correctly place steeply dipping reflectors (Yilmaz, 1987). Ideally it should be as large as the maximum imaging depth, which for the discussed dataset is approximately 40 m. However, due to limited available migration time an aperture of 4 m was used, after testing of apertures of up to 8 m showed that the migrated data could not be significantly improved.

Additionally the migration flow incorporates an algorithm to avoid spatial and temporal aliasing of the data based on Lumley (1994).

With these parameters the migration time was approximately 14 days on a Linux operating system workstation with two 2.66 GHz Intel® Xeon TM processors with 2 GB RAM.

6.4.8 Instantaneous amplitude

In order to increase the interpretability the instantaneous amplitude of the seismic signal is calculated, a processing step routinely used for Chirp data (Quinn et al., 1997c). The instantaneous amplitude is the envelope *Aft)* of the analytical seismic signal *a(t)* given as

cr(f) = x(f) + if(f) = [illegible] $^{i\phi(t)}$, **(6.3)**

where $\hat{x}${t) is the Hilbert transform of the seismic signal *x(t)*, *(j)(t)* is the instantaneous phase of the signal and *i* is the imaginary unit. The Hilbert transform is calculated by performing the convolution

$$\hat{x}(t) = x(t) * \frac{1}{n \bullet t} \qquad (6.4)$$

In the process of calculating the instantaneous amplitude the frequency content of the signal is lowered and polarity information is lost. The instantaneous amplitude measures the reflection strength at a given time value (Taner, 1978). Figure 6.19 shows the 2D sample section obtained by applying instantaneous amplitude calculation to the correlated section shown in Figure 6.9. No 3D pre-stack migration has been applied to the section, the figure is only intended to demonstrate the effect of the instantaneous amplitude calculation on correlated data.

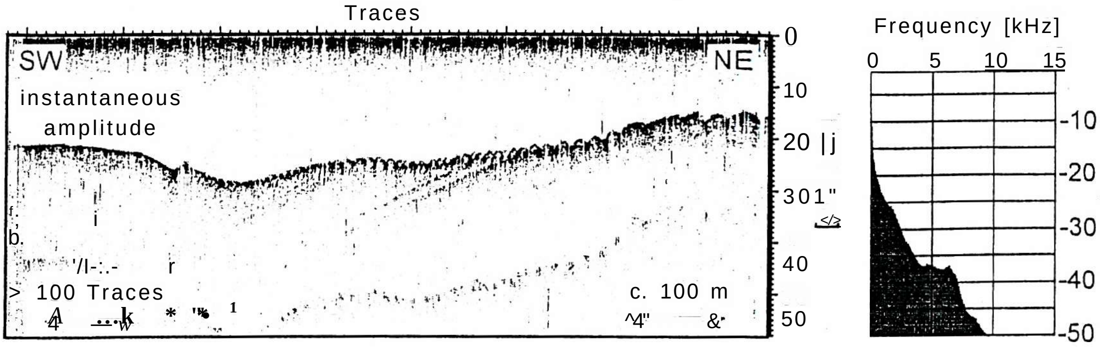

Figure 6.19 Seismic data of single channel 2D seismic line (Figure 6.7a) after calculation of instantaneous amplitude together with power spectrum. Note that no 3D pre-stack migration has been applied to this section.

The bandwidth of the correlated section data (Figure 6.9) is'lowered from 1.5-13 kHz at -40 dB points to 0 - 7 kHz for instantaneous amplitude signal as can be observed in the power spectrum in Figure 6.19. The interpretability of the seismic section is significantly improved in comparison to the correlated section with additional details in the seafloor reflection visible. In particular in the region of the outcrop of the dipping reflector in the centre of the section structural details are revealed. The bow-tie patterns associated with the structural depressions on the seafloor are also better imaged after calculating instantaneous amplitude.

6.4.9 Automatic gain control

Automatic gain control (AGC) is applied to further increase the interpretability of the section, in particular to bring out weaker reflections. The true amplitudes are not preserved and depending on the parameters strong and weak reflections can no longer be distinguished.

The gain for each trace sample is calculated by using a moving window of a certain length, whose mean value is calculated and used to scale to amplitude of its centre sample. A window length of 5 ms was found to yield the best results. Figure 6.20 shows the section obtained by applying AGC to the instantaneous amplitude section shown in Figure 6.19. Note that this section is a sample 2D section and no 3D pre-stack migration has been applied.

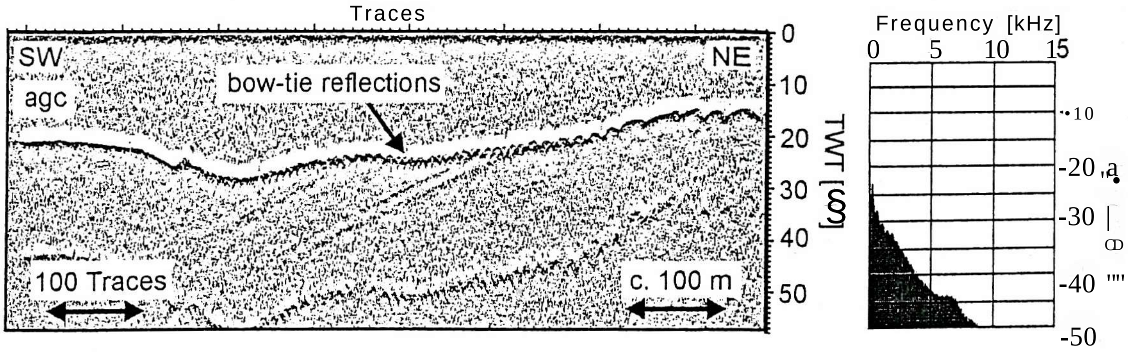

Figure 6.20 Seismic section of single channel 2D line (Figure 6.7a) together with power spectrum. The section shows the instantaneous amplitude section of Figure 6.19 after application of automatic gain control (AGC) with a window length of 5 ms. Note that no 3D pre-stack migration has been applied to this section.

The bandwidth visible in the power spectrum was decreased further by applying AGC compared to the bandwidth of the instantaneous amplitude section (Figure 6.19) with the -40 dB value ranging from 0 - 4 kHz. However, the interpretability was increased, particularly in the vicinity of the seafloor reflector where more details are revealed compared to the instantaneous amplitude section. Bow-tie structures associated with structural depressions appear clearer and the apparent vertical resolution of the seafloor reflector has increased in particular in the north-eastern part of the section. All dipping reflectors can be traced to a greater depth, as weaker events are enhanced.

6.4.10 Data output

The 3D data volume is exported in SEG-Y format with all the relevant information in the trace headers. The file contains 225000 traces with a trace length of 58 ms and sampling interval of 31.25 ps and is 1.7 GB in size. The CDP positions and associated inline and crossline numbers are essential for importing the data into the visualisation and interpretation software.

6.5 Conclusions

In this Chapter the acquisition and processing of 3D high resolution seismic dataset was presented. Both the seismic and navigation systems worked reliably during the data acquisition. However, due to radio interferences the survey area was not fully covered with RTK-GPS position data over the first four survey days. After changing the UHF communication frequency between reference and roving station full data coverage was achieved. A few unfeasibly large height values in the RTK-GPS dataset marked by the system to have RTK-GPS accuracy suggest that the system does not always provide reliable information.

The seismic recording system used was capable of 1 Hz shot-rate, which is lower than the envisaged shot-rate of approximately 4 Hz, required to provide a constant data coverage in inline direction with the given survey speed of approximately 4 knots (= 2.06 m/s).

The collected seismic data show a power spectrum different from the data recorded with the standard 2D system. Within the bandwidth of the source sweep troughs of up to -17dB are present, whose origin could not be determined from the dataset. Future work is necessary to investigate the reason for the troughs and improve the quality of the data recorded in future surveys.

A shift between the time recorded with the seismic and the navigation data needed to be corrected before merging the dataset. A simulation of the effects of the corrections of time shifts provides the correction values. The algorithm used for the simulation is based on linear drift of the time difference during the individual survey days.

The seismic and navigation data are merged using specialised algorithms presented. Residual mismatch between the time values are expected to result in incorrect positioning of the seismic traces producing of smearing of seismic reflectors in the data volume. The data gaps of RTK quality position data due to bad radio coverage, the low shot-rate and wide line-spacing resulted in low seismic data coverage with an average CDP fold of 0.61 for a CDP bin with 12.5 cm bin-size, which reflects the theoretical midpoint spacing.

A 3D pre-stack Kirchhoff migration with a constant migration velocity of 1518 m/s was used to produce a 3D seismic data volume. Instantaneous amplitude calculation and automatic gain control improve the interpretability of the dataset, which is available in SEG-Y format to be used for visualisation and interpretation discussed in the following chapter.

7 Data visualisation and analysis

7.1 Introduction

In this chapter the 3D Chirp data volume is presented and analysed. Inline and crossline sections and time slices are used to illustrate the data cube, which images the seafloor, dominated by a depression and sedimentary waves of variable wavelength and amplitude, while within the sub-seabed volume dipping horizons are imaged. The data quality is assessed by comparing the 3D data volume to 2D sections and furthermore by comparing the data quality to the data coverage expressed by the CDP fold of the data grid. An integrated study of the imaged geological structures shows that the imaged horizons are limestones, shales and marls of the Headon Hill formation of Eocene age situated at the eastern **flank** of the Bouldnor syncline.

7.2 The 3D Chirp data volume

7.2.1 Overview

The 3D Chirp data volume, whose acquisition and processing is described in Chapter 6, is visualised and interpreted using the GeoFrame software (Schlumberger GeoQuest, 1995). The dataset contains 225000 traces, which are ordered in 150 inlines and 1500 crosslines with a length of 58 ms and a sampling interval of 31.25 jo,s. The positions of the lines correspond to the imaging grid described in section 6.5.4, which is shown in Figure 7.1.

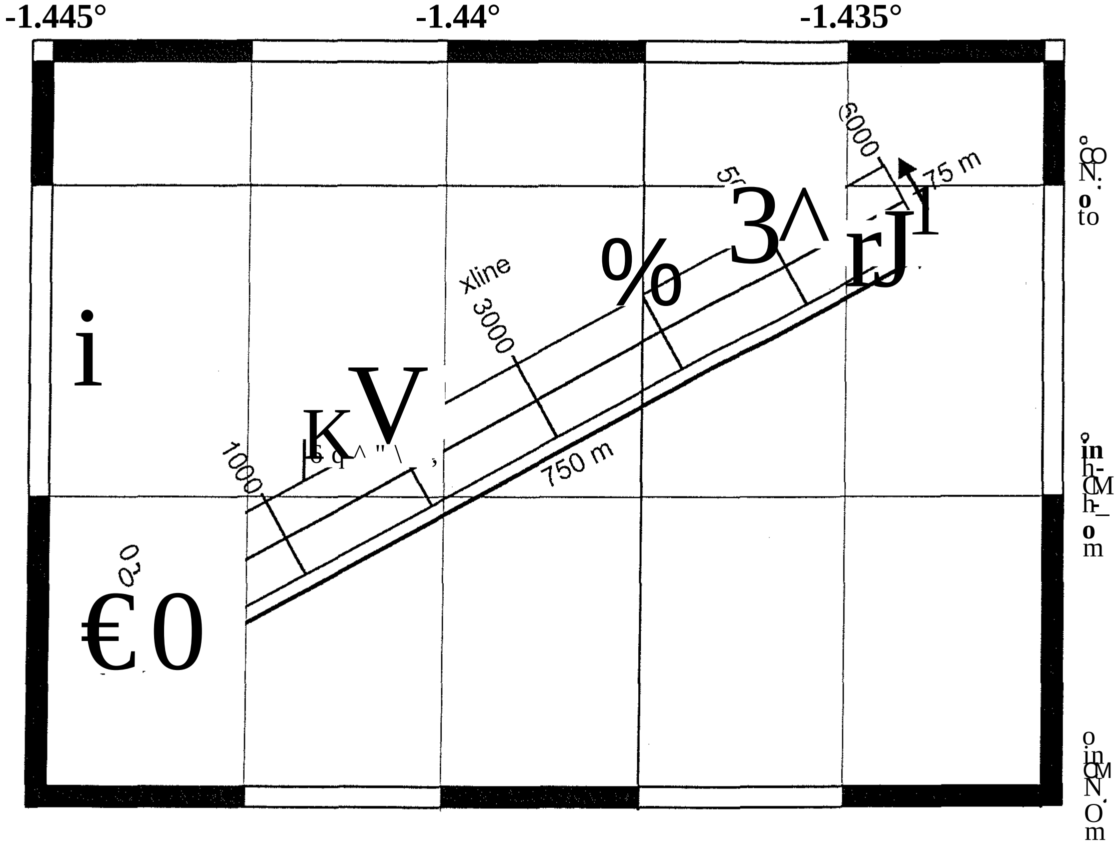

Figure HI Imaging grid of the 3D Chirp dataset. The dataset has 150 inlines (ilines) of 750 m length and 1500 crosslines (xlines) of 75 m length with 50 cm line separation in each direction.

The numbering of the 150 inlines ranges from 1 to 597, in steps of 4, as every 4th inline and crossline are imaged by the migration algorithm described in section 6.4.7. Equally the numbering of the 1500 crosslines ranges from 1 to 5597 in steps of 4. The spacing between every 4th inline and crossline is 50 cm. Thus the data volume extends 75 m in crossline and 750 m in inline direction. Figure 7.2 shows the 3D Chirp data volume with the orientation of the inline-, crossline- and time slice-planes.

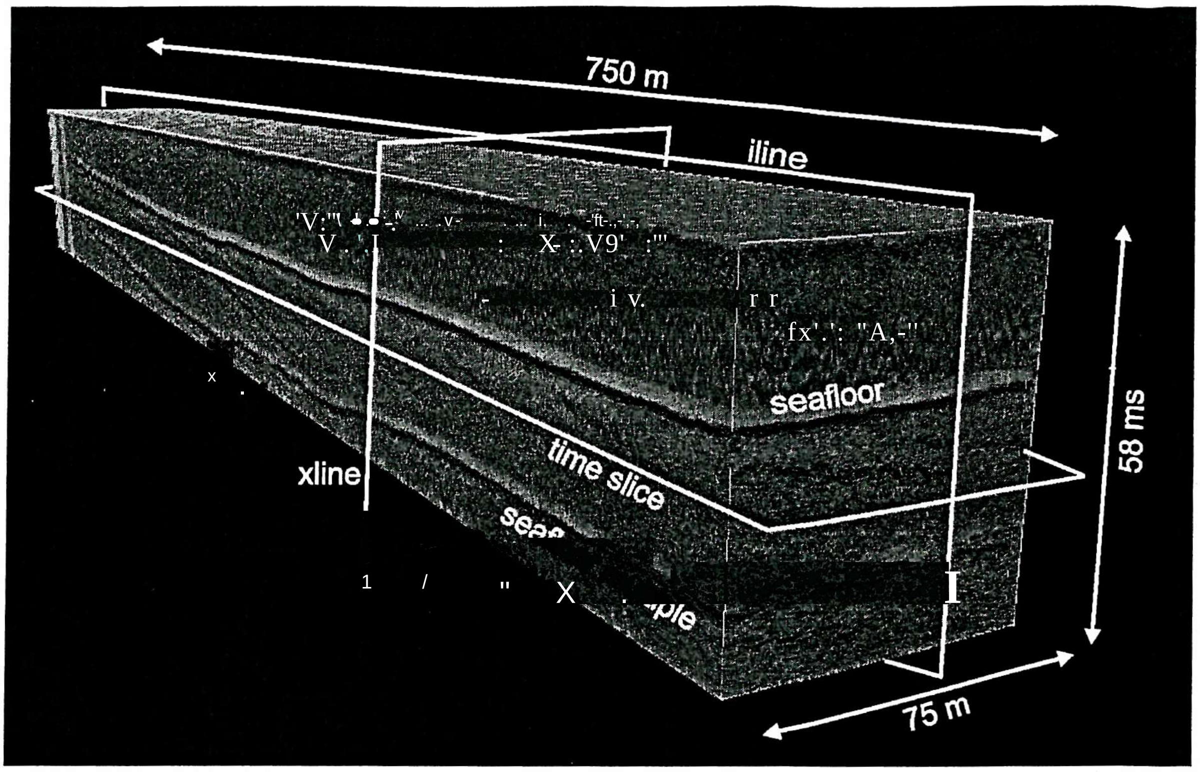

Figure 7.2 3D Chirp volume. Note the orientation of inline (iline) crossline (xline) and time slices in the 750 m x 75 m data cube. The seafloor and its multiple reflection are apparent together with dipping internal reflectors.

Cross sections of the data volume can be displayed in any direction for interpretation. However, to represent the data volume in this chapter, seven inlines with a spacing of 12.5 m (1, 101, 201, ..., 557) are chosen, together with eleven crosslines with a spacing of 75 m (1, 601, 1201, ..., 5997) and 18 time slices with an offset of 2 ms (20, 22, 24, ..., 54 ms). Figure 7.3 shows the position of these sections in the data volume.

The five most prominent internal horizons, distributed over the entire volume, have been interpreted together with the seafloor reflector for analysis presented in section 7.4. The locations of these horizons in the data volume are shown in Figure 7.4.

Inline, crossline and time slice sections are shown in sections 7.2.2, 7.2.3 and 7.2.4 respectively, together with the interpreted horizons. Figure 7.5 shows a close-up of the dataset to illustrate the positions of the interpreted horizons and their representation in inlines, crosslines and time slices. Refer to Chapter 6 for parameters used for processing of the data.

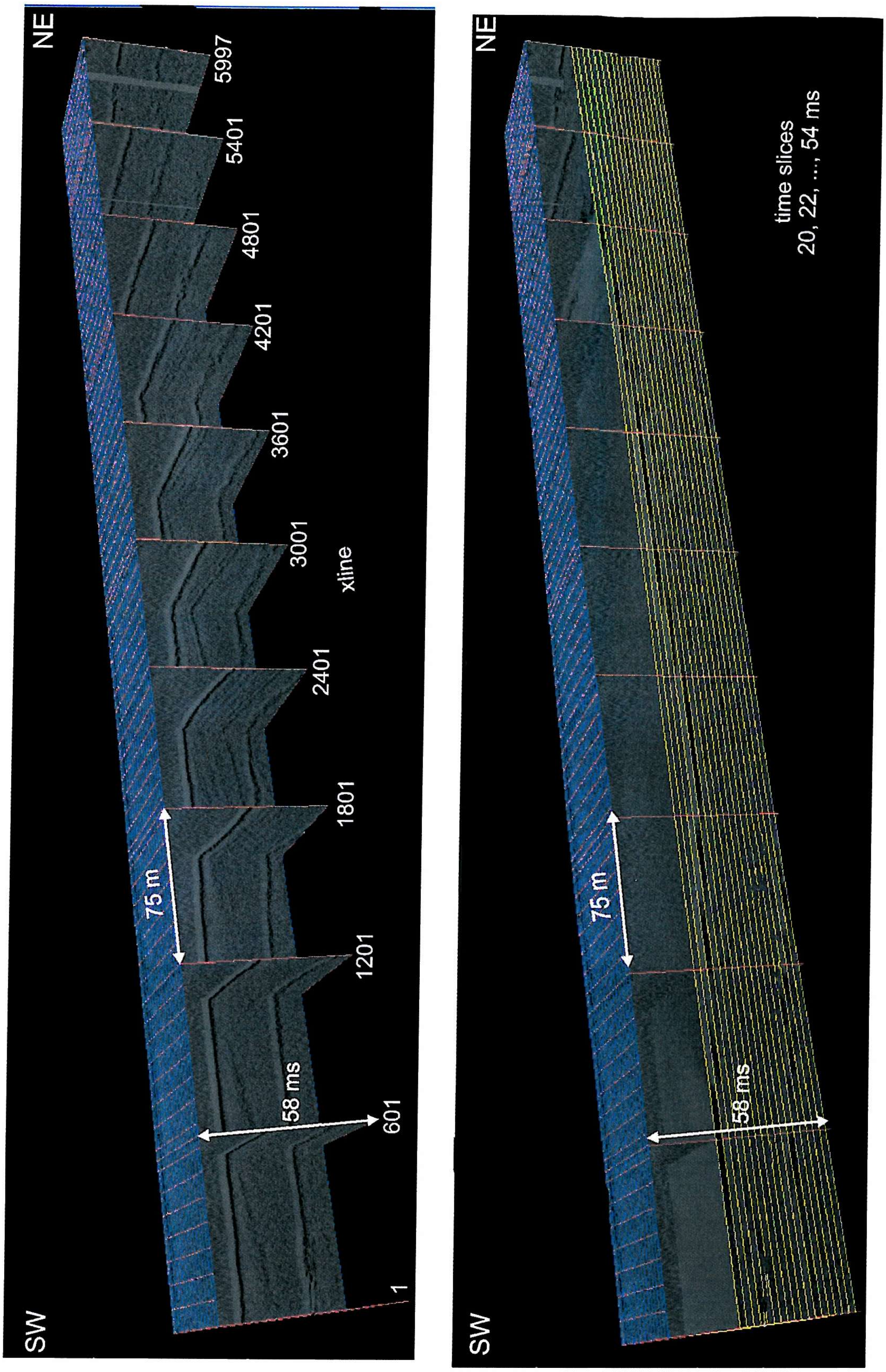

Figure 7.3 Position within the 3D data volume of the eleven crosslines (xlines) with 75 m separation and 18 time-slices with 2 ms separation discussed in sections 7.2.2 and 7.2.3 respectively.

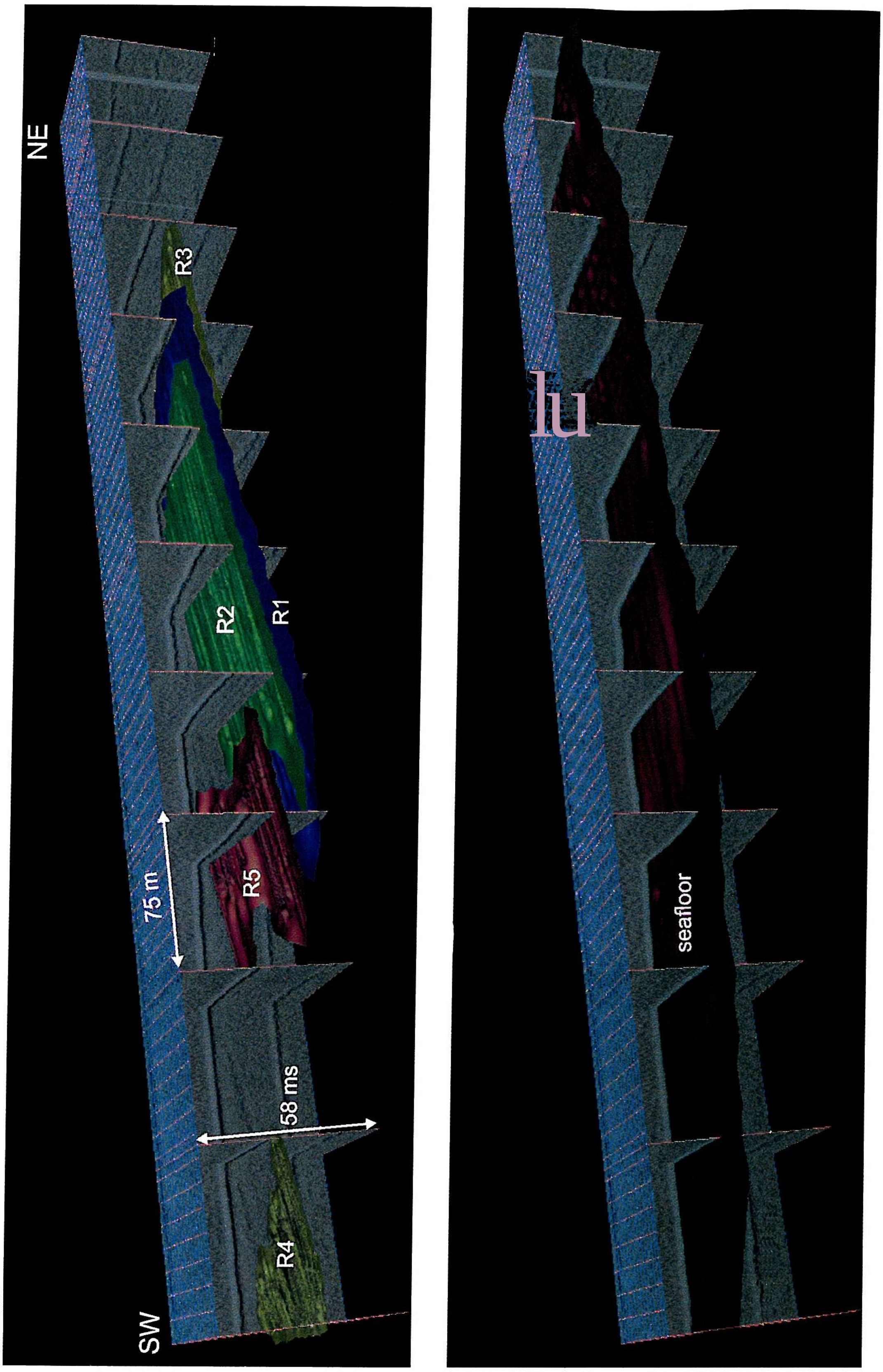

Figure 7.4 Position of five internal reflectors (R1 to R5) and seafloor interpreted. See section 7.3 for analysis and discussion.

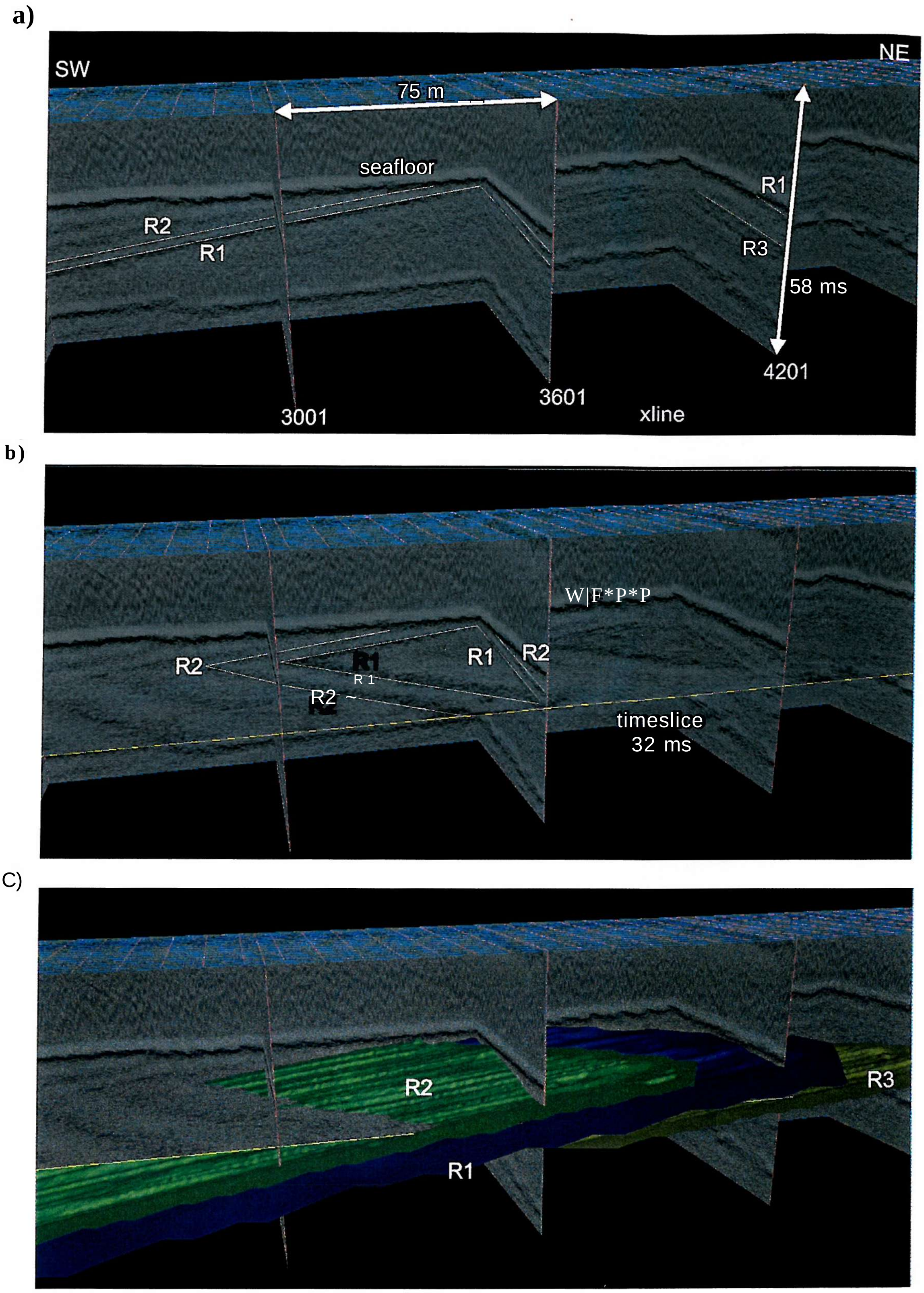

Figure 7.5 Close-up of the 3D Chirp data volume showing a section between crosslines 2401 and 4801 (Figure 7.3). a) Inline 1 together with crosslines 3001, 3601 and 4201. The positions of internal reflectors Rl, R2 and R3 are marked, b) In addition to the sections shown in a) the timeslice at 32 ms is shown together with the positions of the interpreted reflectors, c) Inline, crossline and time slices together with interpreted reflectors.

In the close-up of the dataset the **seafloor** reflector and three internal reflectors, dipping in south-western direction, are apparent. In Figure 7.5a the reflectors R1 and R2 can be easily interpreted in inline and crossline 3601. Additionally reflector R1 and R3 intersect crossline 4201. The time slice at 32 ms TWT in Figure 7.5b shows reflectors R1 and R3. Their intersection lines in the time-slice, inline and crossline form triangles and their intersection lines with the time slice represent their true strike direction. Figure 7.5c shows the interpreted horizons intersecting the inline shown, crosslines and the 32 ms time slice. The linear features apparent in the horizon picks in inline directions are due to the fact that the picking was performed in the inline sections. Constant offsets between the inlines due to picking inaccuracies cause these artefacts. The seafloor shows wave structures, interpreted as sedimentary waves, in the inline section.

7.2.2 Inlines

Figures 7.6 to 7.19 show the representative inlines together with interpretations. Each inline contains 1500 traces with a constant spacing of 50 cm, thus having an overall length of 750 m. See the imaging grid in Figure 7.1 for their position. The data gaps are due to a limited aperture radius of the pre-stack Kirchhoff migration algorithm of 4 m described in section 6.4.7. If the circular area centred at the migration grid point with a radius equal to the migration aperture does not contain any data traces the image trace is empty. This occurs in particular for inlines and crosslines close to the borders of the imaging grid. See the time-slices in Figures 7.22 to 7.27 for the extent of data gaps. Inlines are shown with and without the position of the interpreted horizons R1-R5 and annotations on consecutive pages for easy comparison. The vertical exaggeration of the sections is approximately 7.

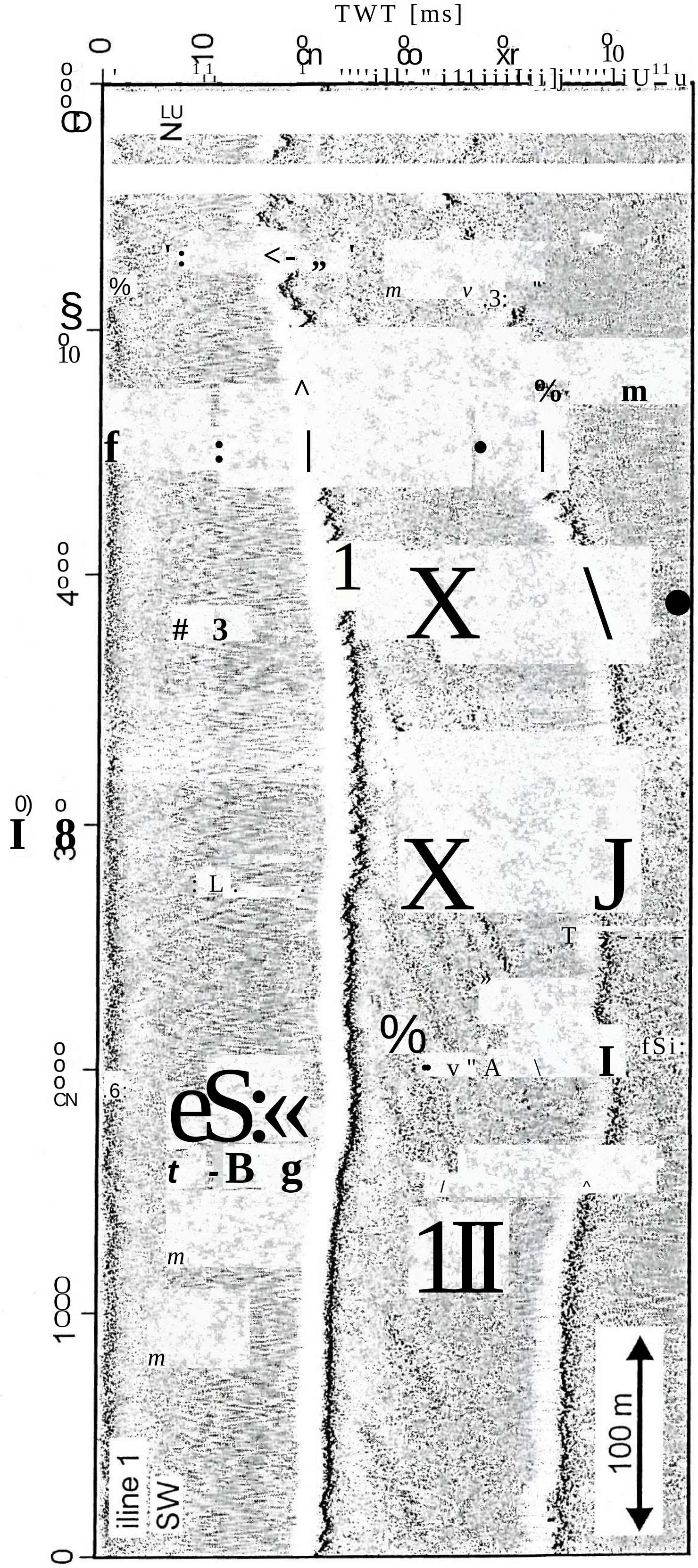

Figure 7.6 Inline 1.

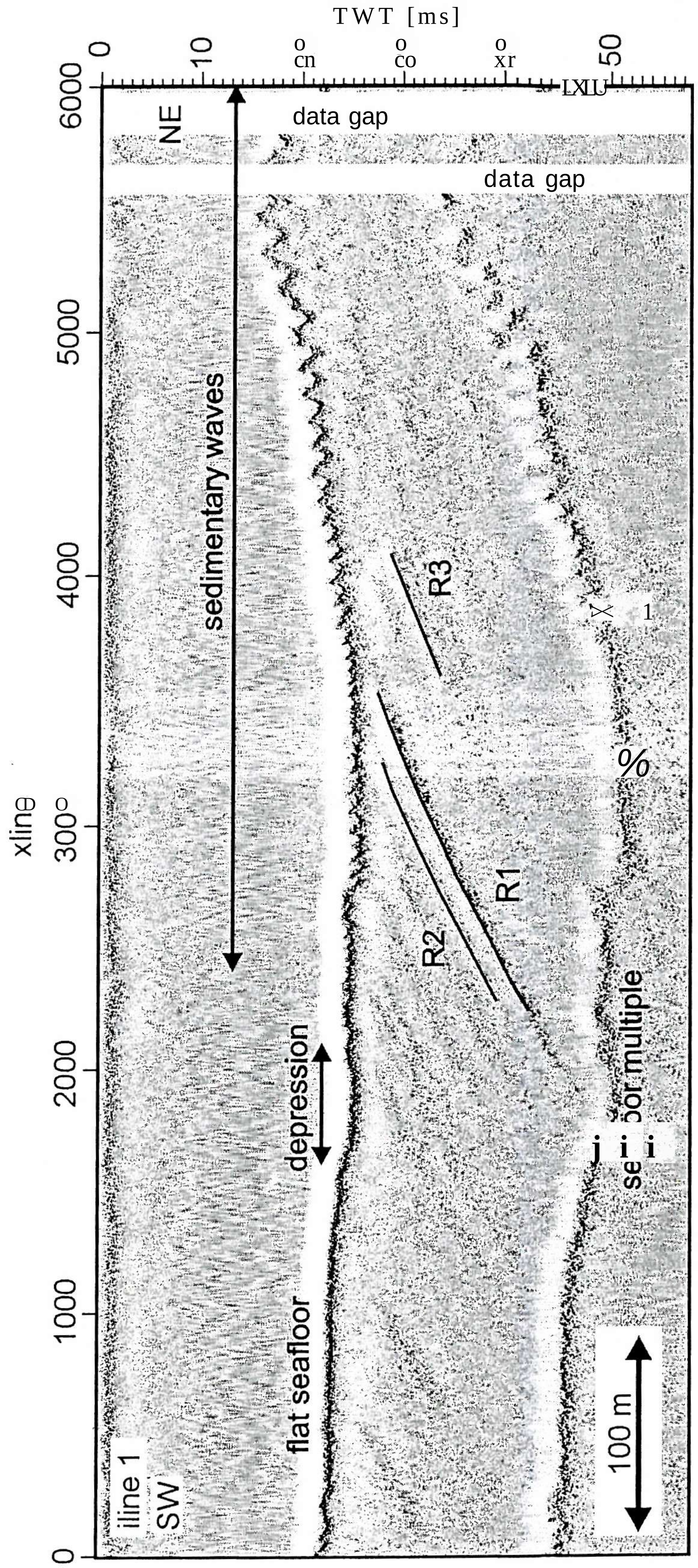

Figure 7.7 Inline 1 with interpretation. The interpreted internal reflectors R1, R2 and R3 are marked.

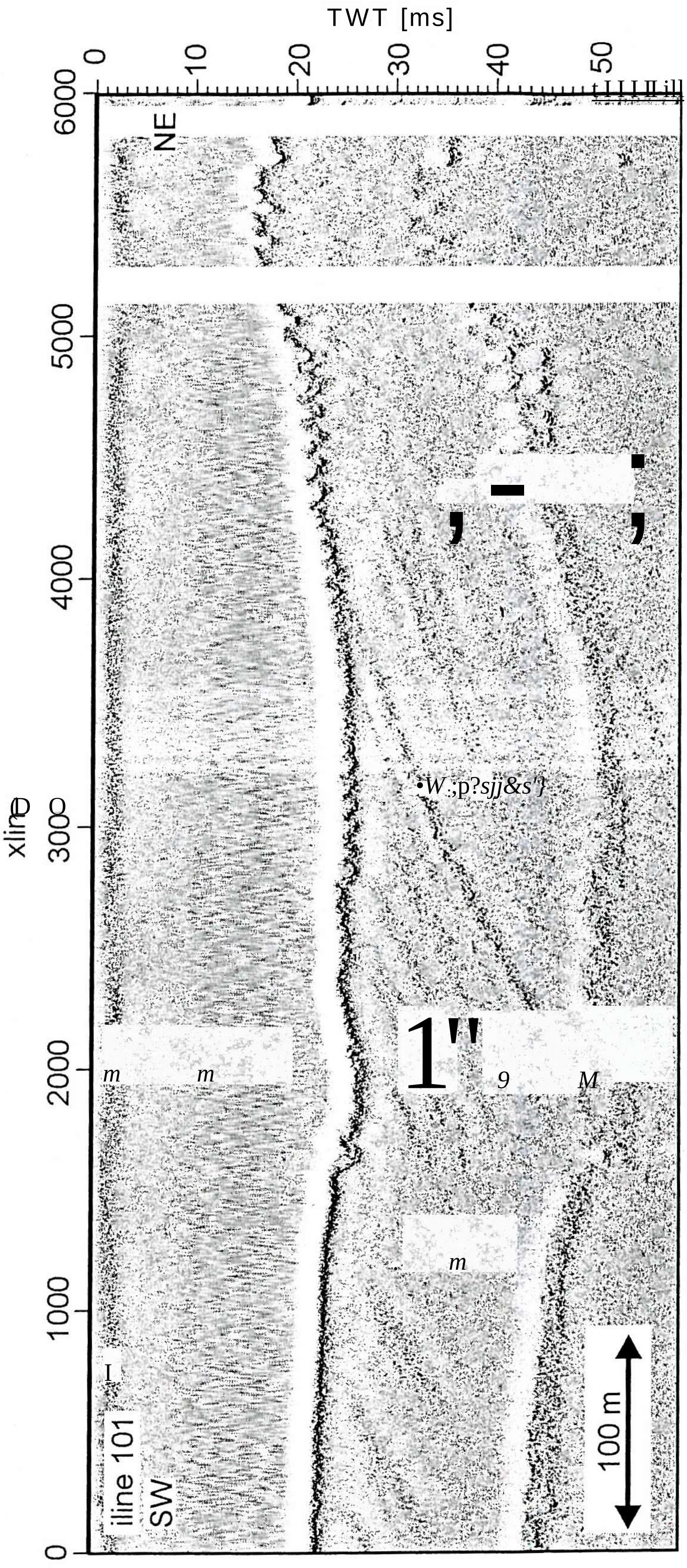

Figure 7.8 Inline 101.

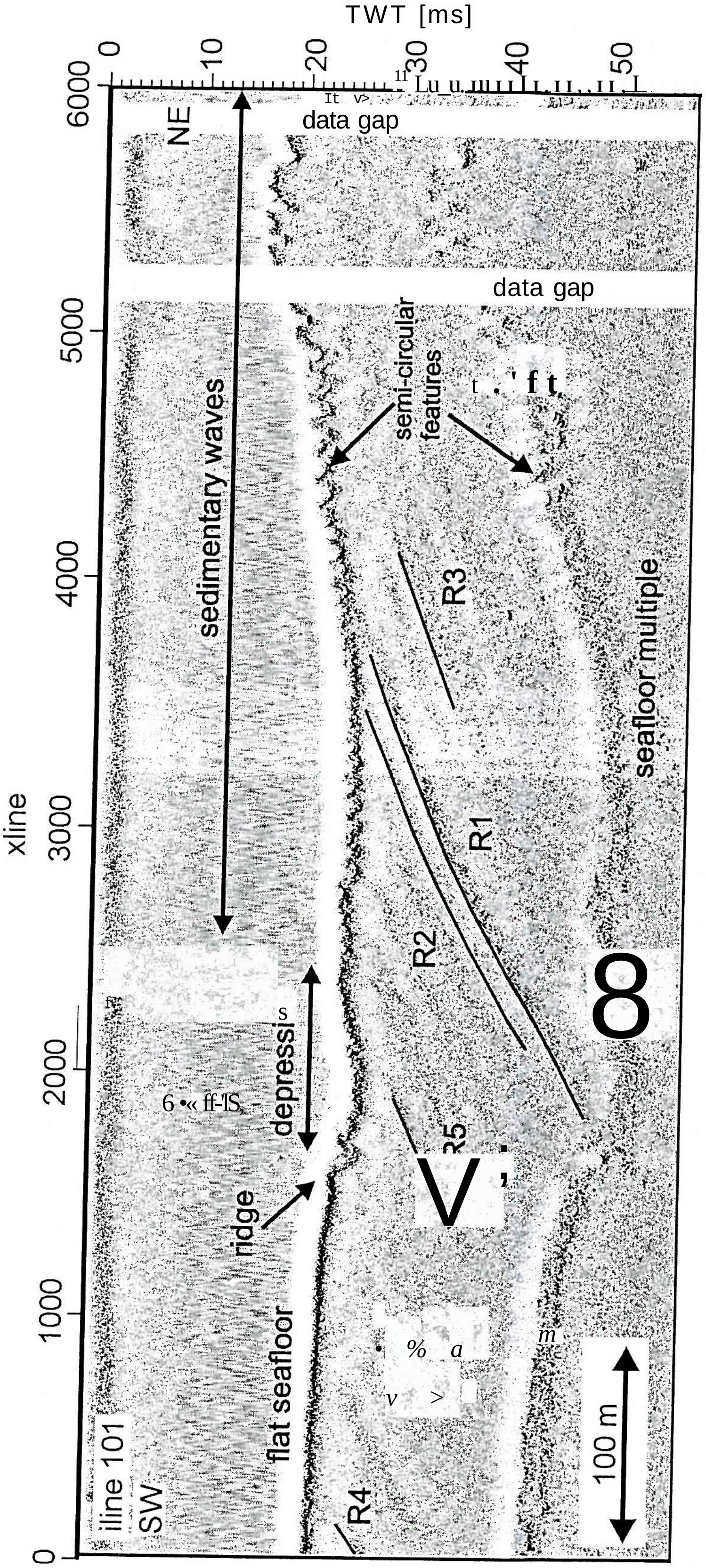

Figure 7.9 Inline 101 with interpretations. The interpreted internal reflectors R1 to R5 are marked.

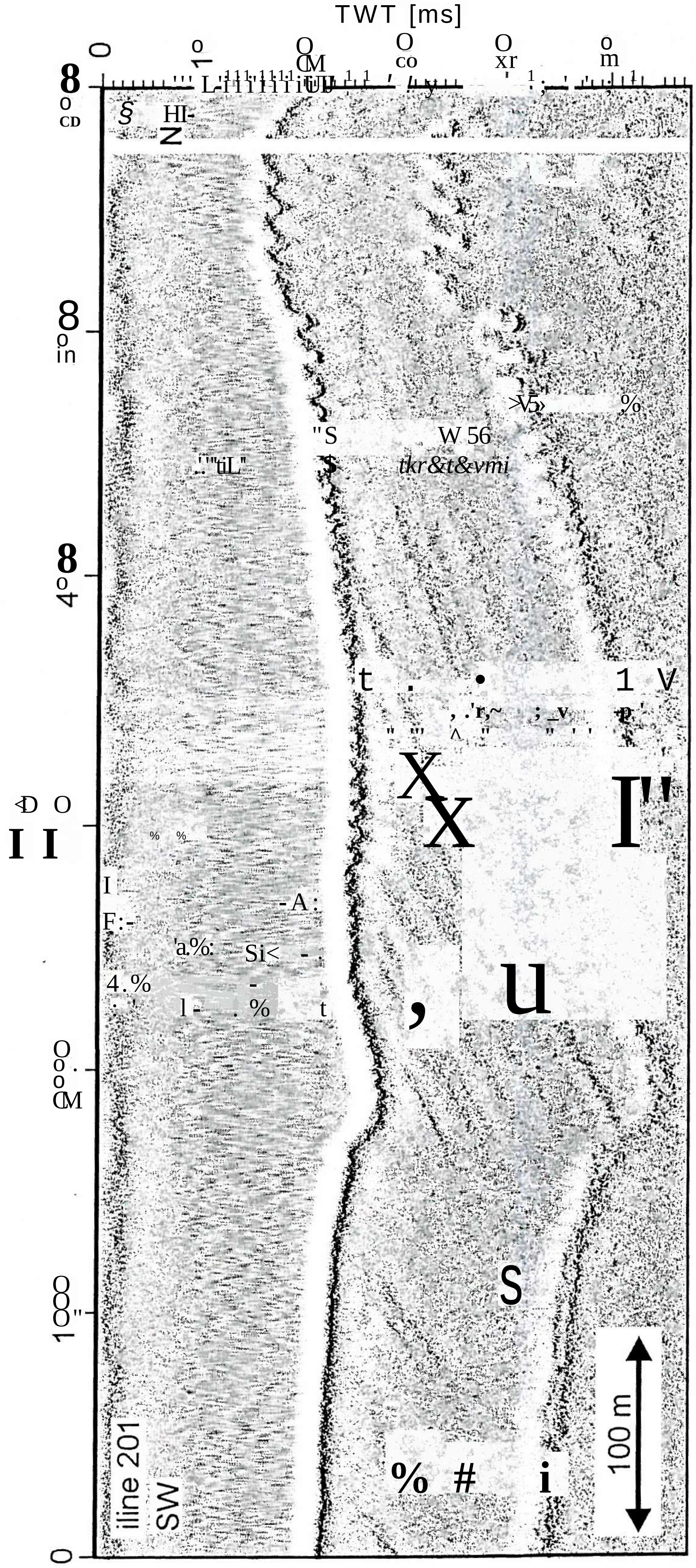

Figure 7.10 Inline 201.

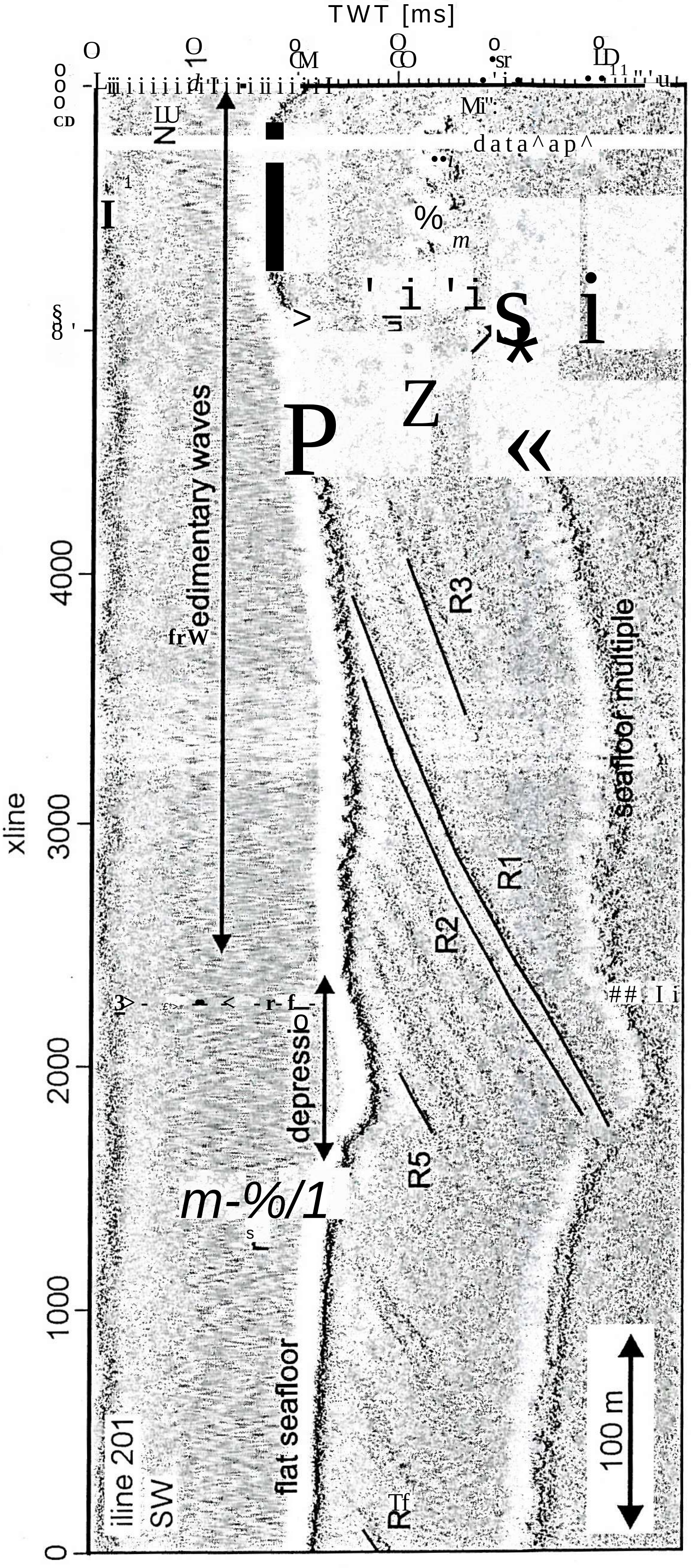

Figure 7.11 Inline 201 with interpretations. The interpreted internal reflectors R1 to R5 are marked.

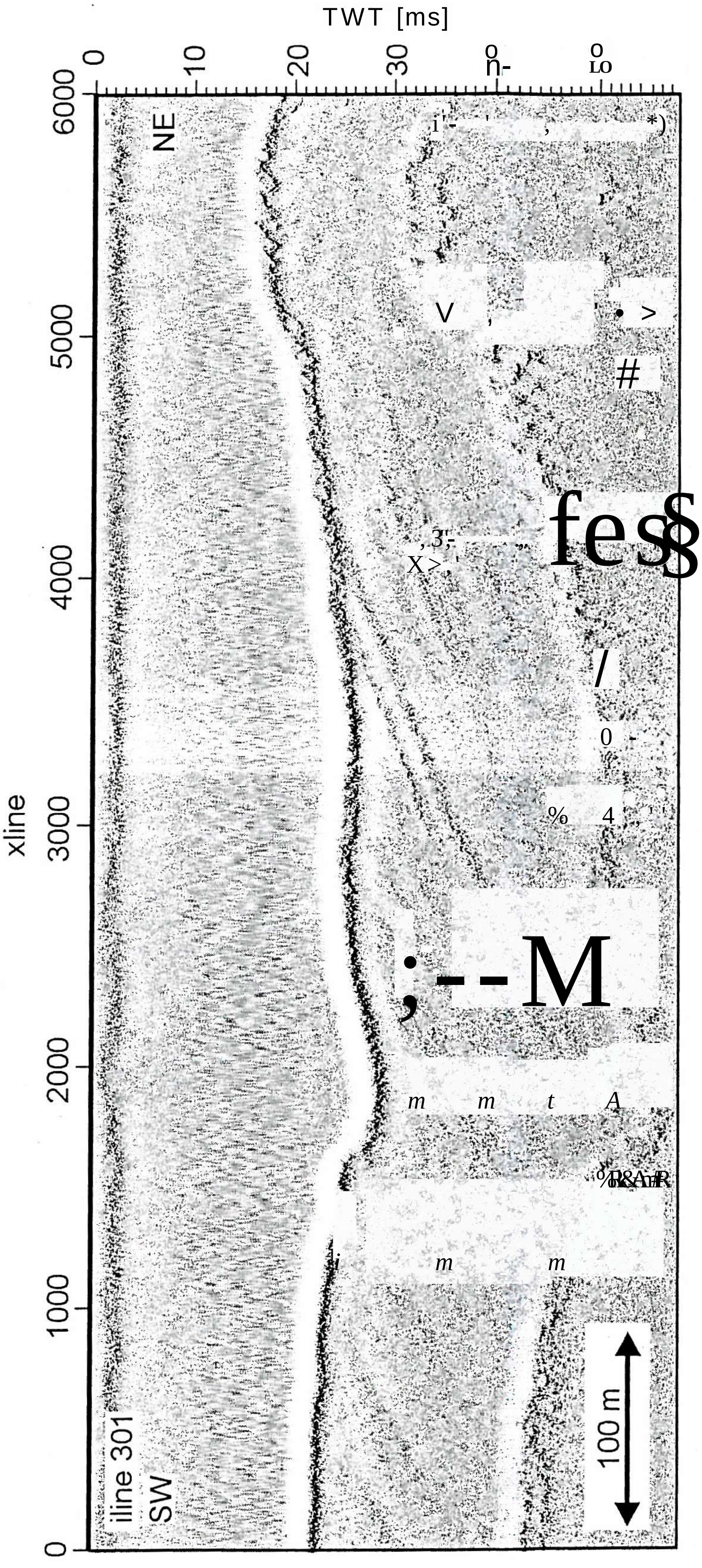

Figure 7.12 Inline 301.

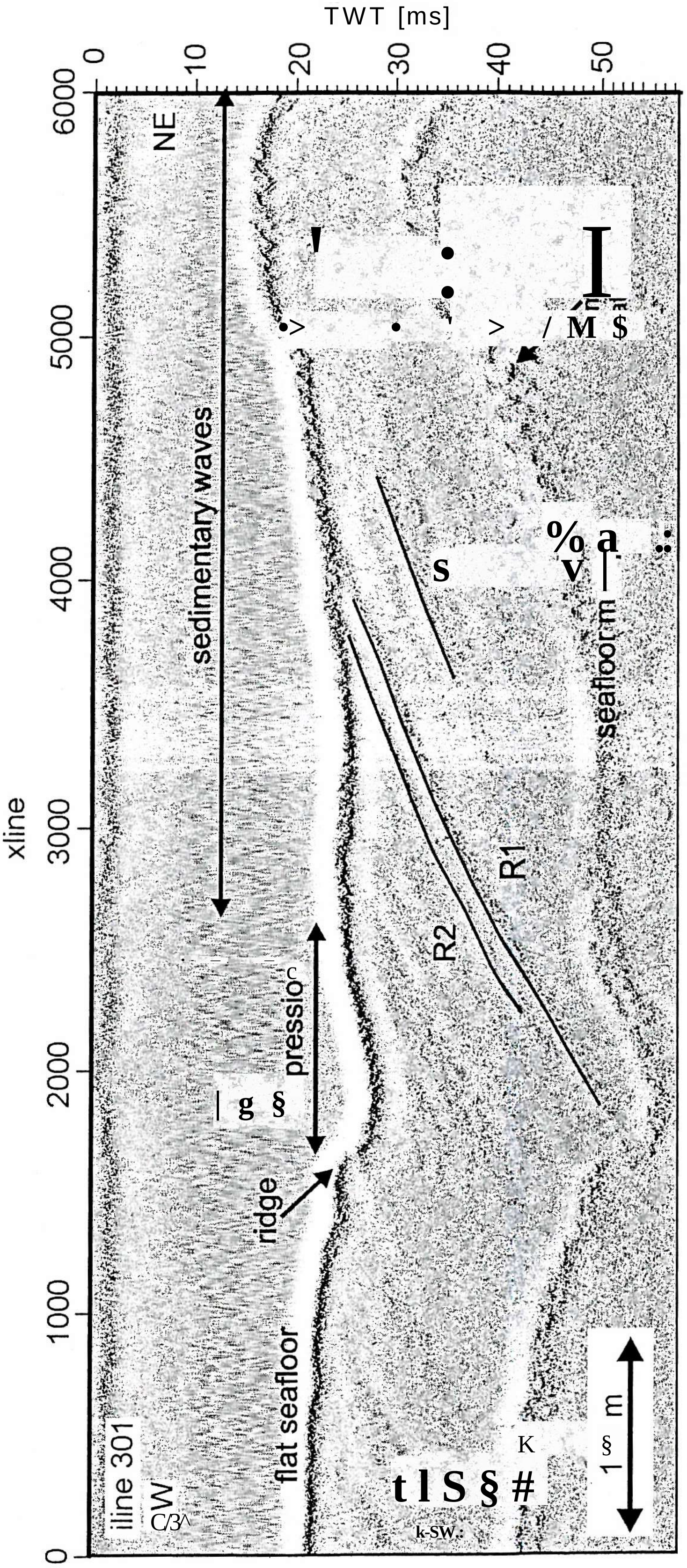

Figure 7.13 Inline 301 with interpretations. The interpreted internal reflectors R1 to R5 are marked.

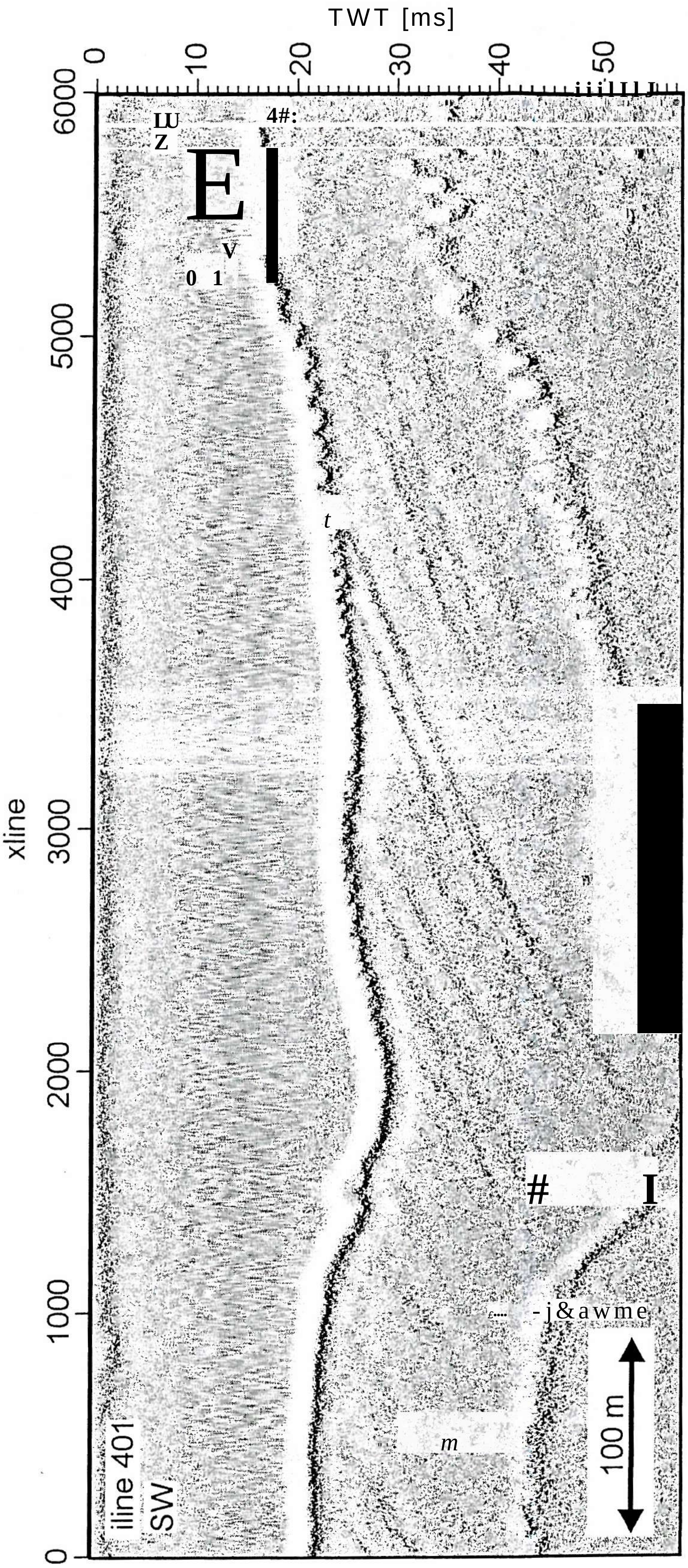

Figure 7.14 Inline 401.

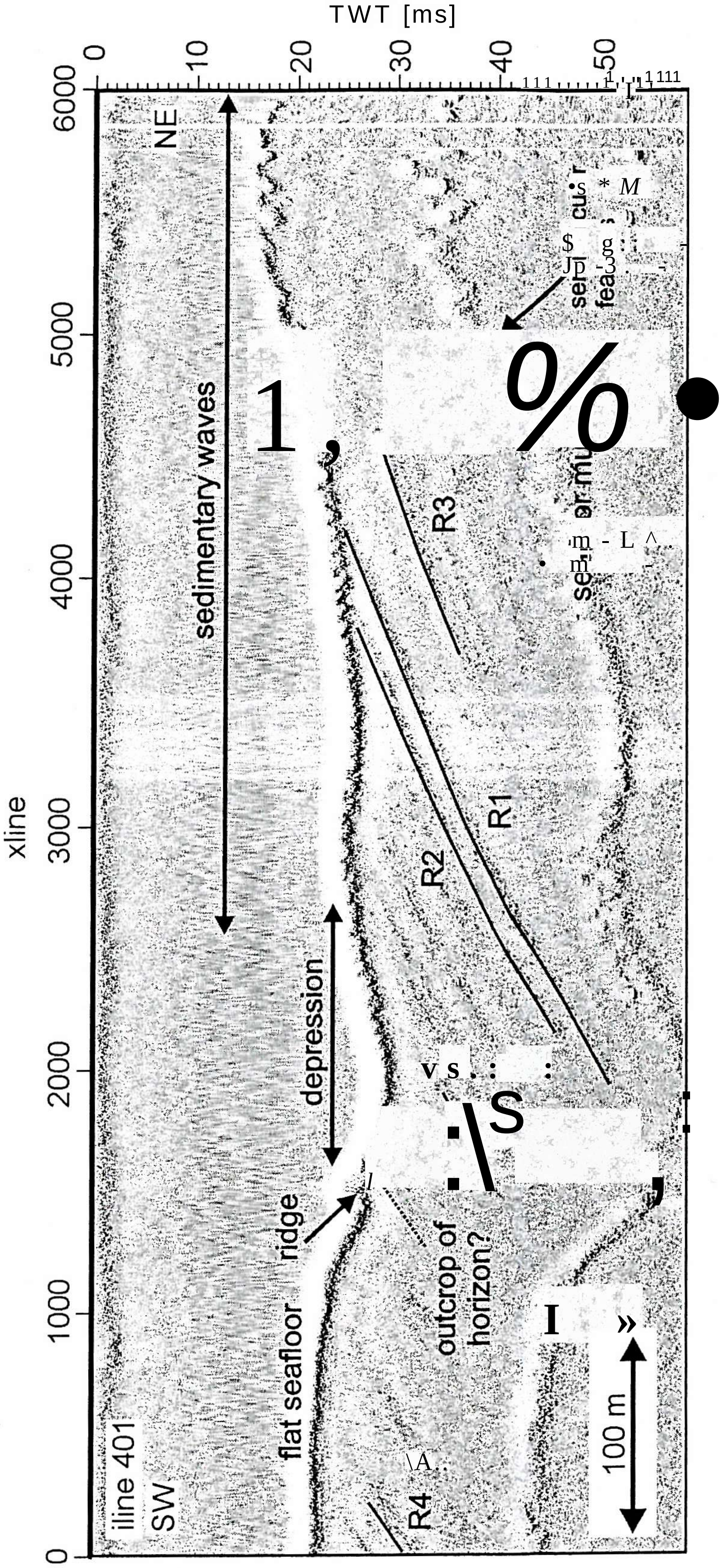

Figure 7.15 Inline 401 with interpretations. The interpreted internal reflectors R1 to R5 are marked together with the possible outcrop of the horizon at the ridge.

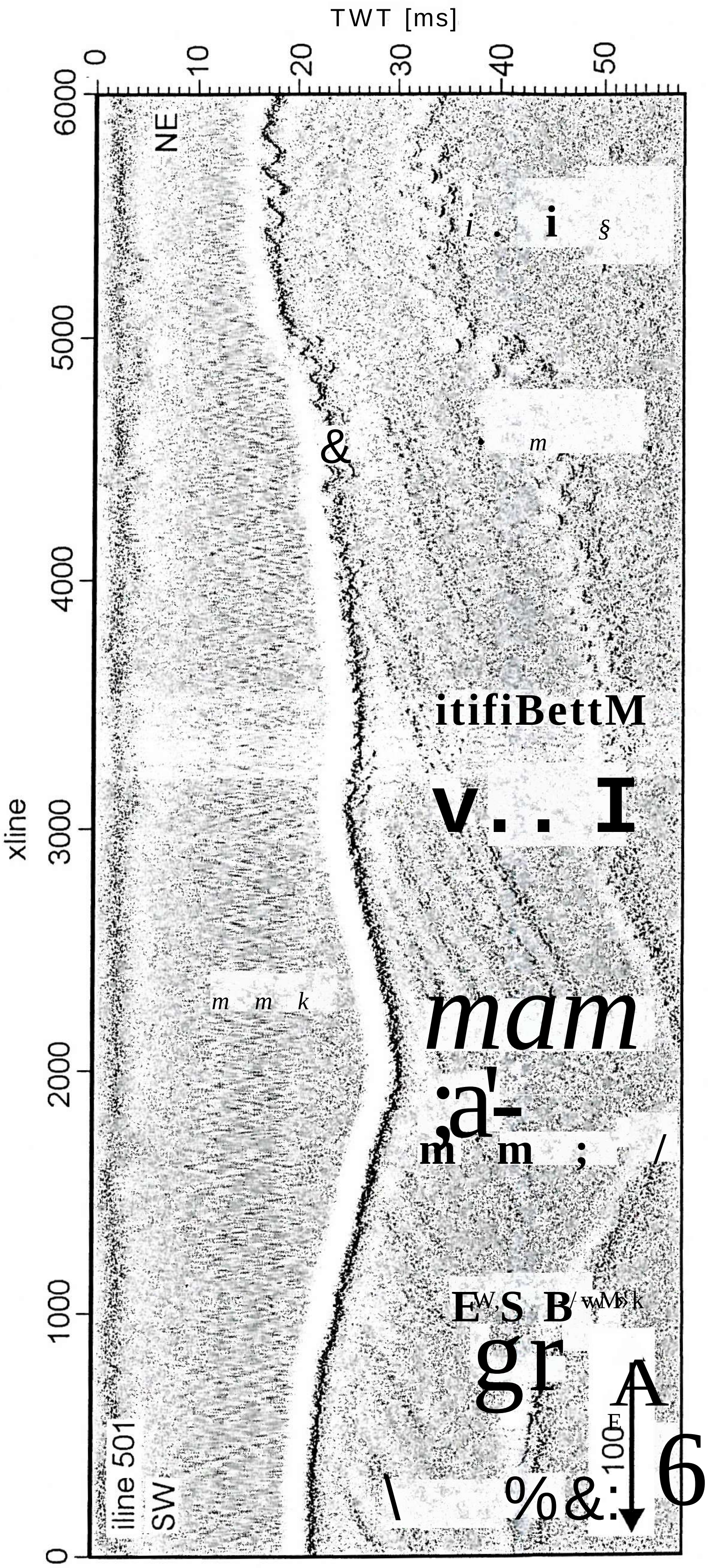

Figure 7.16 Inline 501.

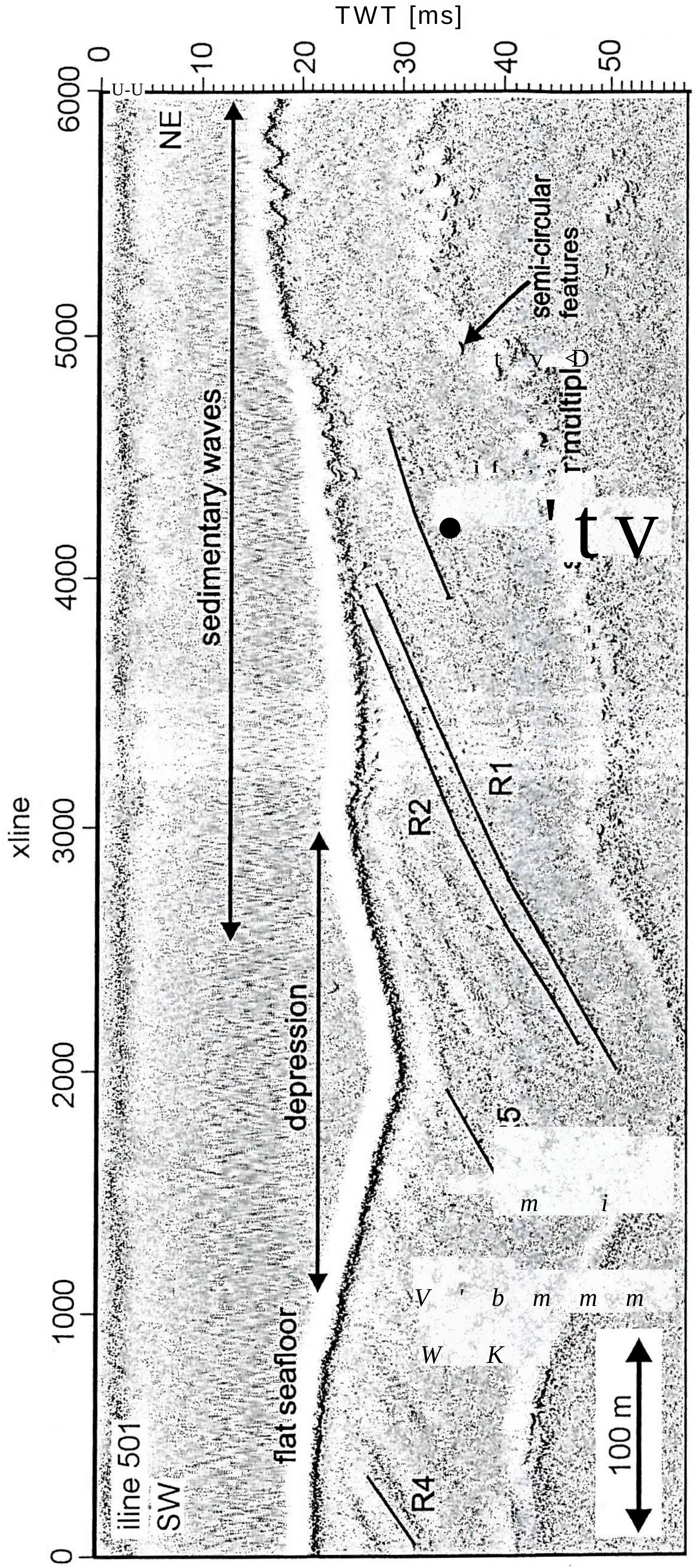

Figure 7.17 Inline 501 with interpretations. The interpreted internal reflectors R1 to R5 are marked.

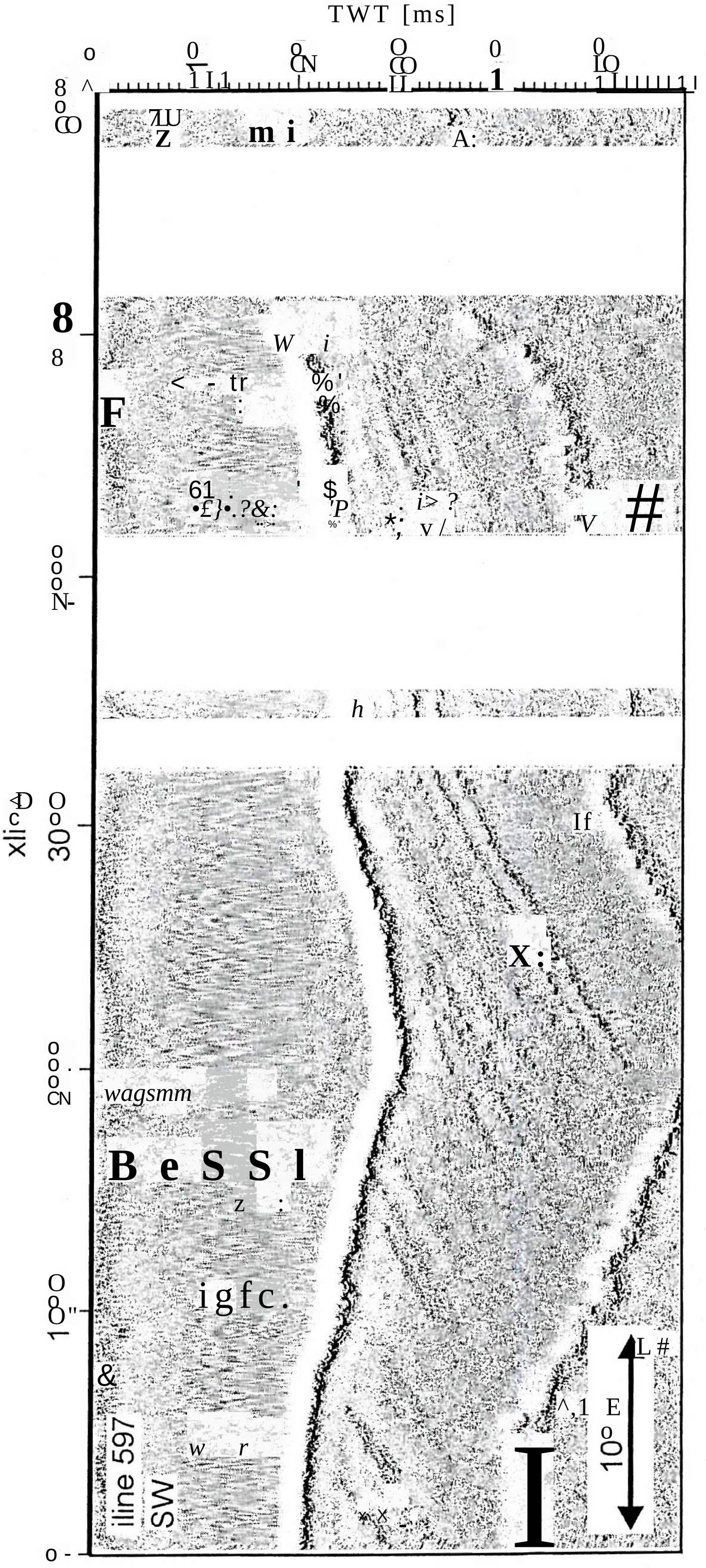

Figure 7.18 Inline 597.

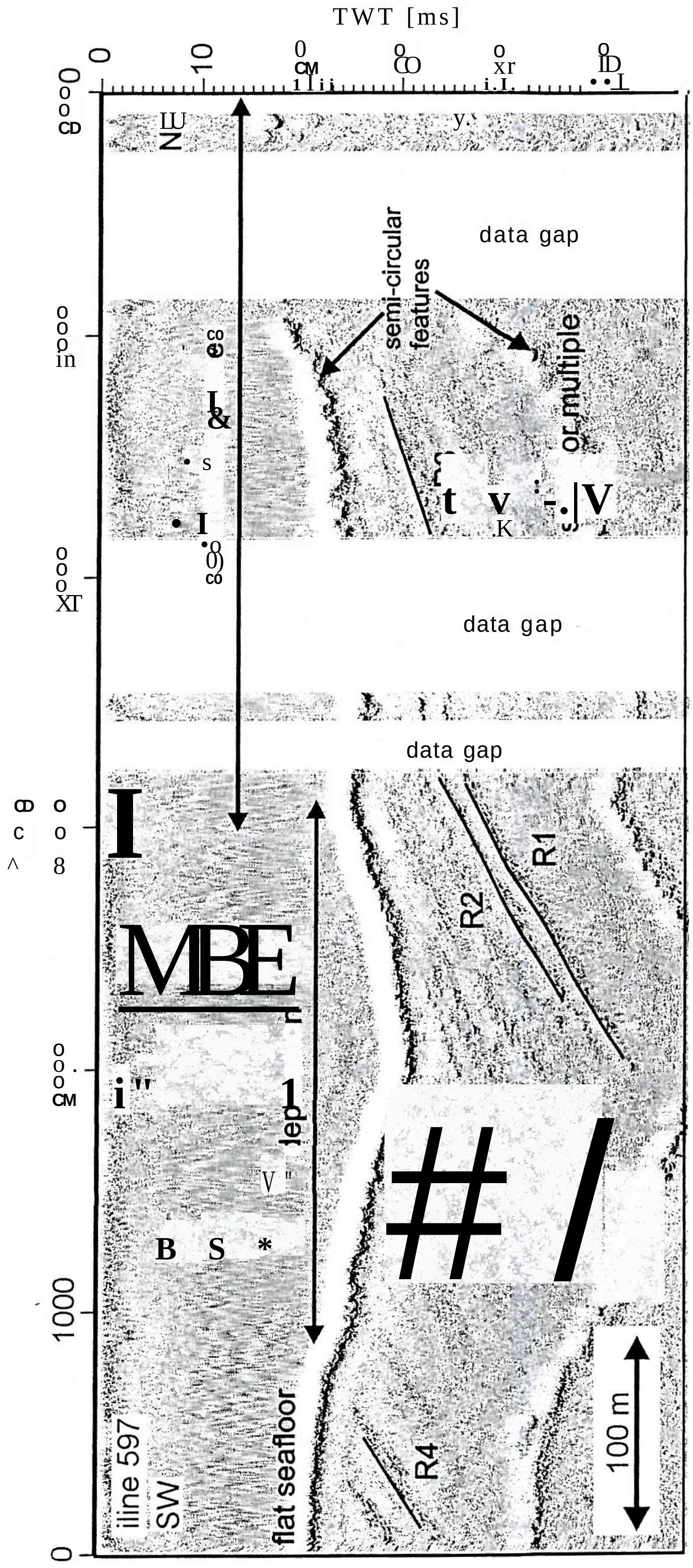

Figure 7.19 Inline 597 with interpretations. The interpreted internal reflectors R1 to R5 are marked. The large data gaps are due to low data coverage of the inline situated at the periphery of the 3D data volume.

The seafloor appears between 15 ms and 32 ms TWT in the inline sections. It is characterised as a flat horizon in the south-western part, followed to the north-east by a depression with increasing width and depth from inline 1 to inline 597. Its width ranges from approximately 60 m between crosslines 1600 and 2100 in inline 1 to 300 m between crosslines 800 to 3200 in inline 597. Its TWT ranges **from** approximately 1 ms (76 cm) for inline 1 to approximately 6 ms (4.6 m) for inline 597. In inlines 101 to 401 a ridge is present on the south-western flank of the depression, centred at crossline 1600 with an approximate width of 25 m. The north western part of the seafloor is dominated by sedimentary waves starting in the depression and reaching to the end of each section. The sedimentary waves increase in height and apparent wavelength from south-west to north-east starting with peak to trough heights of some decimeters (< 1 ms) with wavelength of approximately 2 m to heights of 2.3 m (3 ms) with wavelength of approximately 20 m.

The seafloor multiple is present at approximately twice the TWT of the seafloor. The data contributing to the image was collected over a period of five days with changing water depth due to tides (section 6.3.4) and therefore different TWT for the seafloor multiple. The multiple is hence not clearly defined as in a 2D seismic line, but smeared over a TWT range corresponding to the tidal differences over the period in which the data were collected. In the presented dataset the seafloor multiple is smeared, varying between the inlines, over approximately 4 ms TWT, which corresponds to the difference in tides of approximately 2 m, keeping in mind that the migration algorithm produces additional smearing of incoherently positioned amplitudes.

Up to 14 individual horizons can be identified depending on data quality varying between inlines, with inline 201 revealing the most horizons. The horizons have an apparent dip in south-western direction, which slightly increases from north-east to south-west. A possible interpretation for the ridge is the outcrop of the horizon marked in inline 401 (Figure 7.15). The material of the outcrop of the horizon is possibly less easily eroded than the surrounding material and thus forms a structural high.

7.2.3 Crosslines

Figures 7.20 and 7.21 show the representative crosslines together with interpretation. Each crossline contains 150 traces with a spacing of 50 **cm,** thus having an overall length of 75 m. Refer to Figures 7.1 and 7.3 for their position in the data volume. Data gaps are present in crosslines 5401 and 5997, which are due to the limited migration aperture as explained in section 7.2.2. The vertical exaggeration of the sections is approximately 7.

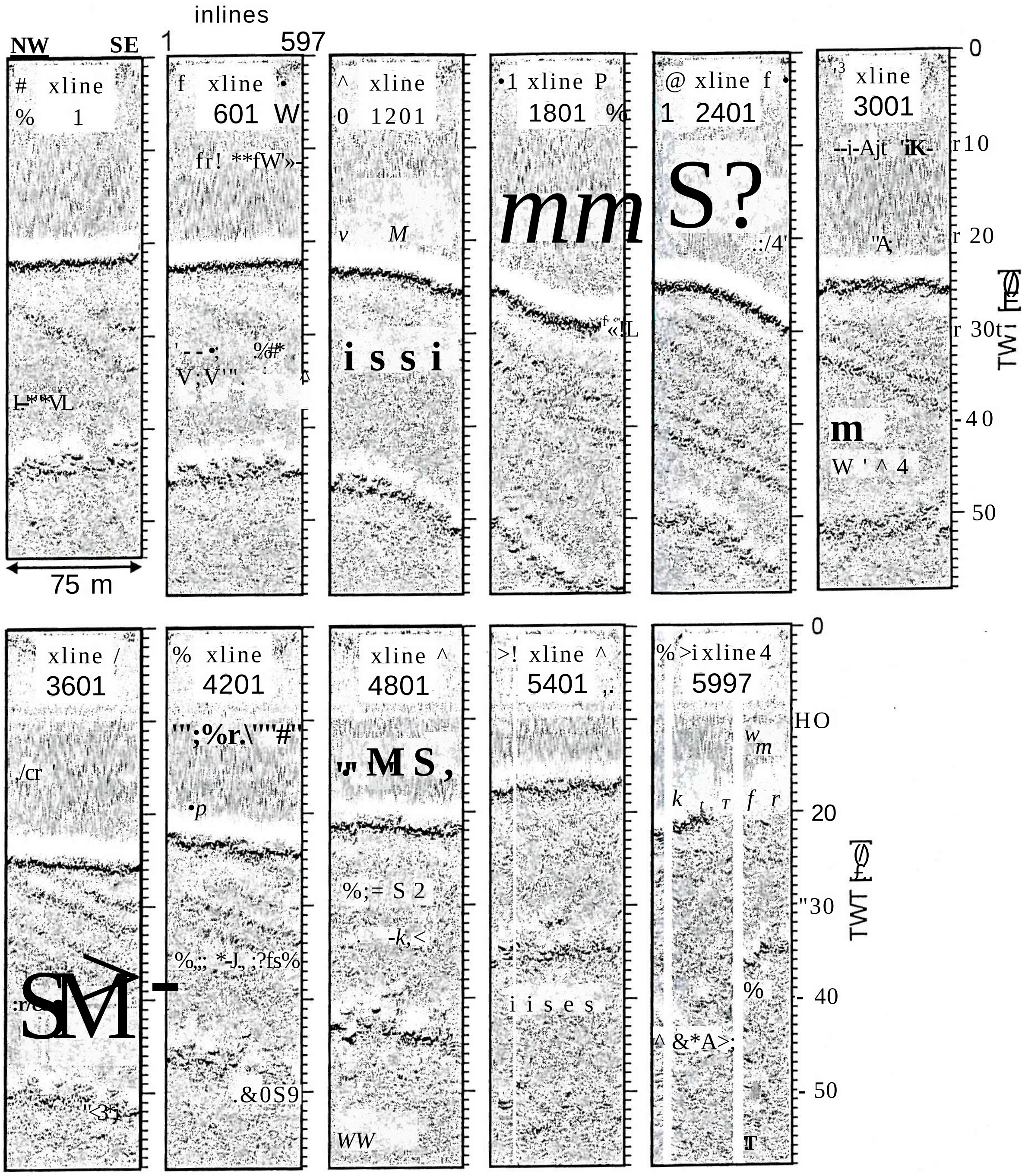

Figure 7.20 Eleven representative crosslines of the 3D Chirp data volume. See Figures 7.1 and 7.2 for their position within the data volume.

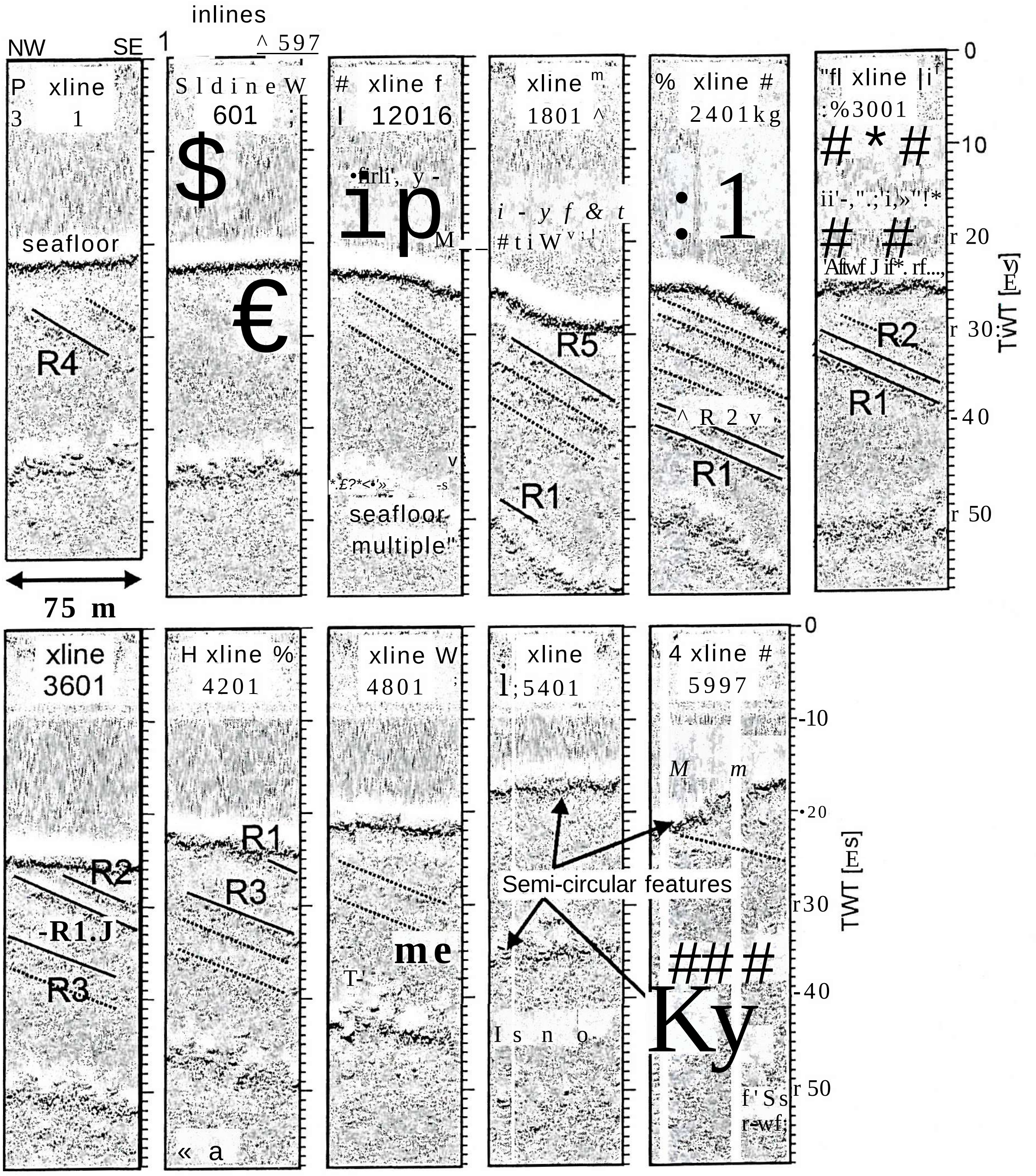

Figure 7.21 Eleven representative crosslines (xlines) of the 3D Chirp data volume with interpretation. See Figures 7.1 and 7.2 for their position within the data volume. The five internal reflectors (R1 to R5) interpreted in the inline sections (Figures 7.6 to 7.19) are apparent in the crossline sections. Note the semi-circular features discussed in the text.

The seafloor appears between 15 ms and 32 ms. The depression that was identified in the inlines as described in section 7.2.2 is reflected in crosslines 1801 and 2401 that show a deepening of the seafloor in south-eastern direction with increasing inline numbers, as the depression widens. The sedimentary waves visible in the inlines north-east of the depression are represented crosslines 1801 to 5597.

The **seafloor** multiple reflection is smeared over up to 4 ms, as could also be observed in the inline sections.

A total of 14 different horizons can be identified throughout the crosslines, matching the maximum number of identifiable horizons in the inline sections. Crossline 2401 is intersected by six horizons, whereas in crossline 5401 no horizon can be identified. The five interpreted horizons show an apparent dip towards the south.

7.2.4 Time slices

Figures 7.22 to 7.27 show the representative time slices from 20 ms to 54 ms with 2 ms spacing, together with their interpretation. Each time slice contains 1500 points in inline and 150 points in crossline direction, with 50 cm spacing in either direction, thus equalling 750 m and 75 m respectively. Refer to Figures 7.3 for their position within the data volume. Time slices are shown with and without interpretation on consecutive pages for easy comparison.

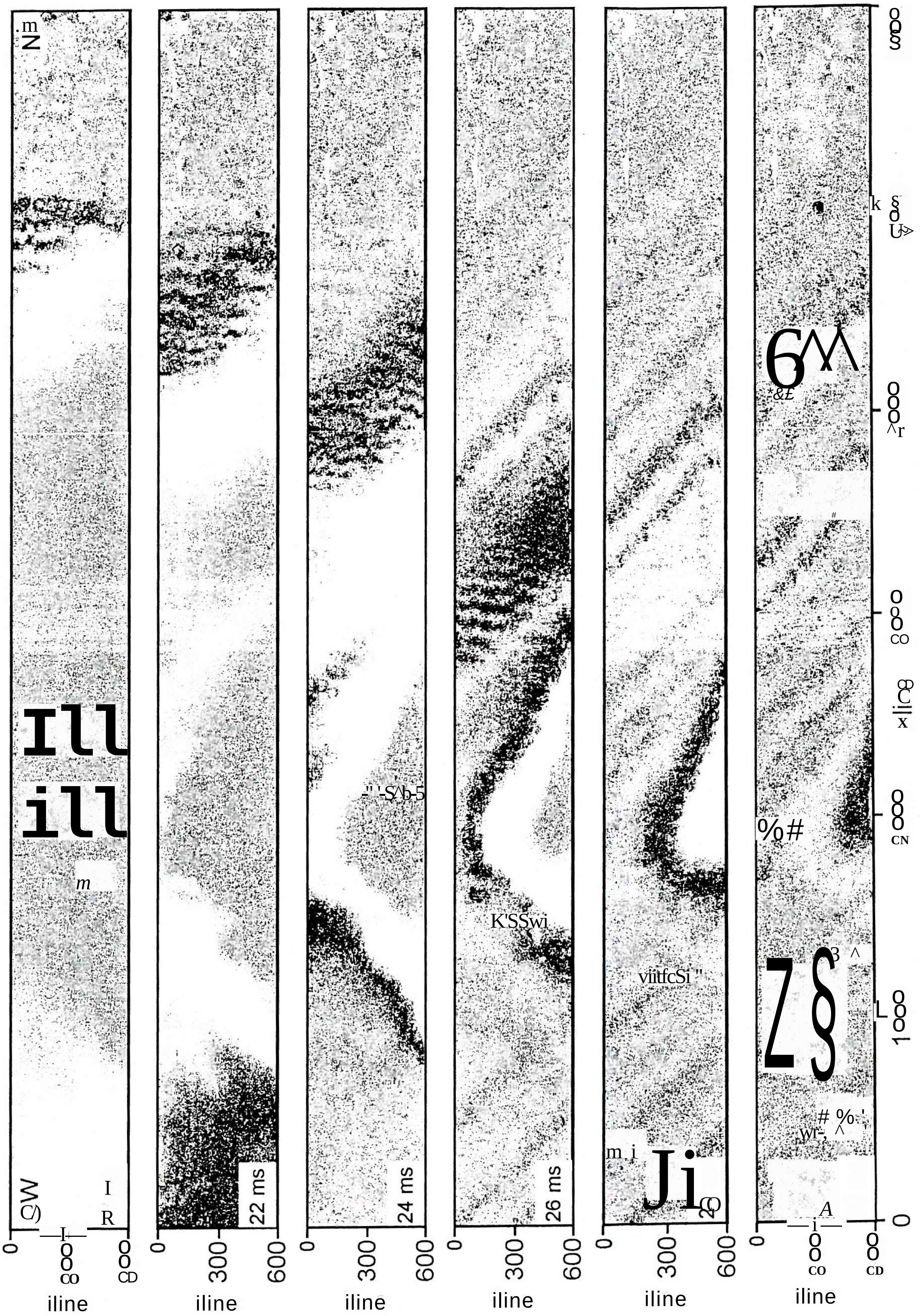

Figure 7.22 Time slices of the 3D Chirp data volume at 20 ms to 30 ms. They are 750 m long and 75 m wide. See Figure 7.3 for their position within the data volume.

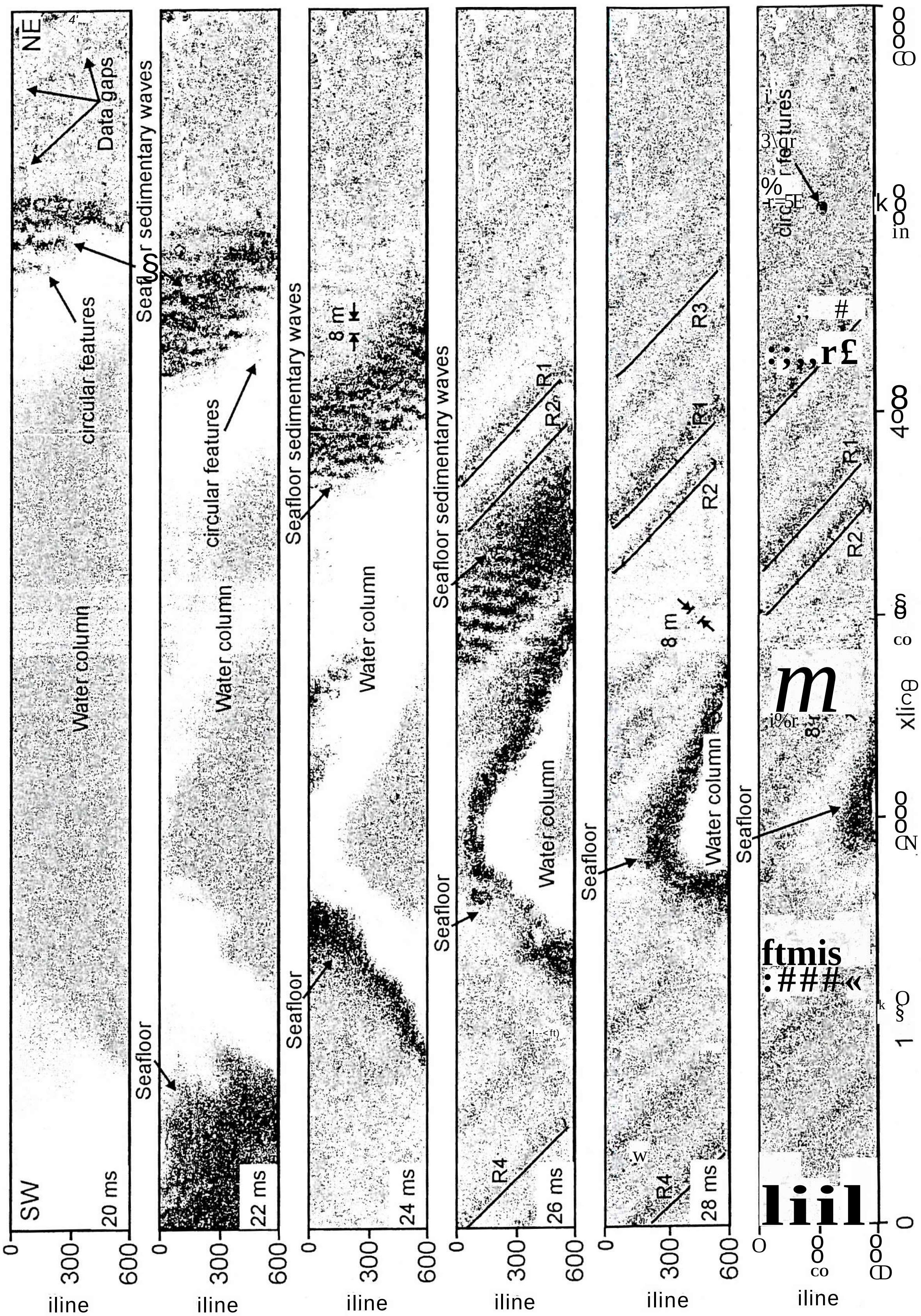

Figure 7.23 Time slices of the 3D Chirp data volume at 20 ms to 30 ms with interpretation. The extend of the data gaps and the circular features discussed in the text are highlighted. The width of the internal reflection horizons is approximately 8 m.

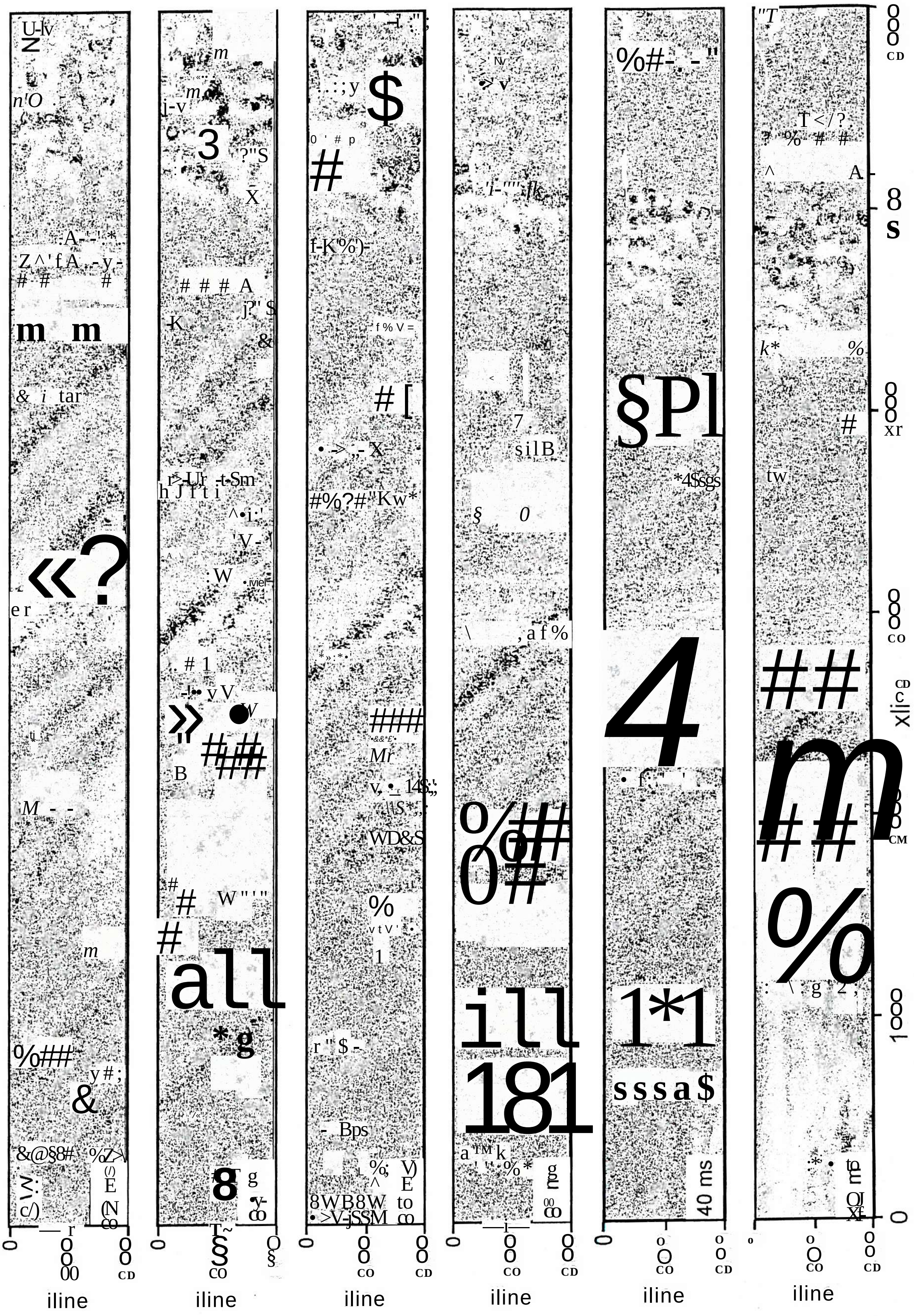

Figure 7.24 Time slices of the 3D Chirp data volume at 32 ms to 42 ms. They are 750 m long and 75 m wide. See Figure 7.3 for their position within the data volume.

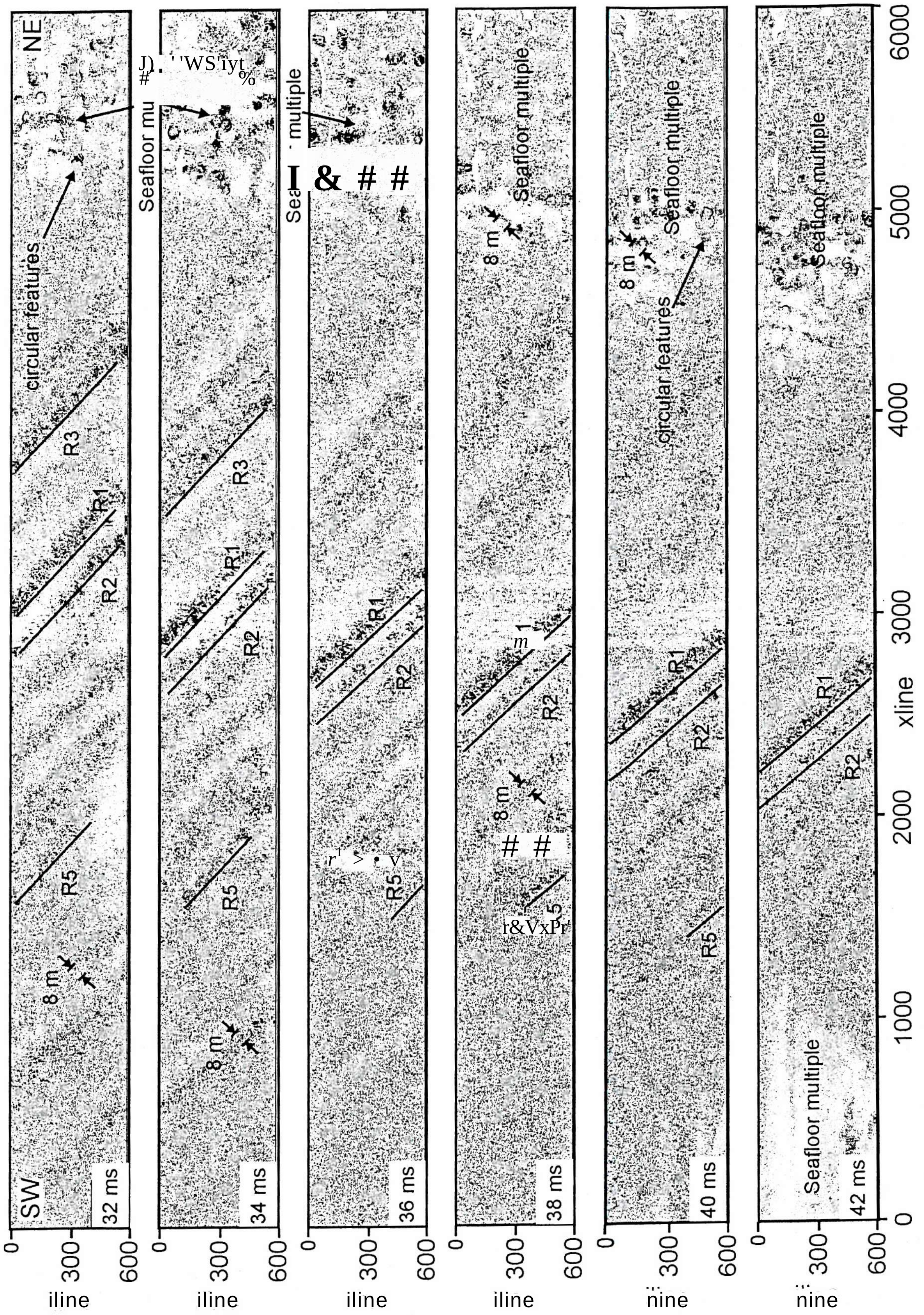

Figure 7.25 Time slices of the 3D Chirp data volume at 32 ms to 42 ms with interpretation.

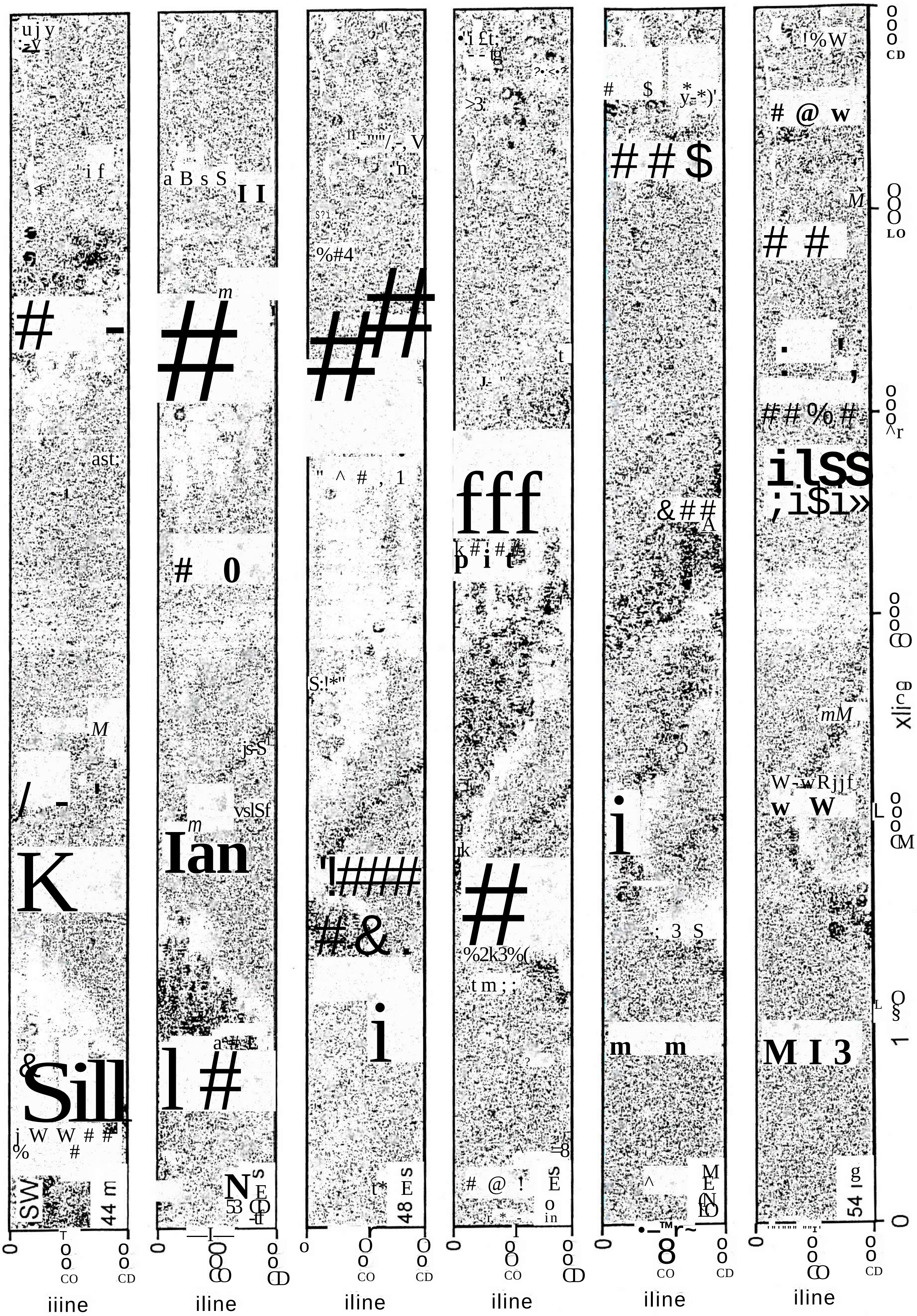

Figure 7.26 Time slices of the 3D Chirp data volume at 44 ms to 54 ms. They are 750 m long and 75 m wide. See Figure 7.3 for their position within the data volume.

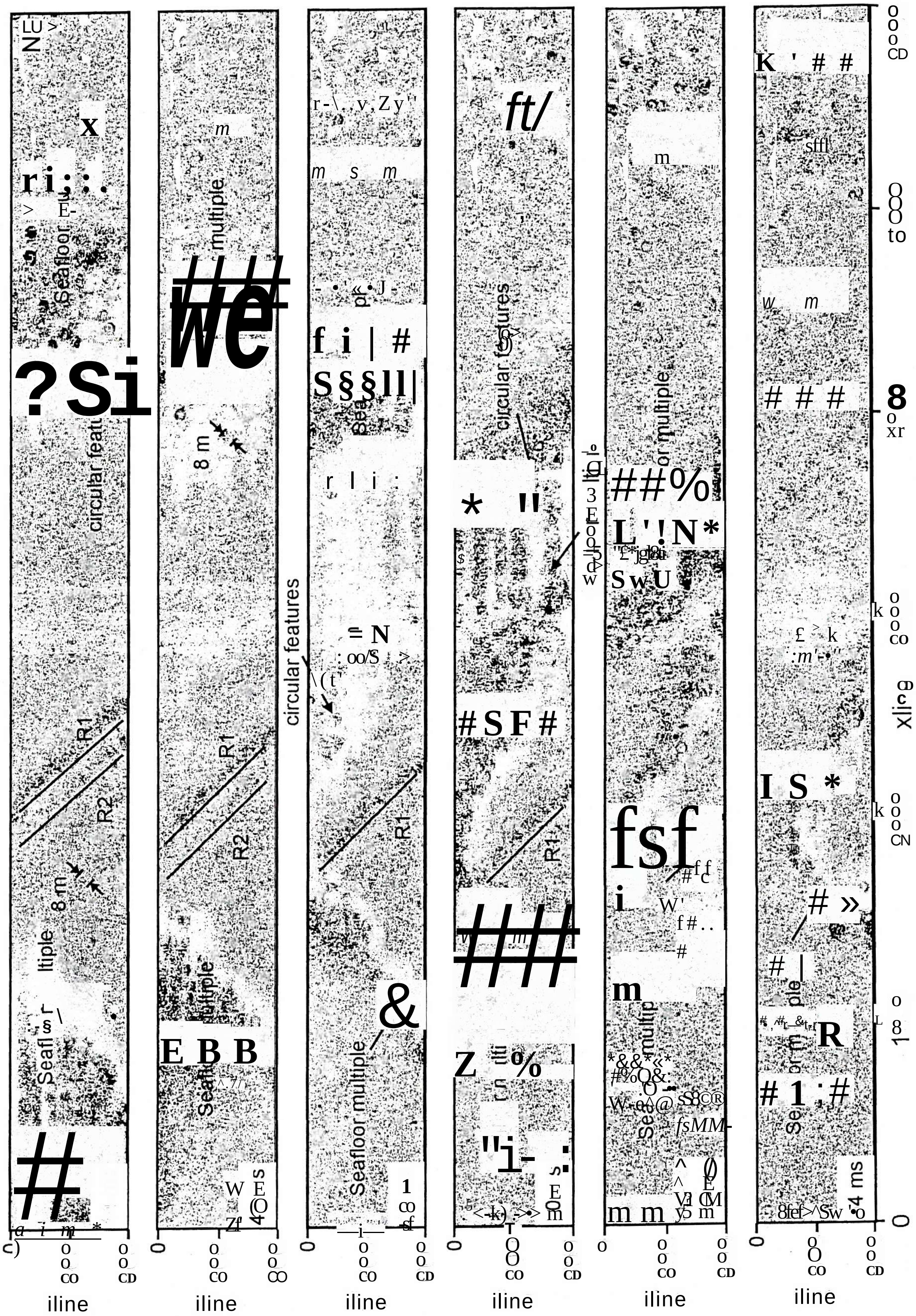

Figure 7.27 Time slices of the 3D Chirp data volume at 44 ms to 54 ms with interpretation. See text for discussion.

The time slice at 20 ms shows largely water column noise except in the north-eastern part from inline 4500 the **seafloor** reflection is visible, in the area with the least water depth. The seafloor in the north-eastern part is characterised by sedimentary waves, as seen in the inlines sections in section 7.2.2. The wave crests are aligned in crossline direction. This corresponds to wave crest formation perpendicular to the prevailing direction of the tidal currents, which is parallel to the inline direction (section 6.3.1). This corresponds to the findings of Langhome et al. (1986) who investigated the sedimentary waves in the survey area. Also in time slices 22 ms to 26 ms sedimentary waves can be observed in the seafloor reflection with decreasing wavelength towards the south-west (with decreasing crossline numbers). The **seafloor** depression identified in the inline sections is apparent in time slices 24 ms to 30 ms. It is represented as a semi-circular feature in the **seafloor** reflection with water column noise in its centre. Its width is decreasing with depth and it disappears in the north-western part (lower inline numbers) before it disappears in the south-eastern part (higher inline numbers) as the depression widens in the south-east.

The same 14 horizons shown in the inline and crossline sections can be identified throughout the time slices 24 ms to 54 ms as straight, smeared lines. The direction of the lines marks the southerly strike direction of the dipping horizons.

Data gaps are present, in the north-eastern parts of the time slices, coinciding with the data gaps present in the inlines and crosslines. They are due to limited migration aperture as discussed in section 7.2.2.

The **seafloor** multiple is present in time slices 32 ms to 54 ms starting in the north-east, moving towards the south-west with increasing TWT. From time slice 44 ms the seafloor multiple appears in the south-west and with increasing TWT the semi-circular feature associated with the seafloor depression is mirrored in the multiple reflection. Time slice 54 ms is fully situated in the multiple reflection apart from the area around inline 2000.

7.3 Data quality

7.3.1 Comparison between 2D and 3D data

Data from the 3D Chirp volume is compared to a single channel 2D line recorded with the 3D Chirp system and a single channel 2D line recorded with the 2D Chirp system described in Chapter 2. Figure 7.28 shows the position of inline 281, which represents the 3D Chirp data in this comparison together with the 2D lines.

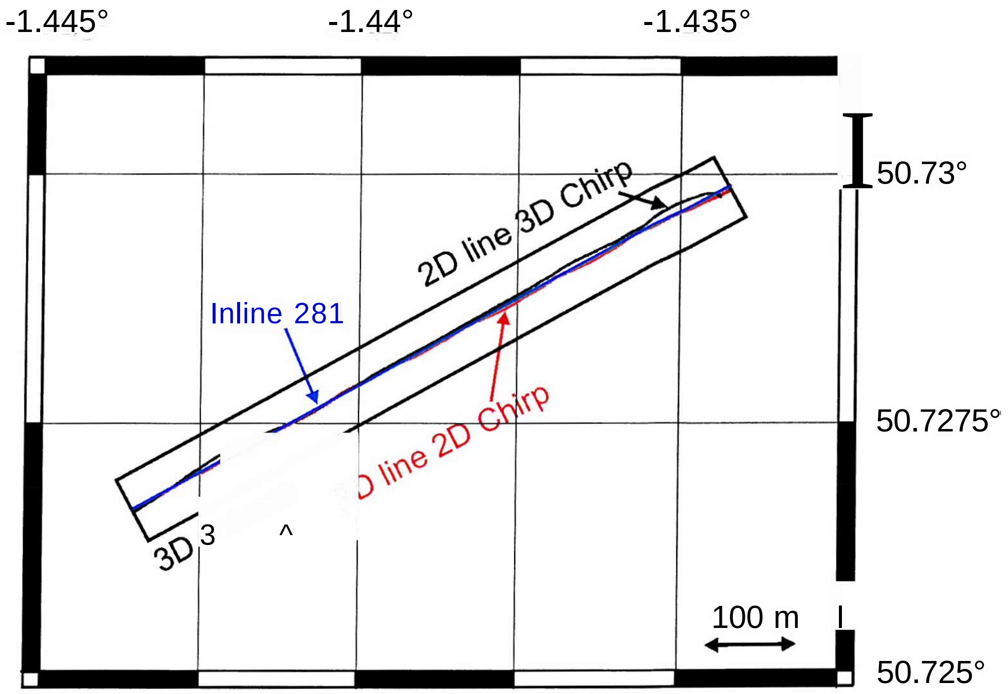

Figure 7.28 Position of inline 281 of the 3D Chirp data volume and 2D lines collected with the 3D and 2D Chirp systems in the vicinity of inline 281.

Note the deviations of the 2D lines from the straight 3D Chirp inline due to navigation inaccuracies. Moreover, the DGPS antenna used for positioning of the 2D Chirp system during data recording was situated on the survey vessel and the position of the towed Chirp system was estimated under the assumption that it is situated straight behind the survey vessel during the survey resulting in inaccuracies in the position of the seismic traces of up to some meters compared to the centimetre position accuracy achieved with the 3D Chirp system.

Figure 7.29 shows the migrated inline 281 of the 3D dataset together with the 2D sections. The inline has a trace spacing of 50 cm and thus 1500 traces over its 750 m length. The 2D line recorded with the 2D Chirp system with a shot rate of 4 Hz has a trace spacing of only

35 cm. The 2D line recorded with the 3D Chirp has a trace spacing of 1.6 m. Both 2D sections are processed using the same algorithms and parameters as the 3D Chirp data described in Chapter 6 apart from the pre-stack 3D Kirchhoff migration. Static corrections have been applied to the 2D data collected with the 3D Chirp system as described in section 6.4.5 but not to the 2D section collected with the 2D Chirp system. Figure 7.30 additionally shows the discussed sections with interpretation and annotations.

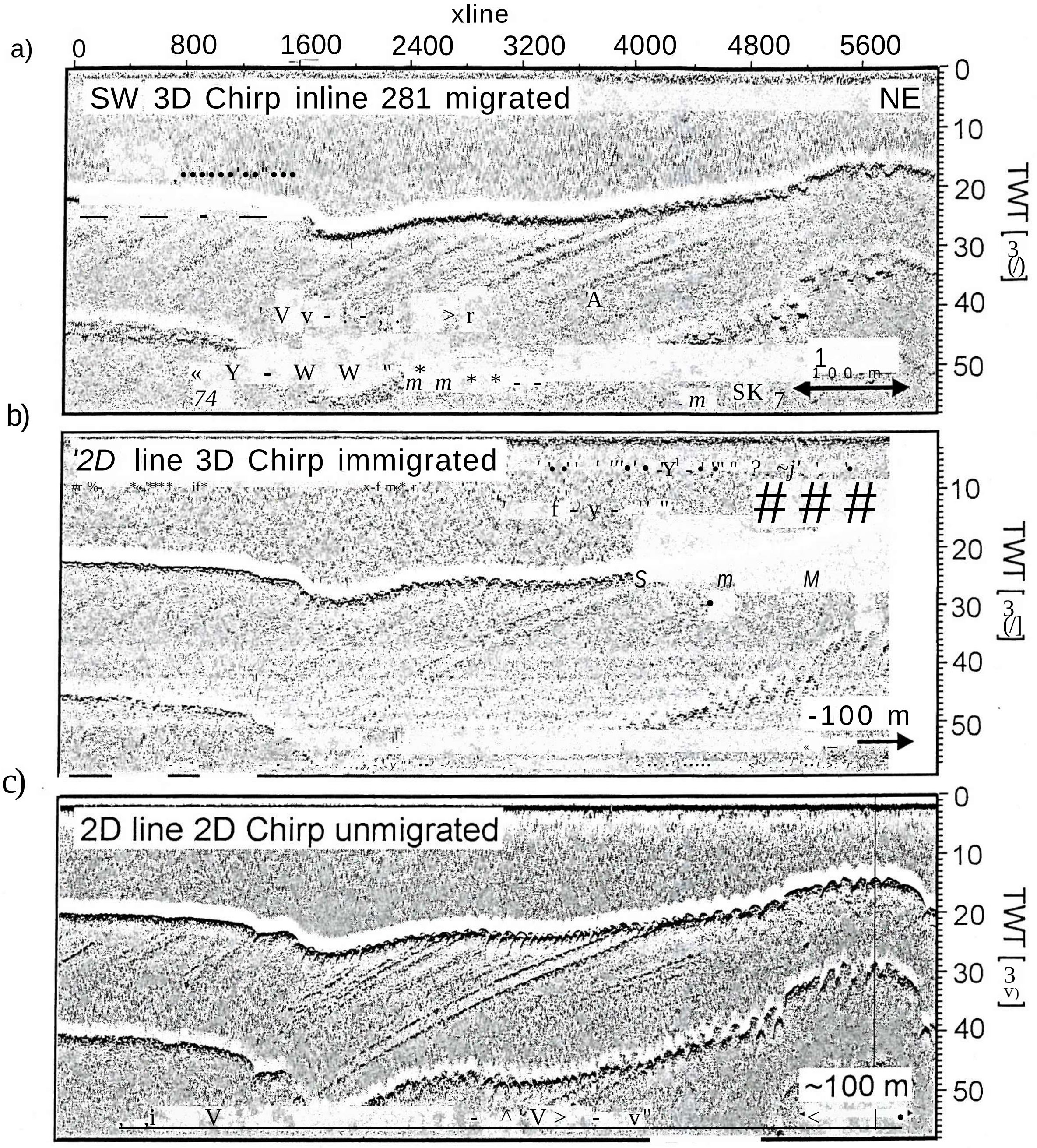

Figure 7.29 a) inline 281 of the migrated 3D Chirp data volume, b) section of 2D line collected with the 3D Chirp system, unmigrated, c) section 2D line collected with the 2D Chirp system. See Figure 7.28 for position of lines. Instantaneous amplitude calculation and automatic gain control with a window length of 5 ms have been applied to the data.

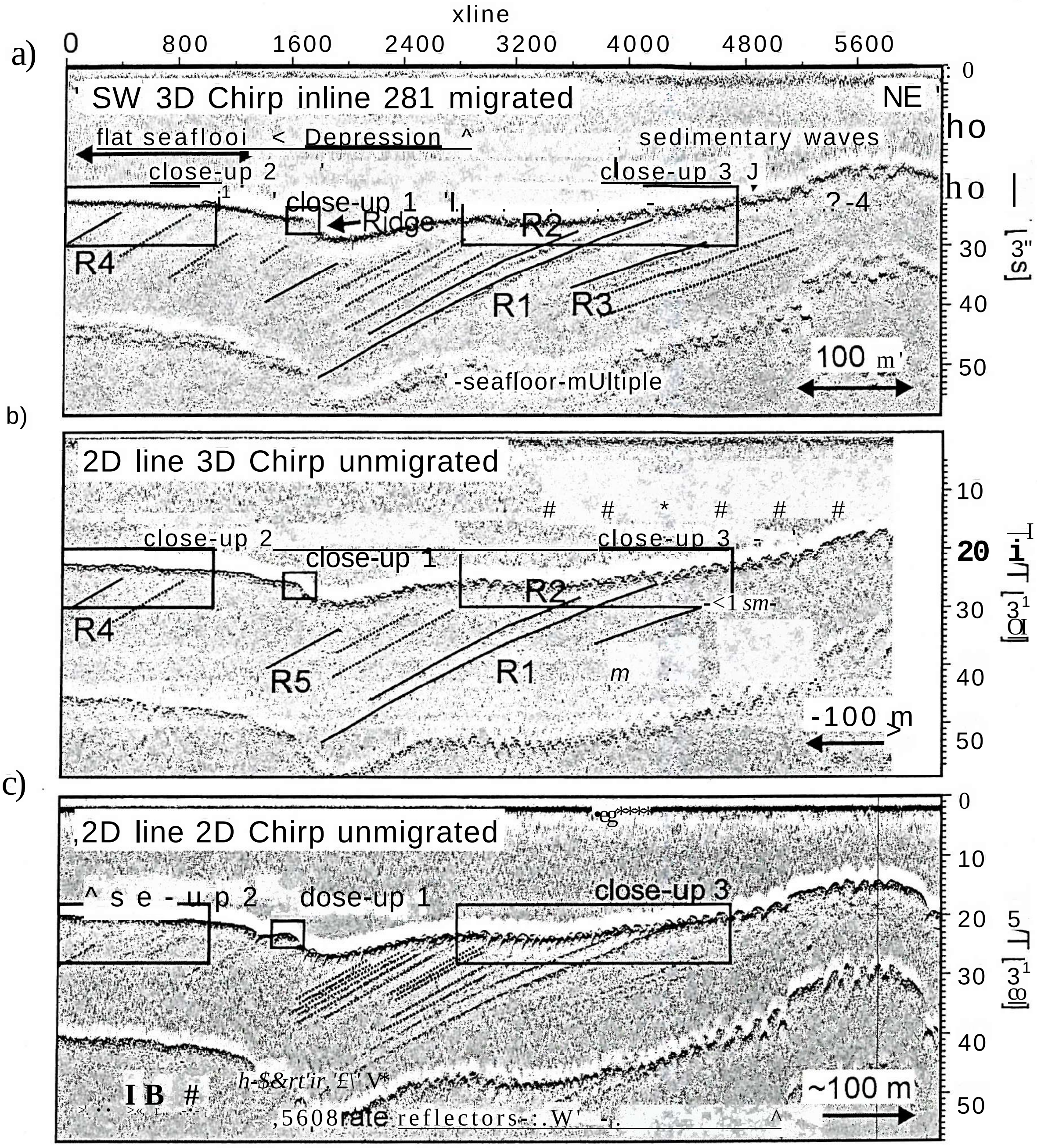

Figure 7.30 a) inline 281 of the migrated 3D Chirp data volume, b) section of 2D line collected with the 3D Chirp system, unmigrated. c) section 2D line collected with the 2D Chirp system. See Figure 7.28 for position of lines. Note the interpretation of the reflectors. Close-up 1 is shown in Figure 7.31; close up 2 in Figure 7.35 and close-up 3 in Figure 7.36.

The sections show a relatively flat seabed reflector in the south-west followed by a depression towards the north east with a ridge situated on its south-western flank. Sedimentary waves are apparent from the ridge towards the north-east with increasing amplitude and wave-length.

The sedimentary waves show bow-tie reflections in the **immigrated** 2D sections. In the 3D inline these features should have been converted into well defined peak and trough structures by the migration algorithm. This can be observed for longer wavelength sedimentary waves from crossline 3200 towards the north east. The seafloor from crossline 3200 towards the south-west however is generally smeared and well defined peak and trough structures are not apparent.

In the 3D section a total of 14 dipping reflectors can be distinguished from which only 8 can be interpreted in the 2D section recorded with the 3D Chirp system. This is possibly caused by low data quality due to wide trace spacing and single channel recording. The 2D section recorded with the 2D Chirp system using an eight-element streamer (Chapter 2) and a 4.6 times tighter trace spacing shows better data quality than the 2D section recorded with the 3D Chirp system. Events that were interpreted as a single reflector in the 3D Chirp sections are split in various horizons in the 2D Chirp section. In particular between crosslines 1600 and 3200 eleven dipping **horizons** are visible beside reflectors R1 and R2, where in the 3D Chirp 2D section only three are distinguishable.

To compare the data recorded with the different systems and to investigate the effect of the pre-stack 3D Kirchhoff migration in detail Figure 7.31 shows the data highlighted as 'close-up 1' **in** Figure 7.30 without instantaneous amplitude calculation and automatic gain control applied (Chapter 6). Figure 7.31a shows the migrated 3D data of inline 281. Figure 7.31b shows the traces of the inline before applying the pre-stack 3D Kirchhoff migration algorithm. The traces are plotted ordered according to their position from south-west to north-east on the inline. Apart from the traces sorted in this inline all traces within the migration aperture radius of 4 m are considered by the algorithm for every image trace (Chapter 6). In Figure 7.31c the data from the 3D Chirp 2D line are shown. Arrows with solid lines indicate the position of the traces in the unmigrated inline 281, arrows with dotted lines their closest position, as these traces are not sorted into inline 281 but adjacent inlines. Figure 7.3Id shows the data recorded with the 2D Chirp system. Due to offset in the position of the lines evident in the map in Figure 7.28 a slightly offset part of the sub-surface is imaged as apparent from the shape of the seafloor reflector.

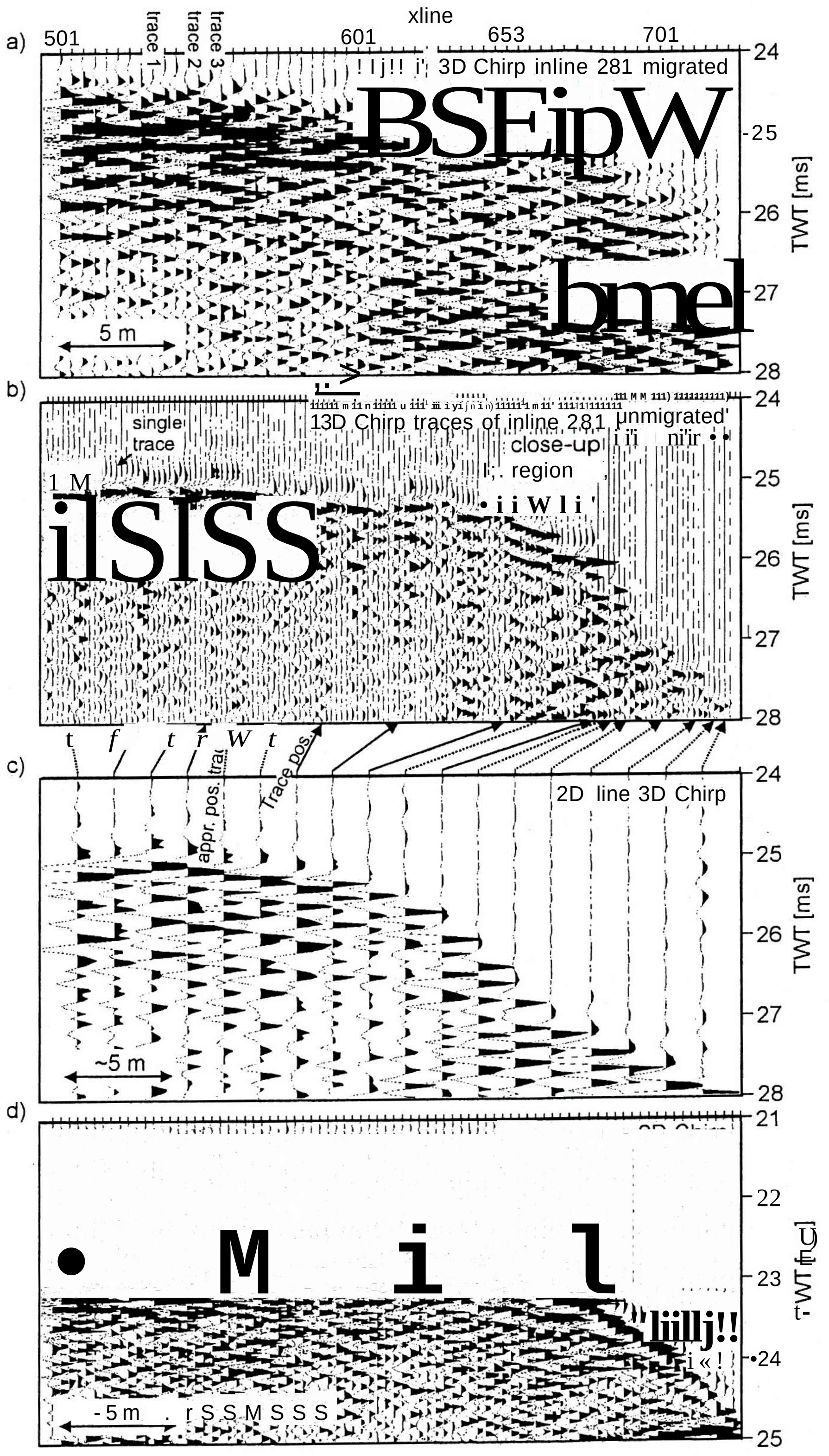

Figure 7.31 Close-up 1 highlighted in Figure 7.30. a) migrated inline 281 from the 3D Chirp data volume, b) unmigrated traces of inline 281 of the 3D Chirp data volume, c) unmigrated 2D line collected with the 3D Chirp system, d) unmigrated 2D line collected with the 2D Chirp system. The highlighted traces are shown in Figure 7.33. The close-up region in b) is shown in Figure 7.32.

The migrated 3D data shows a poorly defined seafloor reflection. Between traces 501 and 620 the reflection is smeared. Between traces 620 and 729 the seafloor can not be clearly identified in the section. In contrast in both 2D sections the seafloor can clearly be identified as a smooth and tight reflector.

It is postulated that the smearing reflection events in the migrated 3D Chirp data is caused by smearing of energy by the migration algorithm due to bad positioning of traces caused by residual time-shifts between positioning and seismic data discussed in section 6.4.6.

The unmigrated data of inline 281 show a relatively flat seafloor reflection between xline 501 and the area marked as close-up region in Figure 7.31b. Steps smaller than 0.1 ms between traces are associated with traces acquired at different shots, as adjacent traces associated with a single shot show peaks aligned in a horizontal line or along a smooth slope. As the slope of the seafloor reflectors increases from approximately maximum 2.5° to 6° in the area marked as close-up region the steps between traces associated with different shots increase. Figure 7.32 shows the data from the close-up region marked in Figure 7.31b.

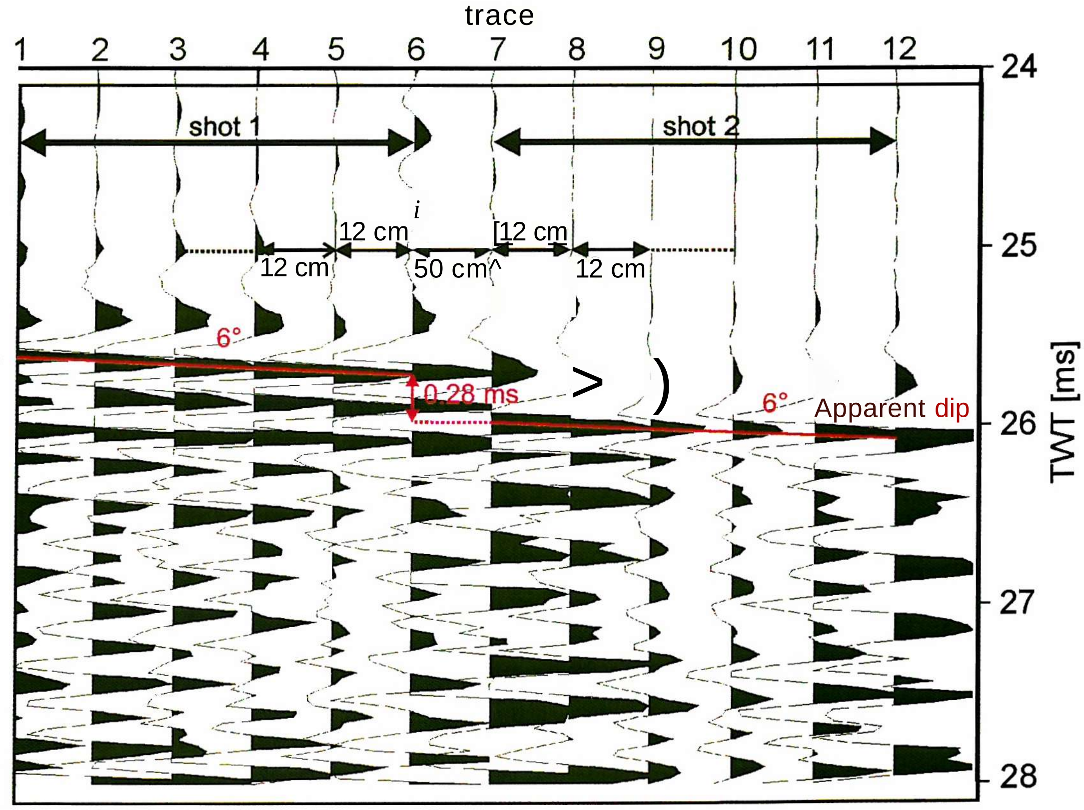

Figure 7.32 Close up region highlighted in Figure 7.31b.

The traces shown are associated with two different shots collected 1:08 hours apart. The traces within a shot recorded with different channels of the 3D Chirp system have a spacing of 12 cm and show a slope of 6°. The distance between traces 6 and 7, associated with different shots, is 50 cm and a step of 0.28 ms TWT is apparent between the traces. Since a step of only 0.07 ms is expected for a slope of 6° the remaining 0.21 ms are suspected to result from a residual position error. After section 6.4.6 a residual time-shift of 1 s produces a step of 0.21 ms TWT for the given slope of 6° and a survey speed of 1.5 m/s (3 kn), which corresponds to the actual survey speed at which these shots were collected. Thus it could be shown in this example that a residual time-shift of just 1 s can produce the observed bad positioning of traces and the associated static shifts.

To investigate the effect of resulting smearing of reflection events in more detail Figure 7.33 shows the seafloor reflection of the single traces marked in Figure 7.31 together with the theoretical Klauder wavelet of sweep S7 used (Figure 2.7).

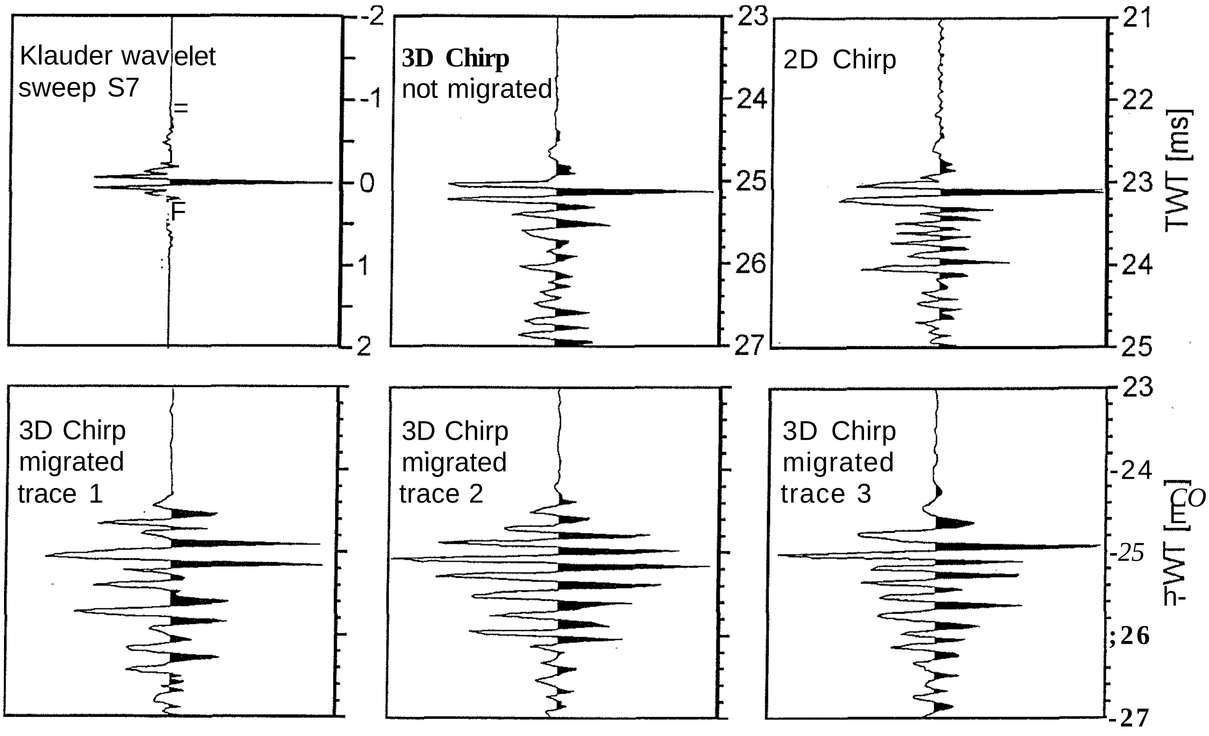

Figure 033 Klauder wavelet of sweep S7 (Figure 2.7) and seafloor reflections of unmigrated 3D Chirp and 2D Chirp data and migrated 3D Chirp data highlighted in Figure 7.31.

Both the reflections of the unmigrated data collected with the 3D Chirp system and the data collected with the 2D Chirp system are very similar to the Klauder wavelet, although the corresponding power spectra for the data shown in section 6.4.4 show that the mean frequency of the 3D Chirp data is, at 5 kHz, 2.25 kHz lower than that of the 2D system data, whose mean frequency of 7.25 kHz corresponds to the mean frequency of the theoretical Klauder wavelet (see section 6.4.4 for discussion).

The example traces for the migrated data show large differences in their seafloor reflections. Trace 1 of the migrated data shows two equal amplitude maxima with 0.14 ms separation, whereas trace 2 shows a single maximum with large amplitude side-maxima with up to 85% of the maximum amplitude as opposed to 8% in the Klauder wavelet. Trace 3 shows the most resemblance with the Klauder wavelet with a single spike. These different seafloor reflections are the result of smearing of amplitudes by the migration algorithm.

Figure 7.34 shows the amplitude build-up curves for the traces calculated as discussed in section 2.4.1.

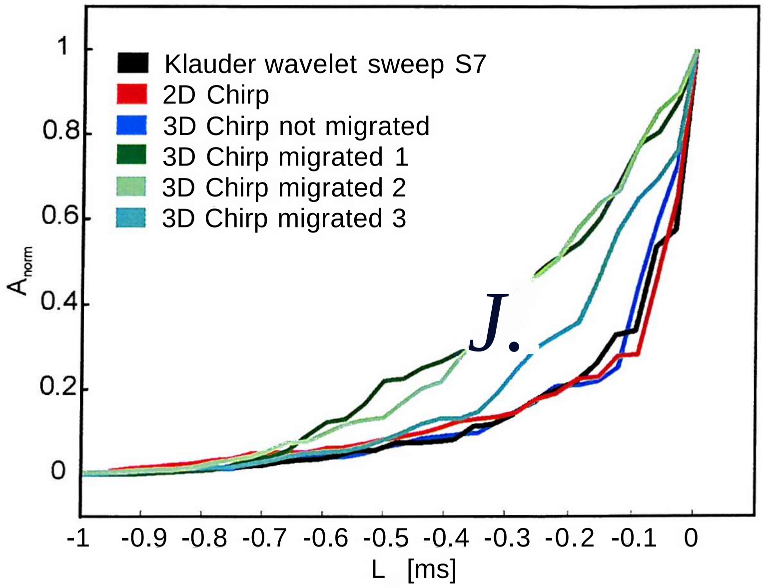

Figure 7.34 Amplitude build-up curves of the traces shown in Figure 7.33.

As expected from the similarity of the seafloor reflections to the Klauder wavelet the unmigrated 2D and 3D data show very similar curves to the theoretical curve with the 2D curve being tighter, reflecting its higher frequency content compared to the 3D data. The curves for the migrated data vary significantly for the different sample traces. The amplitude half-width are listed in Table 7.1.

Sweep	Amplitude build-up half width [ms]
Klauder wavelet S7	0.070
2D Chirp	0.054
3D Chirp not migrated	0.079
3D Chirp migrated trace 1	0.226
3D Chirp migrated trace 2	0.219
3D Chirp migrated trace 3	0.146

Table 7.1 Half-width of amplitude build-up curves shown in Figure 7.34.

For this example the amplitude build-up half-width of the migrated traces is on average 2.8 times wider than the theoretical width.

To investigate the smearing on a larger scale Figure 7.35 shows the data in the area marked as close-up 2 in Figure 7.30. The data shows a relatively flat seafloor reflection in particular north east of crossline 700. The thickness of the seafloor reflection in this area was measured in these instantaneous amplitude sections for comparison.

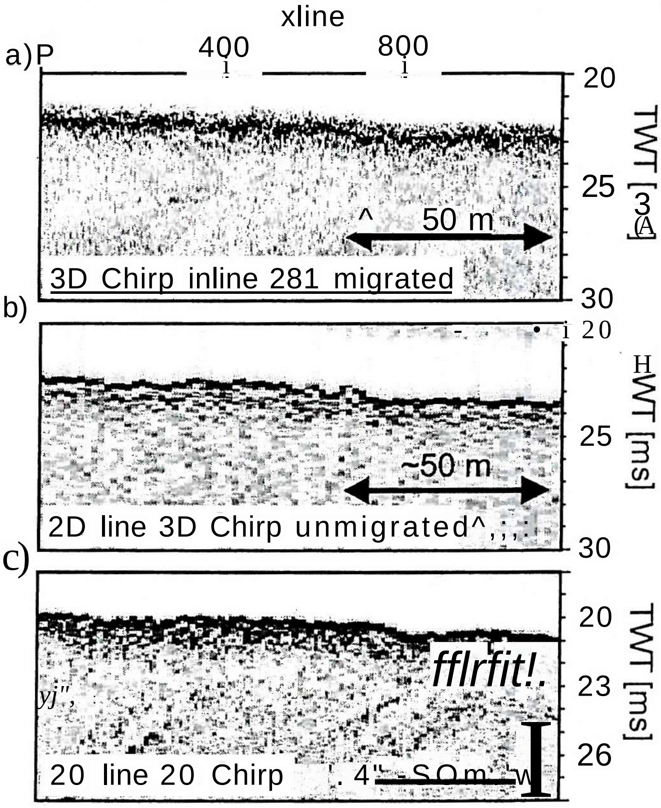

Figure 7.35 Region highlighted as close-up 2 in Figure 7.30. a) migrated 3D Chirp data, b) unmigrated data collected with the 3D Chirp system, c) unmigrated data collected with the 2D Chirp system.

The 2D data collected with the 2D Chirp system shows a seafloor reflection of 0.19 ms ± 0.04 ms TWT, the unmigrated data of 2D section recorded with the 3D Chirp system shows a seafloor reflection of 0.15 ms ± 0.03 ms TWT, whereas the data from the migrated

3D inline shows a seafloor thickness of 0.36 ms ± 0.16 ms TWT. The unmigrated data show similar widths, with the data recorded with the 3D Chirp system being 26% wider. The width for the migrated data is more variable and is 1.6 times wider than the unmigrated 2D data recorded with the 3D system.

As a second example Figure 7.36 shows the data in the area marked as close-up 3 in Figure 7.30. The seafloor reflection in this area is dominated by sedimentary waves resulting in bow-tie reflections in both unmigrated 2D sections recorded with the 2D and 3D Chirp systems. Two dipping internal reflectors, R1 and R2, can be seen in all sections. Additionally there are three reflectors visible south-west of crossline 3200 in the 2D section recorded with the 2D Chirp system. The diameter of 8 m corresponding to the migration aperture is marked in the 2D sections.

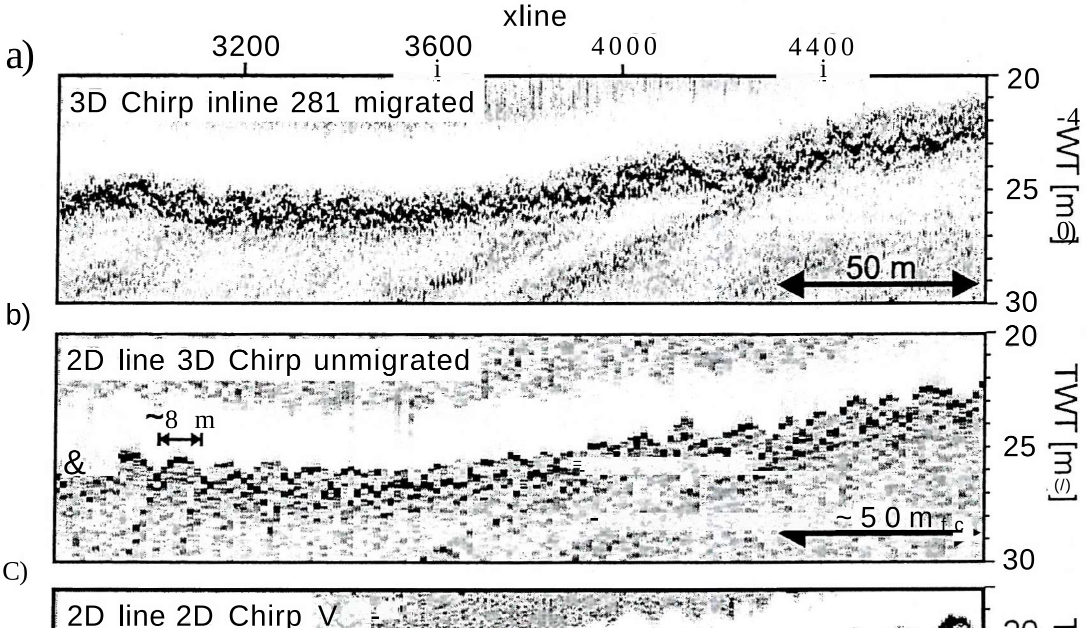

Figure 7.36 Region highlighted as close-up 3 in Figure 7.30. a) migrated 3D Chirp data, b) unmigrated data collected with the 3D Chirp system, c) unmigrated data collected with the 2D Chirp system.

The seafloor reflection of the migrated 3D inline is smeared. Some bow-tie features apparent in the 2D sections have been successfully converted into peak and trough structures by the migration algorithm in particular between crosslines 4100 and 4400. In other parts, for example between crosslines 3400 and 3600 the seafloor shows smeared reflections with no apparent peak and trough structures, although they are expected from the corresponding reflections in the 2D sections. The thickness of the seafloor reflection reaches up to 1 ms TWT.

The 2D section show that the diffraction hyperbola present are wider than the marked migration aperture, which results in additional smearing of energy by the migration algorithm as described in section 6.4.7.

Generally smearing caused by positioning errors due to residual time-shifts is stronger for sloping reflectors, like the dipping internal reflectors and large slopes of the seafloor topography and structures like sedimentary waves than for relatively flat reflectors (section 6.4.6), which could be seen in the above examples. Additionally the limited migration aperture causes smearing in imaging sedimentary waves and steep slopes. The seafloor reflector in the inlines shown in Figures 7.6 to 7.19 show relatively tighter reflections in the area of the **flat seafloor** in the south-western part. Large slopes in the vicinity of the ridge and depression show more smearing, as do the areas with sedimentary waves in particular on the north-eastern flank of the depression with the shorter wavelength and amplitude waves compared to the far north-east of the section. This can also be observed in the crossline sections in Figures 7.20 to 7.21 with relatively tight **seafloor** reflections in crosslines 1 and 601 in the area of the relatively **flat** seafloor and increasing smearing in crosslines 1201 to 2401 in the area of the seafloor ridge and depression and the following crosslines imaging sedimentary waves on the **seafloor.** The time slices shown in Figures 7.22 to 7.27 reveal circular features with a diameter of 8 m, which corresponds to the migration aperture. These features are most abundant in the seafloor multiple. These features can be observed as semi-circular features in the vertical sections. They are caused by smearing of isolated or badly positioned amplitudes by the migration algorithm within its aperture. Isolated amplitudes are particularly abundant in the **seafloor** multiple due the difference TWT of the multiple for traces recorded during different tidal heights as discussed in 7.2.2. These features can also be observed in the **seafloor** reflections in particular in areas with sedimentary waves, highlighting the smearing of energy in these areas.

The internal reflectors, imaged as tight reflections in the 2D sections in Figure 7.29b and 7.29c are smeared in the migrated 3D inline, crossline sections and time-slices. The time-slices reveal their smearing in horizontal direction. Their width is similarly approximately 8 m.

7.3.2 Data quality and coverage

In this section the quality of the data in the shown inline and crossline sections and time slices is compared to the data coverage in their vicinity. The data coverage is represented by the CDP fold discussed in section 6.4.5, which is based on the binning grid with 12.5 cm spacing in inline and crossline direction. However, as only every 4th trace was imaged by the 3D pre-stack Kirchhoff migration (section 6.4.7) the spacing of the imaging grid is 50 cm in either direction and the migration uses an aperture radius of 4 m. The CDP fold reflects the fold of the imaging grid and can be used for this analysis. Figure 7.37 shows the CDP fold versus inline and crossline numbers together with the inline fold, the number of traces in the unmigrated inlines, and the crossline fold, the number of traces in the unmigrated crosslines.

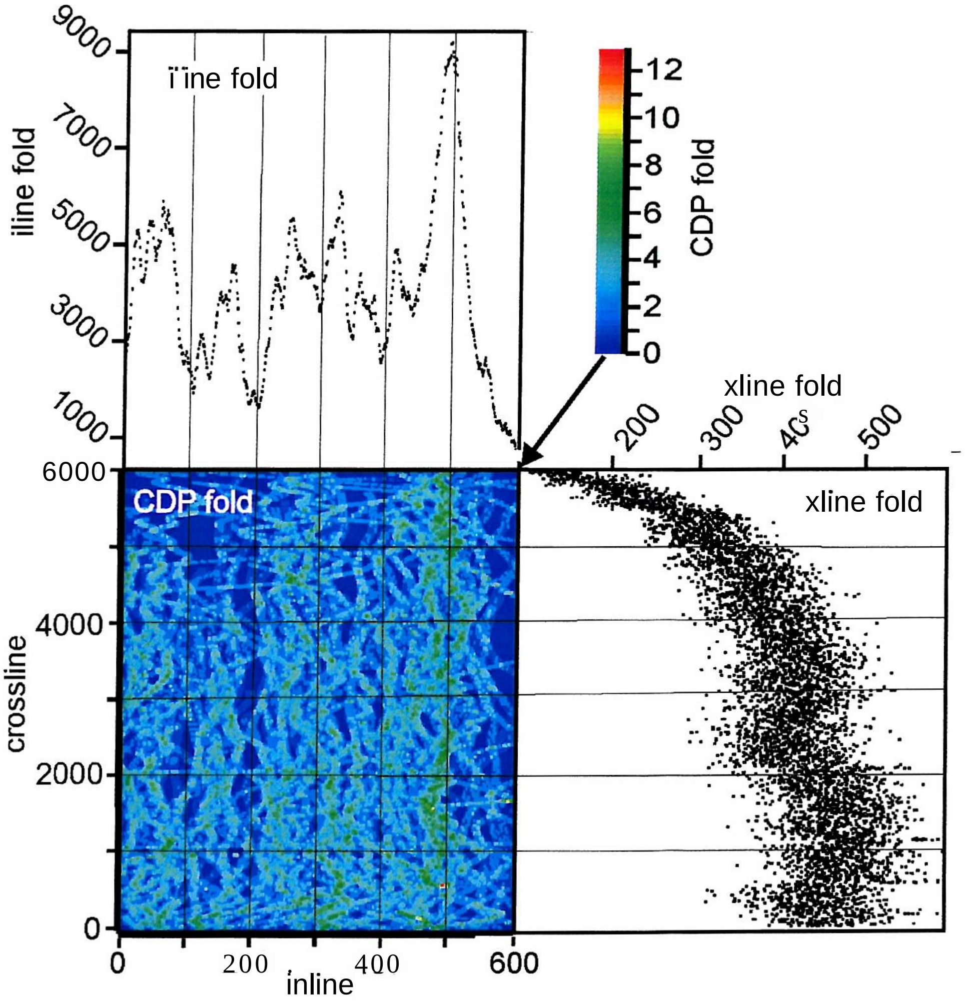

Figure 7.37 CDP fold against inlines and crosslines for the 3D Chirp dataset togther with the integral inline and crossline fold for the individual lines.

The inline fold fluctuates for inline 1 to 500 between approximately 1600 and 9200. From inline 500 the fold declines from the absolute maximum value of approximately 9200 to an absolute minimum value of approximately 700. Equally the crossline fold shows large fluctuations with a large number of local minima and maxima in the range of approximately 300 and 600 for crosslines 1 to 5000. From crossline 5000 to 6000 the fold decays to an absolute minimum value of 10 for crossline 6000.

The maximum value in the inline fold is related to dense acquisition of survey lines. Low values towards inlines 6000 are due to the peripheral position of these inlines; only a few survey lines were collected in this part of the survey area. The low crossline fold for crosslines 5000 to 6000 is due to the lack of radio link during the first four survey days of the acquisition campaign. The lack of radio coverage led to bad position data and ultimately unsuitable associated seismic data as described in Chapter 6. Additionally note that for inline and crossline sections on the peripheries of the area only traces within the area are used as input for the migration, thus decreasing the possible data contribution.

Table 7.2 shows the folds for the inline and crosslines shown in section 7.2.2 and 7.2.3 respectively.

iline	iline fold	xline	xline fold
1	**2801**	1	474
101	**2297**	**601**	**461**
201	1701	**1201**	**479**
301	**4264**	1801	**413**
401	**3353**	**2401**	**369**
501	**765**	**3001**	**352**
		3601	**439**
		4201	**341**
		4801	**338**
		5401	**290**
		5997	**128**

Table 7.2 Inline and crossline fold for the representative inlines and crosslines discussed in sections 7.2.2 and 7.2.3 respectively.

To analyse the effect of data coverage on the data quality firstly areas with low data coverage are investigated, in particular the entire sections of inline 597 (Figures 7.18 and 7.19) and crossline 5597 (Figures 7.20 and 7.21) and areas in the vicinity of data gaps in inlines 1, 101 and 201 between crosslines 5000 and 6000 (Figures 7.6 to 7.11) and all time slices between crosslines 5000 and 6000 (Figures 7.22 to 7.27). These areas of low data coverage are characterised by an abundance of semi-circular features in inline and crossline sections with opening towards the top and circular features in the time slices with their diameter of 8 m corresponding to the migration aperture. They distort the horizons such as the **seafloor** and internal reflectors in inline 597 (Figures 7.18 and 7.19) and crossline 5997 (Figures 7.20 and 7.21), the sedimentary waves between crosslines 5000 and 6000 in inlines 1, 101 and 201 and dipping internal horizons in inline 597. In time slices they are particularly associated with **seafloor** multiples and sedimentary waves at the **seafloor** as discussed in section 7.2.4 but also with areas with data gaps, as can be observed in all time slices between crosslines 5000 and 6000.

Sections with relatively high data coverage (Table 7.2) include inline 501 (Figures 7.16 and 7.17) and to a lesser extent inlines 301 and 401 (Figures 7.12 to 7.15) and crosslines 1 to 1201 and 3601 (Figures 7.20 to 7.21). In the parts of the inline sections with high data coverage these features can mainly be observed at the seafloor multiple and areas of the seafloor with sedimentary waves. Generally the data quality in the sections is variable. For example the **seafloor** in inline section 501 shows tight reflections between crosslines 5500 and 6000, imaging large wavelength sedimentary waves. The seafloor reflections between crosslines 5000 and 5500 are smeared and no small scale topographic features can be interpreted. The seafloor between crosslines 3000 and 5000 shows varying characteristics, with areas of smeared reflections, areas of well defined sedimentary waves and in some places **reflections** below the seafloor, mirroring seafloor sedimentary waves. The section of inline 301 shows a seafloor with similar characteristics throughout. The seafloor in the section of inline 401 shows areas with tight reflections (crosslines 3500 to 5000), alternating with areas with smeared reflections (crosslines 1600 to 3500).

Equally the internal horizons in the high fold inline sections discussed show varying characteristics. In particular horizon R2 in the section of inline 501 shows tight reflections between crosslines 2000 and 2800 and wider, more smeared reflections between crosslines **2800 and 4000.**

Generally there is no clear correlation between data quality and data coverage: although semi-circular and circular features causing deterioration of the data quality are more abundant in areas of lower coverage, they can also be observed in areas of **seafloor** and seafloor multiple reflections in areas with relative high data coverage.

7.3.3 Instantaneous amplitude calculation before migration and migration aperture

By calculating the instantaneous amplitude (section 6.4.8) and subsequently subtracting the constant offset from the signal before applying the pre-stack Kirchhoff migration (section 6.4.7) in the processing flow, shown in Figure 6.6, the frequency content of the dataset is lowered, as shown in Figure 6.19, resulting in wider **reflection** signals and thus improving horizon smearing by the migration process discussed in section 7.3.1.

Figures 7.38 to 7.41 show inline 401 (Figure 7.14 and 7.15) after migration using different migration aperture radii.

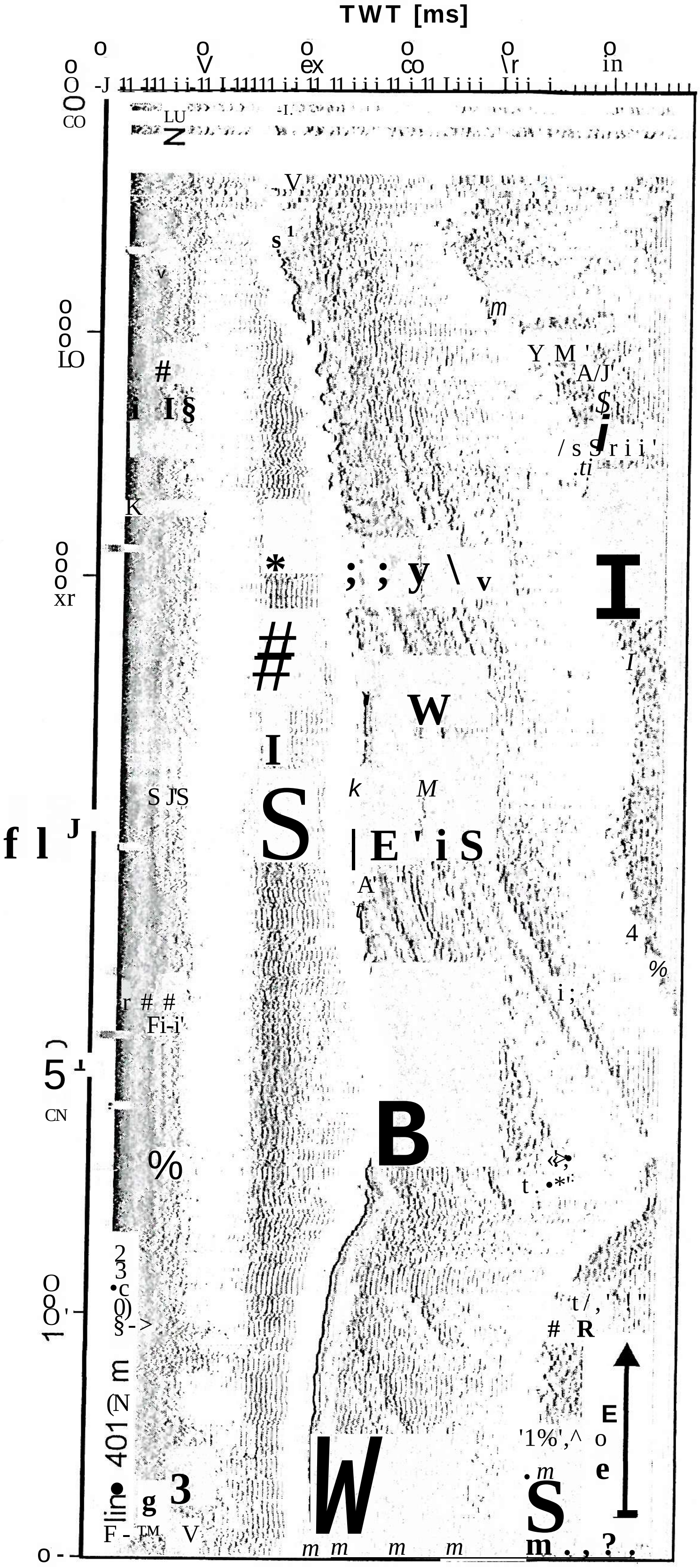

Figure 7.38 Inline 401 with instantaneous amplitude calculation before migration using 2 m aperture radius.

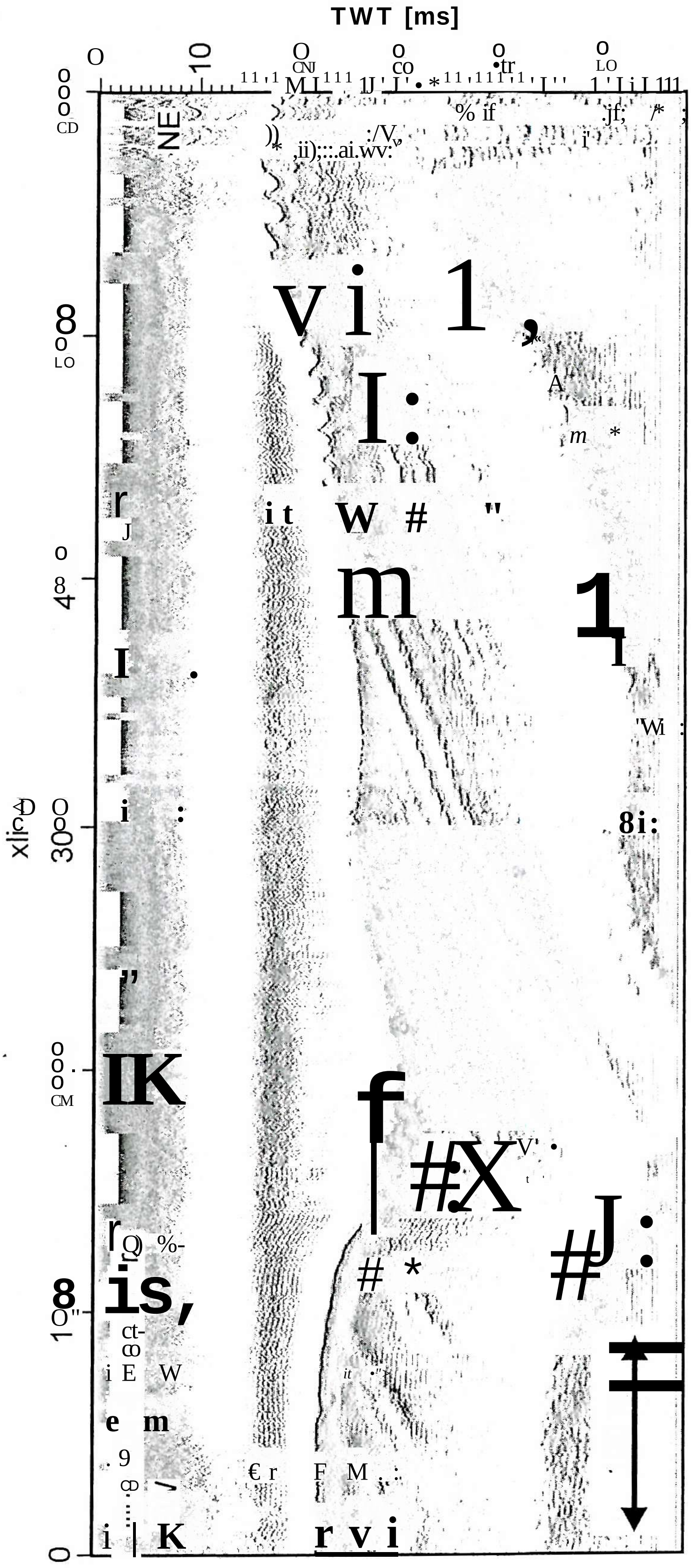

Figure 7.39 Inline 401 with instantaneous amplitude calculation before migration using 4 m aperture radius.

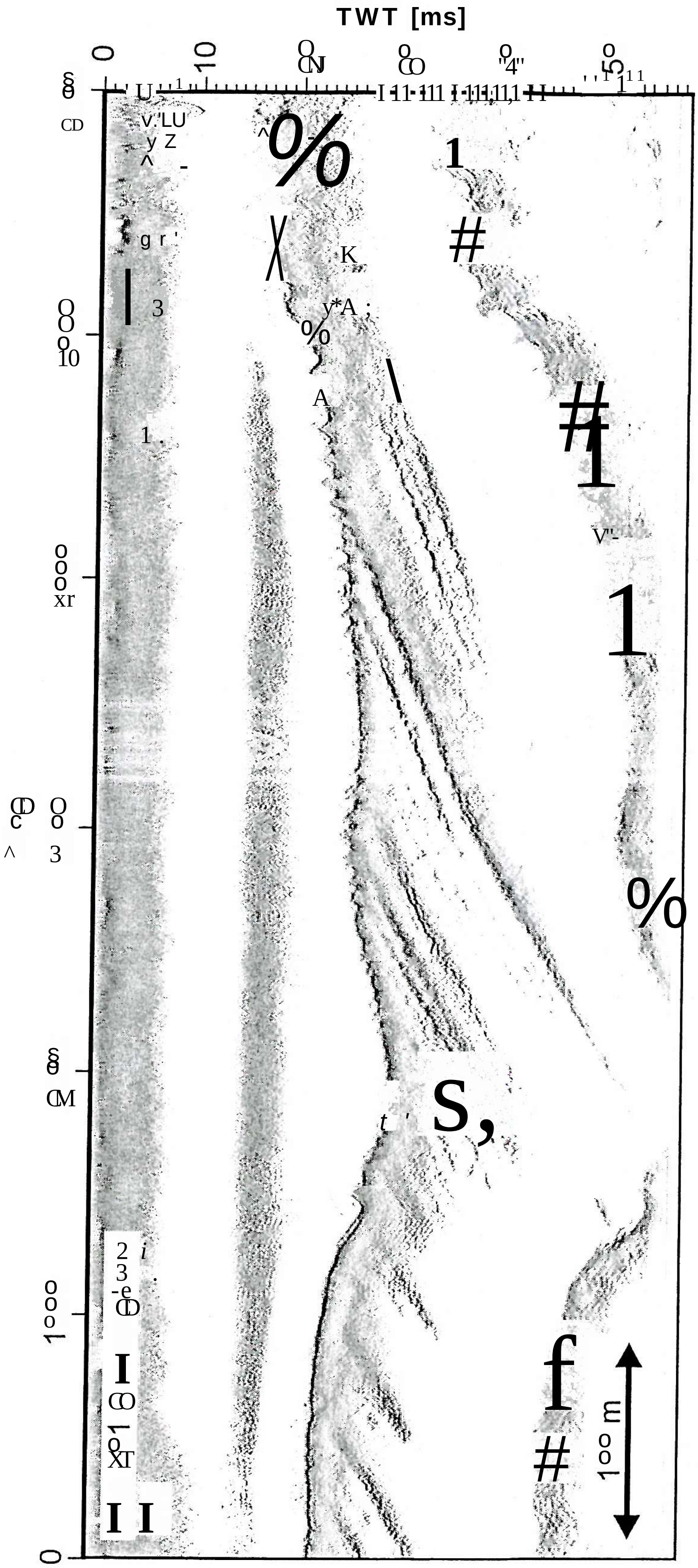

Figure 7.40 Inline 401 with instantaneous amplitude calculation before migration using 8 m aperture radius.

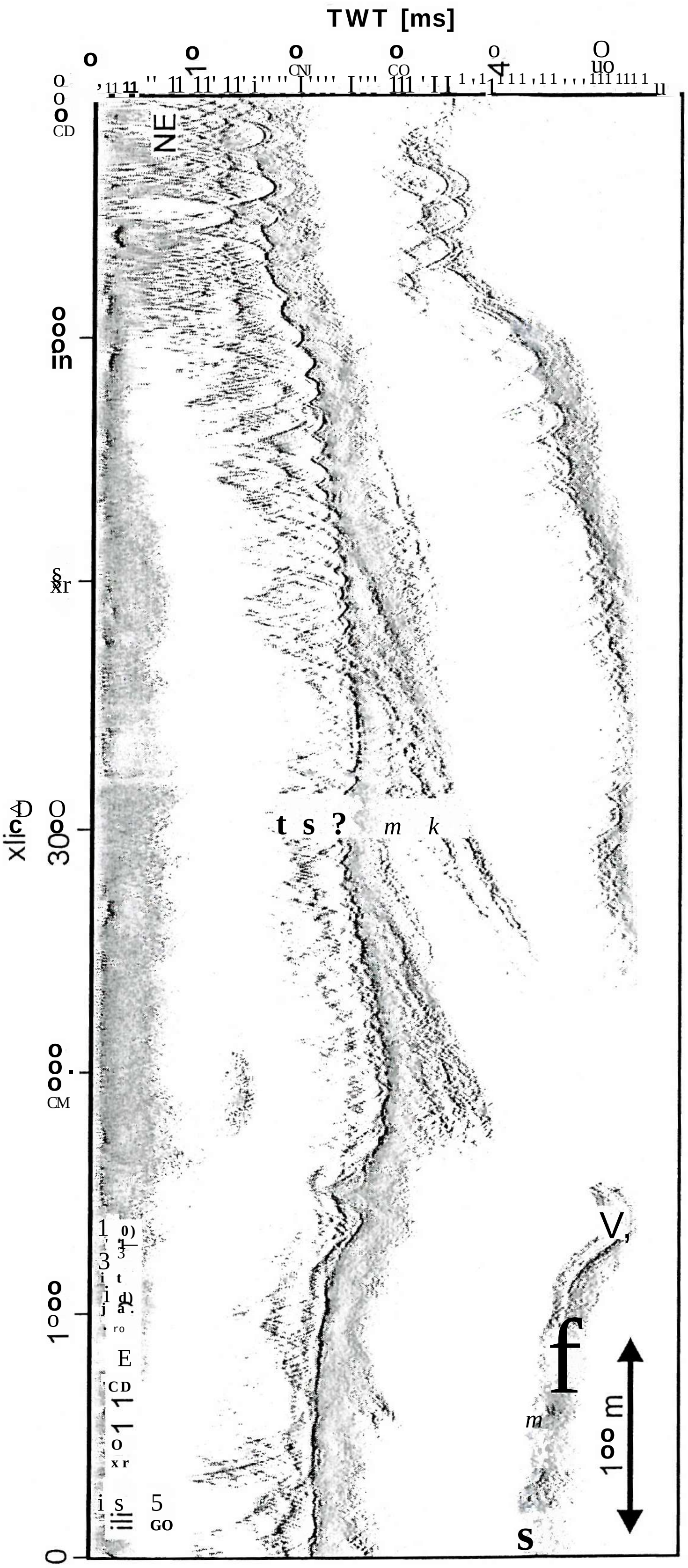

Figure 7.41 Inline 401 with instantaneous amplitude calculation before migration using 16 m aperture radius.

Inline 401 in Figure 7.38, migrated using a 2 m aperture radius, shows a tight, well defined seafloor **reflection** in the south-western part which is less well defined in the north-eastern part were sedimentary waves are imaged. The internal reflectors are more easily identified than in the section with post-migration instantaneous amplitude calculation (Figures 7.14 and 7.15), although they lack continuity. By increasing the aperture radius to 4 m (Figure 7.39) the image quality is improved; the **reflectors** show greater continuity and the sedimentary waves in the north-eastern part are better defined. Further increasing the migration aperture to 8 m leads to deterioration of the quality in deeper parts of the sections below 35 ms, where the internal reflectors that are visible in the section in Figure 7.39 can not be identified. Additionally migration artefacts appear at the **seafloor** reflections in particular between crosslines 0 and 1000 and 5000 and 6000 in the form of 'smiles'. The section in Figure 7.41 using a 16 m migration aperture radius shows further worsening of the image quality with a abundance of 'smiles' at the **seafloor** reflection and disappearance of internal **reflectors** at approximately 5 ms below the seafloor apart from the dominant **reflectors** between crosslines 2000 and 4000 which also show an abundance of smiles and are poorly defined.

The deterioration of the data quality for larger migration apertures is probably due to the inclusion of noisy or badly positioned traces in the migration calculation, which lead to migration 'smiles' and smearing of **reflectors.** For this dataset, with the given trace positioning error, a limited aperture of between 4 m to 8 m leads to the best results. However, for datasets recorded in future surveys, that are expected to contain sufficiently accurately positioned traces, a greater aperture is expected to lead to better image quality. Also the calculation of the instantaneous amplitude before migration is not expected to be necessary to lead to good quality imaging and continuous reflector horizons.

7.3.4 Discussion

The data quality of the 3D data is influenced by three factors:

1. The lower frequency content of the data compared to the data collected with the 2D Chirp system with a mean frequency of 5 kHz as opposed to 7.25 kHz has the following effects on the data resolution:
    a. The maximum vertical resolution limit increases from 0.07 ms TWT (5 cm) to 0.1 ms TWT (7.5 cm) after criterion (2.1).
    b. The Fresnel zone radius increases from 1.44 m to 1.73 m at 20 m depth after equation (3.3).
    c. The maximum horizontal resolution limit increases from 21 cm to 30 cm after collapsing the Fresnel zone by applying migration (section 3.3).
2. The smearing of reflectors caused by the migration algorithm due to bad positioning of the traces and the limited migration aperture radius of 4 m used. The bad positioning can be caused by:
    a. Residual time-shifts as discussed in section 7.3.1.
    b. Insufficient accuracy of the RTK-GPS positioning system. It is possible that due to bad radio connections with the reference station discussed in section 6.3.4 the accuracy was lower than the accuracy derived in Chapter 4.
3. Varying data coverage discussed in section 7.3.2.

The analysis in this section showed that the dominant factor for the data quality is the smearing of horizons by the migration algorithm. It was shown that it varies depending on the dip and topography of the affected reflectors with lower smearing for horizontal reflectors and stronger smearing for dipping reflectors and reflectors which show small scale 3-dimensional topography like sedimentary waves. This results in variable data quality throughout. It showed that low data coverage results in low final image quality although a clear correlation could not be found as the effect is largely disguised by the dominating **reflector** smearing. It was found that the internal reflectors are largely smeared over a horizontal area similar to the migration aperture. The effective vertical and horizontal resolution is governed by the smearing of the horizons. The minimum expected resolution of 0.1 ms (7.5 cm) in vertical and 30 cm in horizontal direction is therefore not achieved. The lack of closely spaced reflectors in horizontal and vertical direction makes it difficult to assess the resolution quantitatively but it is expected to vary in a manner similar to the data quality. In particular the vertical resolution is expected to be higher in areas with flat reflectors than for dipping reflectors. The maximum value for the horizontal resolution can be as large as the migration aperture diameter of 8 m over which reflector smearing is occurring.

7.4 Interpreted horizons

The TWT of the seafloor and five internal horizons R1 to R5 shown in Figure 7.4 have been determined using the picking tool of the GeoFrame software. Their locations are also marked in the inline and crossline sections and time slices in sections 7.2.2, 7.2.3 and 7.2.4 respectively and in Figure 7.30.

7.4.1 Seafloor

Figure 7.42 shows the picked seafloor horizon for the entire imaging grid (Figure 7.1).

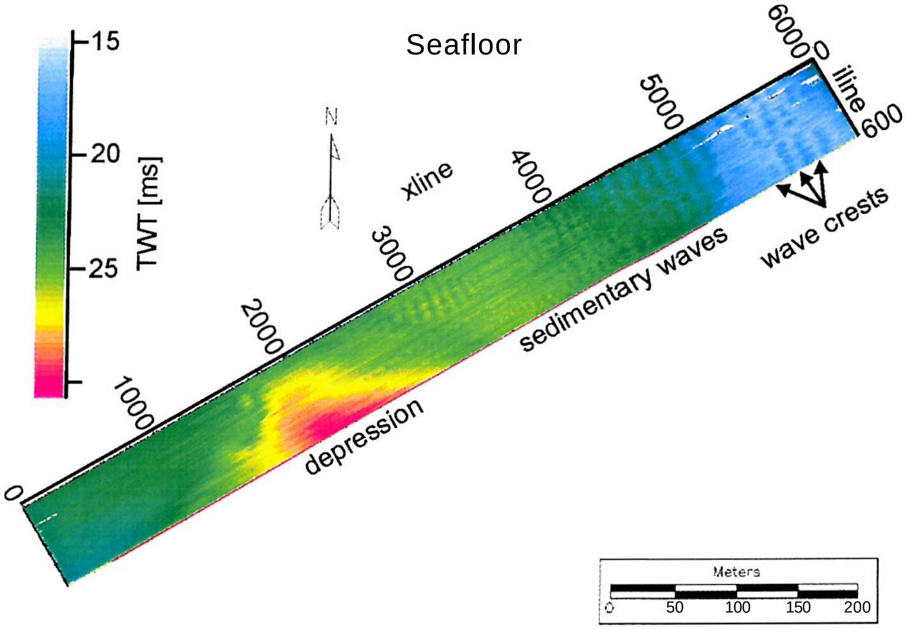

Figure 7.42 Seafloor reflector in the 3D Chirp data volume. A depression in the south-western part of the survey area and sedimentary waves on the north-eastern side of the depression with increasing amplitudes and wavelength towards the north-east are apparent.

The seafloor is characterised by a flat topography in the south-western part (xline 1 to 1500), which is adjacent to a depression that is widening towards the south-east with the greatest water depth in its centre equalling approximately 24 m (32 ms TWT) (xline 1500 to 3000).

The area to the north east of the depression is dominated by sedimentary waves with increasing amplitude and wavelength towards the north-east. The wave crests are aligned in crossline direction, perpendicular to the prevailing tidal current direction, parallel to the inline direction. Trough to crest heights range from some decimetres (< 1 ms) on the north-eastern flank of the depression to approximately 2.3 m (3 ms) in the north-eastern limits of the area. The wavelengths range from approximately 2 m on the north-eastern flank of the depression to approximately 20 m in the north-eastern limit of the area. This corresponds to the findings of Langhorne et al. (1986) who investigated the sedimentary waves in the study area.

7.4.2 Internal horizons

The picks for reflection horizons R1 to R5 are shown in Figures 7.43 to 7.48 respectively. Average dip and strike for the horizons have been calculated on the basis that they are planar. This is equivalent to the assumption that they are linear in inline and crossline sections and time slices (Sections 7.2.2, 7.2.3 and 7.2.4 respectively).

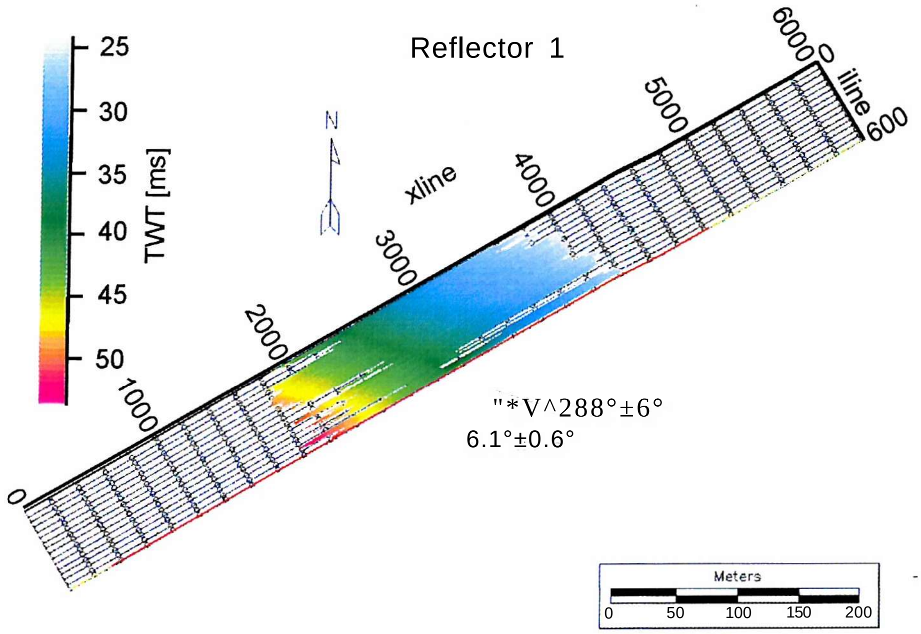

Figure 7.43 Reflector R1 of the 3D Chirp data volume. See Figure 7.4 for its position in the data volume. The strike and dip of the assumedly plane horizon are 288°±676.1°±0.6°.

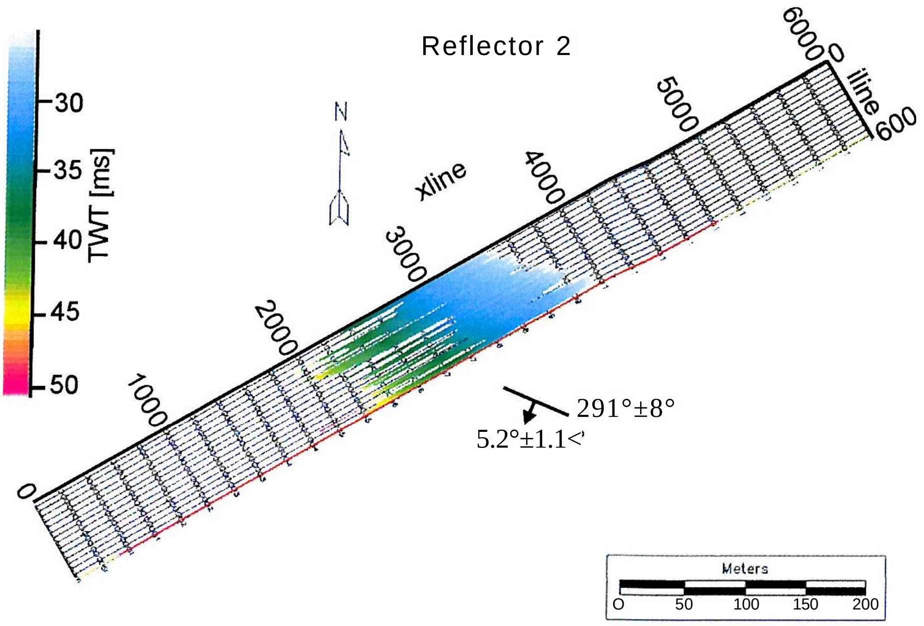

Figure 7.44 Reflector R2 of the 3D Chirp data volume. See Figure 7.4 for its position in the data volume. The strike and dip of the assumedly plane horizon are 291°±8^0/5.2°±1.1°.

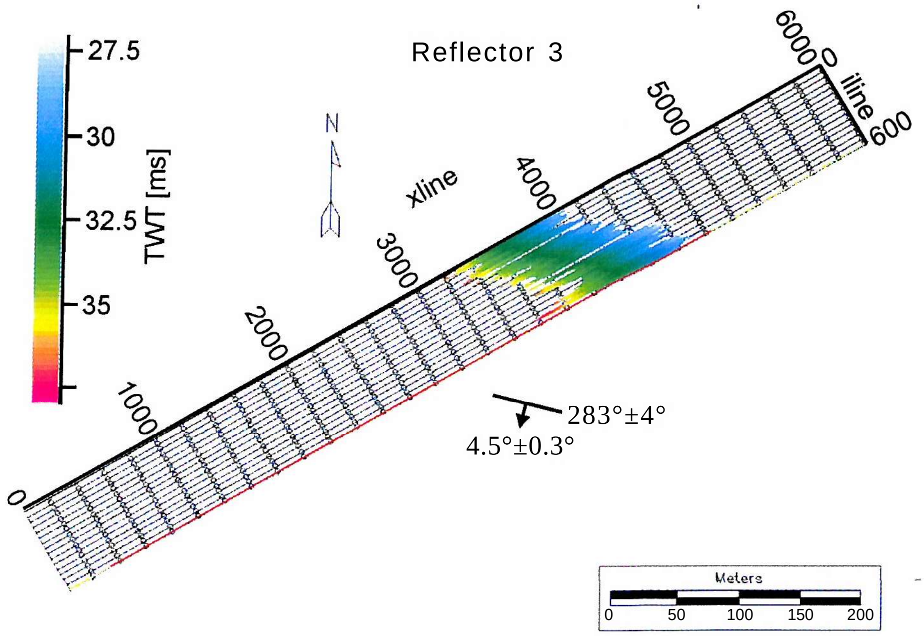

Figure 7.45 Reflector R3 of the 3D Chirp data volume. See Figure 7.4 for its position in the data volume. The strike and dip of the assumedly plane horizon are 283°±474.5°±0.3°.

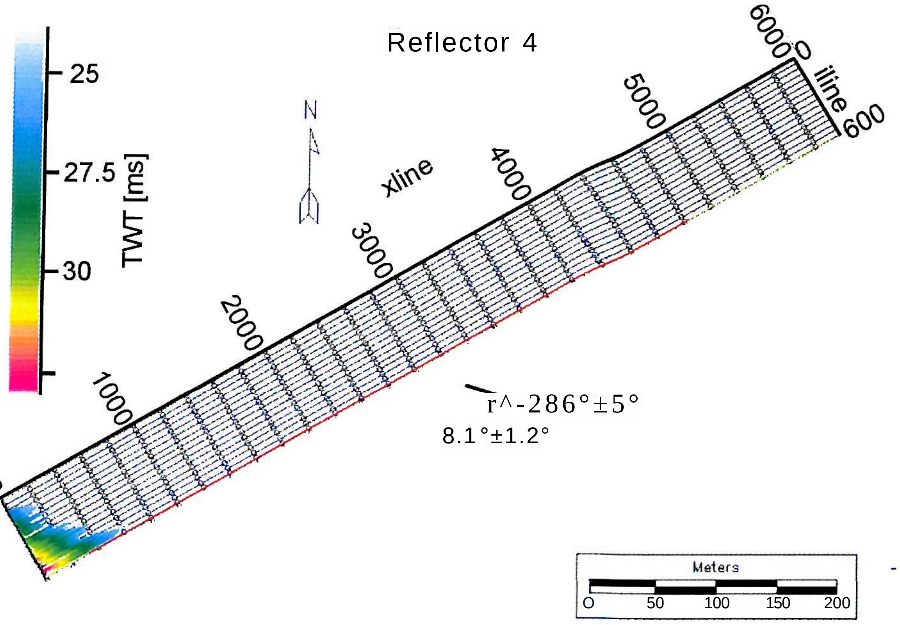

Figure 7.46 Reflector R4 of the 3D Chirp data volume. See Figure 7.4 for its position in the data volume. The strike and dip of the assumedly plane horizon are 286°±578.1°±1.2°.

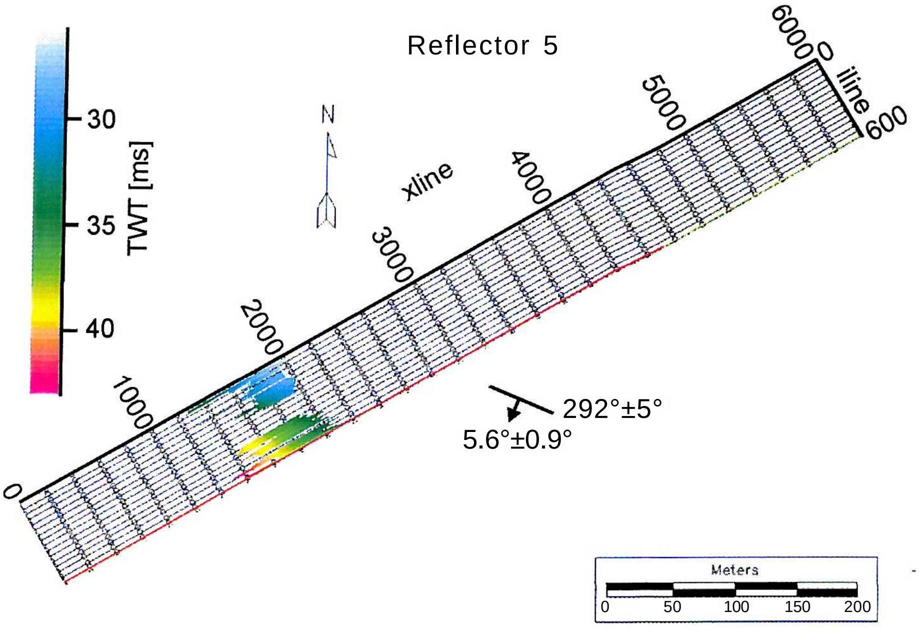

Figure 7.47 Reflector R5 of the 3D Chirp data volume. See Figure 7.4 for its position in the data volume. The strike and dip of the assumedly plane horizon are 292°±5°/5.6°±0.9°.

Table 7.3 summarises the dip and strike of the horizons.

Horizon	Stike	Std dev	**Dip**	Std dev
R1	**288**	6	6.1	**0.6**
R2	**291**	8	5.2	1.1
R3	**283**	4	**4.5**	0.3
R4	**286**	5	**8.1**	1.2
R5	**292**	5	5.6	**0.9**

Table 7.3 Attitude (dip and strike) values for the interpreted horizons (Figure 7.4). The horizons are assumed to be plane for this analysis.

7.5 Geological context of the imaged strata

7.5.1 Geology of Isle of Wight

The Solent and the island form part of the Wessex-Channel basin. Exposures of Cretaceous and Palaeogene outcrop on the island partly covered by remnant Neogene and Quaternary deposits (Insole et al., 1998). Figure 7.48a shows a geological map of the island. The exposed geological formations are sedimentary rocks, deposited in shallow marine, estuarine, deltaic, lacustrine and **lagoonal** environments during sea-level fluctuations in the represented geological times.

The islands geological structure is dominated by series of folds orientated in east-western direction (Figure 7.48b). Daley and Edwards (1971) suggest that warping of the Isle of Wight began during the Lower Oligocene, forming an early Bouldnor syncline and Porchfield anticline. Subsequently the main phase of folding took place during the Miocene, linked to the Alpine orogeny, forming the east-west orientated folds.

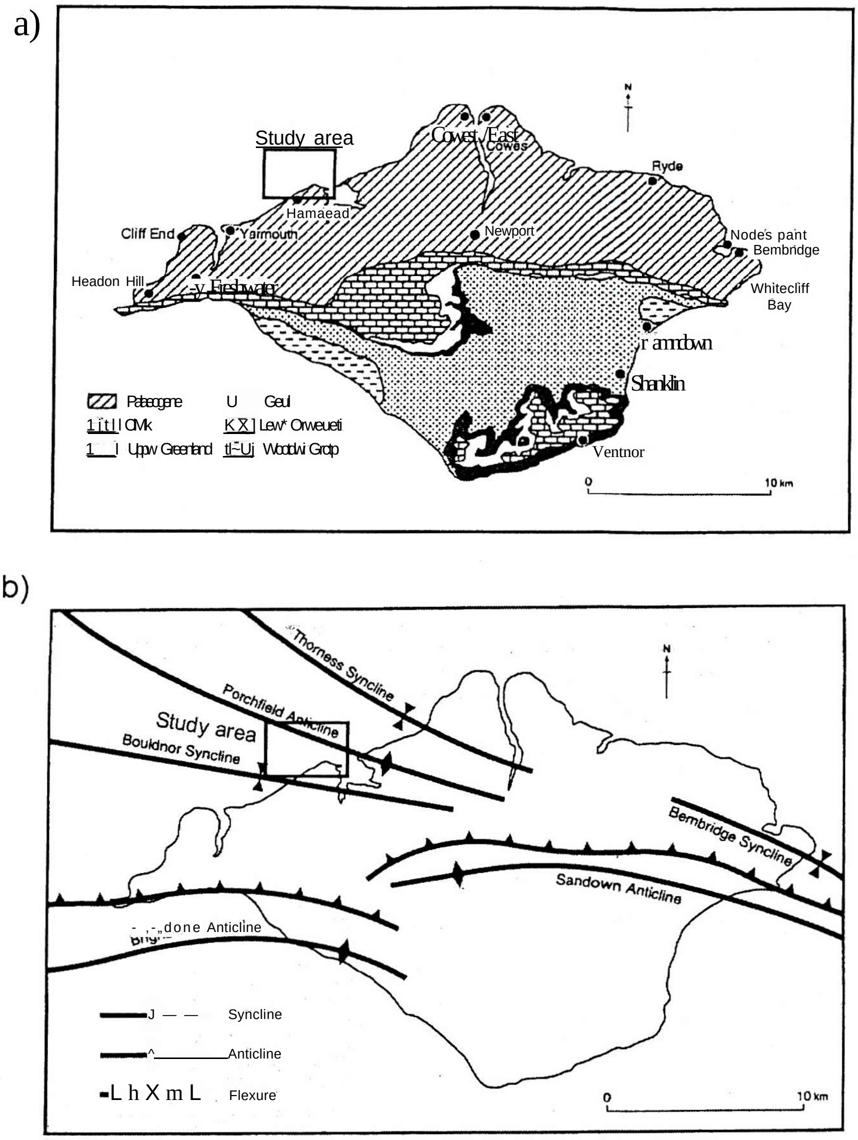

Figure 7.48 a) Geological map of the Isle of Wight. Exposures of Cretaceous (south) and Palaeogene (north) outcrop on the island partly covered by remnant Neogene and Quaternary deposits, b) Structural geology of the Isle of Wight. The island's geology is dominated by an east-west orientated fold system. Both figures adapted from Insole et al. (1998). The position of the study area is marked in both figures.

7.5.2 Stratigraphy and lithology in the study area

The study area, highlighted in Figure 7.48, lies in the West Solent off the north coast of the Isle of Wight on the eastern flank of the Bouldnor syncline in an area of Palaeogene outcrops.

Beside the 3D data volume, the 2D seismic lines used for the experimental source sweep comparison discussed in Chapter 2 were collected in the area together with three additional

2D lines, collected in July 2004. The available seismic data are shown in the survey area map in Figure 7.49.

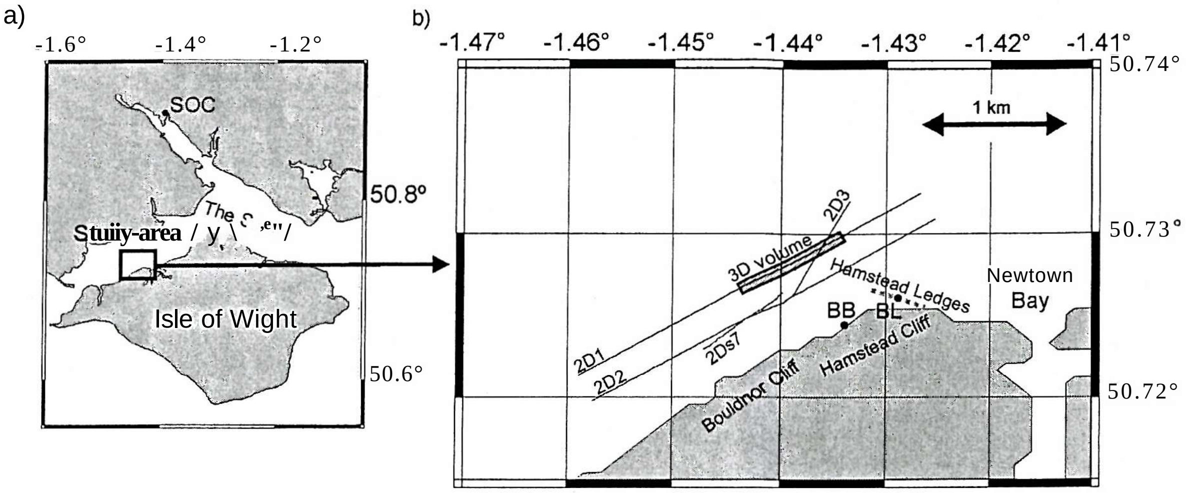

Figure 7.49 a) Location of the study area off the north coast of the Isle of Wight in the East Solent, b) The study area off Bouldnor and Hamstead Cliff west of Newton Bay. Terrestrial outcrops show the Late Eocene Bembridge Limestone Member (BL), that forms the Hamstead Ledges and the Black Band (BB), a band of black clay in the Hamstead member (Table 7.4). Note the position of the 3D imaging grid together with the 2D Chirp lines 2D1, 2D2, 2D3 and 2DS7, which was used in the source signature comparison discussed in Chapter 2.

The survey area is located off Bouldnor and Hamstead Cliff west of Newton Bay. On the beach and cliff outcrop strata of the eastern flank of the Bouldnor syncline is represented, which is also imaged in the seismic data. The onshore geology was studied in an excursion in which Tim Henstock, Jon Bull, Robert Luthwaite and Ian West, an expert on the local geology, took part together with the author.

The eastern flank of the eroded Bouldnor syncline contains Oligocene and Eocene stratigraphy including the Bembridge Limestone member (BL) forming a seabed ridge known as Hamstead Ledges visible both in terrestrial outcrops (Figure 7.52) and seismic sections, thus allowing a correlation of the seismic sections with descriptions of the onshore geology. In addition to the Bembridge Limestone member the Black Band (BB), a carboniferous clay forming the base of the Hamstead member was located on the beach outcrop.

Figure 7.50 shows the stratigraphy of the late Paleogene (Eocene, Oligocene) of the Isle of Wight, together with estimated thicknesses of a selection of members after White (1921).

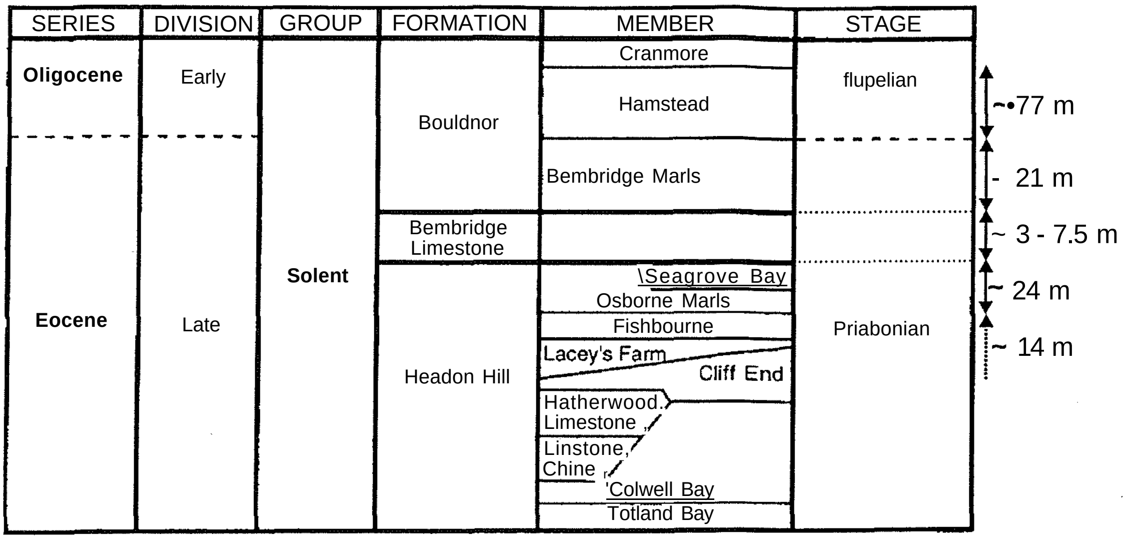

SERIES	DIVISION	GROUP	FORMATION	MEMBER	STAGE	
Oligocene	Early	Solent	Bouldnor	Cranmore	flupelian	~•77 m
				Hamstead		
Eocene	Late			Bembridge Marls	Priabonian	- 21 m
			Bembridge Limestone			~ 3 - 7.5 m
			Headon Hill	Seagrove Bay		~ 24 m
				Osborne Marls		
				Fishbourne		~ 14 m
				Lacey's Farm Cliff End		
				Hatherwood Limestone		
				Linstone Chine		
				Colwell Bay		
				Totland Bay		

Figure 050 Palaeogene stratigraphy of the Isle of Wight adopted from Insole et al. (1998) with approximate thicknesses of members from White (1921).

The lithology of the members is described by White (1921) for different outcrops on the Isle of Wight.

The Hamstead member is, as its name suggests, best represented at Hamstead Cliff. This member consists of bands of clays, loams, sands and shales, deposited in brackish and freshwater environments with marine deposits towards the top. The band of carbonaceous clay at the bottom, named the black band is considered to represent the **Eocene**-Oligocene boundary. Table 7.4 shows the detailed lithology of the Hamstead member at Hamstead **Cliff.**

Hamstead member lithology	appr. thickness [m]
Cranmore member	
Pale bluish clay (much weathered)	**3.35**
Carbonaceous and ferruginous clays	0.3
Stiff blue clay	**2.13**
Black clay	**0.15**
Shaly clay	**1.37**
Shell bed	**1.22**
Shaly clay	**0.23**
Stiff blue clay, carbonaceous at the base	**0.46**
Laminated carbonaceous clay and sand partings	**0.3**
Green clay	1.07
Carbonaceous clay	0.15
Mottled red and green clay	**3.35**
Obscure mottled clay	**5.48**
Carbonaceous seams	**0.61**
Carbonaceous clays	**4.57**
Bluish loam	0.3
Clay with seeds	**0.91**
Obscure	**1.22**
Clays	**6.09**
Obscure	**1.52**
Laminated carbonaceous clays with freshwater molluscs	**0.53**
Green and red marls	**2.44**
Obscure	**18.28**
White band: green clays and white shell marls	**1.83**
Green clay with lines of ironstone nodules at base	**2.13**
Obscure	**7.62**
Nemature bed: black or slate coloured carbonaceous clay	**0.91**
Green clay	**0.46**
Black laminated clay	**0.15**
Green clays	**1.22**
Mixed black and green clay	0.15
Green clays	**6.09**
Black band: black clays	**0.15**
Bembridge Marls: Green clays with large bands of *Paludina lenta*	
	Total: -77

Table 7.4 Lithology of the Hamstead member at Hamstead Cliff. Adopted after White (1921).

The underlying member is the Bembridge Marls consisting of shelly brackish and freshwater clays and marls with some bands towards its base containing marine fossils. Table 7.5 shows the detailed lithology of the Bembridge Marls member at Hamstead.

Bembridge Marls member lithology	appr. thickness [m]
Hamstead series: black band	
Green clays with large bands of *Paludina lenta*	1.37
Ironstone	**0.23**
Clay	**1.22**
Clay with *Paludina*	**1.37**
Concretionary ironstone	**0.07**
Clay with *Paludina*	1.37
Clay with two or three small black bands	**0.76**
Ferrugininous brown sandy clay, thickness variale	**0-0.15**
Thin bituminous bands with reed-like plants and a layer of *Paludina lenta* below, filled with green clay	**0.03**
Grey clay with short zones of *Melania forbesi* and nodules containing *Paludina lenta*	**0.91**
Band of scattered nodules of iron pyrites, overlying verdigris green clays with bands of *Paludina lenta* and *Melania forbesi*	**1.52**
Dark-grey clays with *Paludina* and numerous oval seed vessels, and containing thin carbonaceous sandy bands with (reed-like) plant impressions.	**0.91**
Bands of *Melania turritissima (Potamaclis), Planorbis* and *Paludina*	**0.03**
Greenish shaly clay with concretions of indurated marl	**1.22**
Hard shelly band chifly made up of Melania turritissima, a few Melanopsis and fragment of fish	**0.08**
Pale-grey clay, with bands of compressed shells	**0.61**
Sandy bands full of bi-valves	**0.23**
Pale greenish shaly clay with a thin band of Melania turritissima and a bitumous band at 1 m	**1.83**
Sandy clay	**0.11-0.18**
Bluish irregular shaly clay	**0.91**
Indurated shaly marly clay	**1.37**
Greenish clay with fish remains	**0.23**
Green clays	**0.76**
Verdigris green clay	**0.30**
Bright green clays	**0.61**
Bluish-green clays	**0.46**
Hard sandy marl	0.15
Verdigris green clay	**0.46**
Greenish clay	**0.30**
Green clays	**0.23**
Dark clay with soft green sandy concretions	**0.46**
Blue clay	**0.30**
Bembridge limestone	
	Total -21

Table 7.5 Lithology of the Bembridge Marls member at Hamstead Cliff. Adopted after White **(1921).**

The next member in the down going succession is the Bouldnor Limestone consisting of freshwater limestones intercalated with shaly clays and marls. Although it outcrops at Hamstead, forming the Hamstead Ledge, it is described by White (1921) at Node's Point close to Bembridge (see Figure 7.48 for map).

Bembridge Limestone member	appr. thickness [m]
Bembridge Marls: blue clay	
Limestone, irregular and marly	**1.22**
Dark laminated clay	**0.38**
Compact greenish clay	**0.23**
Earthy limestone, the upper part of the bed soft and of variable thickness	**0.46-0.61**
Hard green marl	**0.76**
Osborne Marls	
	Total: ~ 3

Table 7.6 Lithology of the Bembridge Limestone member at Node's Point (see Figure 7.48 for map). Adopted after White (1921).

The Bembridge Limestone outcrops at various places on the island including Whitecliff Bay in the west (Figure 7.48), Hamstead, Cowes, Ryde, Fishbourne and Node's point in the east and varies in thickness in the outcrops from 2.5 m to 7.5 m with and average of about 3 m.

The Bembridge Limestone overlies the Osborne Marls member, which consist of brackish water sediments with few marine fossils. The member's lithology mainly consists of clays and marls. Table 7.7 shows the detailed lithology of the Osborne Marls member at Headon Hill (see Figure 7.48 for map).

Osborne Marls member	appr. thickness [m]
Bembridge limestone	
Whitish (passing into red and blue) marls with occasional hard bands and courses of nodular concretions of light-grey argillaceous limestone	**12.20**
Grey shale with ferruginous nodular band	
Yellow, red and blue sandy clays	**0.91**
Thick concretionary limestone with siliceous concretions.	**0.91**
Greenish-white calcareous clay	**5.49**
Sandy ferruginous band	**1.22**
Upper Headon Beds: blue and yellow clays and marls	**0.61**
	Total: ~ 21

Table 7.7 Lithology of the Osborne Marls member at Headon Hill (Figure 7.48). Adopted after **White (1921).**

The limestone bed disappears to the north of this location and is missing in the outcrop of the member at Cliff End but is again present in an outcrop in Whitecliff Bay.

The underlying lithology is named Upper Headon Beds by White (1921) and incorporates the Fishbourne and the Lacey's Farm/Cliff End members in the stratigraphy after Insole et al. (1998) (Figure 7.50). The lithology consists of thinly bedded marls and clays with subordinate bands of limestone and sands deposited in brackish and freshwater environments. Table 7.8 lists the detailed lithology of the Upper Headon Beds at Headon **Hill.**

Upper Headon Hill Beds	Member after Insole et **al. (1998)**	appr. thickness [m]
Osborne Marls: sandy ferruginous band		
Blue and yellow clays and marls (Fishbourne member)	Fishbourne	**4.58**
Variegated clays with ironstone band in centre of the bed	Lacey's Farm/Cliff End	**0.38**
Brown and green clays	"	**1.01**
Limestone with carbonaceous, sandy, shelly and rubbly beds	"	**2.44**
Bluish and purple clays passing into limestone	"	**1.52**
Limestone with many shells and lines of nodular concretions in places	"	**3.05**
Greenish white compact sands	"	**0.61**
	"	**Total: ~ 14**

Table 7.8 Lithology of the Upper Headon Hill Beds at Headon Hill (Figure 7.48). Adopted after White (1921). Note the naming of the members after Insole et al. (1998).

In an outcrop of the Upper Headon Hill Beds in Whitecliff Bay the total thickness increased to 18 m.

7.5.3 Geological interpretation of the seismic data

The aim of the interpretation is to broadly correlate the structures imaged in the seismic section with the described onshore geology. Therefore it is not intended to correlate each bed of the lithology to a seismic reflector but merely link the reflectors to geological members.

By overlying swath bathymetry data and the position of the 2D seismic lines with an **aerial** photograph of the Hamstead Ledge area enables the correlation of the Bembridge Limestone member (BL), that forms the Hamstead Ledges as identified in the onshore geology, with seismic section 2D2 (Figure 7.55).

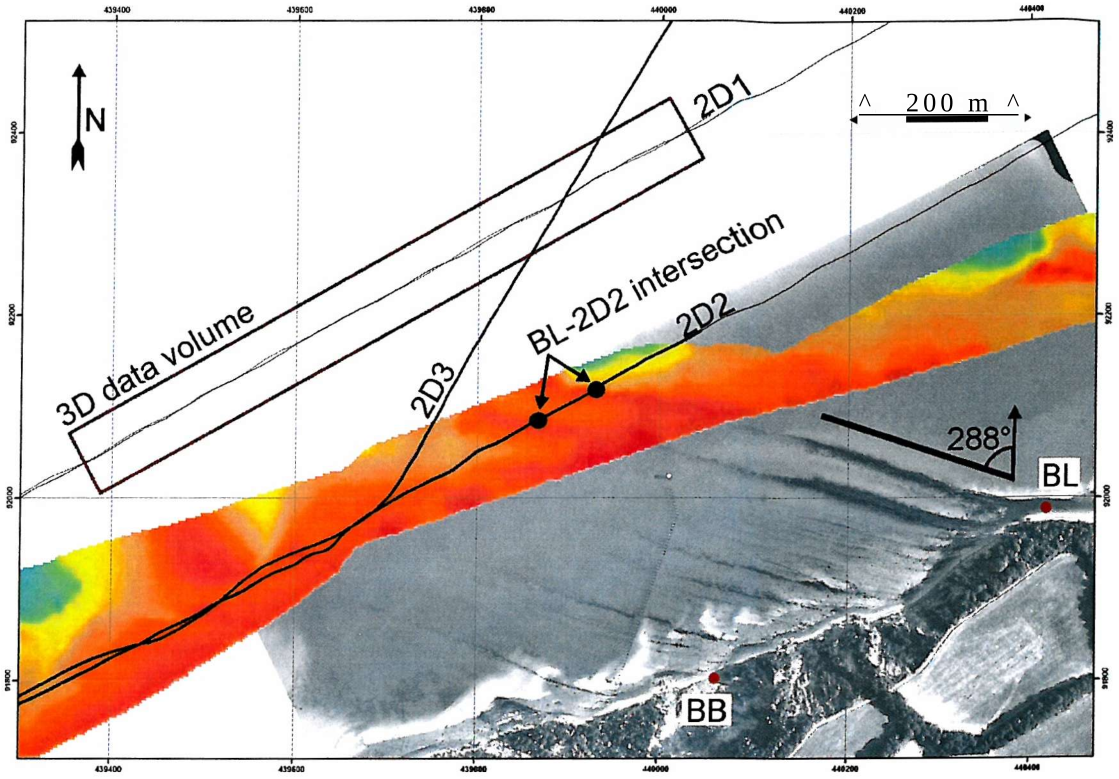

Figure 7.51 Aerial photograph of the Hamstead Cliff area with overlaid bathymetry data and positions of seismic lines 2D1, 2D2, 2D3 and the 3D Chirp data volume. The beach outcrops of the black band bed (BB) marking the Eocene-Oligocene boundary (Table 7.4) and the Bembridge Limestone member (BL) (Table 7.6) forming the Hamstead Ledges are marked. The strata, striking approximately 288° are clearly visible in the shallow water. The Bembridge Limestone member can be identified in the bathymetry data and its intersection with the seismic line 2D2 is marked.

Figure 7.52 shows a photograph of the Hamstead Ledges at the marked location.

Figure 7.52 Hampstead Ledges at low tide looking towards the north-west. These topographical highs made up of the Bembridge Limestone member can be identified in the seismic section 2D1, 2D2 and 2D3 (Figures 7.54, 7.55 and 7.57c).

Figure 7.49 shows a map of the study area containing the seismic data and positions of terrestrial outcrops.

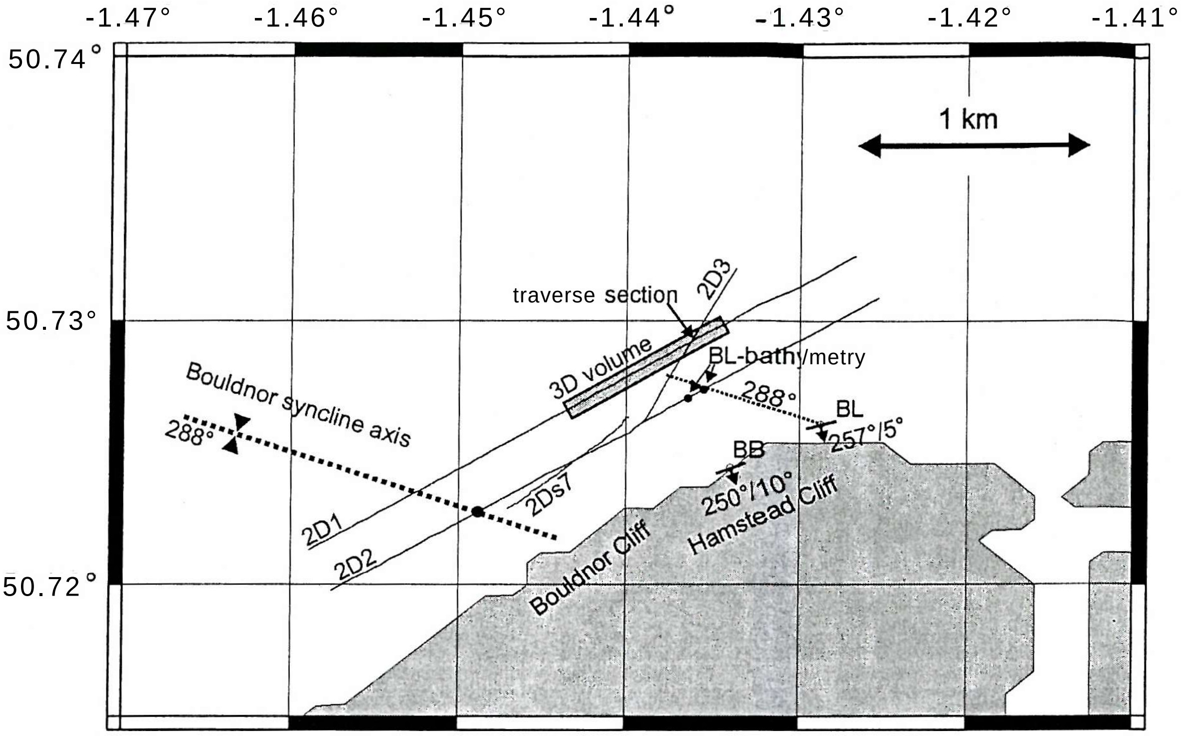

Figure 7.53 The study area off Bouldnor and Hamstead Cliff with positions available seismic data. Terrestrial outcrops show the Late Eocene Bembridge Limestone Member (BL), that forms the Hamstead Ledges. The strike and dip directions measured on the heavily weathered terrestrial outcrops are 257°±4075°±5° and 250°±40710°±5° respectively. The positions of the intersection between the topographic highs of the Bembridge Limestone member and seismic line 2D2 from Figure 7.55 are marked. The approximate position of the Bouldnor syncline axis and its intersection with seismic line 2D2 from Figure 7.56 is also marked.

The strike and dip direction of the Bembridge Limestone was measured by the author as 25775° in the beach outcrop. Due to the heavily weathered state of the strata an error of 40° for the strike direction and 5° for the dip direction is estimated. The aerial photograph suggests a strike of approximately 288°. From the analysis of the reflectors in the 3D data volume (section 7.3) and average strike of 288° and average dip of 5.9° was found. Extending the Bembridge Limestone member outcrop in this direction it coincides with the position of the intersection between the bathymetric high and seismic line 2D2 (Figure 7.51), verifying a strike direction of 288° for the strata.

Figure 7.54 and 7.55 show the seismic sections of line 2D1 and 2D2 respectively, Figure 7.56 shows a line drawing of the section 2D2 and Figure 7.57 shows the sections of line 2D3, 2Ds7 and inline 301 from the 3D data volume. For all sections the 1.5-13 kHz sine-squared envelope source sweep (S7) was used (Chapter 2). The vertical distance between the reflector beds was calculated by assuming plane beds with a constant dip and strike. This assumption is justified since in the areas of the sections studied the reflectors show little variation in their apparent dip in particular close to the seafloor, which is also confirmed in the aerial photograph. The constant dip and strike values of 5.9° and 288° respectively used are given as the average values from the **horizons** R1 to R5 described in section 7.4. The corresponding approximate vertical distance between beds, dependant on the orientation of the sections, is marked in the Figures. A number of horizons are highlighted with arrows inclined with the respective apparent dip for the section.

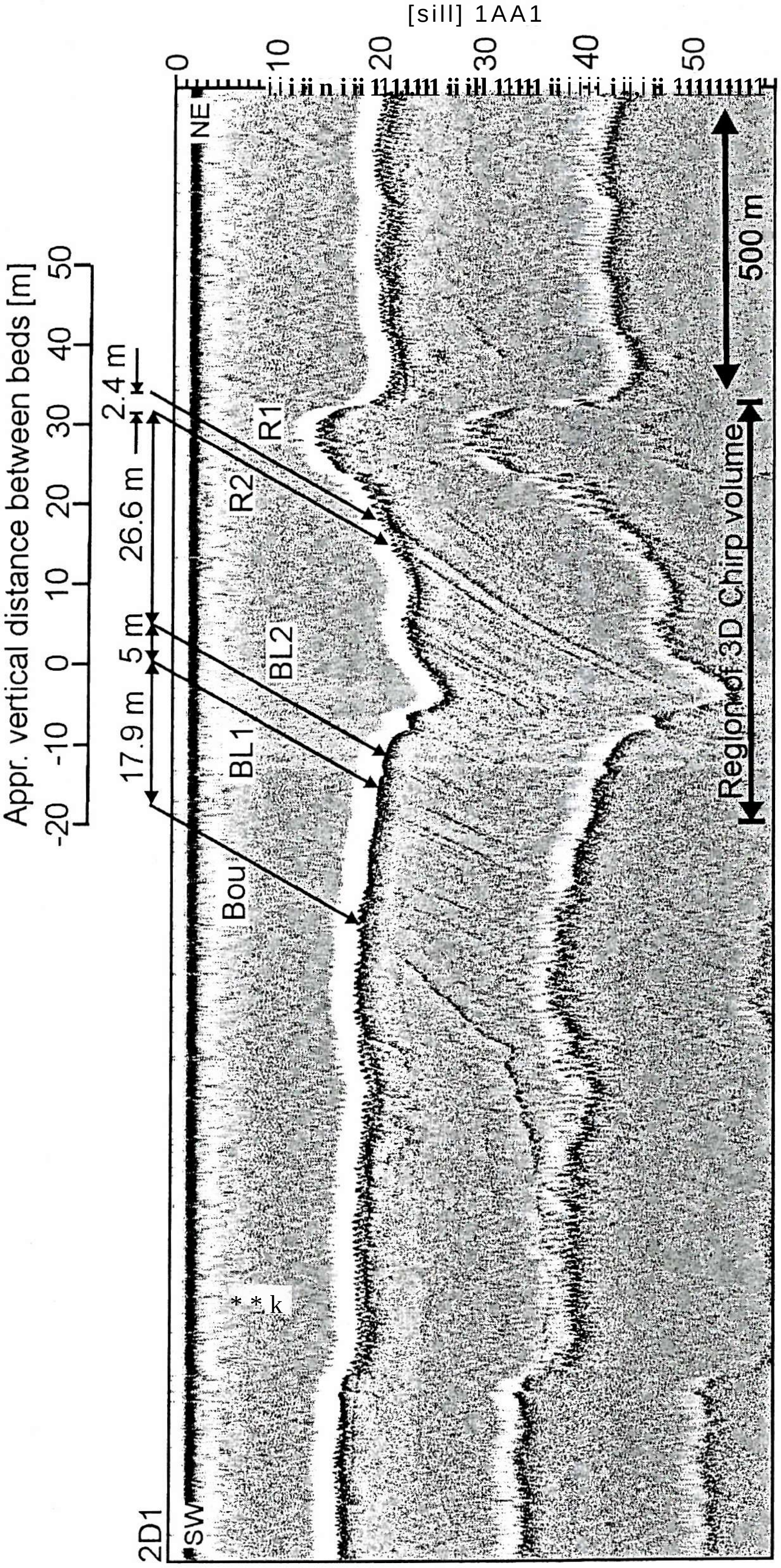

Figure 7.54 2D seismic section of line 2D1 (Figure 7.53). The estimation of vertical distances between reflectors is based on the assumption that the reflectors are plane and have a strike and dip of 28875.9°. The arrows show the resulting apparent dip. See Table 7.10 for correlation of marked horizons.

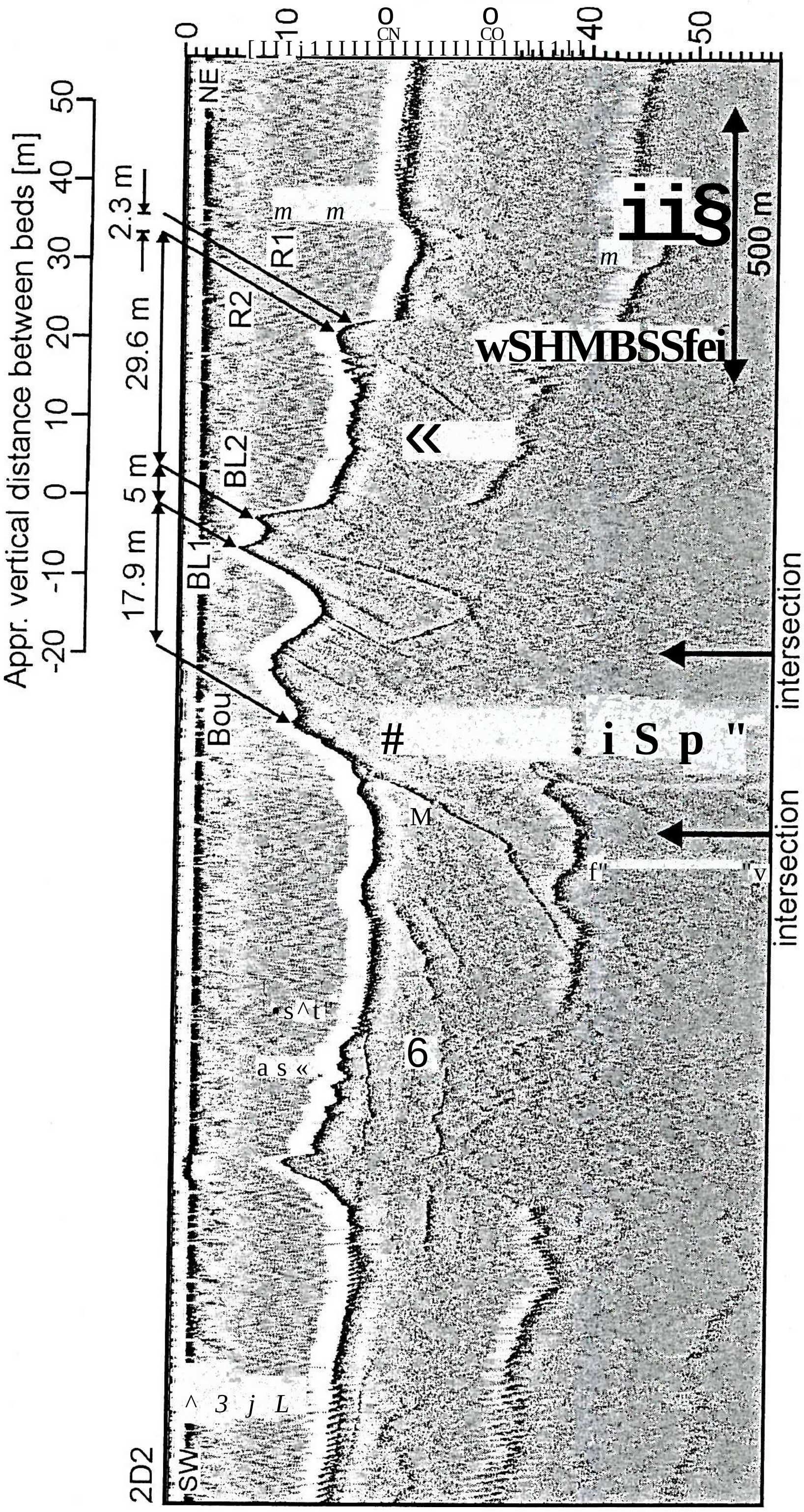

Figure 7.55 2D seismic section of line 2D2 (Figure 7.53). The estimation of vertical distances between reflectors is based on the assumption that the reflectors are plane and have a strike and dip of 28875.9°. The arrows show the resulting apparent dip. See Table 7.10 for correlation of marked horizons.

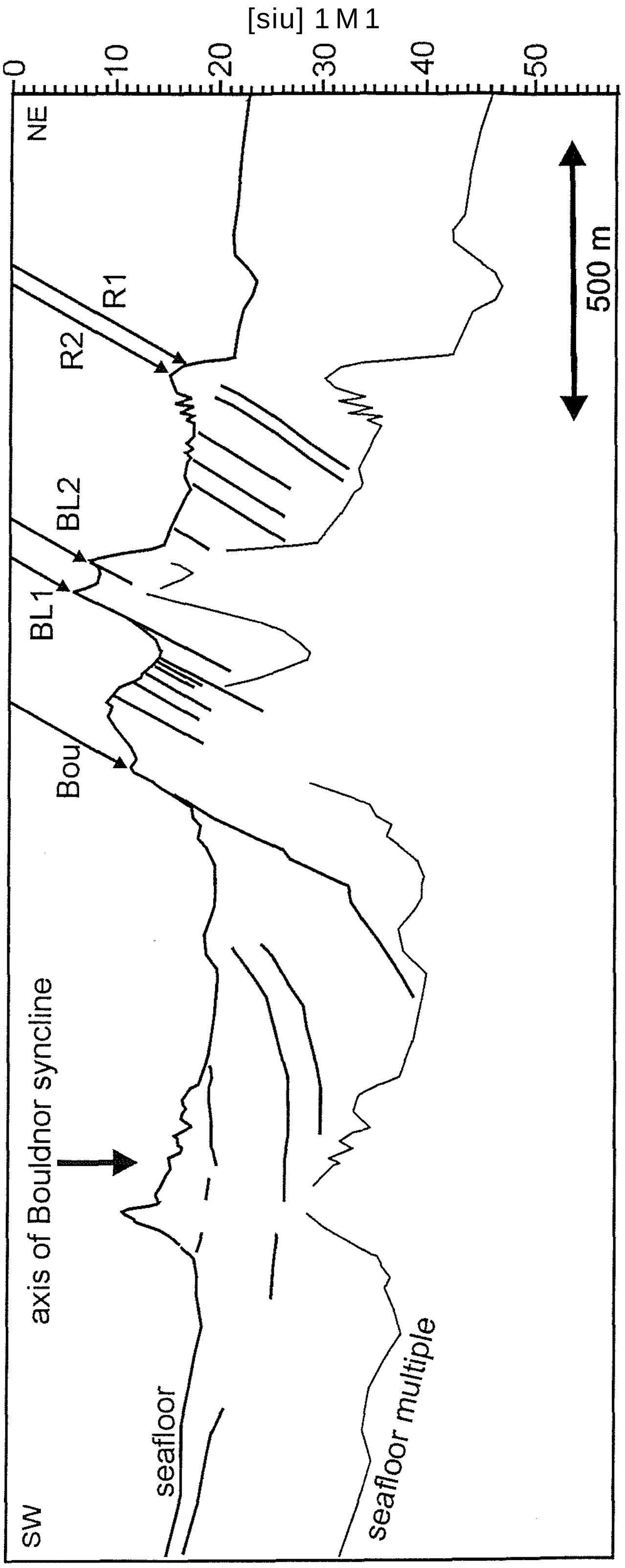

Figure H56 Line drawing for 2D seismic section of line 2D2 shown in Figure 7.55. See Table 7.10 for correlation of marked horizons. The estimated position of the axis of the Bouldnor syncline is indicated.

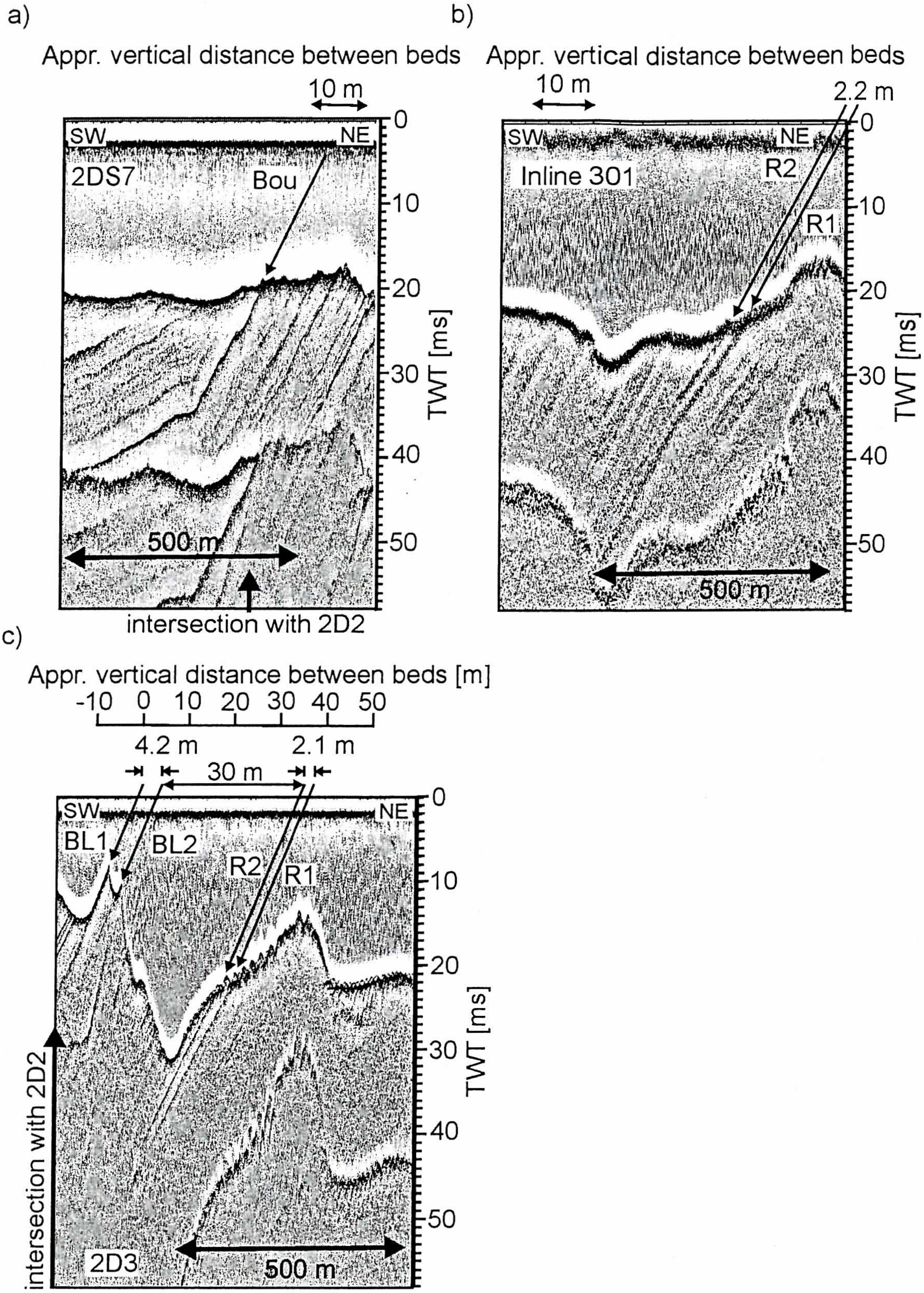

Figure 7.57 2D seismic sections. The estimation of vertical distances between reflectors is based on the assumption that the reflectors are plane and have a strike and dip of 288°/5.9°. The arrows show the resulting apparent dip for each section. a) 2DS7. b) inline 301 from the 3D Chirp data volume. c) 2D3. See Figure 7.53 for position of lines. See Table 7.10 for correlation of marked horizons.

The Bembridge Limestone member (BL) can be identified in sections 2D1, 2D2 and 2D3 (Figures 7.54, 7.55 and 7.57 respectively). Towards the north-east of this member the older Osborne Marls are imaged, which have a thickness of approximately 24 m at their terrestrial outcrop at Headon Hill (Figure 7.48 and Table 7.7). Below, further to the north-east the Upper Headon Beds, including the Fishbourne and Lacey's Farm/Cliff End members, are imaged (Figure 7.48 and Table 7.8). These have a thickness of approximately 14 m at their terrestrial outcrop at Headon Hill. In sections 2D1, 2D2, 2D3 and inline 301 from the 3D data volume two strong **reflection** horizons, interpreted as R1 and R2 in the 3D data volume (section 7.2.1), are apparent. Their average approximate vertical distance from the bottom of the Bembridge Limestone member, interpreted as BL2 in in sections 2D1, 2D2 and 2D3, is 27.3 m. The bed at this vertical distance from the top of the Bembridge Limestone member in the described terrestrial geology is a limestone in the Upper Headon Hill Beds of approximately 2.44 m thickness (Table 7.8). The average approximate vertical separation of R1 and R2 in the sections is 2.3 m. The position and thickness of the imaged bed suggest that they coincide with the limestone bed of the Upper Headon Hill Beds. Additionally the over- and underlying strata consist of clays and marls, similar to the strata above and below the Bembridge Limestone, which suggests that it should show similar reflection characteristics to this member. However, in the lower part of the Upper Headon Hill Beds (Lacey's Farm Limestone) is a second limestone bed of approximately 3.1 m thickness, which, following this postulation does not show an obvious representation in the seismic sections. From the sections it can be deduced that the strata imaged in the inline 301 section and therefore in the 3D data volume are part of the Bembridge Marls, Osborne Marls and Upper Headon Beds (Fishbourne, Lacey's Farm/Cliff End members).

Towards the south-west of the Bembridge Limestone member the younger strata of the Bembridge Marls and Hamstead members are imaged. In an average vertical distance of 17.9 m in sections 2D1 and 2D2 a prominent reflector is present (Bou), also apparent in section 2Ds7. In the terrestrial outcrop this vertical distance corresponds to a clay bed at the top of the Bembridge Marls member (Table 7.5). Above this approximately 1.22 m thick bed lay an approximately 23 cm thick ironstone bed and 1.37 m below it an approximately 7 cm thick bed of concretionary ironstone. It is possible that the boundary between the clay and ironstone band is imaged as a strong **reflector** as seen in the seismic sections. The top ironstone band lies approximately 1.37 m below the black band in the Hamstead member (Table 7.4), which marks the Oligocene Eocene boundary. Therefore the imaged strata further to the south-west, towards the centre of the Bouldnor syncline, constitutes to the Hamstead member.

Table 7.9 summarises the correlation results.

Reflector	Correlated strata	Lithological description
BL1	Top Bembridge Limestone formation	Table 7.6
BL2	Bottom Bembridge Limestone formation	"
R1	Bottom limestone bed in Headon Hill formation?	**Table 7.8**
R2	Top limestone bed in Headon Hill formation?	"
Bou	Ironstone band in Bembridge Marls member close to boundary with Hamstead member in Bouldnor formation?	**Table 7.5**

Table 7.9 Correlation between interpreted reflector in seismic sections shown in Figures 7.54 to 7.57 and stratigraphy.

The axis of the Bouldnor syncline is marked in the line drawing of section 2D2 (Figure 7.56) and transferred to the map assuming a strike of **288°,** the average strike of the interpreted horizons. The position of the syncline axis from the presented data is approximately 1.3 km north east of its position indicated by the geological map after Insole et al. (1998) shown in Figure 7.48.

7.5.4 Traverse section of 3D Chirp volume

Figure 7.58 shows the traverse section of the 3D volume and the part of line 2D3 within the 3D volume (Figure 7.53) together with interpretation. Due to navigation inaccuracies in the 2D line discussed in section 7.2.1 a slightly different section of the seafloor is imaged in both sections. The **seafloor** is dominated by sedimentary waves and the internal reflectors R1 and R2 can be seen close to the **seafloor** in the south-western part of the sections.

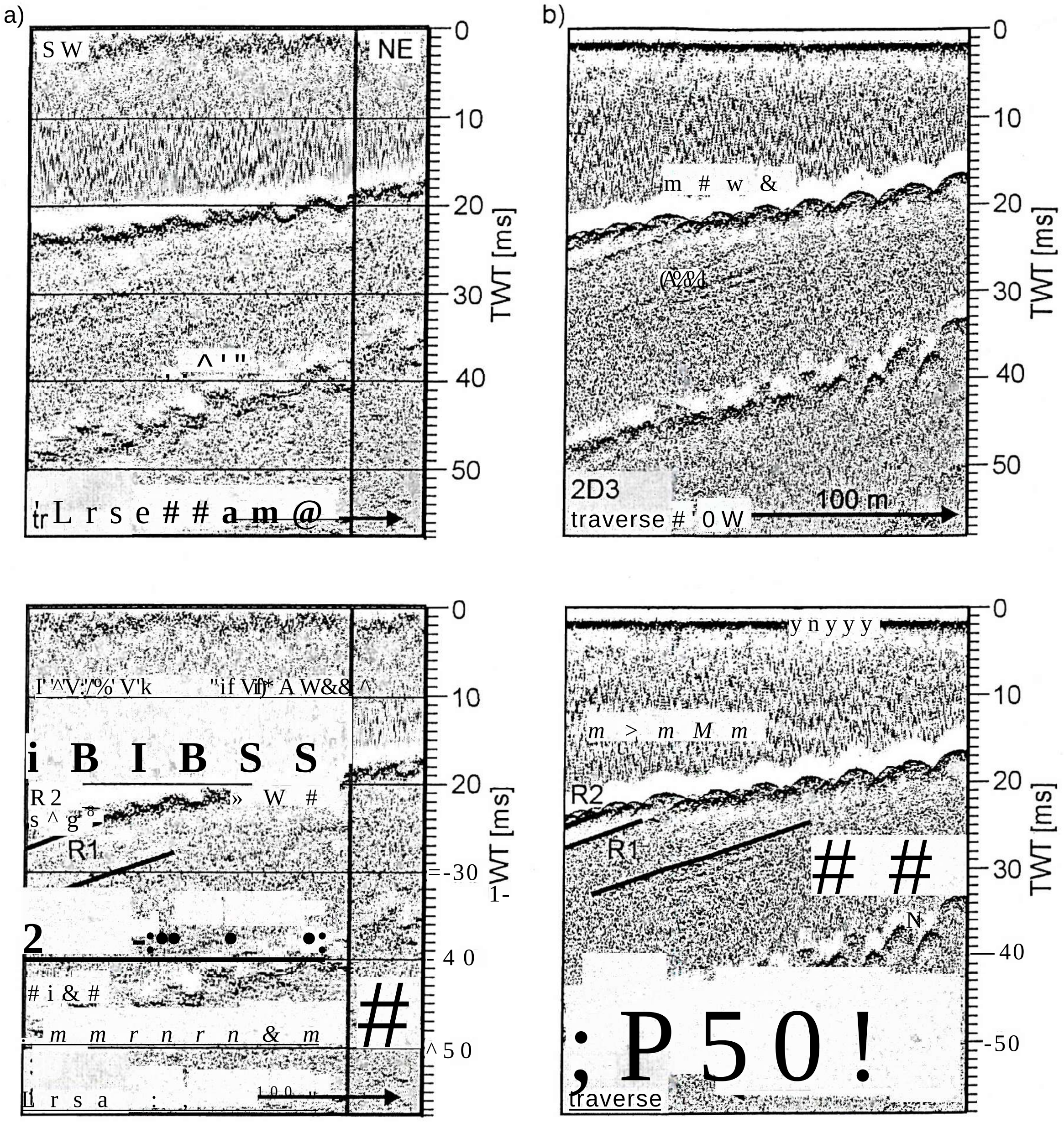

Figure 7.58 a) Traverse section of 3D Chirp data, b) corresponding part of line 2D3 in the 3D Chirp volume. Both sections are shown with and without interpretation. See Figure 7.49 for position of lines.

The bow-tie reflections in the unmigrated 2D section and partly converted into peak and trough features in the 3D section although some parts of the seafloor are smeared.

This demonstrates also that arbitrary sections of the 3D volume can be visualised for interpretation.

7.6 Conclusions

The high resolution 3D Chirp data volume was imaged and cross-sections in any direction can be displayed and analysed including the presented inline and crossline and traverse sections and time slices. **Horizons** can be readily interpreted, revealing their 3D structure. The imaged seafloor topography shows a depression together with sedimentary waves, whose alignments are parallel to the prevailing tidal current direction. Their amplitude ranges from decimetres to approximately 2 m, and their wavelength from 2 m to 20 m. The true dip and strike of internal horizons was determined with an average accuracy of 0.8° and 5° respectively to be gently towards the south.

Comparison between unmigrated single channel 2D data, collected with the 2D and 3D Chirp systems and migrated 3D data revealed a lower data quality of the 3D data caused by smearing of reflectors, which is due to bad positioning of traces and associated static shifts resulting in smearing of reflection amplitudes by the migration algorithm. The bad positioning could be linked to time-shifts between the recorded seismic and position data, which was not fully corrected during data processing. Insufficient accuracy of the RTK-GPS positioning system, possibly caused by bad radio connections between the roving and reference station during data acquisition could be an additional reason. Additional smearing of **reflection** amplitudes by the migration algorithm is caused by the insufficiently small migration aperture radius of 4 m used, chosen to keep the migration time within an acceptable level.

A study of the relationship between data quality and data coverage reveals that areas with low data coverage are associated with bad data quality and abundance of migration artefacts, represented as semi-circular features in vertical cross-sections and circular features in time-slices, whose dimensions equal the migration aperture used. Areas with higher data coverage show varying data quality.

It was deduced that the **reflector** smearing by the migration algorithm is the governing factor for the data quality.

Values for effective horizontal and vertical resolution could not be established due to the lack of structures suitable for a quantitative analysis. However, the lower frequency content of the 3D Chirp data compared to the theoretical expected content, which is achieved by the 2D Chirp system, results in lower expected resolutions of up to 0.1 ms (7.5 cm) in vertical direction and 30 cm after migration in horizontal direction. The effective resolution is expected to vary according to the varying data quality and smearing, which is as large as the migration aperture diameter of 8 m in the horizontal direction.

In future surveys a new acquisition system will be used that assures a full synchronisation between seismic and position data recording and an improved data coverage by using a shot-rate of 4 Hz as opposed to the 1 Hz used for the presented data. Thus it is expected that the data quality can be significantly improved.

The unusual low frequency content, linked to the frequency response of the recording array needs further investigations in tank experiments.

An integrated geological interpretation of the study area showed that the 3D Chirp dataset images clays, shales, marls and limestones of Headon Hill formation of Eocene age with and average strike and dip of 28875.9° located at the eastern **flank** of the Bouldnor syncline. The approximate orientation and position of the syncline axis could be established. The two most prominent reflectors in the 3D data volume (R1 and R2) are associated with a limestone band in the formation described in its terrestrial outcrop.

8 Conclusions and future work

8.1 Conclusions

In this thesis it was demonstrated that a high resolution 3D Chirp data volume can be obtained. The design and application of a high resolution 3D sub-bottom profiler system using a Chirp source was described. The system comprises a rigid array housing the variable source array and 60 receiver groups. It has an overall size of 2.2 m x 2.5 m and is surfaced towed by small survey vessels. A dataset was collected in the West Solent (UK), which was processed to produce the first high resolution 3D Chirp data volume. It images a sedimentary wave covered seafloor and dipping sedimentary rocks of the Headon Hill formation of Eocene age located at the eastern flank of the Bouldnor syncline. Poor time synchronisation of the recorded seismic and positioning data, which could not be fully corrected during data processing has resulted in lower data quality and poorer horizontal and vertical resolution than theoretically expected.

Specifically:

- Chirp source sweeps have been developed, which exploit the entire bandwidth of the source transducers, but which differ in their envelope and instantaneous frequency functions. The sweeps were tested in a seismic reflection sea trial and their resolution and attenuation were compared using novel methodologies. This analysis showed that the newly developed sweeps offer advantages over the 'traditional' sweeps as they improve the resolution capabilities, while having similar or better resistance to attenuation.
- The spatial distribution of maximum possible scattering amplitudes was numerically modelled, using frequency dependent source array and receiver group directivities. The optimal acquisition geometry for the 3D Chirp system, including the geometry of the source array and receiver group and the spacing of the receiver groups, could be deduced from the modelled results to avoid spatial aliasing of the recorded data and assure optimum horizontal resolution.
- It was shown that it is necessary to position the source array and receiver groups of the 3D seismic system with centimetre accuracies in order to correctly sample the wavefield and assure correct processing of the data for the source signatures used. To achieve this accuracy the source array and receiver groups are positioned on a rigid

array and their absolute positions are calculated using a new algorithm that utilises a single position on the array together with its attitude. The position and attitude data is provided by a GPS based RTK-positioning and attitude systems, the only technology that could deliver the required accuracy at the time this research was carried out and that lay within the budget of the project. It was shown that the required accuracies can be achieved.

- The 3D Chirp system design presented comprises a rugged and lightweight structure, which makes it easy to transport and deploy using small survey vessels. Its hydrodynamic behaviour, resulting in low noise generation, allows surveying in typical near coast settings in good sea states.
- The 3D Chirp system performs reliably during data acquisition.
- The processing methods presented, including the newly developed geometry processing algorithms, together with pre-stack Kirchhoff migration, produce a high resolution 3D seismic data volume that can be visualised and interpreted using standard software.
- An integrated geological interpretation of the study area showed that the collected 3D Chirp dataset images clays, shales, marls and limestones of Headon Hill formation of Eocene age located at the eastern flank of the Bouldnor syncline.
- The major shortcoming of the 3D Chirp system is the seismic recording system used for data collection. It is only capable of 1 Hz shot rate and it could not be reliably synchronised with the position data recording. The consequent time shifts between seismic and positioning data, which could not be fully corrected, resulted in positioning errors and significant worsening of the data quality and resolution.

8.2 Future and ongoing work

Since the completion of this work development of a new seismic recording system were advanced and new datasets collected using a shot-rate of 4 Hz, while fully synchronising the positioning and seismic data recording. It is expected that the collected data can be positioned with the required high accuracy, resulting in a significant improvement of the data quality and horizontal and vertical resolution.

The new datasets image small scale objects of archaeological and marine engineering interests and the analysis of the data volumes is expected to reveal the capabilities of the 3D Chirp system for object detection.

The reasons for the lack of high frequencies in the spectrum of the recorded signal need to be investigated and corrected. Water-tank tests are planned to measure the frequency response of the receiver group embedded in the 3D Chirp structure.

The migration algorithm used needs to be adapted for the 3D Chirp data volume. The newly acquired data volumes can be used to investigate a wider range of migration algorithms and parameters than has been done so far. In particular it is necessary to increase the migration aperture, thus increasing data quality and resolution, while keeping the migration time within an acceptable limit. The implementation of an on-line algorithm is desirable to produce a migrated data volume during data collection.

Appendix A

Matlab code for reflection amplitude model

The specular reflection amplitudes from the seafloor back to the array are modelled depending on the frequency dependent source and receiver array and single receiver directivity.

Explanations:

Line 4-33: parameter input. The parameters are waterdepth, maximal penetration expected, frequency, number of model grid elements, seismic velocity and the geometry of the source and receiver arrays.

Line 35-51: load measured transducer directivity depending on frequency chosen (2, 3.5, **5 or 7.5 kHz).**

Line 57-63: determine size of seafloor area modelled and grid element increments from input parameters.

Line 65-90: determine grid element positions and the direction angles for each grid element.

Line 91-114: calculation of reflection amplitudes for source and receiver array and single transducer.

  Line 94-102: Interpolate measured transducer directivity and calculate reflection amplitudes for each grid element.

  Line 104-108: Compute source array reflection amplitudes for each grid element using the function darray.

  Line 110-114: Compute receiver array reflection amplitudes for each grid element using the function darray.

Line 116-118: calculate spreading factor for each grid element.

Line 120-122: calculate total reflection amplitude by multiplying individual terms.

Line 124-148: function darray, which calculates the directivity for the directivity angles of an array with four elements distributed in a plane depending on the frequency and sound speed in water.

```
1       % reflection amplitude model
2       % MATLAB
```

```

% ------• input model parameters-------

rperp=20;                  % waterdepth
twts=0.035;                % max penetration, defines size of area
f=7500;                    % frequency

nox=100;                   % size of grid in x and y dimension
noy=100;

vw=1500;                   % seismic velocity

xa1=0;                     %define source array element positions
ya1=-0.0915;
xa2=0;
ya2=0.0915;
xa3=0.183;
ya3=0;
xa4=-0.183;
ya4=0;

xr1=0;                     % define receiver array element positions
yr1=-0.09375;
xr2=0;
yr2=-0.03125;
xr3=0;
yr3=0.03125;
xr4=0;
yr4=0.09375;

% — end input model parameter------

% load measured transducer directivity
iff=7500
   load dtransmes7500;
   dtransmes=dtransmes7500;
end
iff=2000
   load dtransmes2000;
   dtransmes=dtransmes2000;
end
iff=3500
   load dtransmes3500;
   dtransmes=dtransmes3500;
end
ifp=5000
   load dtransmes5000;
   dtransmes=dtransmes5000;
end


twtw=2*rperp/vw;                              % TWT in water column
lamda=vw/f;                                   % wavelength in water

alphamax=180/pi*acos(twtw/(twtw+twts));       %maximal angle alpha
xmaxpos=tan(pi/180*alphamax)*rperp;

ymax=tan(pi/180*alphamax)*rperp;              % size of seafloor area
xmax=ymax;
yinc=2*ymax/noy;                              % increments in x,y
```

```
xinc=2*xmax/nox;

% coordinates of grid vectors and corresponding directional angles
fori=l:nox+l                          % x(i) vector
   x(i)=-xmax+(i-l)*xinc;
end

forj=l:noy+l                          % y(j) vector
   y(j)=-ymax+(j-1)*yinc;
end

for i=l :nox+l                        % theta(i,j) matrix
   forj=l:noy+l
      theta(i,j)=l 80/pi*atan(y(j)/rperp);
   end
end

fori=l:nox+l                          % psi(i,j) matrix
   forj=l:noy+l
      psi(i,j)=l 80/pi*acos(sqrt(y(j)A2+rperpA2)/sqrt(x(i)A2+y(j)A2+rperpA2));
   end
end

fori=l:nox+l                          % alpha(i,j) matrix
   forj=l:noy+l
      alpha(i,j)=180/pi*acos(cos(pi/180*theta(i,j))*cos(pi/180*psi(i,j)));
   end
end

% directivity functions

% transducer directivity from measurements
polytrans=polyfit(dtransmes(l,:),dtransmes(2,:),5);    % calculate polynomical to fit the
                                                        % measured data for alpha=0-90
fori=l:nox+l
   forj=l:noy+l
      dtrans(i,j)=dtransintxy(polytrans,theta(i,j),psi(i,j),alpha(i,j));
   end
end
dtrans=dtrans./max(max(dtrans));

fori=l:nox+l                                            % array directivity
   forj=l:noy+l
      darray(i,j)=darrayxy(f,theta(i,j),psi(i,j),xal,yal,xa2,ya2,xa3,ya3,xa4,ya4,vw);
   end
end

for i=l :nox+l                                          % receiver directivity
   forj=l:noy+l
      drec(i,j)=darrayxy(f,theta(i,j),psi(i,j),xrl,yrl,xr2,yr2,xr3,yr3,xr4,yr4,vw);
   end
end

% spreading factor
spreadfac=(cos(pi/180*alpha)/rperp).A2;                 % spreadfactor=(cosalpha/waterdepth)A2
spreadfac=spreadfac./max(max(spreadfac));               % normalise

% total amplitude
dtotal=dtrans.*darray.*drec.*spreadfac;
dtotal=dtotal./max(max(dtotal));      % normalise
```

```

function darray=darray(f,theta,psi,xl,yl,x2,y2,x3,y3,x4,y4,vw)

% calculating the directivity of a point array
% theta, phi: directional angles in degrees
% f: frequency
% x,y: point source positions

lamda=vw/f;                        % wavelength
theta=theta*pi/180;                % convert degrees to radians
psi=psi*pi/180;

% real part
realarray=0.25*cos(2*pi/lamda*(xl*sin(psi) + yl*cos(psi)*sin( theta))) ...
      +0.25*cos(2*pi/lamda*(x2*sin(psi) + y2*cos(psi)*sin(theta)))...
      +0.25*cos(2*pi/lamda*(x3*sin(psi) + y3*cos(psi)*sin(theta)))...
      +0.25*cos(2*pi/lamda*(x4*sin(psi) + y4*cos(psi)*sin( theta)));

% imaginary part
imarray=0.25*sin(2*pi/lamda*(xl*sin(psi) + y 1*cos(psi)*sin(theta)))...
     +0.25*sin(2*pi/lamda*(x2*sin(psi) + y2*cos(psi)*sin(theta)))...
     +0.25*sin(2*pi/lamda*(x3*sin(psi) + y3*cos(psi)*sin(theta))) ...
     +0.25*sin(2*pi/lamda*(x4*sin(psi) + y4*cos(psi)*sin(theta))) ;

% magnitude
darray=sqrt(realarray^2+imarray^2);
```

Appendix B

$GPPAT (attitude) and SGPGGA (position) GPS string formats

$GPPAT string (attitude)

$GPPAT,hhmmss.s,ddnrai.irmurim,N,dddmm.m , , , , ff.ff,g.ggg,h.hhh,0/l *hh

hhmmss.s:	**time (hours,minutes,seconds,tenth of second)**
ddmm.mmmm:	**latitude in degrees(d) and minutes(m)**
N:	**latitude north(N) or south(S)**
dddmm.mmmm:	**longitude in degrees(d) and minutes(m)**
W:	**longitude west(W) or east(E)**
±aaaaa.aa:	**altitude in meters**
bbb.bbb:	**heading in degrees**
ieee.ee:	**pitch in degrees**
±fff.ff:	**roll in degrees**
g.ggg:	**attitude phase measurement rms error**
h.hhh:	**attitude baseline length rms error**
0/1 *hh:	**attitude reset flag (0:good attiude, 1:rough estimate or bad attitude) and check sum**

Example:

$GPPAT,061400.00,5043.71351,N,00126.55980, W,00047.60,247.3165,-010.23,-000.02,0.0020,0.0096,0*68

SGPGGA string (position)

SGPGGA,hhmmss.ss,1111.11,N,yyyyy.yy,E,q,ss,d.d,M,s.s,a.a,iiii*hh

hhmmss.ss:	**time (hours,minutes,seconds,tenth and hundredth of second)**	
im.H:	**latitude**	
N:	**latitude north(N) or south(S)**	
yyyyy.yy:	**longitude**	
E:	**longitude east(E) or west(W)**	
q:	**gps quality indicator**	**0:fix not available or invalid**
		1:GPS SPS mode, fix valid
		2differential GPS, SPS mode, fix valid
		4:Real Time Kinematik (KART.LRK)
		5:EDGPS
		6Estimated (Dead Reckoning) Mode
ss:	**number of satellites in use**	
d.d:	**horizontal dilution of precession**	
s.s,M:	**altitude re:mean-sea-level (geoid) in meters**	
x.x,M:	**geoidal separation in meters**	
a.a:	**age of differential GPS data in seconds**	
iiii:	**differential reference station ID (0-1023)**	
***hh:**	**check sum**	

Example:

$GPGGA, 054449.40, 5043.498043,N, 00127.060316, W,4,07,1.1, 46.553,M,0.000, M,1.4,0001*50

Appendix C

Shell script code to combine attitude and position GPS strings and perform quality control

The RTK-GPS position (GPGGA) and attitude (GPPAT) data strings are presented in Appendix B.

Explanations:

- Line1-32: define name of input and output files
- Line 34-53: loop to perform quality control on RTK-GPS position files of day 1
    - Line 36: Julian day for day1 of survey
    - Line 41: discard non-RTK data by checking if column 7 of GPGGA string (Appendix B) contains the value 4 as quality indicator and only use data with ending '.00' in column 2 of the string, i.e. full seconds. Output temporary file to be read in Line 51.
    - Line 44-48: change latitude and longitude format from input string to decimal degree values.
    - Line 51: output temporary qc RTK-GPS file
- Line 55-73: loop to perform quality control on RTK-GPS position files of day 2. The loop is repeated for **day]** to day5 data, but not shown here.
- Line 76-87: loop to perform quality control on ADU5 attitude files of day1
    - Line 82-83: discard data if column 13 of GPPAT string does not start with 0, i.e. bad attitude computation. The heading (column 8) needs to be in the range of 0° and 360°, the heading (column 9) and pitch (column 10) in the range of **-20°** and **20°.** Only full seconds are taken into account, i.e. column 2 ends with '.00'.
    - Line 86: output temporary file
- Line 89-100: loop to perform quality control on ADU5 attitude files of day2. The loop is repeated for **day]** to day5 data, but not shown here.
- Line 104-110: join temporary RTK-GPS and ADU5 attitude files by matching times in their first column for each day separately.

Line 112-121: join separate files into a single output file with formatted output

```
1     #!/bin/ksh

2     # This program reads the rtk and adu strings, discards any invalide data, i.e.
3     # position is not in rtk accuracy and attitude values were not computed
4     # correctly, and combines the files using the time-stamp.
5
6     #######input#####
7     outfile=bc_navcov_juliandays.dat                  #name output file

8
9     #input rtk files dayl                             #defme RTK-GPS files with $GPGGA string
10    infile_rtk0==bc_rtk_090803.Raw
11    infile_rtkl=bcl_rtk_090803.Raw
12    infile_rtk2=bc2_rtk_090803.Raw
13    infile_rtk3=bc3_rtk_090803.Raw
14    infile_rtk4=bc4_rtk_090803.Raw
15    #input rtk files day2
16    infile_rtk5=bc5_rtk_l 00803.Raw
17    infile_rtk6=bc6_rtk_l 00803.Raw
18    inflle_rtk7=bc7_rtk_l 00803. Raw
19    #input rtk files day3 to day5 -not shown-
20
21    #input adu files dayl
22    infile_adul=bc_adu_090803.Raw
23    infile_adu2=bc2_adu_090803.Raw
24    infile_adu3=bc3_adu_090803.Raw
25    infile_adu4=bc4_adu_090803.Raw
26    #input adu files day2
27    infile_adu5=bc5_adu_ 100803 .Raw
28    infile_adu6=bc6_adu_100803.Raw
29    infile_adu7=bc7_adu_l 00803 .Raw
30    #input adu files day3 to day5 -not shown-
31
32    ###################
33
34    # rtk files day 1 manipulation
35    echo starting rtk file manipulation
36    dos=221                                                           #julian day
37    rm temprtkd l.dat
38    for infile_rtk in $infile_rtkO $inflle_rtkl $infile_rtk2 $infile_rtk3 $infile_rtk4
39    do
40            echo $infile_rtk julianday $dos              #print filename and julianday on screen
41            awk -F, '$7=4 && $2 ~ /00$/' $infile_rtk >temp0.dat           #discard any non-rtk data
42            nawk -F, 'BEGIN {dos=ARGV[l];ARGV[l]=""}; #read variable dos from outside awk
43            {
44                    latdeg=int($3/100);latmin=$3-latdeg*100;#position in decimal degrees
45                    latdecdeg=latdeg+latmin/60;
46                    if($4 - /^S$/) latdecdeg=-l*latdecdeg;
47                    londeg=int($5/100);lonmin=$5-londeg*100;londecdeg=londeg+lonmin/60;
48                    if($6 ~ /^W$/) londecdeg=-l *londecdeg;
49
50                    printf "%.6d %d %.8f %.8f %.3f\n" ,$2,dos,latdecdeg,londecdeg,$10;
51                    }' $dos temp0.dat »temprtkdl.dat
52                    rm temp0.dat
53    done
```

```

# rtk files day 2 manipulation
dos=222
rm temprtkd2.dat
for infile_rtk in $infile_rtk5 $infile_rtk6 $infile_rtk7
do
        echo $infile_rtk julianday $dos
        awk -F, '$7=4 && $2 ~ /00$/' $infile_rtk >temp0.dat          #discard any non-rtk data
        nawk -F, 'BEGIN {dos=ARGV[l];ARGV[l]=""};     #read variable dos from outside awk
        {
                latdeg=int($3/100);latmin=$3-latdeg*100;#position in decimal degrees
                latdecdeg=latdeg+latmin/60;
                if($4 ~ /^S$/) latdecdeg=-1 *latdecdeg;
                londeg=int($5/100);lonrnin=$5-londeg*100;londecdeg=londeg+lonmin/60;
                if($6 ~ /^W$/) londecdeg=-l *londecdeg;

                printf "%.6d %d %.8f %.8f %.3f\n" ,$2,dos,latdecdeg,londecdeg,$10;
                }' $dos temp0.dat »temprtkd2.dat
                rm temp0.dat
done
#do same file manipulation for day3 to day5 -not shown-


# adu files dayl manipulation
dos=221
rm tempadudl .dat
for inflle_adu in $infile_adul $infile_adu2 $inf!le_adu3 $inf!le_adu4
do
        echo $infile_adu julianday $dos
        nawk -F, 'BEGIN {dos=ARGV[l];ARGV[l]=""}; #read valuable dos from o. awk
                {if($13-m/&&$8>=0&&$8<=360&&$9>-20&&$9<20&&$10>-20&&$10<20&&$2~/00$/)
                {
                phntf "%.6d %d %.4f %.2f %.2f\n" ,$2,dos,$8,$9,$10}
                }'Sdos $infile_adu »tempadudl.dat
done

# adu files day2 manipulation
dos=222
rm tempadud2. dat
for infile_adu in $infile_adu5 $infile_adu6 $infile_adu7
do
        echo $infile_adu julianday $dos
        nawk -F, "BEGIN (dos=AR.GV[l];ARGV[l]=""}; #read valuable dos &om o. awk
                {if(S13~r0/&&$8>=0&&58<=360&&$9>-20&&$9<20&&510>-20&&S 10<20&&$2-/00$/)
                {
                printf "%.6d%d%.4f%.2f%.2f\n" ,$2,dos,$8,$9,$10}
                }' Sdos $infile_adu »tempadud2.dat
done

echo adu file manipulation done

#join files
echo start joining rtk and adu files
join temprtkdl.dat tempadudl .dat >tempjoindl.dat
join temprtkd2.dat tempadud2.dat >tempjoind2.dat
join temprtkd3.dat tempadud3.dat >tempjoind3.dat
join temprtkd4.dat tempadud4.dat >tempjoind4.dat
join temprtkd5.dat tempadud5.dat >tempjoind5.dat
```

```

nawk '{printf "%d %.6d %.8f %.8f %.3f %.4f %.2f %.2f\n" ,32,$ 1,$3,$4,$5,$7,$8,$9 \
            }' tempjoindl.dat >$outfile
nawk '{printf "%d %.6d %.8f %.8f %.3f %.4f %.2f %.2f\n",$2,$1,$3,$4,$5,$7,$8,$9 \
            }' tempjoind2.dat »$outf!le
nawk '{printf "%d %.6d %.8f %.8f %.3f %.4f %.2f %.2f\n",$2,51,$3,$4,$5,$7,$8,$9 \
            }' tempjoind3.dat »$outfile
nawk '{printf "%d %.6d %.8f %.8f %.3f %.4f %.2f %.2f\n",$2,$1,$3,$4,$5,$7,$8,$9 \
            }' tempjoind4.dat »$outfile
nawk '{printf "%d %.6d %.8f %.8f %.3f %.4f %.2f %.2f\n" ,$2,$1,$3,$4,$5,$7,$8,$9 \
            }' tempjoind5.dat »$outfile
```

Format of output file:

Julian day | Time in hhmmss | latitude | longitude | WGS84 altitude in m | heading | pitch | roll

Example:

221 061446 50.72805117 -1.44436303 48.517 226.1970 -10.96 0.00

Shell script and GMT code to perform WGS84 to UTM conversion.

```
#!/bin/ksh
# convert wgs84 lat Ion into local utm data

infile=bc_navco v J uliandays. dat            #define input file
outfile=bc_navcov_juliandays.utm              #define output file

awk' {print $4,$3,$1,$2,$5,$6,$7,$8}' Sinfile >temp.wgs               #resort columns of input file
gmtset DEGREE_FORMAT 5                  #change degree format to match format in input file
mapproject temp.wgs -Ju30/1 -R-1.46/-1.43/50.72/50.74 -F >temp.utm  #perform transformation
awk '{print $3,$4,$1,$2,$5,$6,$7,$8}' temp.utm >$outfile               #resort colums of output file

rm temp.utm      #delete temporary files
rm temp.wgs
```

Format of outputfile:

Julian day | Time in hhmmss | northing in m | easting in m | WGS84 altitude in m | heading | pitch | roll

Example:

221 061446 1131.22 918.299 48.517 226.1970 -10.96 0.00

Appendix D

FORTRAN code to merge combined navigation data and seismic shot data files

A correction for the time-shift between navigation and seismic data recording is implemented.

Input file formats

Combined navigation file:

Julian day | Time in hhmmss | northing in m | easting in m | WGS84 altitude in m | heading | pitch | roll

Example:

```
221 061446 1131.22 918.299 48.517 226.1970 -10.96 0.00
```

Shotfile:

SIN, Julian day, time, FFID

Example:

```
        1,     221.00 ,  62957.00,  1.0000000,
```

```
program mergesinnav

! define variables
implicit none
logical:: match
integer:: i,j,k,l,eseis,lseis,itl,it2,it3,enav,lnav,ierrl,ierr2,&
          &ierr3,ierr4,ierr5,ierr6,ierr7,ierr8
integer, dimension(:), allocatable :: sin,ffid,dateseis,timeseis&
                                        &,timenav,timeseisnew
real, dimension(:), allocatable :: xa,ya,za,heading,pitch,roll,datenav
real:: datein,timein,ffidin,hour,min,sec,rtl,rt2,rt3,rt4,rt5,rt6
real, dimension(5):: timemin,timemax,imin,imax,sstart,send,iinc
character( 100):: seisfile,navfile,mergefile,timeshiftcontrol

! file name definition
seisfile='sources_all.a_db'             !shot file
navfile='bc_navcovjuliandays.utm'              Icomined navigation file
mergeflle='sinnav.dat'                         {joined output file
timeshiftcontrol='timeshifts.dat'              !control file

! time shifts between seismic and navigation data
! for different days positive values: tseis-tnav>0 i.e. seistime ahead of
! navtime (sections shifted in direction of travel) -> to correct
! subtract values from seismic times

sstart(l)=0                   Itimeshift at start of dayl
send(l)=8                     Itimeshift at end of day 1
sstart(2)=0                   Itimeshift at start of day2
```

```
send(2)=5                   Itimeshift at end of day 2
sstart(3)=0                 Itimeshift at start of day3
send(3)=13                  itimeshift at end of day 2
sstart(4)=0                 Itimeshift at start of day4
send(4)=5                   ! timeshift at end of day 4
sstart(5)=2                 Itimeshift at start of day5
send(5)=9                   Itimeshift at end of day 5

!determine length of seisfile -lseis-
print *,'Determine length of file:§eisfile
open(10,file=seisfile,status='old',access='sequential'&
        &,action='read')
eseis=0
5       if(eseis.eq.O) then
                read( 10,*,iostat=eseis) itl,rtl,rt2,rt3
                lseis=lseis+l
        goto 5
        end if
        lseis=lseis-l
        print *,'length : ',lseis
        close(lO)

! determine length of navigation file -lnav-
print *,'Determine length of file: '.navfile
open(20,file=navfile,status='old',access='sequential',&
        &action='read')
enav=0
6       if(enav.eq.0) then
                read(20,*,iostat=enav) itl,it2,rtl,rt2,rt3,rt4,rt5,rt6
                lnav=lnav+l
        goto 6
        end if
        lnav=lnav-l
        print *,'length: ',lnav
        close(20)

'.allocate memory for seis file variables depending on file length
print *,'Allocating memory for data'
allocate(sin( 1 :lseis),stat=ierr 1)
allocate(dateseis( 1: lseis),stat=ierr2)
allocate(timeseis( 1 :lseis),stat=ierr3)
allocate(timeseisnew(l:lseis),stat=ierr3)
allocate(ffid( 1 :lseis),stat=ierr4)
if(ierrl.ne.0.or.ierr2.ne.0.or.ierr3.ne.0.or.ierr4.ne.0)  then
 print*,'seisfile: allocation request denied'
endif

!allocate memory for nav file variables depending on file length
allocate(datenav(l :lnav),stat=ierrl)
allocate(timenav( 1 :lnav),stat=ierr2)
allocate(xa(l:lnav),stat=ierr3)
allocate(ya( 1 :lnav),stat=ierr4)
allocate(za(l:lnav),stat=ierr5)
allocate(heading( 1 :lnav),stat=ierr6)
allocate(pitch( 1 :lnav),stat=ierr7)
allocate(roll( 1 :lnav),stat=ierr8)
if(ierrl.ne.0.or.ierr2.ne.0.or.ierr3.ne.0.or.ierr4.ne.0&
        .or.ierr5.ne.0.or.ierr6.ne.0.or.ierr7.ne.0.or.ierr8.ne.0)  then
 print*,'seisfile: allocation request denied'
endif
```

```

!read seisfile variables into arrays (length lseis)
print *,'Reading file:', seisfile
open( 10,file=seisfile,status='old',access='sequential'&
            &,action='read')
do i=l,lseis
            read(10,*,end=10) sin(i),datein,timein,ffidin
            dateseis(i)=int(datein)
            hour=int(timein/10000.)                              (change time format into
            min=int((timein-hour*10000)/100.)! seconds
            sec=int(timein-hour* 10000-min* 100)
            timeseis(i)=int(hour*3600+min*60+sec)
            ffid(i)=int(ffldin)
end do
lOclose(lO)


Iread navfile variables into arrays (length Inav)
print *,'Reading file:', navfile
open(20,file=navfile,status='old', access='sequential', &
            &action='read')
doj=l,lnav
            read(20,*,end=20) datenav(j),timein,xa(j),ya(j)&
                        &,za(j),heading(j),pitch(j),roll(j)
            hour=int(timein/10000.)
            min=int((timein-hour* 10000)/100.)
            sec=int(timein-hour* 10000-min* 100)
            timenav(j)=int(hour*3600+min*60+sec)
end do
20close(20)

Itime shift seis file
print *,'time shift correction'

Ifind min and max times position in array for each day
do j=l,5  !initialise timemin, timemax (daystart->dayend) (221->225)
            timemin(j)=999999
            timemax(j)=0
end do
doj=l,5  !
            do i=l,lseis
            if(j.eq.dateseis(i)-220) then
                        if(timeseis(i).lt.timemin(j)) then
                                    timemin(j )=timeseis(i)
                                    imin(j)=i
                        elseif(timeseis(i).gt.timemax(j)) then
                                    timemax(j)=timeseis(i)
                                    imax(j)=i
                        end if
            end if
            end do
end do
            print *,'day, timemin, timemax, imin, imax'
doj=l,5
            print *,j\timemin(j),timemaxO),imin(j),imax(j)
end do
            print *

!subtract timeshifts, calculated from sstart and send to timeseis
do j=l,5  !increment for each day
```

```
    iinc(j)=int((imax(j)-imin(j))/(send(j)-sstart(j)+l))
end do

open( 100,file=timeshiftcontrol,status='replace', access='sequential'&
    &,action='write')
do j=l,5  !add timeshift
    do k=l,send(j)-sstart(j)+l
        do HminO')+(k-l)*iincO'),imin(j)+k*iinc(j)-l
            timeseisnew(l)=timeseis(l)-sstart(j)-(k-l)
        end do
    end do
end do

doi=l,lseis          ! set time values to previous time values+1 if they have
                     !not been calculated because of division and int calculation
                     (slightly lunsymetric splits)
    if(timeseisnew(i).eq.O) then
        timeseisne w(i)=timeseisne w(i-1)+1
    end if
    write(100,*) sin(i),timeseis(i),timeseisnew(i),ffid(i)
end do
close(lOO)

! merge files by date and new time (timeseisnew) variables - if no match ! found zero values
print *,'Merging files. Output: ', mergefile
open(30,file=mergefile,status='replace',access='sequential'&
    &,action='write')
doi=l,lseis
    match=.false.
    doj=l,lnav
        if(dateseis(i).eq.datenav(j).and.timeseisnew(i).eq.timenav(j))  then
        write(30,*) dateseis(i),timeseis(i),timeseisnew(i),sin(i),&
        &ff!d(i),xa(j),ya(j),za(j),heading(j),pitch(j),rollti)
        match=.true.
        end if
    end do
    if(.not.match) then
        write(30,*) dateseis(i),timeseis(i),timeseisnew(i),sin(i)&
        &,md(i),0,0,0,0,0,0
    end if
end do
30close(30)
print *,'Done'

end program mergesinnav
```

Output data-file format:

```
Julian day | time before shift in s | time after shift- in s | SIN | FFID
| easting in m | northing in m | altitude WGS84 in m | heading | pitch |
roll
```

Example:

```
221 23397 23397 1 1 1115.56 711.844 47.181 239.3963 .3.17 -5.22
```

Appendix E

FORTRAN code to merge shot-navigation data and seismic trace data flies

Explanation:

Line 28-116: determine length of input files and read into memory.

Line 117-138: produce shot output-file. For all values of the mergefile that contains valid navigation data the position of the source array is computed using the function cotrans and subsequently performing a translation to the antenna position. See Chapter 2 for details.

Line 140-165: produce trace output-file. The SIN values of the mergefile and trace-input file are matched. For all values of the mergefile that contains valid navigation data the positions of the receiver arrays are computed using the function cotrans and subsequently performing a translation to the antenna position. See Chapter 2 for details.

Line 140-165: Function cotrans: calculating source and receiver array positions depending on heading, pitch and roll. See Chapter 2 for details.

```
1         program mergesinnav_trc
2
3         ! define variables
4         implicit none
5          integer :: date,time,timenew,eml,1ml,ltrc,itl,etrc,ierrl,ierr2,ierT3,ierr4,ierr5,&
6                   &ierr6,ierr7,ierr8,ierr9,ierrl0,ierrl l,i,j,c,ffid
7          integer, dimension(:), allocatable :: sin_m,trc,sin_trc,chn_t
8          integer, dimension(60):: chn_srp
9          real:: chnr,sin_tr,rtl,rt2,xsour,ysour,zsour,pi,x_coord,y_coord,&
10                  &depth,rec_x,rec_y,rec_z,com_x,com_y,com_z
11         real, dimension(:), allocatable :: xa,ya,za,heading,pitch,roll
12         real, dimension (60):: xrecr,yrecr,zrecr,chn_r
13         real, dimension(3):: posrot
14         character(lOO) :: mergefile 1 ,trcfile,srposfile,traceout,shotout
15         parameter(pi=3.14159265358979)
16
17        mergefilel='sinnav.dat'              !SIN-navigation file
18        trcfile='traces_all.a_db'             .'trace file
19        srposfile='srpositionsfmal.dat'       !file containg source and receiver array positions
20        shotout='shotout.dat'                 '.shot output file to be read into ProMax database
21        traceout='traceout.dat'               !trace output file to be read into ProMax database
22
23        ! centre of mass with respect to antenna-> rotation around this point
24         com_x=1.316
25         com_y=0.75
```

```
 com_z=-0.9

 ! determine length of mergefilel -1ml-
print *,'Determine length of file:',mergefilel
open( 10,file=mergeflle 1,status='old',access='sequential'&
          &,action='read')
eml=0
lml =0
 10       if(eml.eq.O) then
                    read(10,*,iostat=eml)
                    lml=lml+l
          goto 10
          end if
          lml=lml-l
          print *,'length : ',1ml
          close(lO)

 ! determine length of trcfile -ltrc-
print *,'Determine length of file:',trcfile
open(20, file=trcfile,status='old', access='sequential'&
          &,action='read')
etrc=0
20        if(etrc.eq.0) then
                    read(20,*,iostat=etrc) itl,rtl,rt2
                    ltrc=ltrc+1
          goto 20
          end if
          ltrc=ltrc-l
          print *,'length : ',ltrc
          close(20)

 !allocate memory for mergefilel variables depending on file length
print  , Allocating memory for data'
allocate(sin_m(l :lml),stat=ierrl)
allocate(xa(l :lml),stat=ierr2)
allocate(ya(l:lml),stat=ierr3)
allocate(za( 1:1ml ),stat=ierr4)
allocate(heading(l:lml),stat=ierr5)
allocate(pitch(l :lml),stat=ierr6)
allocate(roll(l:lml),stat=ierr7)
 !print error message if memory allocation is not successfull
if(ierrr.ne.0.or.ierr2.ne.0.or.ierr3.ne.0.or.ierr4.ne.0.or.ierr5.ne.0&
          .or.ierr6.ne.0.or.ierr7.ne.0) then
 print*,'mergefilel: allocation request denied'
endif

 ! allocate memory for tracefile variables depending on file length
ierrl=0; ierr2=0; ierr3=0;
allocate(trc(l:ltrc),stat=ierrl)
allocate(sin_trc(l :ltrc),stat=ierr2)
allocate(chn_t(l:ltrc),stat=ierr3)
Iprint error message if memory allocation is not successfull
if(ierrl.ne.0.or.ierr2.ne.0.or.ierr3.ne.0) then
 print*,'tracefile: allocation request denied'
endif

!read mergefilel variables into arrays (length lml)
print *,'Reading file:', mergefilel
open( 10,file=mergefile 1,status='old',access='sequential'&
          &,action='read')
```

```
 do i=1,lml
        read(10,*) date,time,timenew,sin_m(i),ffid,&
                &xa(i),ya(i),za(i),heading(i),pitch(i),roll(i)
 end do

 ! express attitude values in radians
 do i= 1,1ml
     heading(i)=heading(i)*pi/180.
     pitch(i)=pitch(i)*pi/180.
     roll(i)=-l*roll(i)*pi/180.       !tilt test showed that angle defined contrary to algorithm!!
 end do

 !read tracefile variables into arrays (length 1ml)
 print *,'Reading file:', trcfile
 open(20,file=trcfile,status='old', access='sequential'&
        &,action='read')
 doj=l,ltrc
        read(20,*) trc(j),sin_tr,chnr
        chn_t(j)=int(chnr)
        sin_trc(j)=int(sin_tr)
 end do

 !read position file into arrays (fixed length of 61 - 1 source and 60 rec positions)
 print *,'Reading file:', srposfile
 open(30, file=srposfile, status='old', access='sequential'&
        &,action='read')
 read(30,*) itl,xsour,ysour,zsour !read rexaive source position
 doc=1,60
        read(30,*) chn_r(c),xrecr(c),yrecr(c),zrecr(c)
 end do

 (produce the shot-outputfile
 print *,'write shotfile: '.shotout
 open(40,file=shotout,status='replace',access='sequential'&
        &,action='write')
 do i= 1,1ml Imergefile
        if(xa(i).eq.0.and.ya(i).eq.0.and.za(i).eq.0) then !data gaps
               ! write zero values for data gaps
               write(40,*) sin_m(i),0,0,0
        else !no data gap
        ! compute position of source array using function cotrans with respect to intrinsic system of
        [coordinates
        posrot=cotrans(heading(i),pitch(i),roll(i),xsour-com_x&
        &,ysour-com_y,zsour-com_z,com_x,com_y,com_z)
        (absolute position by translation: antenna position + source position in intrinsic s.c.
        x_coord=xa(i)+posrot(l)   ! source x-coordinate
        y_coord=ya(i)+posrot(2)   !source y-coordinate
        depth=za(i)+posrot(3)     !source z-coordinate
        write(40,*) sin_m(i),x_coord,y_coord,depth         ! write source output file
        end if
 end do
 close(40)
 print *,'done'

 (produce the trace outputfile
 print *,'write trace file: '.traceout
 open(50,file=traceout,status='replace',access='sequential'&
        &,action='write')

 do j=(60*i-59),(60*i)     ! channels
```

```
        if(sin_trc(j).eq.sin_m(i)) then      !match trace and mergefile SIN
          if(xa(i).eq.0.and.ya(i),eq.0.and.za(i).eq.0) then
           ! write zero values for data gaps
           write(50,*) trc(j),0,0,0
          else !no data-gap
                '.compute position of source array using function cotrans with respect to intrinsic system of
                [coordinates
           posrot=cotrans(heading(i),pitch(i),roll(i),xrecr(chn_t(j))-com_x,&
                       &yrecr(chn_tO'))-com_y,zrecr(chn_tG))-com_z,com_x,com_y,com_z)
           '.absolute position: antenna position + rotated rel. source pos.
           rec_x=xa(i)+posrot(l)          [receiver x-position
           rec_y=ya(i)+posrot(2)          !receiver y-position
           rec_z=za(i)+posrot(3)          [receiver z-position
           write(50,*) trc(j),rec_x,rec_y,rec_z       ! write receiver output file
          end if
        end if
      end do
    end do
     close(50)
    print *,'done'

    contains
    function cotrans(phi,theta,psi,x,y,z,com_x,com_y,comjz)
    [change of coordinates through rotation depending on heading, pitch and roll
    implicit none
    dimension cotrans(3)
    real:: A(3,3),pos(3),x,y,z,cosphi,sinphi,costheta,sintheta,cospsi,sinpsi,&
             &tantheta,phi,theta,psi,cotrans,pi,check,com_x,com_y,comjz,com(3)&
             &rotl(3),rot2(3)
    integer :: i
    parameter(pi=3.141592653 58979)
    pos(l)=x
    pos(2)=y
    pos(3)=z
    com(l)=-com_x
    com(2)=-com_y
    com(3)=-com_z

    [used trigonometric functions of the angles
     cosphi=cos(phi);
     sinphi=sin(phi);
     costheta=cos(theta);
     sintheta=sin(theta);
     cospsi=cos(psi);
     sinpsi=sin(psi);
     tantheta=tan(theta);

    [define unit vectors depending on heading, pitch and roll
    if(phi.eq.0.or.phi.eq.2*pi) then [exception for phi=0,360
       A(l,2)=0;
       A(2,2)=costheta;
       A(3,2)=sintheta;
       A( 1, l)=sqrt( l-(tantheta**2+l)*sinpsi**2);
       A(2,l)=-tantheta*sinpsi;
       A(3,l)=sinpsi;
    elseif(phi.eq.pi) then [exception for phi=180
       A(l,2)=0;
       A(2,2)=-costheta;
       A(3,2)=sintheta;
       A(l,l)=-sqrt(l-(tantheta**2+l)*sinpsi**2);
```

```
      A(2, l)=tantheta*sinpsi;
      A(3,l)=sinpsi;
   else !for all other angles
      A(l,2)=costheta*sinphi;
      A(2,2)=costheta*cosphi;
      A(3,2)=sintheta;
      A(2,l)=- cosphi*tantheta*sinpsi-sinphi*sqrt(cospsi**2-tantheta**2*sinpsi**2);
      A(l,l)=-l/sinphi*(A(2,l)*cosphi+tantheta*sinpsi);
      A(3,l)=sinpsi;
   endif

   !third vector is cross products A(:,3)=c x b
   A( 1,3)=A(2,1 )*A(3,2)-A(3,1 )*A(2,2)
   A(2,3)=A(3,1)*A( 1,2)-A( 1,1)*A(3,2)
   A(3,3)=A(1,1)*A(2,2)-A(2,1)*A(1,2)

   [coordinate transformation
   rotl=matmul(A,pos)
   rot2=matmul(A,com)
   do i=l,3
   cotrans(i)=rotl(i)-rot2(i)
   end function cotrans
   enddo

   end program mergesinnav_trc
```

Input data-file format SIN-navigationfile ('mergefilel '):

```
Julian day | time before shift in s | time after shift in s [ SIN | FFID
 | easting in m  | northing in m  | altitude WGS84 in m  | heading  | pitch  |
roll
```

Example:

```
221 23397 23397 1 1 1115.56 711.844 47.181 239.3963 3.17 -5.22
```

Input data-file format trace-file:

```
TRC, SIN, FFID
```

Example:

```
           1,    1.000000  , 1.0000000,
```

Output data-file format shot-file ('shotout')

SIN |X_COORD x-position |**Y_COORD** y-position |DEPTH z-position

```
1 1115.5599 711.8344 47.09151
```

Output data-file format trace-file ('traceout')

TRC |REC_X x-position |REC_Y y-position |REC_DEP z-position

```
1 1115.662 710.4485 47.2398
```

Input data-file containing source and receiver array positions ('srposfile'):

Number (0: source 1-60: receivers)	x	y	z
0	1.316	0.75	-0.99
1	2.566	1.375	-0.99
2	2.566	1.125	-0.99
3	2.566	0.875	-0.99
4	2.566	0.625	-0.99
5	2.566	0.375	-0.99
6	2.566	0.125	-0.99
7	2.316	1.375	-0.99
8	2.316	1.125	-0.99
9	2.316	0.125	-0.99
10	2.066	1.375	-0.99
11	2.066	1.125	-0.99
12	2.066	0.875	-0.99
13	2.066	0.625	-0.99
14	2.066	0.375	-0.99
15	2.066	0.125	-0.99
16	1.816	1.375	-0.99
17	1.816	1.125	-0.99
18	1.816	0.875	-0.99
19	1.816	0.625	-0.99
20	1.816	0.375	-0.99
21	1.816	0.125	-0.99
22	1.566	1.375	-0.99
23	1.566	1.125	-0.99
24	1.566	0.375	-0.99
25	1.566	0.125	-0.99
26	1.316	1.375	-0.99
27	1.316	1.125	-0.99
28	2.316	0.875	-0.99
29	2.316	0.625	-0.99
30	2.316	0.375	-0.99
31	0.316	0.875	-0.99
32	0.316	0.625	-0.99
33	0.316	0.375	-0.99
34	1.316	0.375	-0.99
35	1.316	0.125	-0.99
36	1.066	1.375	-0.99
37	1.066	1.125	-0.99
38	1.066	0.375	-0.99
39	1.066	0.125	-0.99
40	0.816	1.375	-0.99
41	0.816	1.125	-0.99
42	0.816	0.875	-0.99
43	0.816	0.625	-0.99
44	0.816	0.375	-0.99
45	0.816	0.125	-0.99
46	0.566	1.375	-0.99
47	0.566	1.125	-0.99
48	0.566	0.875	-0.99
49	0.566	0.625	-0.99
50	0.566	0.375	-0.99
51	0.566	0.125	-0.99
52	0.316	1.375	-0.99
53	0.316	1.125	-0.99
54	0.316	0.125	-0.99
55	0.066	1.375	-0.99
56	0.066	1.125	-0.99

57	0.066	0.875	-0.99
58	0.066	0.625	-0.99
59	0.066	0.375	-0.99
60	0.066	0.125	-0.99

Appendix F

Matlab code simulating the effects of time-shift between recording of navigation and seismic data

Matlab function that simulates a correction of time-offset between seismic and navigation data by shifting the elements in the vector containing seafloor TWT picks.

The program performs shifts of vector elements by linearly approximation of the time differences given as the offset between seismic time and navigation time $t_{seis}-t_{nav}$ at the start and at the end of the survey day.

Explanations:

Line 1: function Input: seafloor TWT picks, ostart: $t_{nav}-t_{seis}$ at start of survey day, oend: $t_{nav}-t_{seis}$ at end of survey day. The definition of the time offset given in Chapter 6 changed sign.

Line 9-23: case 1 $t_{nav}-t_{seis} \geq 0$ at start and end of the survey day.

Line 10: introduce constant shift of vector elements according to start value.

Line 11: compute length of parts for the case that seafloor TWT vector is divided in (oend-ostart+1) parts.

Line 13-22: produce vector with addvalue (Line 7) padded in between parts.

Line 23: Reduce length of seafloor TWT vector to original length.

Line 25-40: case 2 $t_{nav}-t_{seis} \leq 0$ at start and end of the survey day. The same algorithms as for case 1 but instead of adding elements to the vector, elements are deleted.

Line 22-44: case 3 $t_{nav}-t_{seis} = 0$ at start and end of the survey day. No change of vector.

Line 44-46: other cases are not considered as they are do not appear in the analysed data.

```
%simulate linear time shift data by splitting vector and introducing values
%in between for positive values (shift to right) tnav-tseis >0 or deleting values for
%negative values (shift to left) tnav-tseis<0 -definition contrary to text in Chapter 6 -

function seafloorshift=timeshift(seafloor,ostart,oend)

addvalue=20;                          % value to be padded for time shifts

if ostart>=0 & oend>0                                    %positive values  > right shift add
   constshift=circshift(seafloor,ostart)';               %constant shift of ostart
   parts=(length(constshift)/(abs(oend-ostart)+l));      %calculate length of parts as start value
                                                         %for loop
   while (abs(parts-double(intl6(parts)))>0)             %padding the file such that parts
                                                         %are equal sized integer length
      constshift=[constshift addvalue];
      parts=abs((length(constshift)/(abs(oend-ostart)+l)));  %flnal length of parts
   end

   seafloorshift=constshift(l :parts);    %split file in parts and pad values between the parts
   for i=2: abs(oend-ostart)+1
      seafloorshift=[seafloorshift addvalue constshift( parts*(i-l)+I  : parts*i)];
   end
   seafloorshift=seafloorshift( 1 :length(seafloor));    %cut to length of original file

elseif ostart<=0 & oend<0                                %negative values -> left shift delete
   constshift=circshift(seafloor,ostart)';               %constant shift of ostart
   parts=(length(constshift)/(abs(oend-ostart)+l));      %calculate length of parts as start
                                                                  % value for loop
   while (abs(parts-double(intl6(parts)))>0)             %padding the file such that parts
                                                         %are equal sized integer length
      constshift=[constshift addvalue];
      parts=abs((length(constshift)/(abs(oend-ostart)+l)));  %flnal length of parts
   end
   seafloorshift=constshift(l :parts-l);    %split file in parts and delete values between the parts
   for i=2:abs(oend-ostart)+l
      seafloorshift=[seafloorshift constshift( parts*(i-l)+l  : parts*i-l  )];
   end
   while(length(seafloorshift)<length(seafloor))
   seafloorshift=[seafloorshift addvalue];                        %add values to end of vector
                                                                  %to make it same lenght as input
   end
elseif ostart==0 & oend=0
   seafloorshift=seafloor;
else
   temp='can not handle data input, choose other values'
end
```

References

Allen, R., Crews, G., Guyton, W., McLemore, C. A., Peterson, B., Rapp, C. S., Walker, L., Whigham, L. R., White, D. A. and Wood, G., 1994, Digital field tape format standards - SEG-D, Revision 1. *Geophysics* **59(4),** 668-684.

Ashtech Sagitta Series User Manual, 2002. Thales Navigation Inc., Santa Clara, California, USA.

Ashtech ADU5 Operation and reference manual, 2002. Thales Navigation Inc., Santa Clara, California, USA.

Bull, J. M., Quinn, R. and Dix, J. K., 1998, Reflection Coefficient Calculation from Marine High Resolution Seismic Reflection (Chirp) Data and Application to an Archaeological Case Study. *Marine Geophysical Researches* **20(1),** 1-11.

Burdic, W. S., 1984, Underwater acoustic system analysis. Prentice-Hall.

Claerbout, J. F., 1976, Fundamentals of geophysical data processing: with applications to petroleum prospecting. McGraw-Hill, New York.

Cunningham, A. B., 1979, Some alternate vibrator signals. *Geophysics* 44, 1901-1921.

Daley, B., Edwards, N., 1971, Palaeogene Warping in the Isle of Wight. *Geological Magazine* **108, 399-405.**

Dupuy, D., Hammami, D., Marillier, F., 2004, Lacustrine sediments bemeath last glacial deposits revealed by 2D/3D VHR seismics in Lake Geneva. 1st General Assembly EGU, Nice, France, 25-30 April 2004, Abstract EGY04-A-02014.

GeoFrame, 1995, Schlumberger GeoQuest, Houston, Texas.

Goupillaud, P. L., 1976, Signal Design in the 'Vibroseis' ® Technique. *Geophysics* **41,** 1291-1304.

Gutowski, M, Breitzke, M., SpieB, V, 2002, Fast static correction methods for high-frequency multichannel marine seismic reflection data: A high-resolution seismic study of channel-levee systems on the Bengal Fan. *Marine Geophysical Researches* 23, 57-75.

Hamilton, E. L., 1980, Geoacoustic modelling of the seafloor. *Journal of the Acoustical. Society of* **America 68(5), 1313-1340.**

Harris, F. J., 1978, On the use of windows for harmonic analysis with discrete Fourier transform. *Proceedings IEEE* **66, 51-83.**

Henriet, J. P., Verschuren, M. and Versteeg, W., 1992. Very high resolution3D seismic reflection imaging of small-scale structural deformation. *First Break* **10,** 81-88.

Hobbs, R., Tong, C H., Pye, J., 2003, Modelling and processing of 3D seismic data collected over the overlapping spreading centre on the East Pacific Rise at 9° 03' N. In: Nieuwland, D. A. (ed.), 2003, New Insights into Structural Interpretation and Modelling. Geological Society, London, Special Publication 212, 251-259.

Huuse, M., Mickelson, M., 2004, Eocene sandstone intrusion in the Tampen Spur area (Norwegian North Sea Quad 34) imaged by 3D seismic data. Marine and Petroleum *Geology* **21,** 141-155.

Huvenne, V. A. I., De Mol, B., Henriet, J.-P., 2003, A seismic study of the morphology and spatial distribution of buried coral banks in the Porcupine Basin, SW of Ireland. *Marine Geology* 198, **5-25.**

Insole, A., Daley, B and Gale, A., 1998, The Isle of Wight. Geologists' Association Guide No. 60. Geologists' Association, London.

Jakobsson, M., 1999, First high-resolution chirp sonar profiles from the central Arctic Ocean reveal erosion of Lomonosov Ridge sediments. *Marine Geology.* 158, 111-123.

Jacobson, R. S., 1987, An investigation into the fundamental relationships between attenuation, phase dispersion, and frequency using seismic refraction profiles over the sedimentary structures. *Geophysics* **52(1),** 72-87.

Kallweit, R. S. and Wood, L. C., 1982, The limits of resolution of zero-phase wavelets. *Geophysics* **47, 1035-1046.**

Kearey, P. and Brooks, M., 1991, An Introduction to Geophysical Exploration, Second Edition. Blackwell Science, Oxford.

Kim, G. Y., Kim, D. C., Park, S. C., Lee, G. H., 1999, Chirp (2-7 kHz) echo characters and geotechnical properties of surface sediments in the Ulleung Basin, the East Sea. *Geosciences Journal* **3(4),** 213-224.

Langhome, D. N., Heathershaw, A., D. and Read, A. A., 1986, Gravel Bedforms in the West Solent, Southern England. *Geo Marine Letters* 5, 225-230.

LeBlanc, L. R., Panda, S., Schock, S. G., 1992, Sonar attenuation modeling for classification of marine sediments. *Journal of the Acoustical Society of America* **91(1),** 116-126.

Lester, A., 2002, Design of a Simple Platform to Carry Scientific Instrumentation and Fly Beneath the Sea Free Surface on a Level Path. Final Report on Third Year Project. Department of Ship Science, University of Southampton.

Lumley, D. E., Claerbout, J. F., Bevc, D., 1994, Anti-aliased Kirchhoff 3-D migration. 64th Annual International Meeting, *Society of Exploration Geophysicsts. Expanded Abstracts* **94,** 1282-1285.

Marsset, B., Missiaen, T., De Roeck, Y.-H., Noble, M., Versteeg, W., Henriet, J.-P., 1998, Very high resolution 3D marine seismic data processing for geotechnical applications. *Geophysical Prospecting* 46, 105-120.

Marsset, B (coordinator). Wardell, N., Henriet, J.-P., Davis, A., Noble, M., Andresen, P., 2001, VHR3D Very High Resolution Marine 3D Seismic Method For Detailed Site Investigation. Contract no MAS3-CT97-0121. Final technical Report. 1st March 1998 - 1st March 2001

Medwin, H. and Clay, C. S., 1998, Fundamentals of acoustical oceanography. Academic Press.

Missiaen, T., Versteeg, W., Henriet, J.-P., 2002, A new 3D seismic acquisition system for very high resolution and ultra high resolution shallow water studies. *First Break* **20,** 227-232.

Mtiller, C., Milkereit, B., Bohlen, T., Theilen, F., 2002, Towards high-resolution 3D marine seismic surveying using Boomer sources. *Geophysical Prospecting* **50,** 517-526.

Panda, S., LeBlanc, L. R., Schock, S. G., 1994, Sediment classification based on impedance and attenuation estimation. *Journal of the Acoustical Society of America* **96(5),** 3022-3035.

ProMAX Version 2003.3, 2003, Landmark Graphics Corporation, Houston, Texas.

Pullan, S. E., 1990, Recommended standard for seismic (/radar) data files in the personal computer environment. *Geophysics* **55(9),**1260-1271.

Quinn, R., Bull, J.M. and Dix, J. K., 1997(a). Buried scour marks as indicators of paleo-current direction at the "Marie Rose" wreck site. *Marine Geology* **140,** 405-413.

Quinn, R., Bull, J.M. and Dix, J. K., 1997(b). Imaging Wooden Artefacts with Chirp Sources. *Archaeological Prospecting.* 4, 25-35.

Quinn, R., Bull, J.M. and Dix, J. K., 1997(c). Optimal processing of marine high-resolution seismic reflection (Chirp) data. *Marine Geophysical Researches* **20,** 13-20.

Scheidhauer, M., Dupuy, D., Beres, M., Marillier, F., 2003, Development of a 3D VHR seismic reflection system for lacustrine settings - a case study in Lake Geneva, Switzerland. EGS-AGU-EUG Joint Assembly, Nice, France, 6-11 April 2003, Abstract EAE03-A-02720.

Schneider, W., 1978, Integral formulation for migration in two and three dimensions. *Geophysics,* **43, 49-76.**

Schock, S. G and LeBlanc, L. R., 1990, Chirp Sonar: New Technology for Sub-Bottom Profiling. *Sea Technology* **31(9),** 35-43.

Schock, S. G., LeBlanc, L. R., Mayer, L. A., 1989, Chirp subbottom profiler for quantitative sediment analysis. *Geophysics* 54(4), 445-450.

Schock, S. G., Leblanc, L. R. and Panda, S., 1994, Spatial and temporal pulse design considerations for a marine sediment classification sonar. *IEEE Journal of Oceanic Engineering* **19(3),** 406-**415.**

Schock, S. G., Tellier, A., Wulf, J., Sara, J., Ericksen, M., 2001, Buried object scanning sonar. *IEEE Journal of Ocean Engineering* 26(4), 677-689.

Selby, I. And Foley, M., 1995, An application of chirp acoustic profiling: monitoring dumped muds at sea bed disposal sites in Hong Kong. *Journal of Marine Environmental Engineering* **1(3), 247-261.**

Sheriff, R. E. and Geldart, L. P., 1995, Exploration seismology. 2nd edition. Cambridge University Press.

Stevenson, I. R., McCann, C., Runciman, P. B., 2003, An attenuation-based sediment classification technique using Chirp sub-bottom profiler data and labatory acoustic analysis. *Marine Geophysical Researches* 23(4), 277-298.

Stolt and Benson, 1986, Seismic migration - theory and practise. Geophysical Press, London - Amsterdam.

StrataView user manual, 1995, Geometrix Inc., San Jose, California, USA.

Solomon, A., McCann, C., Sothcott, J., 1999. Attenuation of P- and S-waves in limestones. *Geophysical Prospecting.* 47(3), 359-392.

Taner, M. T., 1978,Complex seismic trace analysis. *Geophysics* 44, 1041-1063.

Verstegg, W., Verschuren, M., Henriet, J.-P. and De Batist, M., 1992, High resolution 3D and pseudo-3D seismic investigations in shallow water environments. In: Weydert, M. (ed.), 1992, European conference on underwater acoustics. London. Elsevier Applied Science, 497-500.

Wardell, N., Diviacco. P., Sinceri, R., 2001, 3D Pre-processing techniques for marine VHR seismic data. Abstract 63rd EAGE Conference, Amsterdam, 2001.

White, H. J. O., 1921, Short Account of the Geology of the Isle of Wight. Memoirs of the geological survey of Great Britain. HMSO, London.

Widess, M. B., 1973, How thin is a thin bed? *Geophysics* **38,** 1176-1180.

Yilmaz, Ö, 1987, Seismic data processing. Investigations in Geophysics, No.2. Society of Exploration Geophysicists, Tulsa, Oklahoma.